Programa de Doctorado Neurociencias

Instituto de Neurociencias (CSIC-UMH)
Universidad Miguel Hernández de Elche

Intra-modal plasticity of somatosensory maps during early mouse development

Doctoral thesis presented by:

Mar Aníbal Martínez

Director:

Guillermina López Bendito, CSIC

San Juan de Alicante, 2025

INSTITUTO DE NEUROCIENCIAS

This Doctoral Thesis, entitled "*Intra-modal plasticity of somatosensory maps during early mouse development*" is submitted under the format of **thesis by compendium** of the following **publications**:

- **A prenatal window for enhancing spatial resolution of cortical barrel maps**

Mar Aníbal-Martínez, Lorenzo Puche-Aroca, Elena Pérez-Montoyo, Gabriele Pumo, María Pilar Madrigal, Luis Miguel Rodríguez-Malmierca, Francisco José Martini, Filippo M. Rijli and Guillermina López- Bendito. Nature Communications. 2025 March; 16, no. 1955. DOI: 10.1038/s41467-025-57052-w.
Impact factor 14.7 (2025 Q1).

- **Input-dependent segregation of visual and somatosensory circuits in the mouse superior colliculus**

Teresa Guillamón-Vivancos, Mar Aníbal-Martínez, Lorenzo Puche-Aroca, Juan Antonio Moreno-Bravo, Miguel Valdeolmillos, Francisco J. Martini, Guillermina López-Bendito. Science. 2022 Aug; 377(6608):845-850. DOI: 10.1126/science.abq2960.
Impact factor 56.9 (2022 Q1).

Dra. Guillermina López-Bendito, director of the doctoral thesis entitled "**Intra-modal plasticity of somatosensory maps during early mouse development**"

REPORTS:

That Mar Aníbal Martínez has performed, under my supervision, the work entitled "**Intra-modal plasticity of somatosensory maps during early mouse development**" pursuant to the terms and conditions established in the Research Plan and following the Code of Good Practices of the Miguel Hernández University of Elche, successfully meeting the objectives planned for its public defence as a doctoral thesis.

In witness whereof I sign for all pertinent purposes, in Sant Joan d'Alacant, on 27th of March of 2025.

Thesis Director
Dra. Dña. Guillermina López Bendito

Dra. María Cruz Morenilla Palao, Coordinator of the Doctoral Programme in Neurosciences at the Institute of Neurosciences in Alicante, a joint center of the Miguel Hernández University (UMH) and the Spanish National Research Council (CSIC),

REPORTS:

That Ms. Mar Aníbal Martínez has performed, under the supervision of our Doctoral Programme, the work entitled "**Intra-modal plasticity of somatosensory maps during early mouse development**" pursuant to the terms and conditions established in the Research Plan and following the Code of Good Practices of the Miguel Hernández University of Elche, successfully meeting the objectives planned for its public defence as a doctoral thesis.

In witness whereof I sign for all pertinent purposes, in Sant Joan d'Alacant, on 27th of March of 2025.

Dra. Dña. María Cruz Morenilla Palao
Coordinator of the PhD Programme in Neurosciences

The present PhD thesis has been funded by the following research agencies: grants from the European Research Council (ERC) under the European Union's Horizon 2020 research and innovation programme (ERC-2021-ADG-101054313 SPONTSENSE), PID2021-127112NB-I00 from the MCIN/AEI /10.13039/501100011033/ and ERDF A way to make Europe, and Generalitat Valenciana, Conselleria d'Educació, Universitats, i Ocupació (PROMETEO 2021/052).

A mis padres y a mi hermano,

a Vero

INDEX

ABBREVIATIONS

A1	Primary Auditory Cortex
A2	Secondary Auditory Cortex
AC1	Adenylyl Cyclase1
ACSF	Artificial Cerebrospinal Fluid
ALBSF	Antero-lateral Barrel Subfield
BCIP	5-Bromo-4-Chloro-30-Indoly Phosphate p-toluidine salt
BDNF	Brain Derived Neurotrophic Factor
Bi-embWPC	Embryonic Bilateral Whisker Pad Cauterization
BMPs	Bone Morphogenetic Proteins
BP	Biological Processes
BSA	Bovine Serum Albumin
CFAs	Corticogufal Axons
CM	Central Medial nucleus
CN	Cochlear Nucleus
contra	Contralateral
COUP-TF1	Nuclear Receptor Subfamily 2, Group F, Member 1
CP	Cortical Plate
CreER	Cre recombinase fused to Estrogen Receptor
CTAs	Corticothalamic Axons
ctrl	control
CytOx	Cytochrome Oxidase
DAB	3-3' diaminobenzidine tetrahydrochloride hydrate
DAPI	4',6-diamidino-2-phenylindole
DBE	Dibenzyl Ether
DCC	Deleted in Colorectal Carcinoma
DCM	Dichloromethane
DEA	Differential Expression Analysis
DEGs	Differentially Expressed Genes
DI	Discrimination Index
DiA	4-[4-(dihexadecylamino) styryl]-N-methylpyridinium iodide
DiD	1,1'-Dioctadecyl-3,3,3',3'-Tetramethylindodicarbocyanine, 4-Chlorobenzenesulfonate salt
DiI	1,1′-dioctadecyl 3,3,3′,3′-tetramethylindocarbocyanine perchlorate
dLGN	dorsal Lateral Geniculate Nucleus
Dlx	Distal-Less Homeobox
dPrV	dorsal portion of the PrV
dSC	deep Superior Colliculus
DTB	Diencephalon-Telencephalon boundary
E	Embryonic day
EGOs	Early Gamma Oscillations
embBE	embryonic Bienucleation

embWPC	embryonic unilateral Whisker Pad Cauterization	**LJ**	Lower Jaw
Emx	Empty spiracles homeobox	**LP**	Lateral Posterior Nucleus
Egr	Early growth factors	**LTD**	Long Term Depression
F0	Baseline Fluorescence	**LTP**	Long Term Potentiation
FGF	Fibroblast Growth Factor	**L4ss**	Layer 4 spiny stellate
FO	First Order	**L4sp**	Layer 4 star pyramidal
FP	Forepaw	**M1**	Primary Motor Cortex
GABA	Gamma-Aminobutyric Acid	**MADM**	Mosaic Analysis with Double Markers
Gbx2	Gastrulation brain homeobox 2	**Mash1 or Ascl1**	Achaete-scute Family bHLH Transcription Factor 1
GCaMP6f	Calmodulin-based genetically encoded fluorescent Calcium indicator 6–fast	**MD**	Medial Dorsal nucleus
GEO	Gene Expression Omnibus	**MF**	Molecular Functions
GFP	Green Fluorescent Protein	**MG**	Medial Geniculate nucleus
GO	Gene Ontology	**MGB**	Medial Geniculate Body
HP	Hindpaw	**MGd**	dorsal division of the Medial Geniculate body
HO	Higher Order	**MGE**	Medial Ganglionic Eminence
IC	Inferior Colliculus	**mGluR**	metabotropic Glutamate Receptor
iDISCO+	Inmunolabelling Imaging of Solvent-Cleared Organs	**MGv**	ventral division of the Medial Geniculate body
IGL	Intergeniculate leaflet	**NBT**	Nitro-Blue Tetrazolium chloride
IPCs	Intermediate Progenitor Cells	**NCBI**	National Center for Biotechnology Information
ipsi	ipsilateral	**Neurog**	Neurogenin
ITI	Inter-Trial Interval	**NGF**	Nerve Growth Factor
L	Layer	**NMDA**	N-Metyl-D-Aspartate
LGE	Lateral Ganglionic Eminence	**NMDAR**	NMDA Receptor

Nrg1	Neuregulin1
Ns	Neurons
ns	not significant
ODCs	Ocular Dominance Columns
OHCs	Outer Hair Cells
Olig	Oligodendrocyte Transcription Factor
p	Prosomere
P	Postnatal day
P0WPC	Postnatal unilateral Whisker Pad Cauterization
Pax6	Paired box 6
PBS	Phosphate-buffered Saline
PCA	Principal Component Analysis
PCR	Polymerase Chain Reaction
PFA	Paraformaldehyde
pHB	perihabenular nucleus
Plcβ1	G-protein-coupled phosphodiesterase
PMBSF	Postero-medial Barrel Subfield
POm	Posterior medial nucleus
PRN	Perireticular nucleus
PrV	Principal Trigeminal Nucleus
PSPB	Pallium-Subpallium Boundary
PT	Pretectum
PTh	Prethalamus
pTH-C	Caudal thalamic progenitor domain
pTH-R	Rostral thalamic progenitor domain
PV	Parvalbumin
RFP	Red Fluorescent Protein
RGCs	Retinal Ganglion Cells
RL	Rostral lateral nucleus
Rlog	Regularized logarithm
RNA	Ribonucleic Acid
RNAseq	RNA sequencing
ROI	Region Of Interest
Rorα	RAR-Related Orphan Receptor Alpha
Rorβ	RAR-Related Orphan Receptor Beta
RTN	Reticular Nucleus
S1	Primary Somatosensory Cortex
S2	Secondary Somatosensory Cortex
SC	Superior Colliculus
scATAC-seq	single-cell ATAC-seq
scRNA-seq	single-cell RNA sequencing
SEM	Standard Error of Mean
SGNs	Spiral Ganglion Neurons
Shh	Sonic hedgehog
SOC	Superior Olivary Complex
Sox2	Sex determining region Y box 2

sp	star pyramidal
SpVir	rostral portion of the interpolaris spinal trigeminal nucleus
SpVic	caudal portion of the interpolaris spinal trigeminal nucleus
Sp8	Trans-Acting Transcription Factor 8
ss	spiny stellate
sSC	superficial Superior Colliculus
SSNs	Spiny Stellate Neurons
SST	Somatostatin
SP	Subplate
SPNs	Subplate Neurons
SVM	Support Vector Machine
T	Trunk
t_1	sample session
t_2	test session
TCAs	Thalamocortical Axons
TF	Transcription Factor
TG	Trigeminal Ganglion
Th	Thalamus
Th^{kir}	Thalamic Kir
TRN	Thalamic Reticular Nucleus
TTX	Tetrodotoxin
ul	upper lip
uls	upper lip stimulation
ulVPM	upper lip input-receiving VPM
V1	Primary Visual Cortex
V2	Secondary Visual Cortex
vGlut2	vesicular Glutamate transporter type 2
VL	Ventral lateral nucleus
vLG	ventral Lateral Geniculate nucleus
VPM	Ventral Posterior Medial nucleus
VPMvl	ventral lateral VPM
VPN	Ventral posterior nucleus
vPrV	ventral portion of the PrV
VZ	Ventricular Zone
Wnt	Wingless-type MMTV Integration Site Family
wp	whisker pad
WPC	Whisker Pad Cauterization side
wps	whisker pad stimulation
wpVPM	whisker pad input-receiving VPM
ZI	Zona Incerta
ZLI	Zona Limitans Intrathalamica
3V	third ventricle
5-HT	serotonin or 5-hydroxytryptamine

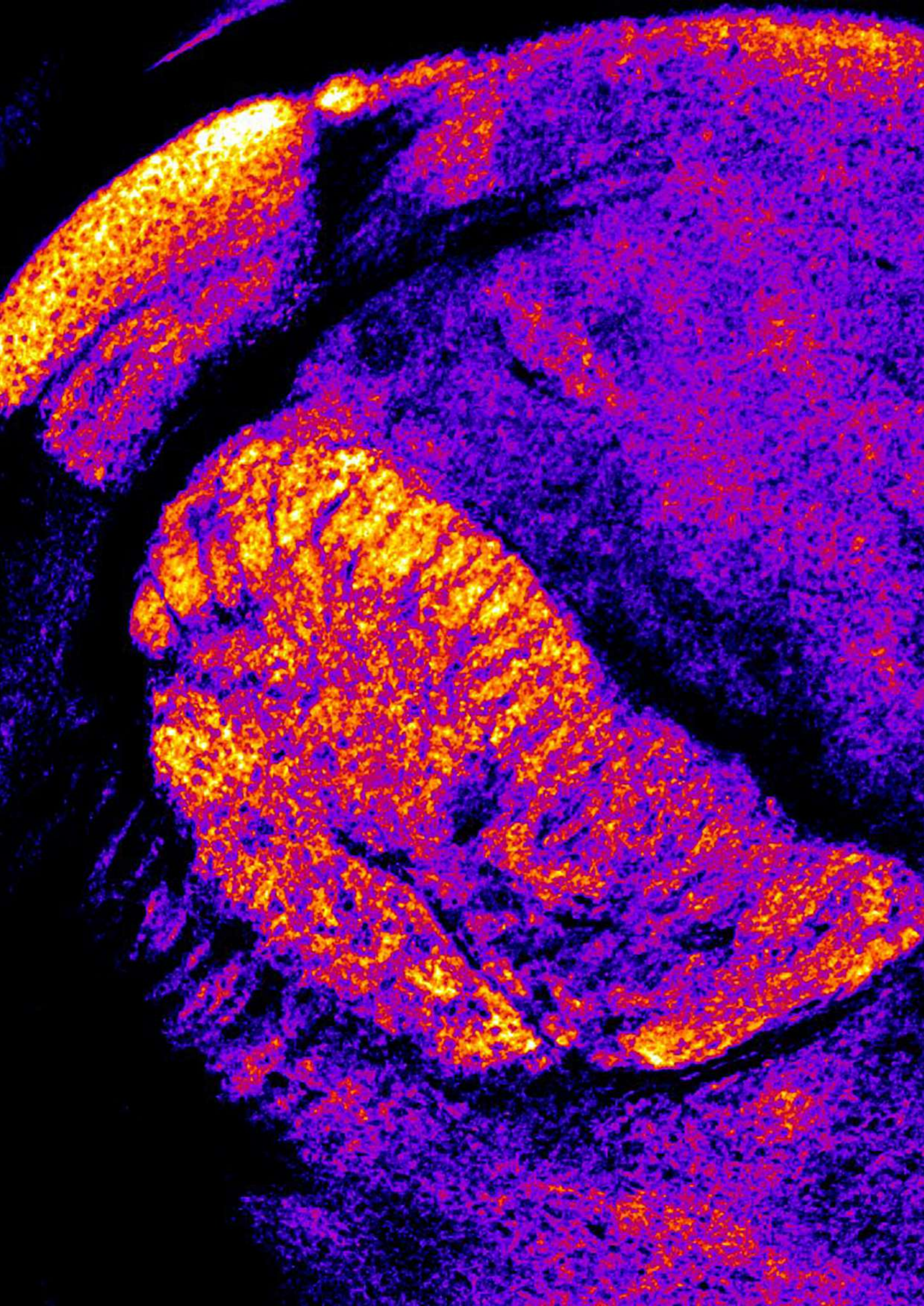

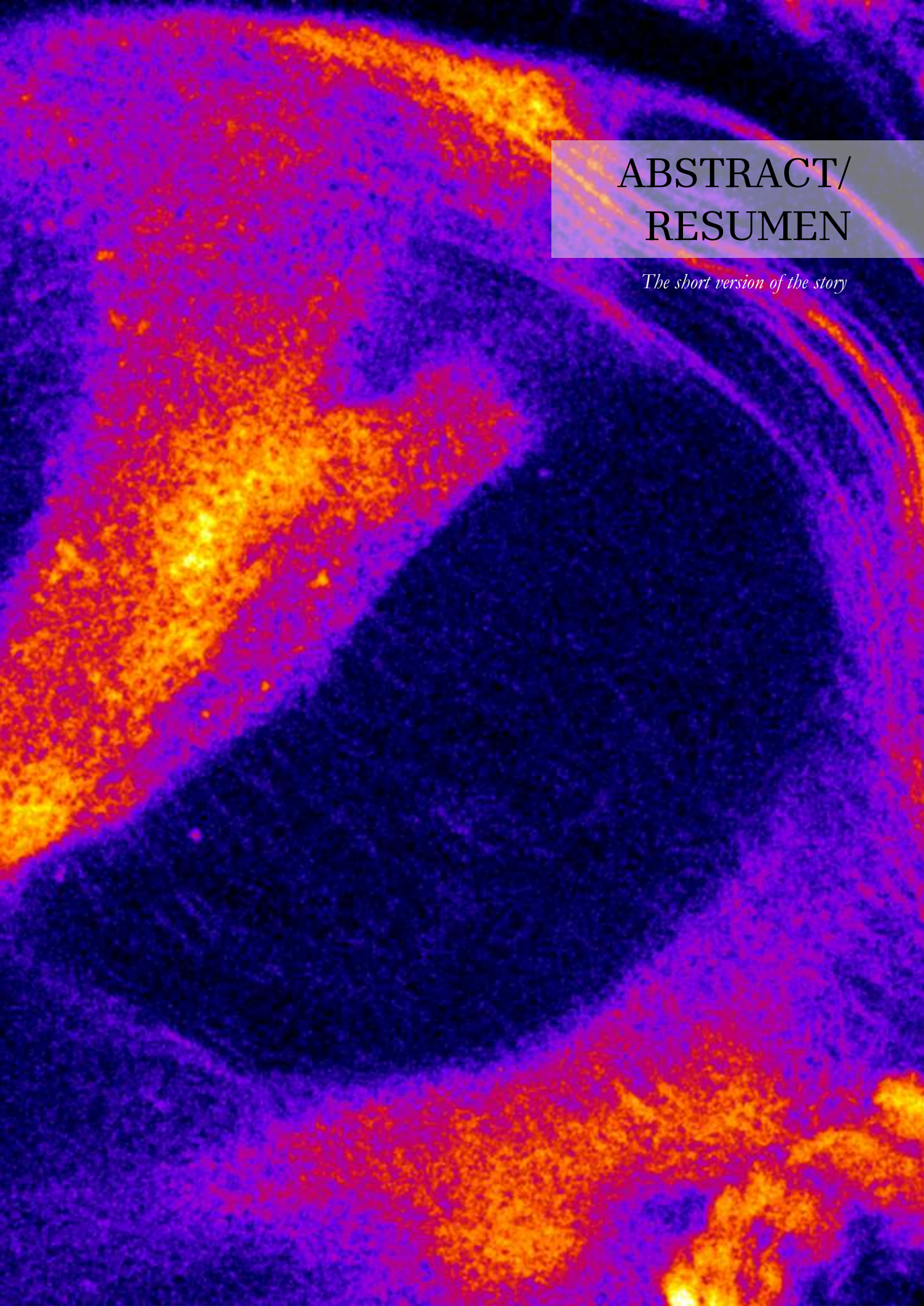

ABSTRACT/ RESUMEN

The short version of the story

ABSTRACT

The precise mapping of sensory inputs onto cortical regions is critical for accurate sensory processing, as illustrated in the rodent primary somatosensory cortex (S1), where mystacial and upper lip whiskers are represented into distinct cortical maps: the postero-medial barrel subfield (PMBSF) and the antero-lateral barrel subfield (ALBSF). While the developmental timeline of PMBSF maps across somatosensory pathways is well-characterized, the mechanisms underlying the intra-modal positioning and dedicated cortical territories of these barrel-field patterns remain elusive. Our findings reveal that as early as embryonic day 18 to postnatal day 0, S1 barrel-field territories can be distinguished by facial stimulation-evoked responses and exhibit region-specific transcriptional profiles in the thalamus. To explore the processes driving this segregation, we developed a mouse model in which the mystacial whisker pad was unilaterally ablated during embryonic development. This model uncovered a critical prenatal window during which cortical maps are established, revealing a profound remapping of barrel-field territories. Specifically, ALBSF barrels, typically smaller and less distinct than the large, sharply defined PMBSF barrels, exhibited enhanced size and definition. These differences, traditionally attributed to variations in receptor density and input type, are instead driven by prenatal mechanisms regulating cortical development and spatial resolution independently of sensory experience. Notably, this reorganization is mediated by transcriptional programs in the thalamus, with neurons receiving upper lip inputs adopting a mystacial-like transcriptional profile. Furthermore, spontaneous activity patterns in the thalamic region corresponding to upper lip mimic mystacial-like frequencies, potentially contributing to the improved spatial resolution of this map. However, ALBSF reorganization occurs independently of this activity. These findings highlight the developmental plasticity of the somatosensory system, providing insights into the intrinsic molecular mechanisms shaping sensory maps and advancing our understanding of cortical development and plasticity in both normal and injury contexts.

RESUMEN

La representación precisa de los estímulos sensoriales en la corteza es fundamental para un procesamiento sensorial correcto, como se ilustra en la corteza somatosensorial primaria (S1) de los roedores, donde los bigotes principales y los del labio superior están representados en mapas corticales distintos: el territorio de barriles postero-medial (PMBSF) y el antero-lateral (ALBSF). Si bien se conoce el desarrollo del mapa PMBSF en el sistema somatosensorial, los mecanismos que subyacen al posicionamiento intra-modal y de las regiones corticales dedicadas a estos territorios siguen siendo desconocidos. Nuestros datos revelan que, entre el día embrionario 18 y el nacimiento, estos mapas se distinguen en la S1 mediante respuestas evocadas por estimulación facial y en el tálamo exhiben perfiles transcripcionales específicos. Para explorar los procesos que impulsan esta segregación, desarrollamos un modelo de ratón al que se privó unilateralmente de los bigotes principales durante el desarrollo embrionario. Este modelo permitió identificar una ventana de tiempo prenatal durante la cual se establecen los mapas corticales y se pueden reorganizar profundamente. Específicamente, los barriles del ALBSF, típicamente más pequeños y menos definidos que los del PMBSF, aumentaron su tamaño y definición. Estas diferencias, tradicionalmente atribuidas a variaciones en la densidad y el tipo de receptores sensoriales, están definidas, en cambio, por mecanismos prenatales que controlan el desarrollo cortical y la resolución espacial, independientemente de la experiencia sensorial. Esta reorganización está mediada por programas transcripcionales talámicos, donde las neuronas del labio superior adoptan un perfil similar al de las que reciben información de los bigotes principales. Además, los patrones de actividad espontánea en el tálamo del labio superior imitan las frecuencias del territorio talámico que corresponde con los bigotes principales, posiblemente mejorando su resolución espacial. Sin embargo, la reorganización del ALBSF no depende de esta actividad. Estos hallazgos destacan la plasticidad del sistema somatosensorial durante el desarrollo, aportando información sobre los mecanismos moleculares intrínsecos que moldean los mapas sensoriales y mejorando nuestra comprensión del desarrollo cortical y la plasticidad en contextos normales y de lesión.

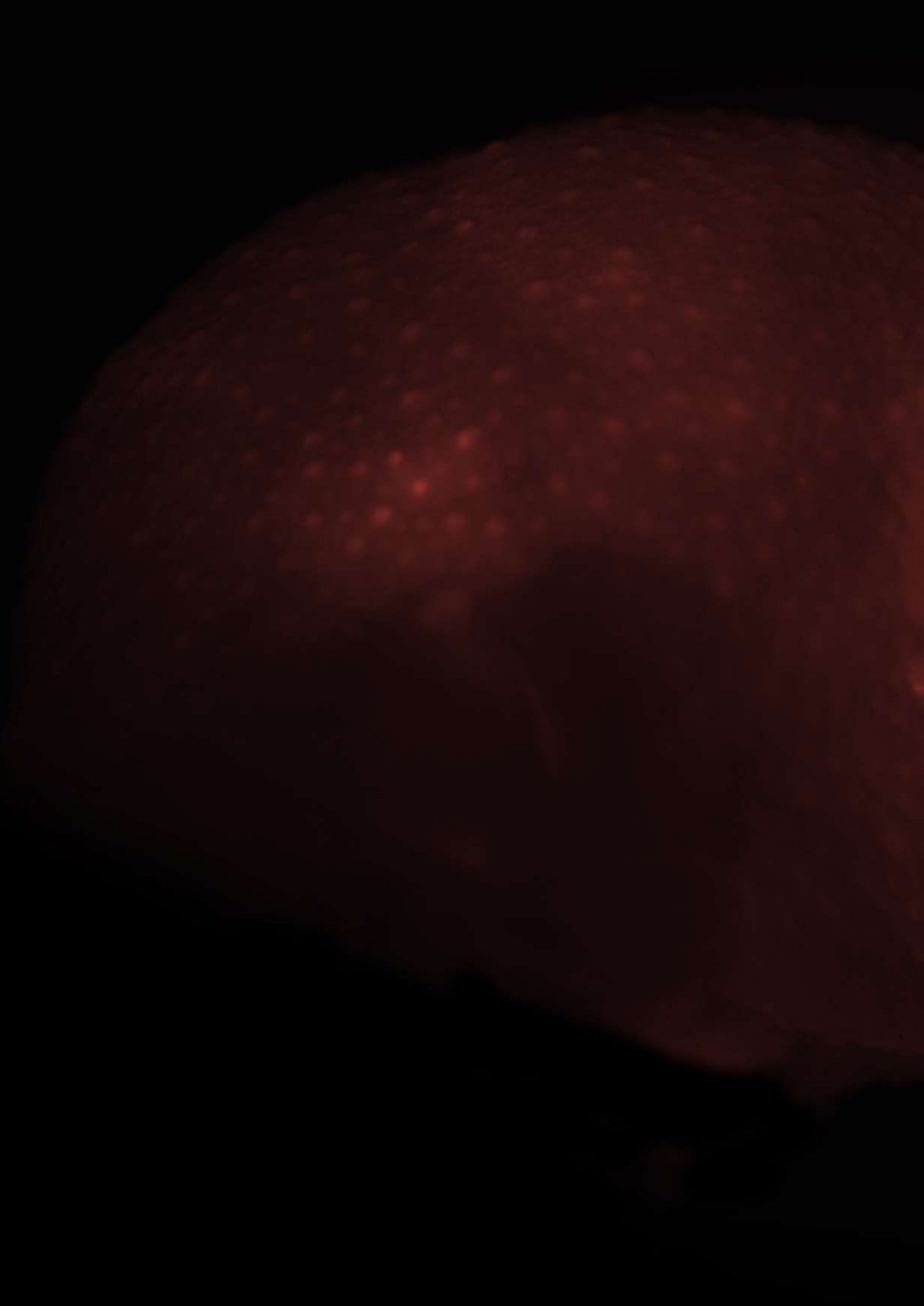

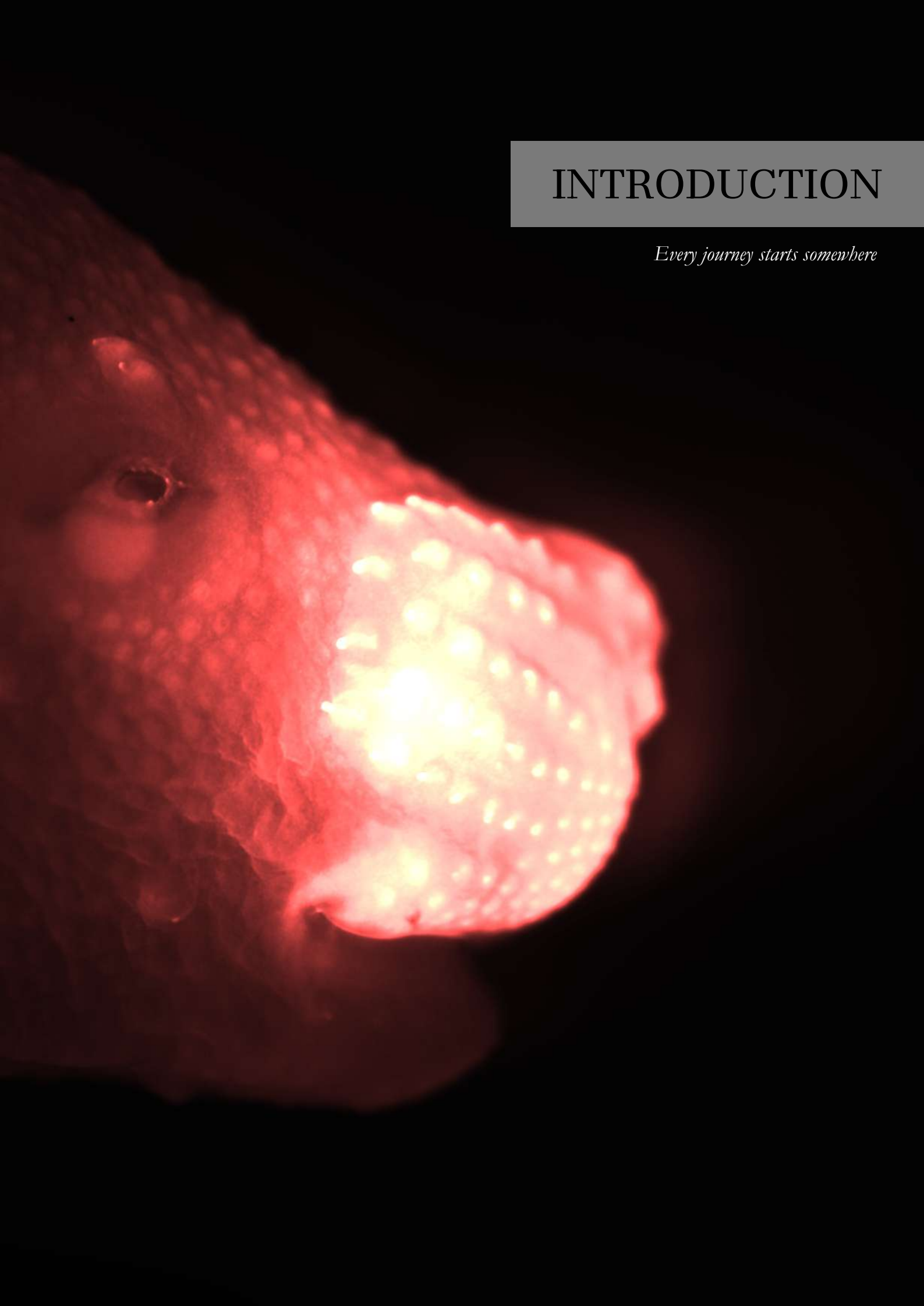

INTRODUCTION

Every journey starts somewhere

INTRODUCTION

1. Overview

The extraordinary complexity of the brain arises from the intricate interplay of genetic programming, cellular interactions, activity patterns, and external cues. A central challenge in neuroscience is understanding how sensory inputs shape the brain's functional architecture. Sensory information from the environment is first detected by sensory receptors in peripheral organs, which are activated and transmit this information to cortical sensory areas for integration and processing. This transmission occurs via parallel sensory pathways that converge in the thalamus.

The thalamus is composed of modality-specific nuclei with precise topographical connectivity, a feature that is established during embryonic development and underpins the functional organization of the thalamocortical loop (Jhaveri et al., 1991; Schlaggar and O'Leary, 1994; Petersen, 2007; Huberman et al., 2008a; Garel and López-Bendito, 2014; Tsukano et al., 2017). By embryonic day 15 (E15), the mouse cortex and thalamus, though disconnected, exhibit parallel temporal patterns of territory specification. Both structures rely on molecular determinants to pre-pattern sensory cortical areas and thalamic nuclei (Mallamaci and Stoykova, 2006; Rash and Grove, 2006; O'Leary and Sahara, 2008; Greig et al., 2016; Moreno-Juan et al., 2017). After birth, cortical areas are refined through activity-dependent mechanisms driven by sensory inputs—both spontaneous and evoked—to form primary sensory cortical maps. Although these cortical areas are highly specialized before birth, they retain some plasticity postnatally, allowing their size, shape and position to adapt to peripheral inputs.

This thesis aims to elucidate the developmental rules governing the establishment of sensory cortical territories and to uncover the mechanisms that confer identity to different sensory maps, focusing on the somatosensory system in the thalamus and cortex.

2. The thalamus

2.1. Fundamental concepts of thalamic development

The mammalian brain is composed of several specialized substructures with unique cellular populations and connectivity. Understanding how the brain develops its finely tuned architecture, essential for proper function, requires a thorough exploration of its developmental processes and the mechanisms driving its compartmentalization. This organization starts with regionalization, a process that occurs during the earliest stages of embryonic development (Metzis et al., 2018). Traditionally, two models have been used to explain this regionalization: the columnar and the prosomeric models. Among these, the prosomeric model, which is consistent with the protomap hypothesis, offers a detailed explanation of how the neural tube, specifically its rostral region, differentiates into the forebrain (prosencephalon), midbrain (mesencephalon), and hindbrain (rhombencephalon). The forebrain's regionalization, as hypothesized by the prosomeric model, includes six prosomeres, which later differentiate into the diencephalon (prosomeres 1-3) and the secondary prosencephalon (prosomeres 4-6) (Martínez et al., 2012; Puelles et al., 2013) (**Fig. 1a**).

The development of the thalamus is regulated by genetic and activity-dependent mechanisms (reviewed in Nakagawa, 2019). It is initiated by morphogen gradients such as Wnt, Sonic hedgehog (Shh), and fibroblast growth factors (FGF) signaling (Kataoka & Shimogori, 2008; Martinez-Ferre & Martinez, 2009, 2012). The diencephalon is subdivided into three prosomeres through the activation of these signaling cascades. Prosomere 1 gives rise to the pretectum, which processes visual information and mediate visual reflexes (Ferran et al., 2009). Prosomere 2 develops into the thalamus and epithalamus, while prosomere 3 forms the prethalamus, including the reticular nucleus (RTN) and zona incerta (ZI) (Puelles & Rubenstein, 2003). The zona limitans intrathalamica (ZLI), a region expressing high levels of Shh, separates prosomeres 2 and 3 and plays a crucial role in differentiating the prospective thalamus from the epithalamus (Chatterjee & Li, 2012; Chatterjee et al., 2014; Mallika et al.,

2015) (**Fig. 1b**). By E10.5 in mice, within the prospective thalamus, Shh gradients establish rostral (pTH-R) and caudal (pTH-C) progenitor domains, leading to the differentiation of glutamatergic projecting neurons in pTH-C and GABAergic projecting neurons in pTH-R. Glutamatergic neurons will compose the thalamic nuclei and project to the cortex (Vue et al., 2007) while GABAergic neurons will form the perihabenular nucleus (pHB) and the intergeniculate leaflet (IGL) (Delogu et al., 2012; Fernandez et al., 2018). pTH-C domain exhibits remarkable heterogeneity, giving rise to the diverse neuronal populations that compose the thalamic nuclei (Vue et al., 2007; Nakagawa & Shimogori, 2012; Wong et al., 2018). Recent studies suggest that the position of thalamic progenitors and exposure to morphogen gradients influence the fate of their thalamic progeny (Shi et al., 2017).

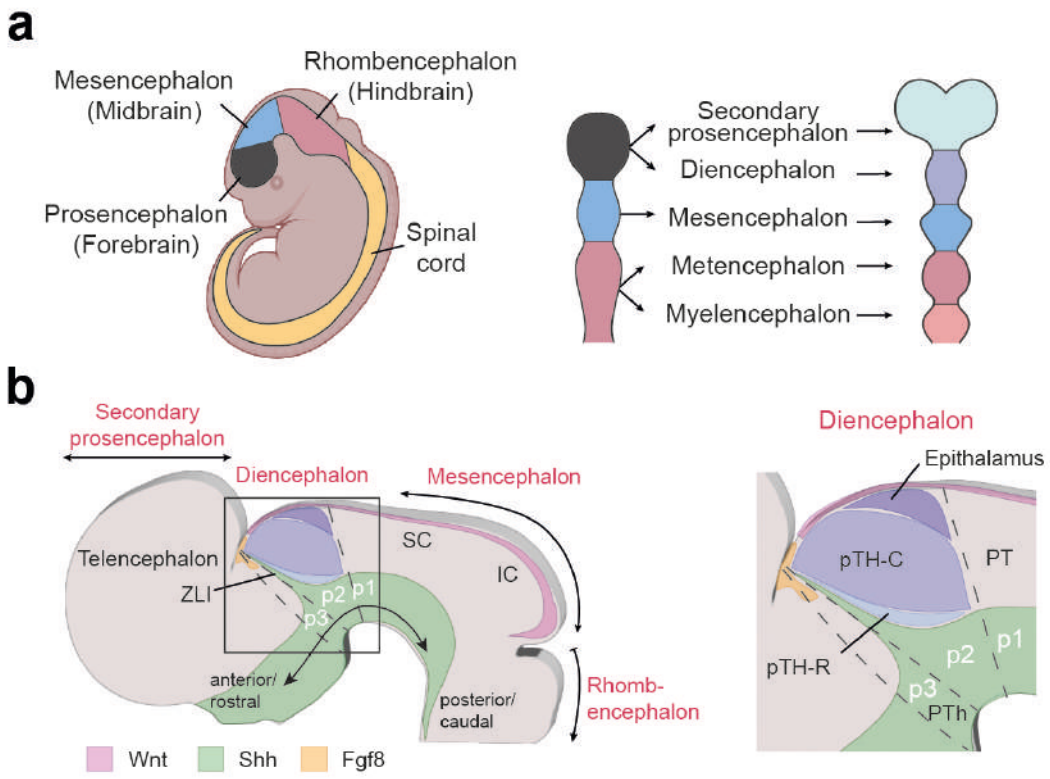

Fig. 1. Early brain regionalization. a Formation of the primary brain subdivisions during early developmental stages. **b** Schematic representation of a sagittal section from an E10.5 embryonic mouse brain, highlighting prosomeres (p) 1-3 and key morphogens. Inset: The black square outlines the main structures involved in the regionalization of the diencephalon. IC, inferior colliculus; p, prosomers; PT, pretectum; PTh, prethalamus; pTH-C, caudal thalamic progenitor domain; pTH-R, rostral thalamic progenitor domain; SC, superior colliculus; ZLI, zona limitans intrathalamica.

Once the prospective thalamic region is established, the progressive expression of the postmitotic transcription factor Gbx2 plays a pivotal role in driving the differentiation of thalamic nuclei. Beginning at E9.0, Gbx2 expression dynamically influences thalamic development by delineating its boundaries from the prethalamus, pretectum and epithalamus, while also subdividing the thalamus into distinct nuclei (**Fig. 2**) (Nakagawa & O'Leary, 2001; Vue et al., 2009; Chen et al., 2009; Li et al., 2012; Mallika et al., 2015; Gezelius & López-Bendito, 2017). The absence of Gbx2 expression disrupts proper development of the thalamus, leading to abnormal thalamocortical axons (TCAs) migration and impairments in cell proliferation, highlighting its critical role (Chen et al., 2009; Chatterjee & Li, 2012; Mallika et al., 2015). In recent years, there has been growing interest in identifying transcription factors involved in the formation of specific thalamic regions. Notably, our laboratory has characterized several nuclei-specific genes (Gezelius et al., 2017), which may be crucial for the organization of TCAs and their precise topographical targeting.

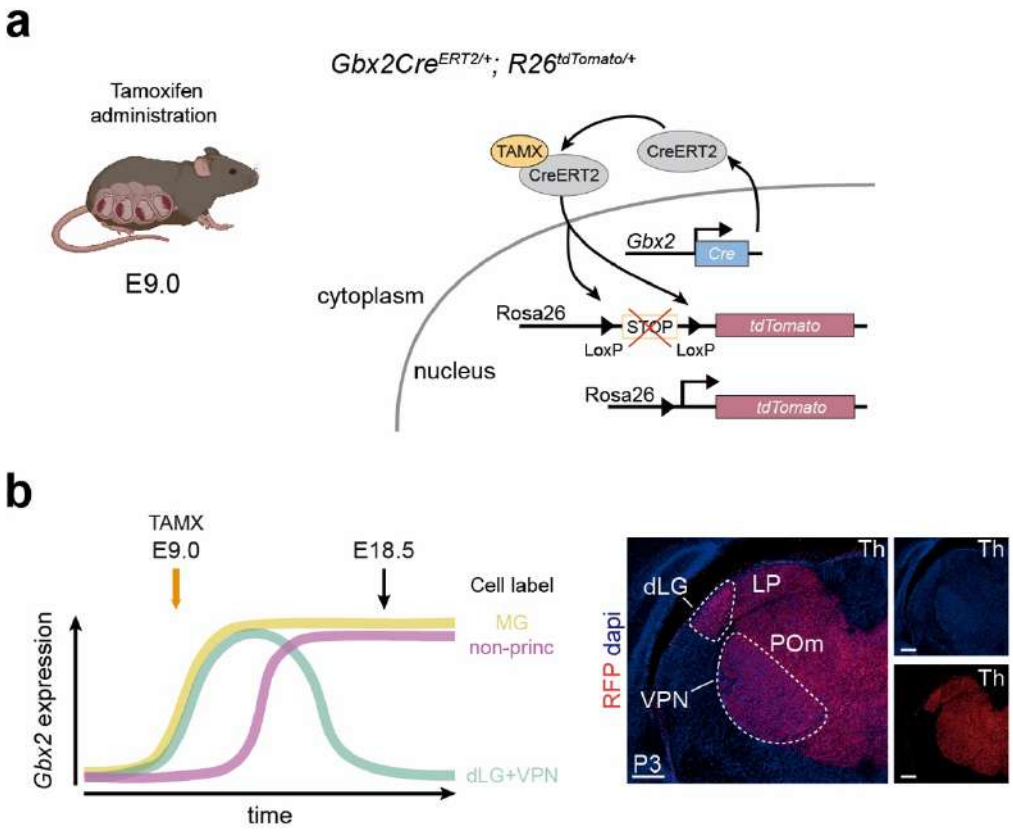

Fig. 2. Gbx2 expression in the developing thalamus over time. a Schematic representation of the transgenic mouse line *Gbx2^{CreERT2}; R26^{tdTomato}* used to study the expression pattern of *Gbx2* in the

developing thalamus. **b** Tamoxifen administration at E9.0 labels the principal thalamic nuclei in red. Coronal section at P3 showing RFP expression following tamoxifen induction at E9.0. dLG, dorsal lateral geniculate nucleus; E, embryonic; LP, lateral posterior nucleus; MG, medial geniculate nucleus; non-princ, non-principal nuclei; P, postnatal; POm, posterior medial nucleus; TAMX, tamoxifen; Th, thalamus; VPN, ventral posterior nucleus. Scales bars, 500 μm. Scheme adapted from Gezelius et al., 2017.

Neuronal activity plays also an important role for proper development of the thalamus by reinforcing connections between neighboring cells. Activity-dependent mechanisms are broadly classified into spontaneous intrinsic activity patterns, and evoked activity triggered by external stimulus. Spontaneous activity waves emerge at various developmental stages of thalamic development (Martini et al., 2018) and propagate along thalamocortical tracts to the neocortex, potentially influencing its structural and functional maturation. These observations emphasize the complex interplay between genetic, molecular, and activity-dependent mechanisms in orchestrating thalamic development and shaping its connectivity with the cortex.

2.2. Differentiation into specialized thalamic sensory nuclei

The thalamus is a highly heterogeneous structure composed of over 40 distinct nuclei, each characterized by unique connectivity patterns, molecular signatures and functions. Anatomically, thalamic nuclei are named according to their relative positions within the thalamic complex, as identified through histochemical techniques (Jones, 1985). Functionally, these nuclei are grouped into associative, motor and sensory categories, with further subdivisions based on sensory modalities such as visual, somatosensory and auditory. Additionally, thalamic nuclei can also be classified as first-order (FO) and higher-order (HO) nuclei based on the origin of their primary input source (Sherman & Guillery, 1998).

FO nuclei function as sensory drivers, receiving ascending sensory inputs from subcortical afferents. For example, in the visual thalamus, the dorsal lateral geniculate nucleus (dLG) is directly innervated by retinal ganglion cells (RGCs) from the retina (Valverde, 1968; Godement et al., 1984; Reichova and Sherman, 2004). Similarly, the ventral posterior medial

nucleus (VPM), the somatosensory thalamus, receives input from the trigeminal pathway, specifically from the principal nucleus (PrV) in the brainstem (Ralston, 1969; Killackey and Fleming, 1985). The auditory thalamic nucleus, represented by the ventral medial geniculate nucleus (MGv), processes sensory input from the inferior colliculus (IC) (Jones and Rockel, 1971; Lee and Sherman, 2010). These nuclei relay sensory information primarily to their respective primary cortical areas—visual cortex (V1), somatosensory cortex (S1) and auditory cortex (A1)—with their axons targeting layer 4 predominantly but also extending to other cortical layers (Clark, 1932; Frost & Caviness, 1980; Sherman & Guillery, 2002) (**Fig. 3**).

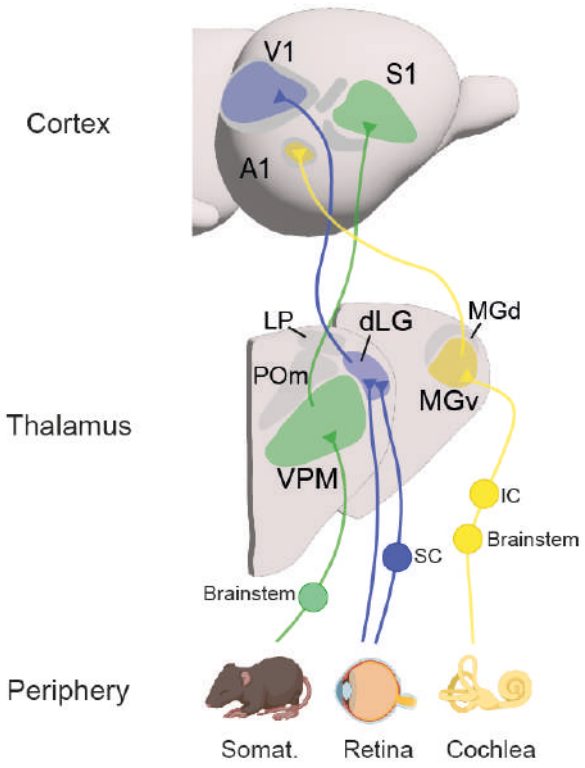

Fig. 3. Organization of the primary sensory pathways. Schematic representation of the three major peripheral sensory inputs—retinal, somatosensory, and cochlear—projecting to their corresponding FO thalamic nuclei: dLG, VPM and MGv, respectively. TCAs then relay sensory information from these nuclei to their respective primary cortical areas: V1, S1 and A1. A1, primary auditory cortex; dLG, dorsal lateral geniculate nucleus; IC, inferior colliculus; LP, lateral posterior nucleus; MGd, dorsal division of the medial geniculate body; MGv, ventral division of the medial geniculate body; POm, posterior medial nucleus; S1, primary somatosensory cortex; SC, superior colliculus; V1, primary visual cortex; VPM, ventral posterior medial nucleus.

In contrast, HO nuclei are considered modulators of the sensory signals since they receive driving inputs from cortical layer 5 neurons rather than the periphery (Sherman & Guillery, 2002; Bickford et al., 2015). They establish connections between the thalamus and different cortical areas (Butler, 2008). HO nuclei also exhibit modality specification: the lateral posterior nucleus (LP) is associated with visual processing; the posterior medial nucleus (POm) is involved in somatosensory functions and the dorsal medial geniculate nucleus

(MGd) is dedicated to auditory processing. This driver/modulator framework indicates that FO nuclei primarily transmit peripheral sensory information, while HO nuclei support cortical processing and integration (Bickford et al., 2015). HO nuclei are essential for establishing cortico-thalamo-cortical loops of information, enabling efficient communication and coordination between different cortical areas (Guillery & Sherman, 2002; Sherman & Guillery, 2002).

Modality-specific FO-HO pairings, such as dLG-LP (visual), VPM-PoM (somatosensory) and MGv-MGd (auditory), reflect the thalamus's organized structure. Despite their diverse functions, FO and HO nuclei share a common embryonic origin from prosomere 2, undergoing early developmental segregation and neuronal precursor specification (Angevine, 1970). This sophisticated organization highlights the thalamus's critical role in sensory processing and its dynamic integration with cortical circuits.

3. The cortex

3.1. General principles of cortical development

The cerebral cortex is the largest and most complex component of the mammalian brain, and has undergone extensive evolutionary adaptations, surpassing all other brain structures in its complexity. It originates from the dorsal telencephalon (pallium) and is divided into three major regions: the archicortex (including the entorhinal cortex, retrosplenial cortex, subiculum and hippocampus), paleocortex (olfactory piriform cortex) and neocortex. The neocortex, hereafter referred to as the "cortex", is the most extensive region and underpins advanced cognitive abilities in higher mammals, including human mental capacities. Its function relies on a highly organized structure along radial and tangential dimensions (Rakic, 1995; Rakic et al., 2009).

Radially, the cortex comprises six layers, each containing heterogeneous populations of neurons differing in morphology, function and connectivity. These cortical neurons are broadly classified into excitatory glutamatergic neurons, which establish both local and long-

range connections, and inhibitory GABAergic interneurons, which mediate local interactions (Petreanu et al., 2009). Neurons in different layers form vertical connections, creating radial columns that are grouped into functional cortical modules with shared physiological properties (Mountcastle, 1997). This columnar organization develops during cortical formation, with radial glial processes providing scaffolds for clonally related neurons (Rakic, 1988; Rakic et al., 2009). Recent studies employing genetic and viral tracing tools have elucidated the lineage of neurons originating from apical progenitors during development (Luskin et al., 1988; Zong et al., 2005; Guo et al., 2013; Gao et al., 2014; Llorca et al., 2019).

The laminar organization of the cortex arises through an inside-out mechanism, generating all the heterogeneity as soon as they are born (Angevine and Sidman, 1961; Greig et al., 2013). Excitatory neurons in mice, which are generated between E10.5 and E18.5, start populating the cortex from the deepest to the most superficial layers (Molyneaux et al., 2007; Lodato & Arlotta, 2015; Jabaudon, 2017; Di Bella et al., 2021). Neurons at different stages of maturation respond uniquely to signaling cues, with superficial, less mature neurons exhibiting greater plasticity than their deep-layer counterparts (Fox & Wong, 2005).

Tangentially, the cortex is divided into functional areas, initially described by Brodmann in the 1900s, including primary areas such as visual, auditory, somatosensory and motor regions. These areas are distinguished by differences in gene expression, cytoarchitecture, chemoarchitecture, and input-output connectivity (O'Leary and Nakagawa, 2002; Sur and Rubenstein, 2005; Rash and Grove, 2006). These primary areas receive sensory inputs from the periphery, control motor outputs and connect to higher-order or secondary areas specialized in integration and complex processing. Ultimately, these areas relay information to multimodal associative cortical regions where it is processed, combined and integrated.

The unique architecture and connectivity of these cortical regions enable their specialized functions. Understanding the emergence, organization and specification of these regions during development is crucial to unraveling the mechanisms underlying cortical function and its role in cognition and consciousness in the adult.

3.2 Arealization of the embryonic cerebral cortex

The process by which newborn neurons reach their final areal localization in the cerebral cortex remains a fundamental question in neuroscience. Two major hypotheses, the Protocortex and the Protomap, provide complementary frameworks for understanding this process. These models have evolved from opposing views into an integrative perspective, highlighting the intricate interplay between intrinsic genetic mechanisms and extrinsic environmental influences.

The Protomap hypothesis, proposed by Rakic (1988), posits that cortical arealization is primarily driven by intrinsic genetic programs. According to this model, cortical progenitor cells in the ventricular zone (VZ) are endowed with a genetic blueprint, predefining their areal and laminar specification. This intrinsic "protomap" establishes the spatial and functional organization of the cortex, ensuring that neurons destined for different regions acquire distinct molecular characteristics before they migrate to the cortical plate. These genetic mechanisms provide the foundational framework for cortical arealization, operating independently of external influences. Conversely, the Protocortex hypothesis, introduced by O'Leary (1989), emphasizes the role of external cues in shaping cortical development. This theory proposes that the embryonic cortical plate is initially composed of equipotent, undifferentiated cells. The final specification of these cells into distinct cortical regions, such as sensory areas, is guided by subcortical inputs, particularly thalamocortical afferents (TCA). These external signals refine synaptic organization and functional specialization, highlighting the importance of environmental influences in cortical arealization.

While these models were historically viewed as contradictory, contemporary research supports an integrative view in which both intrinsic and extrinsic mechanisms work together to drive cortical development (Grove & Fukuchi-Shimogori, 2003; Arai & Pierani, 2014; Cadwell et al., 2019; Oberst et al., 2019). Intrinsic genetic programs, governed by morphogens and transcriptional factors, establish a rudimentary protomap, providing positional identity and early organization to newborn neurons (Telley et al., 2016). Studies employing advanced techniques, such as single-cell transcriptomics, have revealed significant differences in gene

expression among progenitor cells from distinct cortical regions, such as the prefrontal and visual cortices of the fetal human brain. This differences, as shown by Nowakowski et al. (2017) become increasingly pronounced as neurons mature highlighting the importance of intrinsic topographical distinctions and their interaction with external inputs in shaping cortical circuits. Furthermore, radial glial cells enhance neuronal diversity by varying their division patterns, generating progenitors with distinct fates and contributing to the complexity of cortical development (Llorca et al., 2019).

However, this initial framework, while genetically preconfigured, remains plastic and is subject to modulation by extrinsic inputs. For instance, thalamocortical innervation influences the spatial and temporal refinement of cortical areas, as shown by sensory-modality sorting of TCAs inputs during cortical plate development (Schlaggar & O'Leary, 1994; Pouchelon et al., 2012; Vue et al., 2013; Ohtaka-Maruyama et al., 2018; Martini et al., 2018; Antón-Bolaños et al., 2019; Monko et al., 2022). Additionally, other extrinsic factors, such as the membrane potential of the apical progenitors (Vitali et al., 2018) and feedback signals from newborn neurons to these progenitors (Toma et al., 2014), are crucial. These mechanisms not only endow apical progenitors with the competence to generate distinct layer-specific neurons but also help define the identity of the newly formed neurons, ensuring proper cortical specification.

These findings highlight that cortical circuits emerge from dynamic interactions between intrinsic genetic programs and extrinsic inputs, which together define their final architecture and function.

4. Development of connections between thalamus and cortex

The thalamus and cortex establish reciprocal connections that are essential for processing sensory and motor information in the mammalian brain. During the second and third weeks of embryonic development in mice, neurons from these regions begin extending their axons, establishing thalamocortical and corticothalamic pathways. These axons traverse multiple

territories to reach their specific targets, creating one of the brain's most extensive and critical networks. This interconnection enables the integration of sensory input from the periphery into cortical areas, laying the foundation for complex sensory processing.

4.1. Thalamocortical projections

The establishment of thalamocortical connectivity is a tightly orchestrated process that begins in mice at the end of the second embryonic week (E12.5) and continues into the postnatal period. The developmental pathway is regulated by a complex interplay of genetic programs, axon guidance molecules, and spontaneous neuronal activity, each contributing to the precise wiring of TCAs (Dufour et al., 2003; Marcos-Mondéjar et al., 2012; Mire et al., 2012; Molnár et al., 2012; Garel & López-Bendito, 2014; Leyva-Díaz et al., 2014; Castillo-Paterna et al., 2015; López-Bendito, 2018; Antón-Bolaños et al., 2018; Quintana-Urzainqui et al., 2020; Callejas-Marin et al., 2022).

TCAs initiate their journey projecting ventrally from the thalamus before turning laterally to cross the diencephalic-telencephalic boundary (DTB). Their trajectory is guided by repulsive cues, including Slit1 and Slit2 (Bagri et al., 2002; López-Bendito et al., 2007; Braisted et al., 2009; Bielle et al., 2011). This phase is further refined by molecular gradients of Semaphorins/Plexin, ephrins/Eph and netrins/DCC, which organize the axons topographically as they navigate towards their cortical targets (Braisted, 1999; Molnár et al., 2012; Garel and López-Bendito, 2014). Upon reaching the internal capsule at E13.5, they traverse the subpallium through a permissive corridor formed by GABAergic neurons derived from the lateral ganglionic eminence (LGE) (Uemura et al., 2007). These corridor cells temporarily localize between the proliferative zone of the medial ganglionic eminence (MGE) and the globus pallidus, creating a pathway that facilitates TCAs navigation. Additionally, these cells secrete Neuregulin-1 (Nrg1), a critical axon guidance molecule that steers TCAs toward their cortical targets, ensuring proper connectivity (López-Bendito et al., 2006; Bielle et al., 2011).

By E14.0, TCAs slow down at the pallial-subpallial boundary (PSPB), pausing to encounter corticofugal axons from subplate neurons (SPNs) (McConnell et al., 1989; de Carlos & O'Leary, 1992). This interaction, described as the "handshake hypothesis", suggests that TCAs use corticofugal axons as scaffolds to guide their navigation toward the cortex (Blakemore & Molnár, 1990). By E15.5, TCAs move dorsally to reach the neocortex and halt in the subplate (SP), where they form transient connections with SPNs. These temporary circuits facilitate early cortical communication and are instrumental in refining the topographic innervation of TCAs to their target cortical layers (Allendoerfer & Shatz, 1994; del Río et al., 2000; Little et al., 2009; Kanold & Luhmann, 2010; Viswanathan et al., 2012, 2017; Hoerder-Suabedissen & Molnár, 2015; Kanold et al., 2019; Molnár et al., 2020; Pal et al., 2021).

At E17.5, TCAs begin invading the cortical plate, primarily targeting layer 4 (L4), the principal recipient of sensory inputs (**Fig. 4**). During the first postnatal week, TCAs undergo a refinement process, forming specialized structures such us barrels in the somatosensory cortex (S1), which represent sensory input topography (López-Bendito & Molnár, 2003). While L4 remains their principal target, TCAs also establish collateral projections to other layers, including L5b, facilitating diverse cortical connectivity.

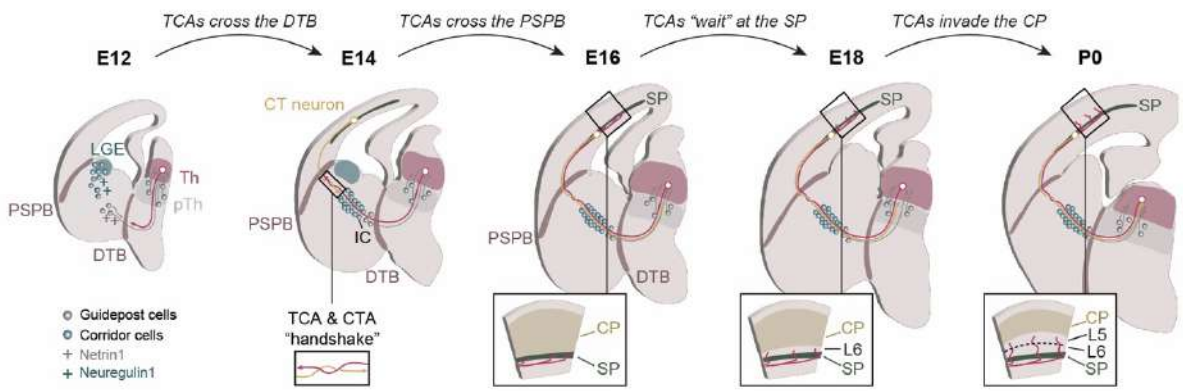

Fig. 4. Development of thalamocortical connections. Schematic representation of the developmental time course of TCAs from E12 to E18. During this period, TCAs extend from the thalamus, navigating through major boundaries such as the DTB and the PSPB, guided by attractant and repulsive cues. CP, cortical plate; CT, corticothalamic, CTA, corticothalamic axon; DTB, diencephalon-telencephalon boundary; IC, internal capsule; L4, layer 4; L5, layer 5; L6, layer 6; LGE, lateral ganglionic eminence; PSPB, pallium-subpallium boundary; pTh, prethalamus; SP, subplate; TCAs, thalamocortical axons.

The arrival of TCAs coincides with ongoing corticogenesis, during which cortical layers, especially granular layers like L4, are still forming. TCAs are thought to act as extrinsic regulators of cortical development by influencing progenitor proliferation and the organization of cortical architecture (Molyneaux et al., 2007). Furthermore, spontaneous neuronal activity, such as embryonic calcium waves, plays a critical role in refining thalamocortical connectivity and ensuring the proper formation of functional cortical circuits (Mire et al., 2012; Molnár et al., 2012; López-Bendito, 2018; Antón-Bolaños et al., 2019).

4.2. Corticothalamic projections

All sensory cortical areas receive input from the thalamus and reciprocally project to specific thalamic nuclei, forming a bidirectional communication pathway (Caviness & Frost, 1980). Corticothalamic axons (CTAs) constitute approximately 50% of the synaptic input received by sensory thalamic neurons. These projections play a critical modulatory role, refining and shaping the relay of sensory information for cortical processing (Sherman & Guillery, 1998; Briggs & Usrey, 2008; Olsen et al., 2012). The specificity of CTAS is determined by the laminar origin of the cortical neurons, leading to the identification of three distinct populations with unique temporal sequences and thalamic targets: SPNs, Layer 6 (L6), and Layer 5 (L5) neurons. Notably, classical research has highlighted SPNs as the pioneering CTAs, which provide essential structural guidance for the pathfinding of corticofugal axons (CFAs) originating from L5 and L6 neurons (McConnell et al., 1989; Kim et al., 1991). L5 and L6 CTAs originate from corticofugal pyramidal neurons and constitute an essential component of thalamocortical circuitry (Auladell et al., 2000; Price et al., 2006; Molyneaux et al., 2007).

During embryonic development, postmitotic cortical neurons begin migrating toward the preplate at E10.5, initiating neurite extension (Bicknese et al., 1994; Noctor et al., 2004; Lickiss et al., 2012). By E13.5, corticofugal neurons project ventrolaterally and reach the PSPB (Erzurumlu & Jhaveri, 1992; Jacobs et al., 2007), where CTAs pause for approximately one day before advancing through the subpallium toward the thalamus (De Carlos and

O'Leary, 1992; Molnar and Cordery, 1999) (**Fig. 4**). They enter the internal capsule at E15.5, guided by corridor cells (Richards et al., 1997; López-Bendito et al., 2006). After traversing the DTB, they encounter a second waiting period within the prethalamus between E16.5 and E17.5, potentially in the thalamic reticular (TRN) and perireticular (PRN) nuclei (Molnár & Cordery, 1999; Garel & Rubenstein, 2004; Simpson et al., 2009; Chen et al. 2012; Molnár et al. 2012; Deck et al. 2013; Lokmane et al. 2013; Lokmane & Garel 2014). At this point, corticofugal axons are sorted, with axons from layer 5 predominantly projecting to cerebral peduncle, while the remaining axons from L5 and those from L6 to their respective thalamic nuclei (Clascá et al., 1995; Molnár & Cordery, 1999; Jacobs et al., 2007). Axons start to invade the thalamus at E17.5 and continue into the early postnatal period (Miller et al., 1993; Molnar and Cordery, 1999; Jacobs et al., 2007), with somatosensory (VPM) and motor (ventrolateral, VL) nuclei innervated by birth (E18.5-P0), while visual (dLG) and auditory (MGv) nuclei by postnatal day 8 (P8) (Jacobs et al., 2007; Grant et al., 2012).

Layer 6 CTAs primarily project to FO thalamic nuclei (dLG, VPM and MGv) (Guillery, 1967; Jones and Powell, 1968; Diamond et al., 1969; Hoogland et al., 1987), forming glutamatergic synapses with relay cells and contacting TRN neurons to establish inhibitory circuits that modulate thalamic activity (Guillery, 1995; Sherman and Guillery, 1998; Rouiller and Welker, 2000; Guillery et al., 2002; Jones, 2002). Conversely, layer 5 CTAs target HO nuclei, facilitating cortico-cortical communication by integrating signals from corticospinal and corticobulbar neurons (Sherman & Guillery, 2002; Hoerder-Suabedissen & Molnár, 2015). This hierarchical organization underscores the thalamus's dual role as a sensory relay and inter-cortical communication hub, enabling coordination across cortical areas for complex cognitive processes (Fries, 2009; Sherman, 2016).

Notably, the development of CTAs is influenced by both intrinsic molecular programs and peripheral sensory activity. For instance, aggrecan, a repulsive chondroitin sulfate proteoglycan that is enriched in the dLG perinatally, regulates CTAs invasion of this nucleus (Brooks et al., 2013). Sensory deprivation or input ablation can induce transcriptional and connectivity changes, altering CTAs innervation of FO and HO thalamic nuclei and

demonstrating the plasticity of these circuits (Frangeul et al., 2016; Grant et al., 2016). Despite significant advances, the mechanisms regulating final thalamic invasion and functional maturation of CTAs remain incompletely understood.

4.3. Developmental interplay between thalamus and cortex

The development of the thalamus and cortex occurs simultaneously, with each structure governed by distinct genetic programs but capable of influencing one another during the maturation process (Antón-Bolaños et al., 2018).

4.3.1. Thalamic influence on cortical development

The thalamus plays a pivotal role in numerous aspects of cortical development, including radial organization, cell proliferation, CTAs navigation, cortical area specification, interneuron maturation and circuit assembly (Rakic, 1991; Dehay et al., 1996; Zechel et al., 2016). TCAs, for instance, release glutamate, which is essential for the proper growth of Reelin-expressing interneurons in the cortex (de Marco García et al., 2015). Thalamic input also regulates the integration of parvalbumin (PV) and somatostatin (SST) interneurons in the cortical circuitry (Wamsley & Fishell, 2017). Recent studies highlight the significance of SST interneurons during the first postnatal week, as they ensure the accurate targeting of thalamocortical input to L4 PV interneurons and pyramidal neurons, supporting the assembly of the cortical excitatory-inhibitory circuit (de Marco García et al., 2015; Marques-Smith et al., 2016; Tuncdemir et al., 2016; Che et al., 2018; Takesian et al., 2018). Additionally, L4 pyramidal neurons depend on TCA input for proper segregation and the establishment of barrel walls in S1 (Li et al., 2013; Assali et al., 2017).

The interaction between TCAs and CTAs is further emphasized by studies showing aberrant CTAs trajectories in the absence of TCAs, highlighting the latter´s role in guiding proper CTAs pathfinding (Deck et al., 2013). Thalamic input is also critical for differentiating primary and secondary cortical areas, as the genetic mechanisms driving this specification are dependent on its arrival (Chou et al., 2013). For instance, the absence of FO thalamic nuclei results in primary cortical regions defaulting to a higher-order fate (Vue et al., 2013;

Pouchelon et al., 2014). Ablation of the FO somatosensory thalamic nucleus (VPM) leads to the HO nucleus (POm) targeting L4 neurons in S1 (Pouchelon et al., 2014), further underscoring the influence of TCAs on L4 cortical neuron identity and circuit formation.

Early thalamic activity also fosters cortical development by promoting neuronal identity acquisition, axon refinement, and neuronal migration (Kirischuk et al., 2017; Luhmann & Khazipov, 2018; Martini et al., 2018; Molnar et al., 2020; Antón-Bolaños et al., 2019). During the first postnatal week, early gamma oscillations in the thalamus synchronize activity between the thalamus and corresponding cortical regions (Minlebaev et al., 2011). Disruption in thalamic activity or presynaptic release can impair the formation of cortical maps such as barrels in S1 (Narboux-Nême et al., 2012; Li et al., 2013; Arakawa et al. 2014a; Suzuki et al., 2015; Antón-Bolaños et al., 2019). Moreover, spontaneous thalamic activity during embryonic development is crucial for maintaining sensory systems homeostasis, potentially influencing cross-modal cortical plasticity through coordinated activity patterns across sensory thalamic nuclei (Moreno-Juan et al., 2017). These findings underscore the central role of thalamic activity in driving cortical plasticity and functional organization.

4.3.2. Cortical influence on thalamic development

The cortex exerts significant influence over various developmental processes in the thalamus. Cortical intrinsic factors, such as transcription factors and positional cues, play a pivotal role in guiding TCAs to their appropriate cortical targets. For example, ectopic expression of FGF8 causes duplications or positional shifts in sensory cortical areas, altering TCAs pathfinding (Shimogori & Grove, 2005; Assimacopoulos et al., 2012). Similarly, transcription factors such as Emx2, Pax6, Sp8, and COUP-TF1 critically modulate TCAs innervation patterns (Hamasaki et al., 2004; Manuel et al., 2007; Borello et al., 2014; Armentano et al., 2007; O'Leary & Sahara, 2008). Misexpression of Pax6, for instance, reduces body map representations in S1 and VPM, providing evidence of a top-down plasticity effect (Zembrzycki et al., 2013).

Beyond genetic regulation, early cortical activity is crucial for thalamic development, influencing key processes such as dendritic and axonal arborization, and axon navigation

(Simi & Studer, 2018). Disruption of cortical activity in knock-out models targeting NMDA receptor 1 (NMDAR1), metabotropic glutamate receptor 5 (mGluR5), and adenylyl cyclase 1 (AC1) results in profound TCAs deficiencies. These models exhibit smaller, poorly defined barrels in S1, alongside disrupted neuronal organization and the absence of well-formed barrel walls (Iwasato et al., 2000, 2008; Datwani et al., 2002; Lee et al., 2005; Ballester-Rosado et al., 2010, 2016; Antón-Bolaños et al., 2018; Martini et al., 2018). These findings demonstrate the influence of cortical activity on the precise arrangement of thalamic and cortical territories.

Overall, the interplay between cortical genetic programs, intrinsic activity, and thalamic input highlights a tightly coupled relationship between these structures, underscoring the bidirectional nature of thalamocortical development, essential for establishing functional sensory circuits.

4.4. Hierarchical feed-forward connectivity between thalamus and cortex

FO thalamic nuclei receive sensory input from peripheral sensory organs, either directly or via intermediate hindbrain structures. These nuclei project to cortical layers L4, L5b and L6, with spiny-stellate neurons in L4 serving as their primary recipients (Alonso & Swadlow, 2017). This pathway allows FO nuclei to transmit driving sensory information to the cortex, initiating intracortical processing. Within the cortex, these signals propagate through intra-columnar pathways, progressing from L4 to L2/3 and subsequently to L5 and L6, which serve as output layers to other brain regions (Lee & Sherman 2010; Thomson 2010; Lee et al. 2012).

Both FO and HO thalamic nuclei receive modulatory feedback input from L6 of their corresponding cortical areas. However, only HO nuclei establish feedback loops with the cortex, receiving feedforward input from L5b neurons in the primary cortex (Sumser et al., 2017; Hoerder-Suabedissen et al., 2018). This unique arrangement positions HO nuclei to mediate reciprocal communication between cortical areas, forming a dynamic thalamus-cortex-thalamus loop. This interplay of feedforward and feedback inputs allows HO nuclei

to process and relay information from one cortical area to another, facilitating integration and refinement of sensory inputs (Sherman & Guillery, 2002; Reichova & Sherman 2004; Theyel et al. 2010; Lee & Sherman 2010; Viaene et al., 2011).

Peripheral sensory information (driving input) transmitted through FO nuclei reaches L4 of primary cortical areas and follows two main pathways: intracortical communication, where signals move from L4 to L2/3 and subsequently to secondary sensory or motor areas, and the cortico-thalamo-cortical loop, where L4 neurons connect to L5b neurons that project to HO thalamic nuclei, which in turn target L4 neurons in secondary cortical areas (Viaene et al., 2011) (**Fig. 5**). This transthalamic pathway enables cortico-cortical communication, linking distinct cortical regions and supporting cooperative processing essential for cognitive functions (Seidemann et al., 1998; Fries, 2009; Sherman, 2016).

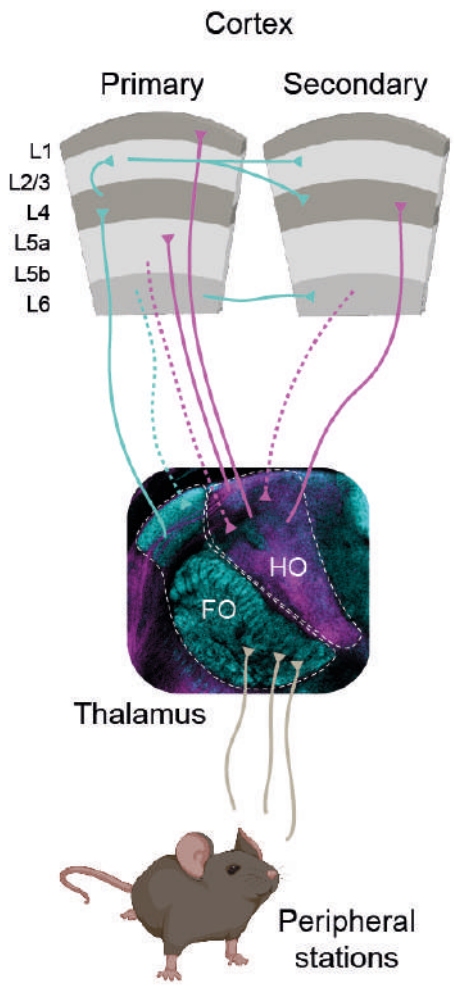

Fig. 5. Thalamocortical connectivity. FO thalamic nuclei receive input from peripheral sensory stations and relay it to L4 neurons in the primary sensory cortex. These L4 neurons then project to L2/3, which in turn sends cortico-cortical connections to L2/3 and L4 of the secondary sensory cortex. The thalamocortico-thalamic loop is completed as HO thalamic nuclei project to L4 in the secondary sensory cortex. Additionally, HO nuclei receive input from L5 of the primary cortex and L6 of the secondary cortex, while also establishing connections with neurons in L1 and L5 of the primary sensory cortex. Cyan and magenta lines represent thalamocortical connections of FO and HO nuclei, respectively. Solid lines represent thalamocortical projections while dashed lines represent corticothalamic projections. FO, first order nuclei; HO, high order nuclei; L, layer.

Thus, the thalamus, plays a dual role as a sensory relay station and a mediator of inter-areal communication. Optogenetic and calcium imaging studies have shown that L5 cortical neurons can induce waves of activity in distant cortical areas through transthalamic pathway (Stroh et al., 2013). Cortico-cortical communication occurs via three mechanisms: intra-columnar pathways within cortical layers, horizontal connections between primary and secondary cortices by L2/3 and L6 neurons, and the transthalamic pathways that integrate cortical areas through thalamic relays. Although direct connections between cortical areas are present, the parallel transthalamic pathway provides an additional mechanism for information transfer, highlighting the thalamus's critical role in sensory processing and higher-order cognitive integration (Sherman, 2016).

5. Development of sensory systems

5.1. Sensory maps

The sensory pathways are inherently designed to detect stimuli through peripheral sensory receptors, which transmit this information via specialized pathways to the thalamus and ultimately to the cerebral cortex. In the cortex, sensory information is represented topographically, reflecting the spatial arrangement of sensory receptors in the peripheral sensory organs. These maps are fundamental to sensory processing, with each cortical region representing a specific modality through a structured layout. For example, visual maps (retinotopy) correspond to the arrangement of photoreceptors in the retina, somatosensory maps (somatotopy) mirror the layout of mechanoreceptors on the body, and auditory maps (tonotopy) organize sound frequencies as detected by cochlear hair cells (Hubel & Wiesel, 1962; Woolsey, 1978; Merzenich et al., 1975).

The development of sensory maps is largely governed by self-organizing principles, driven by activity-dependent mechanisms and local neuronal interactions. These processes are thought to refine synaptic connections and establish precise arrangements, enabling neighboring neurons to exhibit similar response properties. This organization is particularly

evident in species with smooth, continuous maps, such as primates and carnivores, where lateral cortical connectivity contributes to the emergence of orderly representations (Bednar & Wilson, 2016). The formation and refinement of these maps are orchestrated by a combination of axon guidance molecules, axonal competition, and activity-dependent mechanisms, collectively ensuring the accurate representation of sensory inputs within the cortex.

Despite variations across species and sensory modalities, the fundamental principles underlying the development of sensory maps remain highly conserved. These maps are essential for organizing cortical circuits, enabling efficient representation and processing of sensory information that underpins perception and behaviour (Wilson & Bednar, 2015). Exploring these common features provides valuable insights into the mechanisms governing the organization and maturation of sensory pathways.

5.2. The visual system: retinotopy

The visual system is responsible for receiving, processing and interpreting visual information to create a coherent representation of the environment. It follows a hierarchically organized pathway, beginning with the retina, a peripheral structure that translates light into bioelectrical signals. The retina is composed of three main layers of cell bodies: the outer nuclear layer, the inner nuclear layer and the retinal ganglion cell (RGC) layer, separated by two synaptic layers. The outer cell layer contains photoreceptors, rods and cones, which detect changes in light. Visual signals are then processed by horizontal and amacrine cells in the inner nuclear layer, which filter and shape the input before transmitting it to bipolar cells. Bipolar cells integrate this information and relay it to RGCs in the ganglionic layer, acting as an intermediary between photoreceptors and the central nervous system (Masland, 2012).

RGCs, a highly specialized class of neurons with over 30 subtypes, respond to specific visual stimuli, such as contrasts between light and dark or motion direction (Baden et al., 2016; El-Danaf & Huberman, 2019). Their axons converge to form the optic nerve, which carries visual information to central brain structures (Erskine & Herrera, 2014). In mice, RGC

axons begin extending toward the central nervous system at E12.5, with most crossing the optic chiasm to the contralateral side, while 2-3% remain ipsilateral (Dräger & Olsen, 1980). Contralateral and ipsilateral axons reach the dorsolateral geniculate nucleus (dLG) in the thalamus by E15.5 and the superior colliculus (SC) in the midbrain by E18.5 (Godement et al., 1984) (**Fig. 6a**). The dLG transmits visual information along the image-forming pathway to V1, while the SC regulates head movements and eye coordination (Bickford et al., 2015). Both structures receive feedback cortical projections.

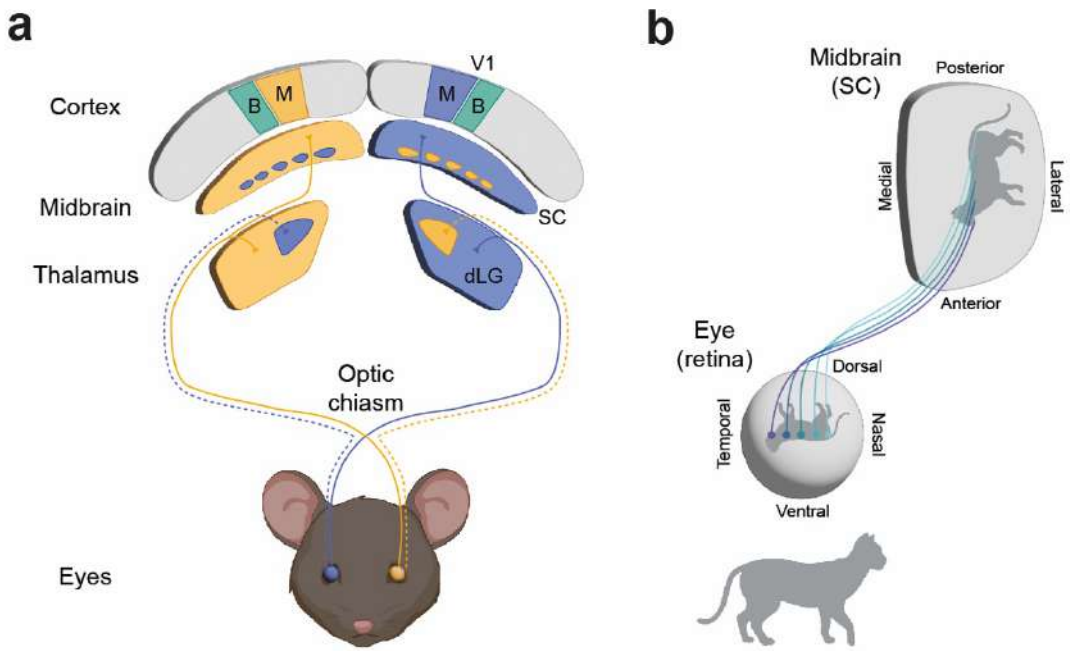

Fig. 6. Organization and retinotopy in the mouse visual pathway. a Axonal projections from both eyes are segregated into distinct domains within specific retinorecipient targets that receive binocular input. Neurons in the dLG project to V1, which in mice consists of two distinct zones: the monocular zone (M), receiving input exclusively from the contralateral eye via the dLG, and the binocular zone (B), integrating input from both eyes. **b** Neighboring points in a visual scene are mapped onto adjacent neurons in the retina, forming retinotopic maps. This spatial organization is maintained in RGCs targets such as the SC, ensuring that visual information is processed in a topographically ordered manner. dLG, dorsal lateral geniculate nucleus; SC, superior colliculus; V1, primary visual cortex. Adapted from Seabrook et al., 2017.

In the dLG, approximately 90% of its area is occupied by contralateral axons, whereas ipsilateral axons cover about 10% and arrive later, around P0–P2. Throughout the visual pathway, contralateral and ipsilateral projections from RGCs remain segregated to preserve the topographical representation of eyes, which is essential for binocular vision (Muir-

Robinson et al., 2002; Jaubert-Miazza et al., 2005; Huberman et al., 2008a). Initially, contralateral and ipsilateral axons overlap within the dLG at P0. Segregation begins at P4 and undergoes refinement by P10 through processes involving synapse and axon elaboration, followed by elimination. By the time of eye opening, these projections are organized into distinct, non-overlapping areas (Bickford et al., 2010; Huberman et al., 2008b; Pfeiffenberger et al., 2005). Although retinal axons contribute only 5-10% of the synapses in the dLG, they provide the primary source of excitatory input for thalamic relay cells. Additional inputs to the dLG originate from L6 projections of V1, thalamic reticular nucleus (TRN) and brainstem nuclei (Bickford et al., 2010; Sherman & Guillery, 2002).

The resulting organization forms a retinotopic map, a spatial representation of the visual field that mirrors the retinal image (**Fig. 6b**). This precise mapping arises from a combination of genetic programs, axon guidance molecules (e.g., Ephrins/Eph), and spontaneous neuronal activity (Brown et al., 2000; Vanderhaeghen et al., 2000; Ellsworth et al., 2005; Huberman et al., 2005, 2006; Pfeiffenberger et al., 2006; Ackman & Crair, 2014). While genetically encoded mechanisms provide positional cues, activity-dependent processes play a critical role in refining connections and ensuring the accurate transmission of visual information.

5.3. The auditory system: tonotopy

The auditory system processes sound through a complex pathway that begins in the middle ear and extends to the auditory cortex. Sound vibrations are collected by the auricle and transmitted as mechanical vibrations through the ossicles of the middle ear (the malleus, incus and stapes) to the cochlea in the inner ear. Within the cochlea, these mechanical signals are transduced into electrical impulses by the organ of Corti, a specialized sensory epithelium. This structure contains inner hair cells (IHCs), which act as the primary sensory receptors, and outer hair cells (OHCs), which amplify low-level sounds to enhance sensitivity and frequency selectivity (Mann & Kelley, 2011; Ashmore et al., 2010). IHCs connect to type I spiral ganglion neurons (SGNs), encoding auditory signals for transmission to the brain

(Meyer et al., 2009). OHCs are innervated by type II SGNs, which modulate cochlear sensitivity through the olivocochlear reflex, a mechanism essential for adjusting hearing sensitivity and frequency selectivity (Berglund & Ryugo, 1987; Jagger, 2003; Thiers et al., 2008; Froud et al., 2015).

In mice, cochlear development begins at E11.5, with IHCs and OHCs undergoing differentiation by E18.5. However, the cochlea remains functionally immature at birth, and auditory responses emerge around P12, when cochlear nerve fibers fully innervate the IHCs (Koundakjian et al., 2007; Lim & Anniko, 1985). Auditory information then travels via the vestibulocochlear nerve to the cochlear nucleus (CN) in the brainstem, proceeding through the lateral lemniscus to the inferior colliculus (IC) in the midbrain, and onward to the medial geniculate body (MGB) in the thalamus, before reaching the auditory cortex (A1). Feedback loops at multiple levels of the pathway, including those involving the superior olivary complex (SOC), fine-tune auditory processing and spatial sound localization (Malmierca & Ryugo 2012; Terreros & Delano, 2015).

Like other sensory systems, the auditory system develops a topographic map known as tonotopy, which organizes sounds spatially based on their frequency (Russell & Sellick, 1977; Mann & Kelley, 2011). This arrangement begins in the cochlea, where neurons are distributed along its longitudinal axis according to their frequency sensitivity: high frequencies are detected in the basal region, while lower frequencies are processed in the apical region. This precise tonotopic segregation is maintained throughout the auditory pathway, including the CN and brainstem, through well-organized axonal projections that preserve this spatial arrangement.

Notably, the tonotopic map in the cochlea is established before auditory stimuli can elicit responses in the auditory nerve. In mice, for instance, hearing onset begins around P12, suggesting that the initial formation of tonotopy occurs independently of external auditory input. Instead, this early organization is thought to rely on intrinsic mechanisms, such as gradients of signaling molecules, including such tyrosine kinase receptors and Ephrin receptor families, which are crucial for guiding the development of this spatial mapping

(Fariñas et al., 2001; Cramer, 2005; Huffman & Cramer, 2007; Koundakjian et al., 2007; Kandler et al., 2009).

This tonotopic organization enables sounds of different frequencies to activate specific regions along the auditory pathway, ensuring precise frequency discrimination and efficient processing of auditory signals from the cochlea to higher auditory centers.

5.4. The somatosensory system: somatotopy

The somatosensory system is essential for interacting with the environment. It provides tactile information about objects and proprioceptive feedback on body position and movement. Additionally, this system regulates body temperature and enables the detection of painful stimuli, ensuring both sensory perception and physiological homeostasis. Like the visual and auditory systems, the topographical representation of the different body parts is not confined to the cortex but is established throughout all sensory stations of the somatosensory pathway, preserving a precise somatotopic organization and connectivity.

In the 1970s, Woolsey and Van der Loos identified cytoarchitectonic units in L4 of the cortex, which they termed "barrels" (Woolsey & Van der Loos, 1970; Woolsey et al., 1975). These barrels are a hallmark of the somatosensory cortex, specialized for processing sensory input from whisker follicles in the rodent's snout. Corresponding whisker-specific neural patterns in subcortical structures are known as "barreloids" in the thalamus (Van der Loos, 1976) and "barrelettes" in the brainstem (Ma & Woolsey, 1984). The spatial distribution of barrels mirrors the organization of whiskers and sinus hairs on the snout. A similar, albeit less robust barrel-like pattern can also be found in cortical maps representing the upper lip, lower jaw, forepaw and hidpaw pads (Belford & Killackey, 1978; Dawson & Killackey, 1987; Killackey et al., 1995). The entire somatosensory map is revealed as a "musculus" or "ratunculus" (Erzurumlu and Gaspar, 2012) serving as the rodent equivalent of the well-known "homunculus" map in humans.

Whisker follicles are innervated by neurons from the trigeminal ganglion (TG), which project to various trigeminal nuclei in the brainstem, forming at least four axonal pathways:

lemniscal 1, lemniscal 2, extralemniscal and paralemniscal (Deschênes & Urbain, 2009; Pouchelon et al., 2012; Feldmeyer, 2012). These pathways differ in their brainstem origins, thalamic targets and cortical projections, including distinct regions and layers. Moreover, each pathway is associated with distinct somatosensory modalities, reflecting their specialized roles in processing sensory information. The lemniscal pathway is primarily involved in processing the combined whisking-touch signal, the paralemniscal pathway plays a key role in the whisking signal associated with sensory-motor control, and the extralemniscal pathway is responsible for detecting contact signals (Yu et al., 2006). The lemniscal pathway, the most extensively studied, is divided into two subcategories, both of which originate at the principal trigeminal nucleus (PrV) in the brainstem, which contains barrelettes, as the primary trigeminal station. In lemniscal 1 pathway, PrV axons target the core of VPM barreloids and TCAs predominantly innervate neurons in L4 and L6a, with minor projections to L3 and L5b neurons within the corresponding barrel in S1. These neurons are characterized by single-whisker receptive fields (Meyer et al., 2010; Oberlaender et al., 2012; Ueta et al., 2023). Conversely, in the lemniscal 2 pathway, PrV axons innervate the head of VPM barreloids and TCAs project exclusively to L4 barrel septa neurons, which are distinguished by their multi-whisker receptive fields (Brecht & Sakmann, 2002; Kitazawa & Rijli, 2018). The paralemniscal pathway originates from neurons in the rostral part of the interpolaris spinal trigeminal nucleus (SpVir), which lacks discernible barrelette domains (Pierret et al., 2000), and projects to the POm thalamic nucleus, a structure also devoid of barreloid organization. Axons from this pathway predominantly target L1 and L5a neurons in S1, as well as L4 neurons in S2, particularly within septal regions. Additionally, the paralemniscal pathway extends projections to the primary motor cortex (M1), highlighting its role in integrating sensory and motor signals (Wimmer et al., 2010; Bosman et al., 2011; Viaene et al., 2011; Pouchelon et al., 2014; Kitazawa & Rijli, 2018; Ueta et al., 2023). The extralemniscal pathway arises in the caudal portion of the interpolaris spinal trigeminal nucleus (SpVic), in which barrelette-like organization is present, and targets the ventro-lateral VPM (VPMvl), a region that lacks the barreloid-like structures (Pierret et al., 2000; Bokor et al., 2008; Ueta et al., 2023). This

pathway project to neurons in L3, L4, and L6 of both S1 and S2 cortices, with particularly dense innervation in S2 (Pierret et al., 2000).

In rodents, the whisker system, particularly the barrel cortex, has been widely studied as a model for understanding somatosensory processing, due to its precise topographical organization. Moreover, it serves as a powerful tool for exploring the mechanisms underlaying the development and plasticity of cortical maps (Erzurumlu & Gaspar, 2020).

5.4.1. Development of the somatosensory pathway

To gain deeper insights into the somatosensory circuitry, this section delves into the developmental sequence of its pathway, which is crucial for the proper assembly and functional maturation of the somatosensory system.

The development of the somatosensory pathway begins early in embryogenesis, with TG neurons forming by E9.0 (Erzurumlu et al., 2010). These neurons differentiate into three facial divisions: ophthalmic, mandibular and maxillary (whisker-related), based on intrinsic transcriptomic programs independent of peripheral connections (Hodge et al., 2007; Pouchelon et al., 2012). TG axons enter the hindbrain at E9.5, innervate cutaneous receptors (e.g., whisker follicles) by E12.5, and extend oriented collaterals to the PrV in the brainstem by E14.5, concurrent with PrV genesis (E10.5-E15.5) (Kitazawa & Rijli, 2018). This marks the onset of topographic mapping, which is refined with whisker-specific precision by E17.5 (Laumonnerie et al., 2015). Maxillary (upper lip and whisker-related) TG axons target the ventral PrV (vPrV, rombomere3-derived) while mandibular (lower jaw) axons innervate the dorsal PrV (dPrV, rombomere2-derived) (Erzurumlu & Killackey 1983; Oury et al. 2006; Erzurumlu 2010; Kitazawa & Rijli 2018; Iwasato & Erzurumlu 2018). Recent unpublished findings indicate that the upper lip is positioned between the vPrV and dPrV and is derived from both rhombomere 2 and 3 (unpublished date from our lab in collaboration with Filippo Rijli). PrV afferents cross the midline at E11.5 and reach the contralateral VPM nucleus by E16.5, a process directed by intrinsic genetic programs, including the expression of Drg11 and Hoxa2, which ensure accurate VPM targeting (Ding et al., 2003; Oury et al., 2006;

Bechara et al., 2015). By P2-P3, PrV-derived VPM afferents refine their diffuse arbors into whisker-specific patches (barreloids) (Kivrak & Erzurumlu, 2013). VPM axons extend topographically organized projections to the cortex by E18.5, forming barrels in L4 of S1 between P3 and P4 (**Fig. 7**) (Woolsey & Van der Loos, 1970; Woolsey et al., 1975; Pasternak & Woolsey et al., 1975). This process is guided by molecular cues such as Fgf8 and Ephrins (Fukuchi-Shimogori & Grove, 2001; Shimogori & Grove, 2005) and activity-dependent mechanisms (Jensen & Killackey, 1987; Fox et al., 1996; Mitrovic et al., 1996; Martini et al., 2018, 2021; Antón-Bolaños et al., 2019). Early postnatal disruptions such as infraorbital nerve sectioning can interfere with barrel formation, emphasizing the influence of peripheral and thalamic inputs in shaping cortical map development (Van der Loos & Woolsey, 1973; Killackey et al., 1976).

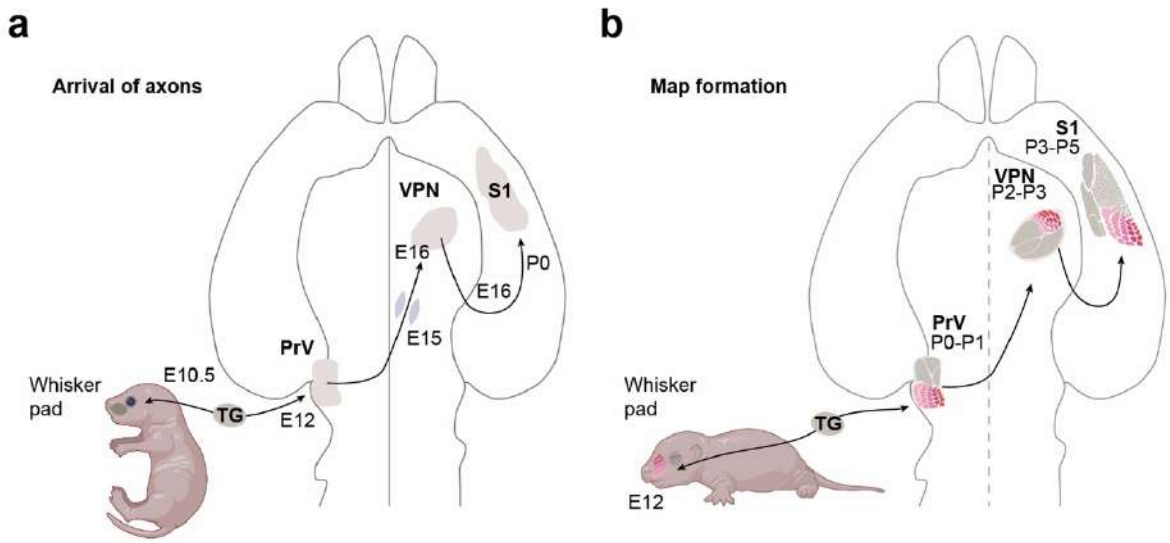

Fig. 7. Development of the mouse somatosensory system. a Timeline showing the sequential arrival of afferent inputs along the somatosensory pathway during development. **b** Timing of axonal and cellular pattern formation essential for somatotopic map organization. E, embryonic; P, postnatal; PrV, principal trigeminal nucleus; TG, trigeminal ganglion, VPN, ventral posterior nucleus; S1, primary somatosensory cortex. Adapted from Erzurumlu & Gaspar, 2012.

TCAs initially form extensive, unrefined branches, with improperly positioned branches undergoing elimination ("pruning"), while correctly located ones are stabilized and mature into definitive thalamocortical arbors (Senft & Woolsey, 1991a; 1991b; Rebsam et al.,

2002). Furthermore, some studies suggest that TCAs are pre-organized into columns as they grow through the cortical plate. During the final stages of TCAs clustering and barrel map formation, an initial phase of unrefined branching is followed by selective and restrictive process of arborization (Agmon et al. 1993; Agmon et al. 1995; Crandall et al. 2017; Martini et al., 2018). Moreover, disruptions to the topographic organization of TCAs along their pathway have been shown to impair clustering, resulting in aberrant barrel maps (Lokmane et al. 2013). Collectively, these findings support the hypothesis of a pre-patterned organization of TCAs before they reach the immature layer 4, underscoring the interplay between intrinsic genetic programs and subsequent peripheral input in refining somatosensory maps.

5.4.2. Columnar circuitry

One of the defining features of sensory cortices is their organization into radial columnar units, which serve as integrative hubs for afferent, intrinsic, and efferent neuronal information. This columnar framework begins to emerge early during corticogenesis, as clonally related neurons migrate from the VZ along radial glial cells to form ontogenic columns (Rakic, 1988; Noctor et al., 2001; Fishell & Kriegstein, 2003). These primitive structures provide the foundation for the functional columnar architecture observed in the mature somatosensory cortex, particularly within the barrel cortex.

Layer 4 forms the core of intracolumnar information flow, receiving the primary input from the VPM thalamic nucleus and distributing excitation accross all layers of the column to establish barrel connections (Bruno, 2006). This layer is primarily populated by two types of excitatory neurons, both adhering to columnar connectivity: spiny stellate (ss) and star pyramidal (sp) neurons. L4ss neurons exhibit highly localized connectivity, predominantly targeting neurons within the same barrel and extending to adjacent barrels. In contrast, L4sp neurons demonstrate long-range connectivity, integrating information horizontally across multiple neighboring barrels and infragranular layers (Schubert et al., 2003; Egger et al., 2008; Narayanan et al., 2017). L4ss neurons form the barrel wall and orient their dendrites toward the barrel hollow, where they establish connections with TCA arbors.

These neurons primarily target other L4ss neurons and pyramidal neurons in L2/3 within the same barrel, while also extending additional projections to layers 5a, 5b and 6 (Lefort et al., 2009; Feldmeyer, 2012).

In contrast to other sensory cortices, like the mouse motor cortex, where L2/3 to L5 connectivity dominates the intracortical circuitry (Weiler et al., 2008), L4 plays a central role in the barrel cortex (Lefort et al., 2009), linking thalamic input to L2/3 and creating a robust columnar network (Petersen & Sakmann, 2001; Feldmeyer et al., 2002). Focusing on the barrel-septa organization, numerous studies have demonstrated that L2 and L3 neurons located above the barrel receive strong activation from L4 neurons, whereas L2 neurons situated above the septa are predominantly excited by L5a pyramidal neurons. This distinction highlights the cortical continuity of the lemniscal (VPM-L4-L2/3 barrel) and paralemniscal (POm-L5a-L2) pathways, with L2 serving as a key convergence point for these two somatosensory processing streams (Shepherd & Svoboda, 2005; Bureau et al., 2006). L2/3 pyramidal neurons are vertically connected within the column to both L5a and L5b neurons (Shepherd & Svoboda, 2005; Lefort et al., 2009; Hooks et al., 2011). However, their defining characteristic is the presence of long axons that extend vertically while also giving rise to numerous long-range horizontal collaterals. These collaterals facilitate connections with adjacent cortical domains, including neighboring columns within S1 as well as ipsilateral regions such as S2 and M1 (Yamashita et al., 2018). Notably, L2/3 neurons also project to the contralateral whisker-related S1 via the corpus callosum, thereby integrating sensory information across both cortical hemispheres (Petreanu et al., 2007).

Layer 5, the primary output layer of the cortex, can be subdivided into L5a and L5b based on differences in histological features, connectivity patterns and functional roles (Wise & Jones, 1977; Larsen & Callaway, 2006). L5a neurons predominantly process paralemniscal input from the POm, whereas L5b neurons relay lemniscal signals from the VPM, reflecting their distinct contributions to sensory processing. Meanwhile, L6 is divided into L6a and L6b. L6a mainly consists of pyramidal neurons, whereas L6b is highly heterogeneous, characterized by a diverse range of dendritic domains found in both barrel and non-barrel

regions. L6b neurons primarily innervate the POm, with a subset extending axons to L1. These neurons originate from various cortical regions, including the subplate and cortical plate, reflecting their developmental diversity. L6a neurons can be further subdivided based on their projection targets: those projecting intracortically and those targeting the thalamus. L6a is considered the primary source of CT connectivity, playing a key role in feedback regulation of thalamic function (Jones & Wise, 1977; Thomson, 2010; Fox & Woolsey, 2009). These neurons can be further categorized into three groups based on their thalamic targets: (1) neurons projecting exclusively to the VPM with columnar collaterals to L4; (2) neurons targeting both the VPM and POm, with widespread collaterals to L4 and L5 across multiple barrels in a non-columnar pattern; and (3) neurons projecting only to the POm, located in the lower portion of L6a, with some branches extending to L5b. Intracortically projecting L6a pyramidal neurons primarily innervate L5 and L6 across multiple barrels, facilitating transcolumnar interactions in the infragranular layers of the barrel cortex. L6a neurons integrate inputs from L5b, other L6a neurons, and L4 excitatory neurons, reflecting their central role in the intracortical and corticothalamic connectivity essential for sensory processing and feedback mechanisms.

This columnar circuitry underscores the somatosensory cortex's sophisticated organization, with its layers interconnected through distinct pathways that balance local and global signal integration. The interplay of thalamocortical and intracortical circuits ensures precise sensory representation, integrating inputs across layers, barrels, and hemispheres.

5.4.3. Somatosensory maps

In rodents, the somatosensory system is organized into precise topographic maps that represent different body parts, with the size of each map reflecting the functional significance of the corresponding region. The most prominent feature of these maps is the extensive representation of the whiskers, which are critical for tactile exploration and environmental sensing. In the primary somatosensory cortex, each whisker is represented in a single barrel (Van der Loos & Woolsey, 1973). This whisker-related representation is known as the postero-medial barrel subfield (PMBSF) (Welker, 1976; Diamond et al., 2008). The PMBSF

occupies a disproportionately large portion of the somatosensory cortex, highlighting the behavioural importance of the mystacial whiskers. Complementing the PMBSF, the antero-lateral barrel subfield (ALBSF) is another barrel field territory, characterized by smaller and less refined barrels (Woolsey & Van der Loos, 1970). The ALBSF represents the small follicles located in the upper lip of the snout (Brecht et al., 1997) and occupies a cortical area in S1 comparable in proportion to the PMBSF (**Fig. 8**).

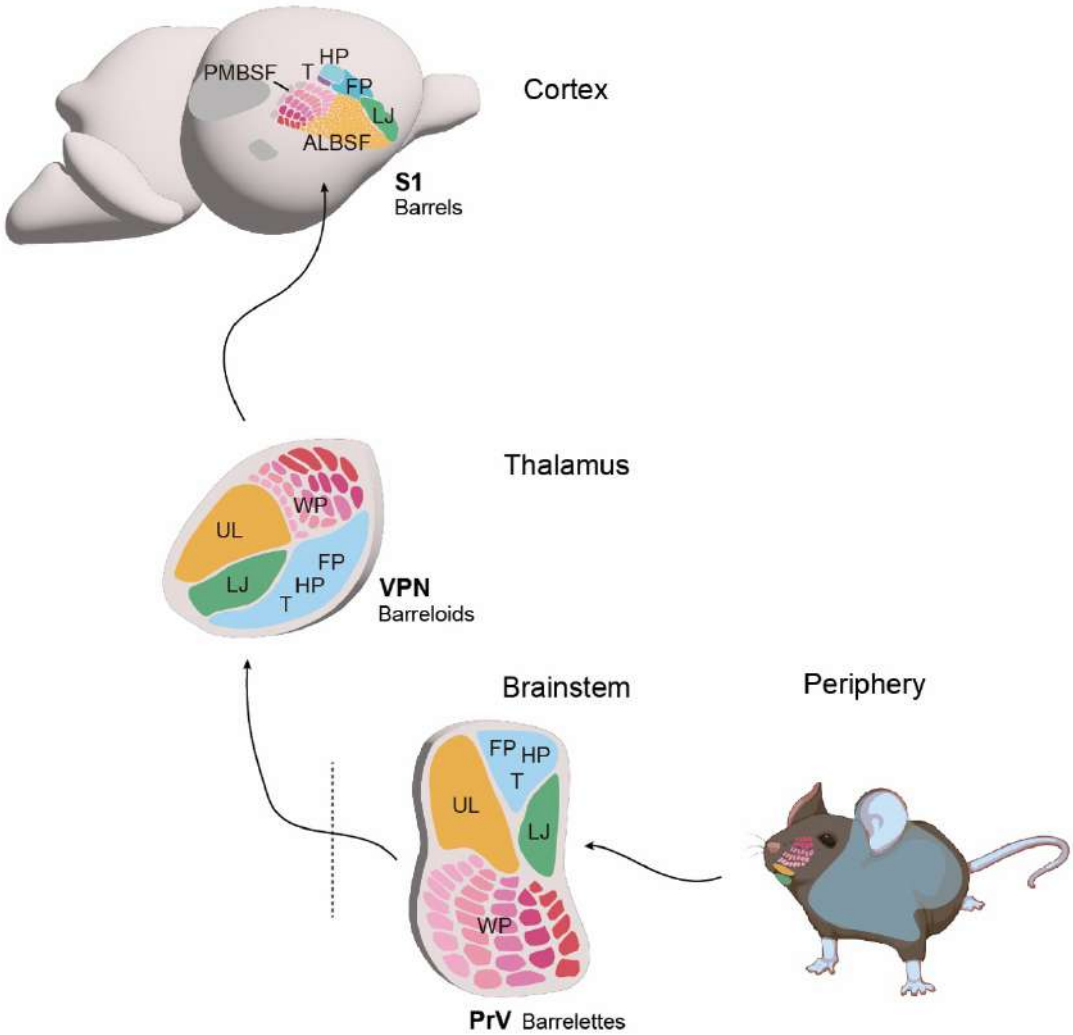

Fig. 8. Mapping of the somatosensory pathway in mice. Schematic representation of the organization of peripheral sensory receptors from different body parts across the key stations of the somatosensory pathway. Sensory inputs from the whisker pad, where mystacial whiskers are arranged in five distinct rows, are transmitted in a precise topographic manner, preserving somatotopic connectivity at each relay station. This organization is maintained through the principal trigeminal nucleus (PrV) in the brainstem, where whisker-related structures form barrelettes, the ventral posterior nucleus (VPN) of the thalamus, where they appear as barreloids, and finally in primary somatosensory cortex (S1), where they form barrels. The

gray dashed line represents the midline, marking where axons cross to the contralateral hemisphere. To facilitate visualization, different body parts are color-coded: whisker pad (WP)-magenta gradient; upper lip (UL)-orange; lower jaw (LJ)-green; forepaw (FP), hindpaw (HP) and trunk (T)-blue gradient. ALBSF, antero-lateral barrel subfield; PMBSF, postero-medial barrel subfield.

Other body parts, such as the paws, trunk, and lower jaw, are also represented in the somatosensory pathway but occupy smaller cortical regions compared to the barrel subfields. For instance, the forepaw and hindpaw are mapped in regions adjacent to the barrel subfields, while the trunk and tail are represented more caudally in S1 (Zembrzycki et al., 2013). The relative size of these cortical representations mirrors the density of sensory receptors and the functional importance of each body part. The whisker map, being the largest, reflects the high tactile sensitivity and receptor density of the whisker follicles, whereas less innervated regions, like the trunk, have proportionally smaller cortical representations (Feldmeyer, 2012; Erzurumlu & Gaspar, 2012). Subcortical structures also exhibit these somatosensory maps. In this work, the corresponding barrel field areas in the thalamus are referred to as the whisker pad VPM (wpVPM) and upper lip VPM (ulVPM). Additionally, the ventral part of the PrV (vPrV) is assumed to represent the major whiskers on the snout, while the dorsal PrV (dPrV) encompasses regions corresponding to the upper lip's small whiskers, lower jaw, paws, and trunk.

6. Spontaneous activity in sensory systems development

6.1. Overview

Spontaneous activity is widely recognized as a fundamental driver of brain development, particularly during the early developmental stages. This intrinsically generated activity, which operates independently of external sensory input, is essential for shaping neural circuits (Huberman et al., 2008a). Remarkably, even before sensory experience, the newborn brain possesses the capacity to perceive and interpret its environment. This capability relies on the precise establishment of neural circuits prior to birth, guided by two key mechanisms: molecular guidance cues that direct axons to their appropriate targets (Sanes and Yamagata,

2009) and activity-dependent processes driven by spontaneous neuronal activity (Blankenship and Feller, 2010; Ackman and Crair, 2014; Antón-Bolaños et al., 2019). Together, these mechanisms orchestrate the proper assembly of functional neural networks, laying the foundation for sensory processing and cognitive development. Subsequently, evoked neuronal activity, primarily driven by external peripheral sensory input, becomes crucial in refining these networks, playing a fundamental role in the final assembly and maturation of sensory maps and the establishment of functional circuitry (Landers & Philip Zeigler, 2006; Hagihara et al., 2015; Van der Bourg et al., 2017; Gribizis et al., 2019; Murata & Colonnese, 2019; Martini et al., 2021).

Spontaneous activity is involved in numerous developmental processes, including cell differentiation, migration, apoptosis, axon refinement and synapse formation (Katz and Shatz, 1996; Hanson and Landmesser, 2004; Kilb et al., 2011; Yamamoto and López-Bendito, 2012; Cang and Feldheim, 2013). Ongoing research continues to explore the mechanisms underlying communication between thalamic and cortical neurons during early development. Furthermore, spontaneous activity conveys topographic information essential for the accurate formation of sensory circuits (Erzurumlu and Gaspar, 2012; Arakawa et al., 2014b; Mizuno et al., 2018a). These findings underscore the importance of spontaneous neuronal activity in establishing the precise neural architecture required for sensory processing.

6.2. Spontaneous activity in the developing thalamus

Spontaneous neuronal oscillations in the thalamus, known as thalamic calcium waves, are mediated by gap junctions and are critical for the initial development of thalamocortical connectivity. In mice, this spontaneous activity begins toward the end of the second gestational week, displaying endogenous and uncorrelated patterns of activity between E12 and E14. By E14, this activity becomes synchronized, generating waves that travel across prospective thalamic nuclei. These waves initially involve only FO nuclei but, by E18, also encompass HO nuclei (Moreno-Juan et al., 2017; Martini et al., 2018; Martini et al., 2021). As development proceeds, the frequency of thalamic waves decreases, with somatosensory and

auditory waves ceasing around birth, and visual waves fading by P2 in *ex vivo* preparations. However, whether these patterns are consistent *in vivo* remains unclear (**Fig. 9**).

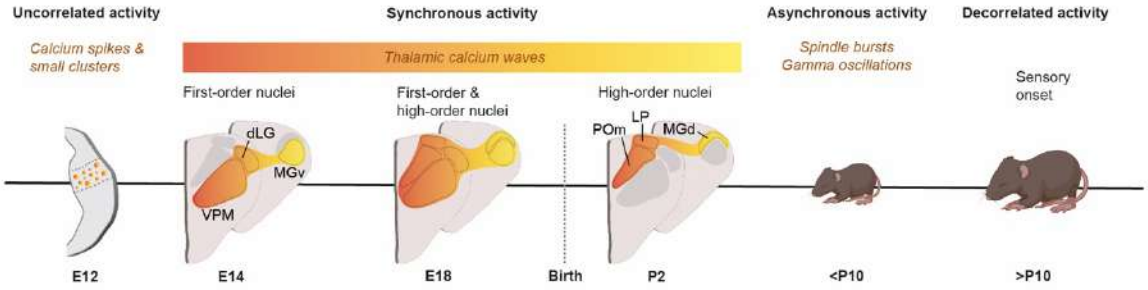

Fig. 9. Developmental timeline of thalamic spontaneous activity patterns. Thalamic spontaneous activity undergoes dynamic transitions throughout embryonic and early postnatal development in mice. Initially, early uncorrelated activity consists of calcium spikes and small localized clusters. As development progresses toward late gestation and birth, this activity becomes more synchronized, forming thalamic calcium waves that coordinate activity across the first-order thalamic nuclei. At perinatal stages, these waves begin to propagate toward high order nuclei. After birth, during the early postnatal period, spontaneous thalamic activity is characterized by spindle bursts and gamma oscillations, which gradually diminish and become sparse and decorrelated following sensory onset. dLG; dorsal lateral geniculate nucleus; E, embryonic; LP, lateral posterior nucleus; MGd; dorsal division of the medial geniculate body; MGv; al division of the medial geniculate body; P, postnatal; POm, posterior medial nucleus; VPM, ventral posterior nucleus. Adapted from Martini et al., 2021.

Synchronized thalamic activity is key to synaptic refinement, aligning sensory inputs to cortical regions, and driving activity-dependent developmental processes that shape thalamocortical circuits. Experimental disruptions of this activity have revealed changes in gene expression that impact the growth and branching of thalamocortical axons (Herrmann & Shatz, 1995; Uesaka et al., 2007; Mire et al., 2012; Yamamoto & López-Bendito, 2012; Castillo-Paterna et al., 2015; Moreno-Juan et al., 2017; Antón-Bolaños et al., 2018). For instance, thalamic waves influence the expression of receptors such as Robo1 and Dcc, which regulate axonal growth by acting as inhibitory or stimulatory signals, respectively (Mire et al., 2012; Castillo-Paterna et al., 2015). This spontaneous activity patterns also influence the size of cortical regions, with an increased frequency of thalamic calcium waves promoting the expansion of primary cortical areas through modulation of the expression of the transcription factor *Rorβ* in the thalamus (Moreno-Juan et al., 2017). *Rorβ* fine-tunes axonal arborization

within thalamocortical projections, affecting their axonal length and branching. This activity-dependent regulation contributes to cortical enlargement and the structural organization of thalamocortical pathways. Notably, thalamic calcium waves have been implicated in cross-modal plasticity processes during development—a topic that will be explored further in Section 7.1. "Cross-modal plasticity".

Thalamic waves are also involved in synaptic pruning. Early in development, an excess of synaptic connections is formed, which is later refined through activity-dependent mechanisms. By synchronizing the firing of neuronal populations, thalamic waves generate activity patterns that selectively strengthen relevant synaptic connections while eliminating unnecessary ones (Yamamoto & López-Bendito, 2012; Cang & Feldheim, 2013). This refinement process sculpts the architecture of thalamocortical circuits, preserving only functionally relevant connections, which is essential for effective sensory processing and transmission (Hanganu-Opatz, 2010; Molnár et al., 2020). Disruptions in this activity patterns, caused by genetic mutations, environmental factors, or neurodevelopmental disorders (O'Donnell & Grace 1998; Herrera & Tarokh, 2024; Uhlhaas & Roux, 2016; Benoit et al., 2022), can lead to aberrant synaptic connections in thalamocortical pathways and sensory impairments, underscoring the importance of early synchronized activity in the formation of these circuits (López-Bendito & Molnár, 2003; Yamamoto & López-Bendito, 2012).

Another significant function of thalamic waves is their role in establishing topographic maps. These waves coordinate neuronal firing patterns in the developing thalamus and cortex, aligning sensory inputs with their corresponding cortical regions. This precise organization is crucial for forming sensory representations, such as the somatotopic map in the somatosensory cortex (Antón-Bolaños et al., 2019). Antón-Bolaños and colleagues (2019) demonstrated that embryonic thalamic waves guide the development of cortical columns and the emergence of functional somatotopic maps. Through the temporal and spatial synchronization of neuronal activity, thalamic waves ensure the proper

topographical organization of sensory inputs, forming the foundation for accurate sensory perception and interaction with the environment.

Thalamic calcium waves diminish by P2 in brain slices; however, their precise electrical counterpart *in vivo* remains unidentified (Moreno-Juan et al., 2017). Extracellular recordings from early postnatal mice reveal that thalamic activity features spontaneous, discontinuous bursts of gamma, spindle, or mixed oscillations (Khazipov et al., 2013; Murata and Colonnese, 2016). While primarily driven by sensory organs, these oscillations can also be evoked by external stimuli but are not wholly dependent on them. Importantly, this activity is synchronized with the cortex, playing a crucial role in forming proper thalamocortical connections, as demonstrated by the coordinated activity between somatosensory barreloids and their corresponding cortical barrels (Minlebaev et al., 2011; Yang et al., 2013). By the end of the first postnatal week, thalamic activity transitions into a continuous pattern influenced by the behavioural state of the animal (Murata and Colonnese, 2018). This shift facilitates the integration of sensory-driven neuronal activity, essential for refining neural networks. Collectively, these processes culminate in the maturation of sensory maps, enabling the formation of functional neural circuits (Hagihara et al., 2015; Van der Bourg et al., 2017; Gribizis et al., 2019).

6.3. Spontaneous activity in the visual system

Spontaneous activity in the retina arises before eye opening and the onset of visual experience, playing an important role in the development of the visual system (Wong, 1999; Akerman et al., 2002; Rochefort et al., 2011). This activity is characterized by propagating retinal waves —spatially and temporally correlated bursts of neuronal firing within RGCs. Retinal waves begin during late embryonic stages and persist until the second postnatal week, overlapping briefly with sensory-driven activity following eye-opening (Ackman et al., 2012; Syed et al., 2004). These waves are categorized into three distinct developmental stages—type I, II, and III—each defined by specific molecular mechanisms and functional roles in circuit formation.

Type I retinal waves, which emerge prenatally around E16 and continue until ~P1, are mediated by gap junctions that facilitate communication between adjacent RGCs. These waves include both large propagating events and smaller, non-propagating events (Bansal et al., 2000; Syed et al., 2004; Kähne et al., 2019; Voufo et al., 2023). Our group has made a significant discovery, demonstrating for the first time that type I retinal waves influence early sensory circuit development. Specifically, we found that visual and somatosensory circuits initially emerge intermingled, undergoing functional segregation in the SC during perinatal stages. This segregation process is driven by the activity of type I retinal waves within the SC (Guillamón-Vivancos et al., 2022), highlighting the critical role of these early spontaneous activity patterns in specifying sensory modalities. Interestingly, while gap-junction blockers partially inhibit type I waves, their persistence suggests the involvement of additional mechanisms in generating this activity. This observation underscores the need of further investigation into the genesis and regulation of type I retinal waves (Voufo et al., 2023).

Type II retinal waves, mediated by cholinergic signaling in amacrine cells, dominate from ~P1 to ~P10 (Ford et al., 2012). This phase coincides with the refinement of retinotopic maps and the eye-specific segregation in the dLG (Huberman et al., 2008a; Zheng et al., 2004). Experimental manipulations, such as blocking nicotinic acetylcholine receptors using epibatidine or generating β2nAChR-knockout mice (lacking the β2-acetylcholine receptor), reveal that disruption of type II waves impairs eye-specific segregation and changes the ocular dominance columns, leading to diffuse axonal arborization and enlarged receptive fields (Penn et al., 1998; Torborg & Feller, 2005; Huberman et al., 2006, 2007, 2008a; Blankenship & Feller, 2010). These deficits underscore the importance of type II waves in establishing precise retinogeniculate connections.

Type III retinal waves, emerging from ~P10 and lasting until eye-opening (~P12-P14), are driven by glutamatergic transmission and exhibit localized, fast propagation patterns (Feller et al., 1996; Syed et al., 2004; Firth et al., 2005; Blankenship et al., 2009; Ackman et al., 2012; Martini et al., 2021). The overlap of type III waves with early sensory experience suggests their role in integrating spontaneous and evoked activity to further refine visual

circuits, including ocular dominance columns and orientation selectivity in V1 (Ackman & Crair, 2014; Hooks & Chen, 2006) (**Fig. 10**).

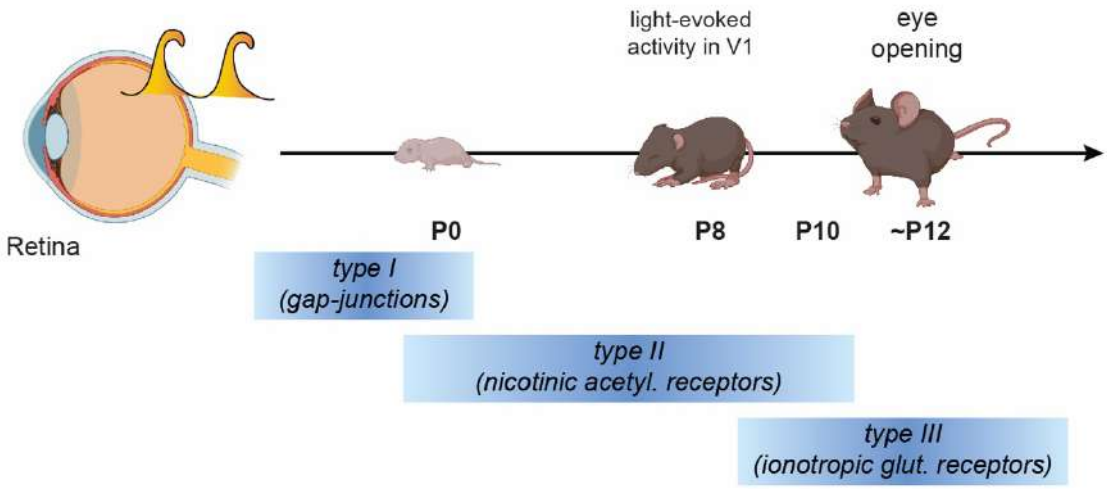

Fig. 10. Developmental timeline of retinal waves. Type I retinal waves emerge around E16.5 and persist until approximately P1, mediated by gap junctions. Type II retinal waves begin at P1 and continue until around P10, relying on nicotinic cholinergic receptors. Type III retinal waves airse around P10 and conclude by P14, coinciding with eye opening. These waves are driven by ionotropic glutamate receptors. E, embryonic; P, postnatal; V1, primary somatosensory cortex. Adapted from Martini et al., 2021.

Throughout development, spontaneous retinal waves propagate beyond the retina to the dLG, SC and V1, where they influence the formation of retinotopic maps and dendritic arborization (Mooney et al., 1996; Ackman et al., 2012; Siegel et al., 2012; Ackman & Crair, 2014; Kerschensteiner, 2016). Notably, wave-driven activity has been shown to synchronize neural firing across these structures, as observed in *in vivo* simultaneous calcium imaging studies of the SC and V1 (Ackman et al., 2012). The corticothalamic loop further amplifies these patterns, highlighting the integrated nature of spontaneous activity throughout the visual system (Murata & Colonnese, 2016). Retinal activity is also involved in shaping map formation and refining dendritic structures within the visual cortical regions (McLaughlin et al., 2003; Siegel et al., 2012; Burbridge et al., 2014).

Experimental approaches, such as blocking retinal activity with tetrodotoxin (TTX) or pharmacologically targeting specific receptors, have demonstrated the indispensability of

retinal waves in visual development. For example, blocking type II waves disrupts eye-specific segregation in the dLG of ferrets and mice, while type III waves can partially rescue these deficits, emphasizing their complementary roles (Shatz & Stryker, 1988; Huberman et al., 2008a).

In addition to spontaneous activity, evoked activity plays a crucial role in shaping visual circuits. Light passing through closed eyelids before eye-opening activates intrinsically photosensitive RGCs and photoreceptors, potentially influencing the generation of stage III retinal waves and refining retinogeniculate projections (Krug et al., 2001; Tu et al., 2005; Tiriac et al., 2018; Shen & Colonnese, 2016; Tiriac & Feller, 2022). This interaction between spontaneous and evoked activity ensures the precise development of visual pathways, including retinotopy and functional connectivity (White et al., 2001; Huberman, 2007; Renna et al., 2011; Ackman & Crair, 2014).

Finally, retinal activity is involved in regulating gene expression patterns within the dLG, as evidenced by several studies. Transcriptional analyses of the visual cortex in monocularly enucleated mice at various developmental stages revealed significant downregulation of specific genes, including transcription factor Fos, brain-derived neurotrophic factor (BDNF), early growth factors 1 and 2 (Egr1 and Egr2), and genes associated with MAPK signaling pathway regulation (Majdan & Shatz, 2006). Strikingly, in binocular enucleated mice, the dLG showed a downregulation of ephrinA5 expression (Dye et al., 2012). Further insights came from studies ablating RGCs, which demonstrated differential expression of ADAMs metalloproteinases in the dLG of sensory-deprived mice (Brooks et al., 2013). Collectively, these findings underscore the influence of retinal activity in modulating the genetic landscape of the dLG during development (Brooks et al., 2013).

Overall, the sequential stages of retinal waves, coupled with their propagation throughout the visual system, highlight their fundamental role in establishing the structural and functional architecture of the visual pathway. These insights provide a foundation for understanding how early activity shapes sensory circuits and prepares the visual system for sensory-driven refinement.

6.4. Spontaneous activity in the auditory system

The maturation of the auditory system relies on a complex interplay of spontaneous and sound-evoked neural activity, with spontaneous events predominating in early development before the onset of hearing (Geal-Dor et al., 1993; Meng et al., 2020). From embryonic stages, the cochlea generates rhythmic bursts of spontaneous activity intrinsic to IHCs. These bursts, driven by calcium-dependent action potentials, have been extensively observed through electrophysiological studies in neonatal rodents (Tritsch and Bergles, 2010; Johnson et al., 2011; Kennedy, 2012; Sendin et al., 2014; Wang and Bergles, 2015; Leighton and Lohmann, 2016). Supporting cells periodically release ATP, triggering depolarization in nearby IHCs and amplifying activity patterns along the cochlear axis (Tritsch et al., 2007; Tritsch & Bergles, 2010; Babola et al., 2021). Additionally, IHCs inherently generate action potentials with distinct spatial firing patterns along the cochlea's baso-apical axis, suggesting an intrinsic mechanism for localized signal propagation (Kros et al., 1998; Johnson et al., 2011; Sendin et al., 2014; Eckrich et al., 2018; Harrus et al., 2018). These IHCs-generated signals excite SGNs which, by birth (P0), display characteristic intermittent bursts of action potentials (Glowatzki and Fuchs, 2002; Zhang-Hooks et al., 2016; Coate et al., 2019; Babola et al., 2021).

SGNs act as conduits during the first postnatal week, relaying cochlear-driven spontaneous activity to brainstem auditory nuclei, including the IC. *In vivo* extracellular recordings from P4–P8 rats reveal spontaneous bursts of action potentials in these brainstem regions, emphasizing the peripheral origin of this activity, as it is abolished following contralateral cochleotomy (Tritsch et al., 2010). By P8–P10, neurons in the auditory nuclei from the brainstem transition from a predominantly bursting firing pattern to a more continuous, non-bursting activity profile, which is fully established by P12 (Sonntag et al., 2009) (**Fig. 11**). This temporal evolution of firing patterns aligns closely with critical periods of refinement of auditory circuits and development of tonotopic maps, underscoring the essential role of spontaneous activity in shaping the functional and structural organization of the ascending auditory pathway.

Recent advances in imaging techniques, including mesoscale calcium imaging and two-photon microscopy, have revealed bilaterally aligned spontaneous activity bands in the IC as early as P1 (Martini et al., 2021). These bands, originating in the cochlea, increase their frequency until P11-P12 and exhibit topographic organization correlating with the auditory cortex (Babola et al., 2018; 2021), underscoring the role of cochlear activity in establishing nascent tonotopic maps before ear opening. Despite these insights, the auditory thalamus remains an underexplored domain in this developmental framework, leaving its role in early auditory pathway refinement largely unresolved.

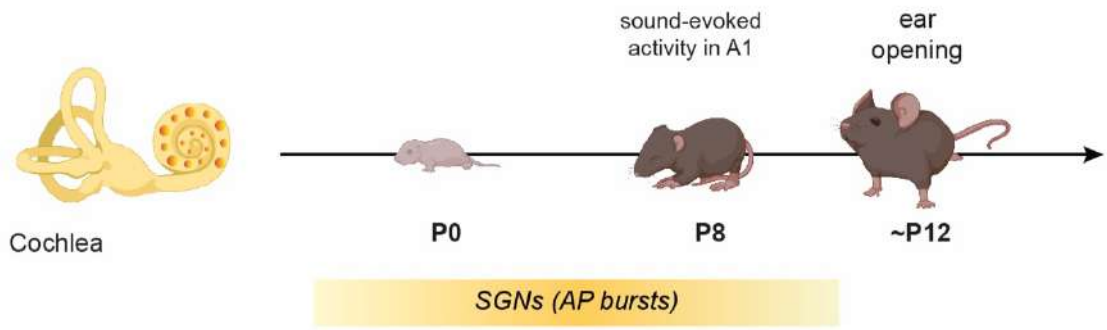

Fig. 11. Developmental timeline of spontaneous activity in the cochlea. During embryonic development, the cochlea generates spontaneous activity, which is relayed to spiral ganglion neurons as bursts of action potential. This activity persists until approximately P12, coinciding with ear opening. A1, primary auditory cortex; AP, action potential; E, embryonic; P, postnatal; SGNs, spiral ganglion neurons. Adapted from Martini et al., 2021.

6.5. Spontaneous activity in the somatosensory system

The development of the somatosensory system is profoundly influenced by spontaneous activity, which emerges during perinatal stages and is closely tied to self-generated body movements (Blumberg and Dooley, 2017; Fagard et al., 2018). These spontaneous movements have been shown to originate intrinsically within the spinal cord, independent of sensory afferent input or supraspinal control, as demonstrated by lesion studies in chick embryos (Hamburger et al., 1966; Hamburger and Narayanan, 1969). Extracellular recordings in freely moving chick embryos demonstrated a direct link between neuronal bursts in the

spinal cord and spontaneous limb movements, providing the first evidence of spontaneous neuronal activity in the developing nervous system (Provine et al., 1970). Similar patterns of intrinsic activity have been recorded in neonatal rodents, where spinal motor circuits spontaneously activate to drive limb movements without supraspinal involvement (Robinson et al., 2000; Inácio et al., 2016). This spinal activity predominates until the end of the second postnatal week, when the brainstem assumes primary control over motor functions (Kreider and Blumberg, 2000; Karlsson et al., 2005).

A key outcome of these spontaneous body movements is the activation of reafferent sensory pathways, which provide feedback to somatotopically organized regions in the spinal cord (Inácio et al., 2016). Reafferent signals, which encode spatiotemporal features of self-generated somatosensory stimuli, are thought to play a pivotal role in shaping thalamocortical networks during early development, particularly since the somatosensory pathway is functionally established at birth (Blumberg et al., 2013; Iwasato and Erzurumlu, 2018; Antón-Bolaños et al., 2019). Two types of body movements—local twitches during active sleep and complex movements during waking states—trigger distinct reafferent responses. Twitch-induced signals during sleep evoke robust responses in the somatosensory and motor cortices, as well as the thalamus (Khazipov et al., 2004; McVea et al., 2012). In contrast, waking movements either fail to elicit any supraspinal responses, or produce only highly unreliable responses associated with whisker movements (Tiriac et al., 2012; Dooley et al., 2020). This state-dependent gating is mediated by the external cuneate nucleus of the brainstem, which selectively transmits reafferent signals during sleep by comparing them with motor corollary efferent discharges (Tiriac and Blumberg, 2016). In rats, prior to P11, the external cuneate nucleus suppresses reafferent signals during waking periods but allows their transmission during sleep when twitches generate reafference (**Fig. 12**). This state-dependent modulation regulates the flow of sensory information to higher-order brain structures, potentially playing a key role in shaping the developing somatosensory pathway (Martini et al., 2021).

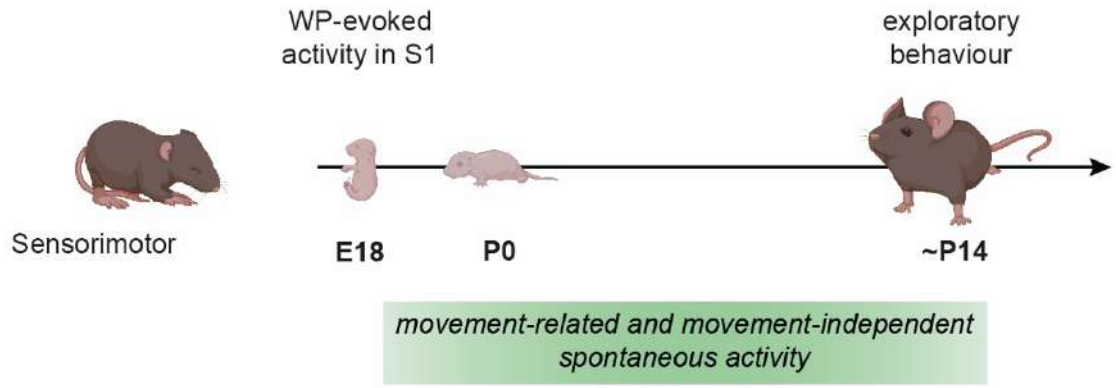

Fig. 12. Developmental timeline of spontaneous activity in the somatosensory system. During early development, spontaneous activity originates either from intrinsic sensory activity or through sensory-motor feedback. This activity persists until approximately P14, coinciding with the onset of exploratory behaviour. E, embryonic; P, postnatal S1, primary somatosensory cortex; Adapted from Martini et al., 2021.

Beyond reafferent signaling, spontaneous electrical activity in the spinal cord can occur independently of movement or as a response to external mechanical stimuli (Inácio et al., 2016). This sensory activity is transmitted to central somatosensory circuits, eliciting cortical responses even during embryonic stages (Yang et al., 2009; Mizuno et al., 2018a; Antón-Bolaños et al., 2019). Interestingly, activity in the primary somatosensory cortex persists even after spinal cord lesions, suggesting additional mechanisms influencing the functional interplay between spinal and cortical circuits during early development (Khazipov et al., 2004).

In neonatal mice, sensory input to the barrel cortex primarily originates from spontaneous whisker movements and passive interactions with littermates (Akhmetshina et al., 2016). Early evoked activity is a key element in driving cortical processes essential for the development of the somatosensory map. The onset of "mature" activity patterns, which are shaped by experience, is linked to exploratory behaviours and the initiation of active whisking around P12 (Landers & Philip Zeigler, 2006). Notably, early gamma oscillations (EGOs) and spindle bursts appear in the barrel cortex during a specific developmental window, and their contributions to somatosensory map formation have been extensively investigated (Yang et

al., 2013; Minlebaev et al., 2011; Khazipov & Luhmann, 2006; Luhmann & Khazipov, 2018; Yang et al., 2018).

In S1, early spontaneous activity plays a vital role in forming functional pre-columns that later develop into barrel columns (Golshani et al., 2009; Yang et al., 2013). Spindle bursts, EGOs, and other cortical oscillations emerge in the critical period (discussed in detailed below), driven by glutamatergic inputs from thalamic afferents and subplate neurons (Dupont et al., 2006; Tolner et al., 2012; Luhmann et al., 2016). Disrupting this activity, such as by lesioning the thalamus or silencing peripheral inputs, leads to severe impairments in cortical map formation (Molnár et al., 2003; Yang et al., 2013). Interestingly, even in the absence of fully formed barrels, cortical activity exhibits nascent topographic organization, suggesting that early spontaneous activity encodes topographic information for cortical network assembly (Khazipov et al., 2013; Mitrukhina et al., 2015; Luhman, 2017; Mizuno et al., 2018b). Thalamic spontaneous activity has been shown to influence the size of the cortical barrel map independently of peripheral activity. Moreno-Juan and colleagues (2017) showed that postnatal whisker trimming, which eliminates whisker-evoked sensory input, does not inhibit the enlargement of the PMBSF induced by increased thalamic calcium waves activity in the VPM. This finding highlight that the expansion of this cortical map is governed by thalamic spontaneous activity, functioning independently of external sensory input. Furthermore, embryonic thalamic waves play a crucial role in directing the accurate formation of cortical columns and are essential for the refinement of somatotopic maps (Antón-Bolaños et al., 2019).

The development of the somatosensory map is influenced by both intrinsic neuronal activity and external sensory inputs. Studies employing infraorbital nerve (ION) lesions, whisker manipulations, and genetic approaches have demonstrated that peripheral activity is critical for proper barrel formation during the first postnatal week, a key window of plasticity (Van der Loos and Woolsey, 1973; Iwasato et al., 1997; Erzurumlu and Gaspar, 2012). Genes like NMDA receptor subunits, adenylyl cyclase 1 (AC1), mGluR5, phospholipase C-β1, cAMP-dependent protein kinase type II regulatory subunit, monoamine oxidase A or

sodium-dependent 5-HT transporter, are essential for presynaptic and postsynaptic mechanisms involved in barrel map refinement, as evidenced by mutant models exhibiting aberrant barrel patterns (Li et al., 1994, 2013; Cases et al., 1996; Iwasato et al., 1997, 2008; Abdel-Majid et al., 1998; Iwasato, 2000; Salichon et al., 2001; Hannan et al., 2001; Persico et al., 2001; Lu et al., 2003, 2006; Rudhard et al., 2003; Gheorghita et al., 2006; Inan, 2006; Watson, 2006; Wijetunge et al., 2008; She et al., 2009; Suzuki et al., 2015; Martini et al., 2018).

These findings highlight the intricate role of activity-dependent processes in shaping the somatosensory system and emphasize the need for further research to unravel the interactions between peripheral inputs and centrally generated spontaneous activity patterns within somatosensory structures during development.

7. Early plasticity in developing sensory systems

The plasticity of thalamocortical circuits in early development plays a crucial role in enabling the brain to adapt and fine-tune sensory information processing. This process can be divided into two main types: cross-modal plasticity, which involves interactions and adaptations between multiple sensory modalities, and intra-modal plasticity, which focuses on changes occurring within a single sensory modality. Both types of plasticity rely on a complex interplay of activity-dependent mechanisms, molecular pathways and the dynamics of critical developmental periods, emphasizing the sophisticated flexibility of the thalamocortical system throughout development.

7.1. Cross-modal plasticity

Blind individuals exhibit enhanced abilities in auditory, olfactory, and tactile discrimination, which arise from compensatory neuroplasticity following sensory deprivation (Röder et al., 1999; Renier et al., 2013; Goldreich & Kanics, 2006). Similarly, deaf individuals demonstrate superior visual discrimination skills, supported by studies showing increased activity in visual regions and structural reorganization in auditory areas (Bavelier & Neville, 2002; Bavelier & Hirshorn, 2010; Lomber et al., 2010; Alencar et al., 2019; Zimmermann et al., 2024).

Additionally, congenitally deaf individuals display heightened tactile discrimination, likely reflecting somatosensory system rewiring, further emphasizing the brain's capacity for cross-modal plasticity (Auer et al., 2007; Cardon & Sharma, 2018). These observations underscore the brain's extraordinary ability to redistribute sensory processing resources across modalities in response to sensory loss.

Contrary to the traditional view that cross-modal plasticity depends solely on sensory experience, evidence from animal models with perinatal sensory deprivation reveal that it can occur even before the onset of sensory input. Such early deprivation significantly impacts the maturation of thalamocortical networks, laying the foundation for subsequent experience-driven adaptations (Kozanian et al., 2015; Mezzera & López-Bendito, 2016; Moreno-Juan et al., 2017). Understanding these mechanisms is essential for developing strategies to leverage the brain's adaptive potential to support individuals with sensory impairments.

In animal models of blindness (enucleated animals), significant neural reorganization has been observed. For example, in visually deprived rodents and kittens, the presumptive visual cortex becomes activated by auditory and somatosensory stimuli (Rauschecker & Korte, 1993; Yaka et al., 1999; Chabot et al., 2007; López-Bendito et al., 2022). This plasticity enhances tactile sensitivity, with expanded and improved sensory representations in regions like the whisker-related barrel cortex (Toldi et al., 1994; Fetter-Pruneda et al., 2013; Abbott et al., 2015). Similarly, naturally blind mole rats exhibit auditory activation in both the visual thalamus and cortex due to rewired auditory projections, reflecting extensive neural remodeling (Bronchti et al., 2002; Chabot et al., 2007). In these animals, the dLG receives atypical innervation from the IC, which also connects to the visual cortex (Chabot et al., 2008). Notably, in opossums enucleated at birth, the auditory thalamic nucleus establishes abnormal projections to V1 (Karlen et al., 2006). Enucleation in mice at birth, leads to altered ephrinA5 expression associated with changes in cortical arealization, suggesting a role for ephrinA5 in compensatory adaptations at somatosensory-visual boundaries in the absence of visual input (Dye et al., 2012). Embryonic enucleation has been shown to induce an enlargement of barrel size, an elevated frequency of thalamic calcium waves and altered *Rorβ*

expression in the VPM. These changes contribute to an increase in the structural complexity of TCA terminals (Moreno-Juan et al., 2017). These thalamic calcium waves are thought to mediate cross-modal plasticity processes by regulating gene expression patterns that shape primary cortical areas size before sensory experience. This mechanism enables communication between different sensory modalities, facilitating sensory maps reorganization. Additionally, unexplored pathways may mediate the transfer of somatosensory information into visual circuits. For example, in sighted animals, connections exist between the HO somatosensory thalamic nucleus POm and V1, as well as between POm and HO visuo-tactile regions (Charbonneau et al., 2012; Olcese et al., 2013). These data suggest that early visual deprivation can induce substantial reorganization of subcortical pathways, enabling the rerouting of somatosensory inputs.

In models of auditory deprivation, cross-modal plasticity involves the repurposing of the auditory cortex for visual processing. For instance, in neonatal deaf ferrets, experimentally rerouting retinal axons to the MG enables visual input to be processed within the auditory cortex. This adaptation allows A1 to develop visual cortical functions, including orientation and motion detection (Sur et al., 1990; Sur & Leamey, 2001). Transgenic mouse models with altered thalamic sensory input have also provided insights into these mechanisms. In particular, following IC ablation, mice lacking ephrin-A2/A5 receptors exhibit significantly more pronounced abnormal retinal innervation of the MG compared to wild-type controls (Lyckman et al., 2001). This suggests that ephrin-A gradients are involved in guiding and shaping these rewired visual projections.

Together, these studies illustrate the brain's extraordinary ability to adapt to sensory loss, with regions deprived of their primary sensory input being repurposed to process alternative sensory modalities. This remarkable plasticity not only deepens our understanding of neural reorganization but also opens promising avenues for developing targeted interventions to support sensory rehabilitation.

7.2. Intra-modal plasticity

Intra-modal plasticity is crucial for the development and refinement of cortical sensory maps, allowing for precise encoding of sensory stimuli. This form of plasticity is deeply rooted in activity-dependent synaptic modifications, with sensory input serving as a critical driver in shaping these maps. A prominent example is found in the somatosensory system, specifically in the barrel cortex, where whisker input during early postnatal stages organizes TCAs into well-defined cortical barrels. Woolsey and Van der Loos (1970) were the first to describe the barrel cortex as a somatotopic representation of whiskers, providing a foundational model to explore sensory-driven plasticity. Later research by Belford and Killackey (1979) and Killackey and Dawson (1989) revealed that sensory deprivation during early developmental stages, such as the removal of whiskers or forelimbs, leads to significant remodeling of somatosensory maps and alterations in thalamocortical connectivity.

Further studies by Killackey et al. (1976) and Woolsey et al. (1979) highlighted the role of thalamic inputs in cortical map development, showing how competition among inputs refines synaptic connections to form precise sensory representations through activity-dependent mechanisms. In recent work, Renier et al. (2017) explored the role of sensory input in shaping the organization and refinement of cortical barrel maps. In mutant mice with misrouted trigemino-thalamic inputs, alterations in sensory input resulted in prominent changes to whisker map representation within the barrel cortex. Notably, these mutant mice develop bilateral whisker maps instead of the typical unilateral representation and their findings emphasize the critical role of sensory inputs in organizing cortical representations, a core principle of intra-modal plasticity.

The critical period represents a developmental window in which sensory input has a profound impact on neural circuit organization. For instance, damage to whiskers during early postnatal stages disrupts the formation of cortical barrels, while similar manipulations at later stages produce negligible changes, highlighting the time-sensitive nature of this period (Woolsey & Wann, 1976). This plasticity window aligns with the ongoing development of thalamocortical connections in the somatosensory system (Erzurumlu & Gaspar, 2012).

Comparable findings in the visual system, as shown in Hubel and Wiesel's classical studies (1963), demonstrated that monocular deprivation during the critical period causes lasting deficits in ocular dominance column formation and visual acuity. These reports illustrate how monocular deprivation influences neural competition and cortical representations (Hensch, 2005; Craddock et al., 2023; Takahata, 2024; Chen et al., 2024). Cabelli and colleagues (Cabelli et al., 1997) further showed that during the ocular dominance plasticity period, thalamocortical projections undergo significant processes of refinement driven by sensory input and modulated by BDNF signaling.

Neurotrophic factors, including nerve growth factor (NGF) and BDNF are essential to intra-modal plasticity, as they regulate synaptic strength, promote axonal growth and facilitate circuit refinement (Xu et al., 2000; Park & Poo, 2013). Synaptic plasticity mechanisms such as long-term potentiation (LTP) and long-term depression (LTD) also play a role in refining thalamocortical circuits by weakening or enhancing synapses in response to activity patterns mediated by molecular components like AMPA and NMDA receptors (Allen et al., 2003; Feldman & Brecht, 2005; Bender et al., 2006; Petersen, 2007). The onset of critical periods for plasticity relies on consistent and reliable input to sensory circuits, which requires a precise balance between inhibitory and excitatory networks. Notably, GABAergic signaling is particularly important for setting this balance, ensuring that plasticity can occur efficiently (Foeller & Feldman, 2004; Hooks & Chen, 2007). These findings highlight the intricate interaction between activity-dependent processes and neurotrophic factors in refining sensory maps, ensuring their alignment with environmental inputs. This dynamic interplay forms the basis for precise sensory processing that persists throughout life.

In this thesis, we aim to build upon the foundational knowledge of intra-modal plasticity by focusing on an unexplored embryonic critical window during which the size and spatial resolution of somatosensory maps can be precisely regulated. Our work investigates a novel mechanism involving thalamic calcium waves and associated transcriptional programs that drive these developmental processes. This study provides new insights into the early molecular and cellular events shaping thalamocortical circuits.

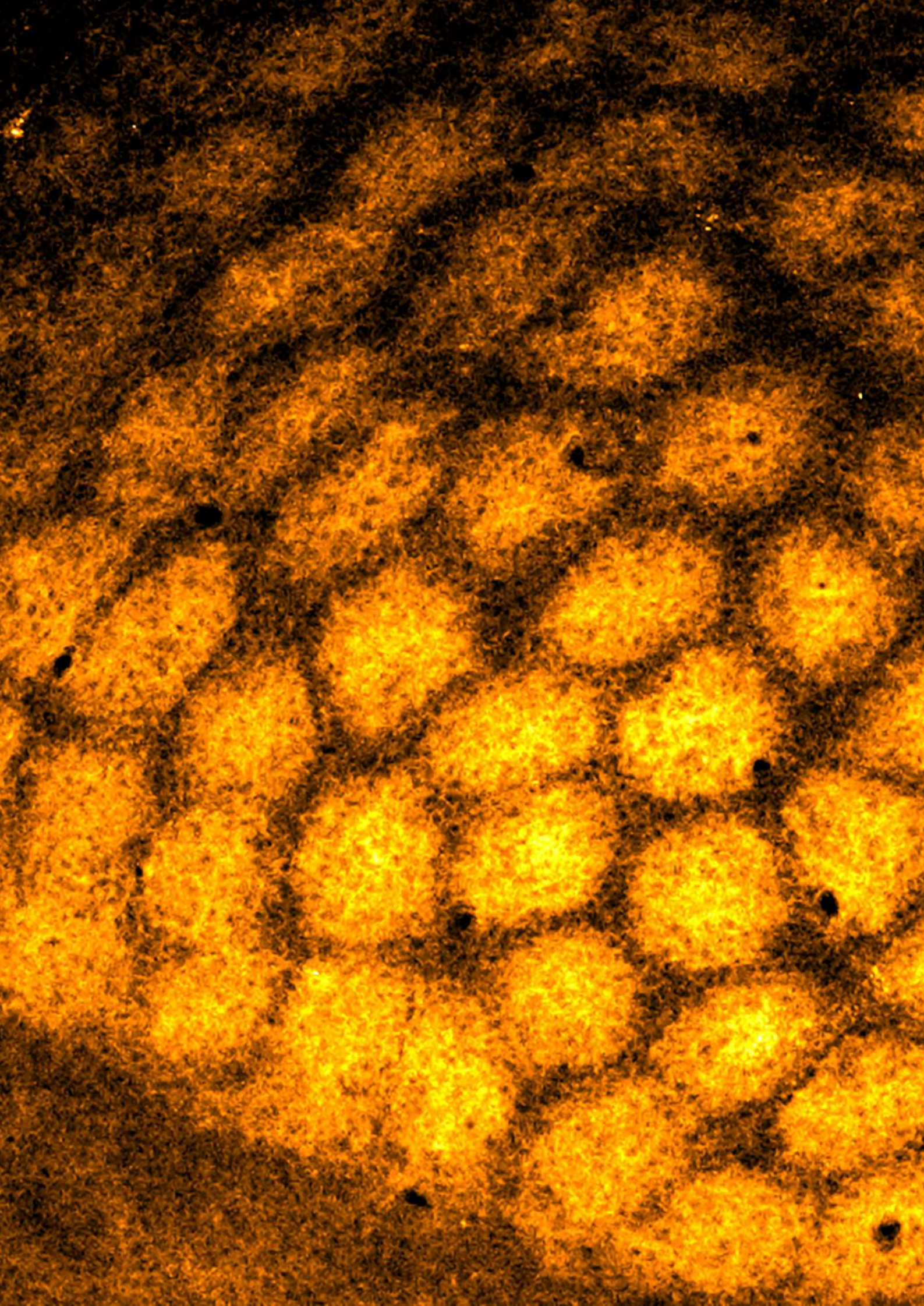

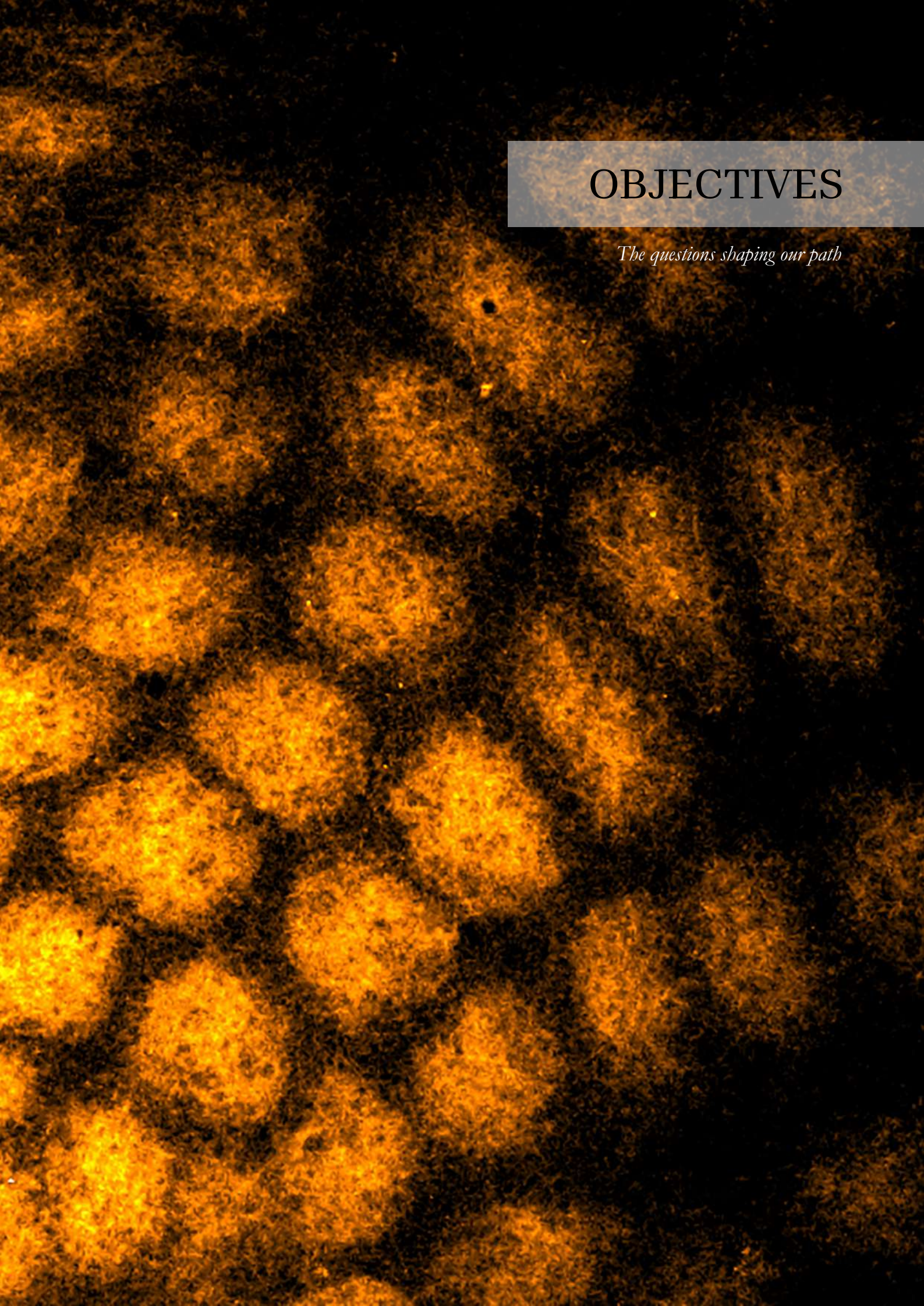

OBJECTIVES

The questions shaping our path

OBJECTIVES

This thesis seeks to uncover the mechanisms underlying the formation of somatosensory maps and the acquisition of spatial resolution. To achieve this overarching goal, the following specific objectives are outlined:

- To understand the principles that govern the establishment of somatosensory territories.
- To investigate the timing of intra-modal plasticity within the somatosensory territories that occurs following sensory deprivation.
- To unravel whether experience-independent functional reorganization can be induced between somatosensory territories.
- To elucidate the interplay between patterns of spontaneous activity and transcriptional programs in the prenatal thalamus in shaping the resolution of somatosensory maps.

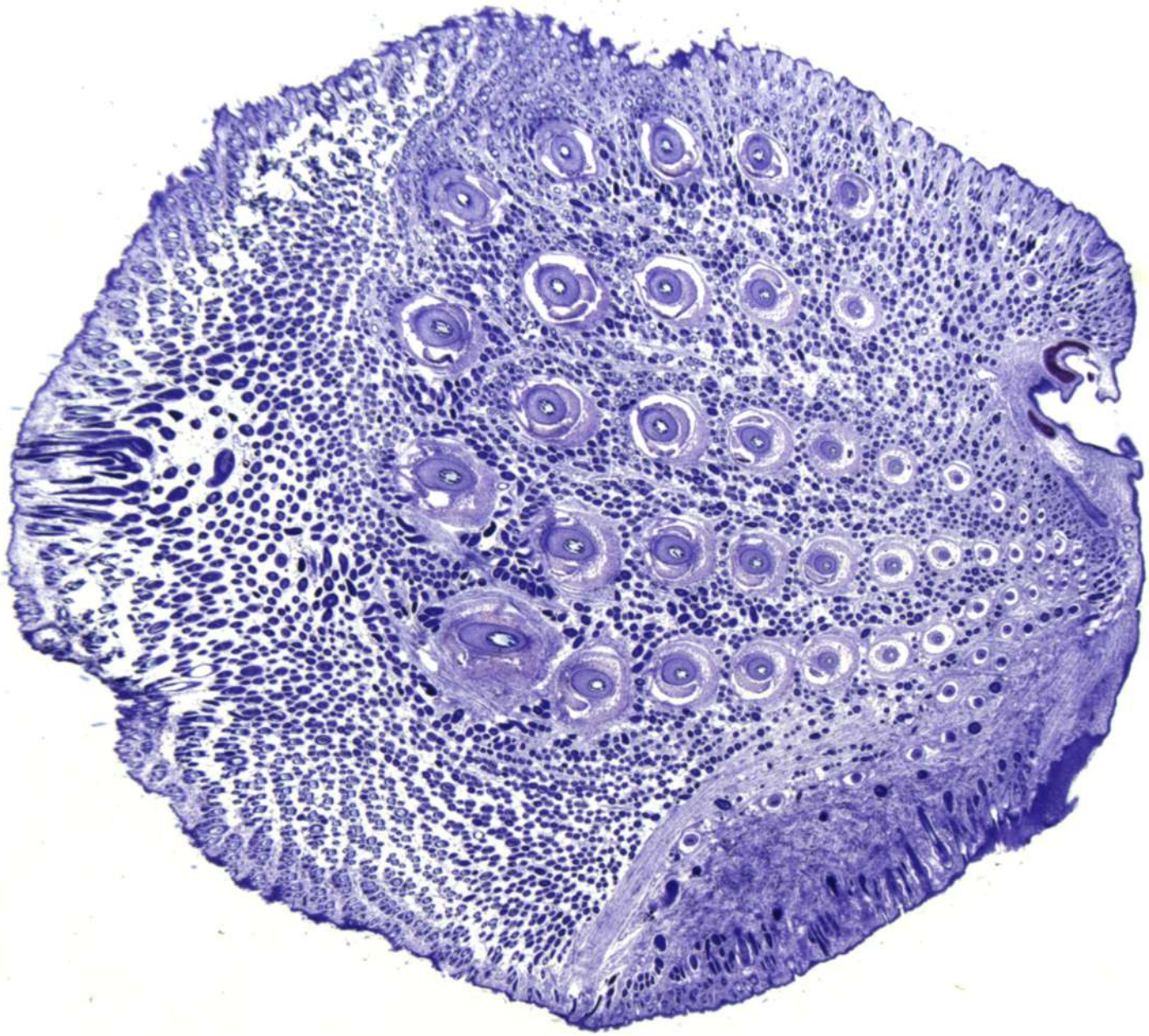

MATERIALS & METHODS

Our recipe for discovery

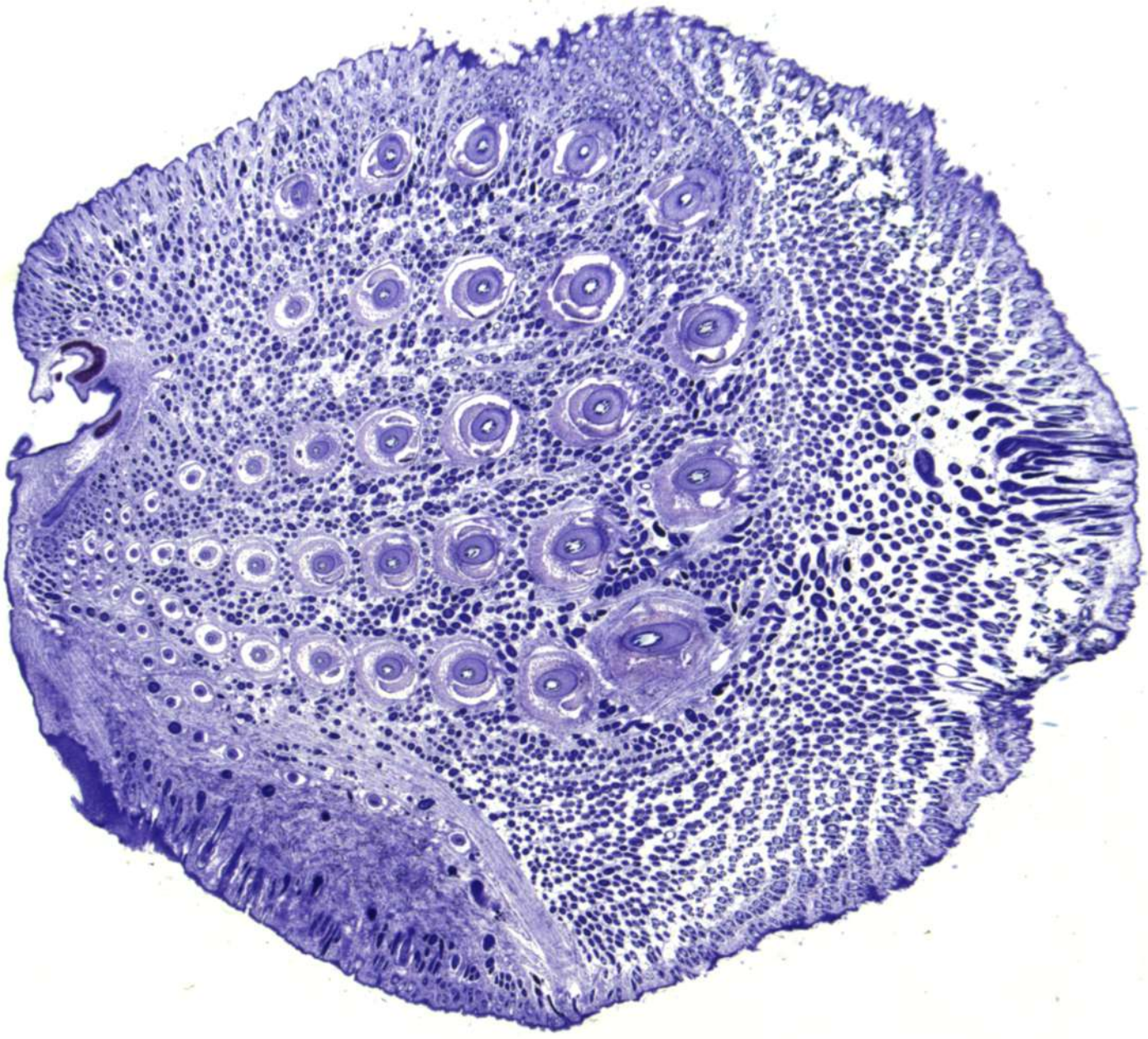

MATERIALS AND METHODS

Mouse strains

All animal experiments were conducted in accordance with the Committee on Animal Research at the University Miguel Hernández that approved all the animal procedures, which were carried out in compliance with Spanish and European Union regulations. Similar numbers of male and female mice were used interchangeably. No sex-related differences were observed in the measurements throughout the study. Mice were maintained in pathogen-free facilities under standard housing conditions with continuous access to food and water on a 12h light-dark cycle. The number of animals used in each experiment is noted in the figure legends.

All mouse transgenic lines in this study were maintained on an ICR/CD-1 genetic background and genotyped by PCR. The *TCA-GFP Tg*, in which the TCAs are labelled with GFP, the $R26^{Kir2.1\text{-}mCherry}$, mouse lines were previously described (Moreno-Juan et al., 2017; Mizuno et al., 2014; Antón-Bolaños et al., 2019). The Cre-dependent mouse line, $R26^{GCaMP6f}$ was obtained from Jackson Laboratories (Stock number 024105) and crossed with an $Emx1^{Cre/+}$ transgenic mouse (Gorski et al., 2002) to conditionally express the fast calcium indicator GCaMP6f in glutamatergic cortical neurons ($Emx1^{GCaMP6f}$) (Antón-Bolaños et al., 2019; Guillamón-Vivancos et al., 2022). The $R26^{Kir2.1\text{-}mCherry}$ mice were crossed with an inducible Cre^{ERT2} mouse line driven by *Gbx2*, an early specific thalamic promoter ($Gbx2^{CreERT2/+}$) (Chen et al., 2009). Double mutants are referred as Th^{Kir} and triple mutants as $TCA\text{-}GFP\text{-}Th^{Kir}$ (Antón-Bolaños et al., 2019). Tamoxifen induction of Cre recombinase in the double/triple mutant embryos was performed by gavage administration of tamoxifen (5 mg dissolved in corn oil, Sigma) at E10 to specifically target all primary sensory thalamic nuclei. Tamoxifen administration in pregnant mice produces non-desirable side effects such as delivery problems and decrease survival of newborn pups (Franco et al., 2012). To increase the survival rate of young pups, we administered 125 mg/Kg of progesterone (DEPO-PROGEVERA®) intraperitoneally at E14 and implemented C-section procedure at E19.

Pups were then placed with a foster mother. In all cases, the Cre^{ERT2}-negative littermates were used as controls of the experimental condition. The *r2*^{mCherry} (Bechara et al., 2015), *Krox20*^{Cre} (Voiculescu et al., 2000) and *R26RZsGreen* (Jackson Laboratories, Stock number 007906) (Madisen et al., 2015) lines, were as described. We crossed *Krox20*^{Cre} with *R26RZsGreen* to generate double transgenic *Krox20*^{ZsGreen} mice and we also generated *Krox20*^{ZsGreen}*::r2*^{mCherry} triple transgenic mice.

Histology

For *in situ* hybridization and immunohistochemistry at postnatal stages, mice were perfused with 4% paraformaldehyde (PFA) in PBS (0.01 M), and their brains were subsequently removed and post-fixed in the same fixative overnight. For immunohistochemistry of embryonic tissue, the brains were dissected out and immediately fixed in 4% PFA overnight. For Nissl staining, a microtome (MICROM) was used to cut paraffin slices of 5 μm. Next, the sections were stained in 0.5% cresyl violet (Sigma) solution for 15-25 min and then rinsed quickly in distilled water. After decolorization in 70% ethyl alcohol for few seconds, the sections were dehydrated in 95%, 100% ethyl alcohol for 2 to 3 min, cleared in xylen (Sigma) for 2 min and mounted with Eukitt (Merk). Cytochrome oxidase staining was performed to label the PrV territories. For cytochrome Oxidase (CytOx) staining, 80 μm vibratome coronal sections were incubated overnight at 37 ºC in a CytOx solution: 0.03% cytochrome c (Sigma C2506), 0.05% 3-3' diaminobenzidine tetrahydrochloride hydrate (DAB, Sigma D5637) and 4% sucrose in PBS. For tangential sections, cortical hemispheres were flattened and cryoprotected through steps of 10%, 20% and 30% of sucrose in PBS. Then, a cryotome (MICROM) was used to cut at 80 μm tangential sections. Immunohistochemistry was performed on 80 μm vibratome or cryotome brain sections (coronal and tangential), which were first incubated for 1h at room temperature in a blocking solution containing 1% BSA (Sigma) and 0.25% Triton X-100 (Sigma) in PBS. Afterwards, the slices were incubated overnight at 4 °C with the following primary antibodies: guinea pig anti-vGlut2 (1:10000, Synaptic Systems, 135404), chicken anti-GFP (1:3000; Aves Labs, GFP-1020), rat anti-RFP

(1:1000, Chromotek, 5F8), rabbit anti-cFos (1:500, Synaptic Systems, 226003), rabbit anti-PV (1:5000, Swant PV27), and rabbit anti-RFP (1:1000, Rockland, 600-401-379). Sections were then rinsed in PBS and incubated for 2h at room temperature with secondary antibodies: Alexa488 donkey anti-guinea pig (1:500, ThermoFisher, A11073), Alexa488 goat anti-chicken (1:500, ThermoFisher, A11039), Alexa594 donkey anti-rat (1:500, ThermoFisher, A21209) and Alexa goat 568 anti-rabbit (1:500, Invitrogen, A11011). Counterstaining was performed using the fluorescent nuclear dye 4',6-diamidino-2-phenylindole (DAPI) (Sigma). *In situ* hybridization was performed on 60 μm vibratome sections using digoxigenin-labelled antisense probe for *Rorα*, *Epha4*, *Pou2f2*, *Hs6st2*, *Plxna2* and *Cdh9*. Hybridization was carried out overnight at 65 ºC, and after hybridization, the sections were washed and incubated overnight at 4 ºC with an alkaline phosphatase-conjugated anti-digoxigenin antibody (1:2500-1:4000, Roche). To visualize the RNA-probe binding, colorimetric reaction was performed for 1-2 days at room temperature in a solution containing NBT (nitro-blue tetrazolium chloride, Roche) and BCIP (5-bromo-4-chloro-30-indoly phosphate p-toluidine salt, Roche). After development, the sections were washed and mounted in Glycerol Jelly (Merck Millipore). Images were acquired with a Leica DFC550 camera into a Leica DM5000B microscope, Leica K5 camera into Leica DMi8 microscope or with an Axioscan Z1 widefield microscope (Zeiss).

Immunolabeling-enabled three-dimensional imaging of solvent-cleared organ (iDISCO+)

Whole mount for the iDISCO+ protocol was conducted following the previously described methods (Renier et al., 2014, 2016). After perfusing mice with 4% PFA, heads (without any dissection) were dehydrated using a series of methanol concentrations (50, 80, 100, and 100%) and subsequently incubated overnight in 6% H_2O_2 in methanol to bleach the samples. Following this, heads were incubated in Permeabilization solution (TritonX-100, Glycine, DMSO) and blocked with Blocking solution (TritonX-100, Donkey Serum, DMSO) for 2 days, respectively. For the clearing process, heads underwent dehydration in methanol (20,

40, 60, and 80%) at room temperature on a rotating shaker. Specimens were then immersed twice in 100% methanol for 1 hour and treated overnight in 1/3 volumes of 100% dichloromethane (DCM; Sigma-Aldrich; 270997). The subsequent day, heads were incubated in 100% DCM for 30 minutes. Finally, samples were cleared in 100% dibenzyl ether (DBE; Sigma-Aldrich; 108014) until they became translucent.

Ultramicroscopy and Image Processing

3D imaging was primarily performed with an ultramicroscope I (LaVision BioTec) using ImspectorPro software (LaVision BioTec). The light sheet was generated by a laser (wavelength 488 nm, LaVision BioTec). A binocular stereomicroscope (MXV10, Olympus) with a 23x objective (MVPLAPO, Olympus) was used at different magnifications (1.25x). Samples were placed in an imaging reservoir made of 100% quartz (LaVision BioTec) filled with ethyl cinnamate and illuminated from the side by the laser light.

Images were generated using Imaris x64 software (version 9.3.1, Bitplane). Stack images were first converted to Imaris files (.ims) using ImarisFileConverter. The whisker pad and upper lip areas reconstruction were generated by creating a mask around each one using the "surface tool" and they were pseudo-coloured (whisker pad area in magenta and upper lip area in cyan). Each individual follicle was isolated also manually using the same tool, selecting nine follicles arbitrarily at three different points from medial to lateral. The septa volume reconstruction from coronal sections of 80 μm was generated by creating masks around each barrel using the "surface tool" and they were pseudo-coloured (orange).

***In utero* and postnatal whisker pad cauterization**

Embryonic unilateral and bilateral whisker pad cauterization (embWPC and bi-embWPC, respectively) were performed at E14 as described previously for enucleation (Moreno-Juan et al., 2017. Dams were deeply anesthetized with isoflurane, and the uterine horns were exposed through a midline laparotomy. Using a fiber optic light source, embryos were

visualized within the uterus. The whisker pads of selected embryos were then cauterized with a 0.1mm platinum wire (ThermoFisher) connected to a cautery unit. All follicles within the whisker pad were carefully cauterized. After cauterizing half of the litter, the embryos were returned to the abdominal cavity, the surgical incision was closed, and the embryos were allowed to develop until either E18 or postnatal stages. Postnatal unilateral whisker pad cauterization (P0WPC) was performed on P0 pups. Animals were deeply anaesthetized on ice. The right whisker pad was cauterized under the loupe to specifically burn the principal whiskers follicles. Pups were then warmed up to 37°C on a heating pad, before being returned to the mother.

Measurement of brain areas and data analysis

ImageJ software was used to measure the size of individual barrels, barrel field territories in the cortex, thalamus and brainstem, as well as the snout areas in slices. For barrel field territories and snout areas data were normalized. Each barrel field or snout area from a given experimental condition was normalized to the corresponding barrel field or snout mean area in the control, which was considered as 1. For the snout measurements, the skin of the snout was flattened and post-fixed in 4% PFA. Paraffin slices of 5 μm were obtained to quantify the number of follicles and the upper lip snout area using Nissl staining. We measure two slices per animal, one medial and one more lateral, and calculated the average. To quantify the number of cells in the vPrV, dPrV, PrV, wpVPM, ulVPM and VPM regions, we counted DAPI-stained nuclei within a 55.35 μm^2 region of interest (ROI) in 80 μm coronal sections. This cell count was extrapolated to estimate the total number of cells in each target area. Four slices per animal were analyzed, and the cell count across these slices were summed. TCA-GFP mouse was used for the quantifications of the barrel field definition in flattened tangential sections, barrel field areas in toto and thalamic territories in slices. To assess the rostro-caudal gradient of increased barrel size in embWPC mice, we analyzed three distinct levels along the caudal-to-rostral axis, measuring 4 barrels per level and calculating the average. The most caudal level was positioned near the remaining PMBSF territory, the most

rostral near the S1 rostral boundary, and the medial level at the midpoint between these two. For thalamic rescaling analysis, we examined brain slices at P3, when barreloids become more prominent, facilitating anatomical analysis. For cortical barrels analysis, we chose P8, as barrels are well-established at this stage, allowing for clearer visualization and analysis. To quantify the size of cortical areas *in toto*, TCA-GFP (control, embWPC, P0WPC and embWPC-Th^{Kit}) mice were perfused and directly processed to obtain images under the stereo fluorescent microscope (Leica MZ10 F). Coronal serial slices of 80 μm were obtained from TCA-GFP brains, and thalamic barrel field territories were immunolabel with GFP and vGlut2 in order to better detect the areas. For $\Delta F_b/F_s$ quantifications, we used ImageJ to measure the gray value of EGFP labelling in barrels of flattened tangential sections. $\Delta F_b/F_s$ was calculated using the maximum value of the baseline signal average as F_s in single barrels. To measure the gray value, we used a 20-width segmented line, covering 5 barrels per condition, and calculated the average. To compare the barrel profile for the different conditions, we normalized each barrel´s gray values to the lowest number (septa), which was considered as 0. Next, we took 11 gray value data points per barrel to normalize the length for all the conditions. To quantify the mean gray value in septa, coronal serial slices of 80 μm were obtained from TCA-GFP brains, and barrels from PMBSF and ALBSF (control and embWPC) were immunolabel with GFP to measure the fluorescence of three barrels septa per condition using Imaris x64 software, and calculated the average. For PV+ cells quantifications in PMBSF and ALBSF barrels and septa, we counted the number of PV+ cells within four barrels and their septa for each condition in flattened tangential sections of 80 μm immunolabel with PV and vGlut2. We quantified cFos expression within PMBSF and ALBSF layer IV in flattened tangential sections of 80 μm immunolabel with cFos. The region of interest (ROI) was a square of 600x1000 μm on each territory measuring the mean gray value.

Dye-tracing studies

For axonal tracing, animals were perfused with 4% PFA in PBS. Heads were post-fixed overnight to trace innervation from the snout to the trigeminal nucleus, while brains were dissected and post-fixed overnight to trace thalamocortical axons. Small DiI (1,1'-dioctadecyl 3,3,3',3'-tetramethylindocarbocyanine perchlorate; Invitrogen), DiA (4-[4-(dihexadecylamino) styryl]-N-methylpyridinium iodide; Invitrogen) and DiD (1,1'-Dioctadecyl-3,3,3',3'-Tetramethylindodicarbocyanine, 4-Chlorobenzenesulfonate Salt; Invitrogen) crystals were inserted under a stereo fluorescence microscope (MZ10 F, Leica) into the PMBSF, ALBSF, vPrV, dPrV, the whisker pad and upper lip. The dye was allowed to diffuse at 37 °C in PFA solution for 4 to 8 weeks to trace the innervation from the snout to the PrV, and 6 weeks to trace from the vPrV and dPrV to the VPM. To trace the thalamocortical pathway, small DiI and DiA crystals were inserted into distinct PMBSF barrels (C2, C3, D3 and C4) and DiI, DiA and DiD crystals were placed into ALBSF territory. To reveal the PBMSF and ALBSF, a TCA-GFP transgenic specific mouse line was used. The dye was allowed to diffuse at 37 °C in PFA solution for 3 weeks. Vibratome sections (80 μm thick) were obtained and counterstained with the fluorescent nuclear dye DAPI (Sigma-Aldrich). Three sections per animal were imaged using a Leica K5 camera into Leica DMi8 microscope. Image analysis was performed on ImageJ. To quantify the translocation of the backlabeling in the VPM, the distance from the dorsolateral geniculate (dLG) nucleus border was measured to the center of the backlabeled cells in the VPM. The distance from the dLG nucleus border to the separation between wpVPM and ulVPM was determined following the barreloids rows in the VPM of ctrl mice.

Measurement of PrV axons overlap in VPM and data analysis

To label rhombomere 3-derived vPrV neurons, we used the *Krox20*^{Cre} line (Voiculescu et al., 2000) to drive the Rosa-Zsgreen reporter (*R26RZsGreen*) (Madisen et al., 2010), whereas to label rhombomere 2-derived dPrV neurons, we used the *r2*^{mCherry} reporter line (Bechara et al.,

2015). Brains from *Krox20*^{Cre}; *R26RZsGreen*; *r2*^{mCherry} animals, in which vPrV and dPrV projections are labeled simultaneously, were collected at embryonic stages (E16.5, E18.5) and postnatal stages (P0, P4, P8) for analysis. Embryonic brains were directly post-fixed in 4% PFA in PBS, while postnatal brains were perfused before post-fixation in the same fixative. Brains were cut on a Vibratome (Leica) at 60 μm thickness throughout the VPM and PrV. To enhance the r2::mCherry signal, the sections were stained with a rabbit anti-RFP primary antibody (1:1000, Rockland, 600-401-379) coupled to an anti-rabbit Alexa 568 secondary antibody (1:500, Invitrogen, A11011), while the endogenous Zsgreen fluorescence was not amplified. At least five sections per animal were imaged using Axioscan Z1 widefield microscope (Zeiss), using a 10x (NA=0.45) plan-APOCHROMAT objective. Subsequent image analysis was conducted using ImageJ. To quantify the percentage of overlap of vPrV-dPrV axons in the VPM, wand tool connecting pixels of the same intensity level in a 15-pixel range, was used to automatically delineate the innervation area of Krox20+ and R2+ axons, generating the Regions of Interest (ROIs). Subsequently, the overlapping area and the total innervation area of both Krox20+ and R2+ axons were measured with the measure tool in ImageJ to calculate the percentage of overlap of PrV axons in the VPM.

In vivo **mesoscale calcium imaging**

As previously described (Guillamón-Vivancos et al., 2022), embryos at E18 were extracted from the uterus and maintained at 35 ºC. E18 pups were immobilized using soft clay. P4 mice underwent anesthesia with ice, followed by surgical removal of the scalp. A 3D-printed plastic holder was attached to the skull using cyanoacrylate adhesive and dental cement, then affixed to a ball-joint holder to stabilize the head. To maintain body temperature, pups were placed on a controlled temperature heating pad, ensuring a range of 32-34 ºC. For recording calcium activity, we used a 16-bit CMOS camera (ORCA-Flash 4.0, Hamamatsu) coupled to a stereo microscope (Stereo Discovery V8, Zeiss), which offered 470 nm LED illumination. For *Emx1*^{GCaMP6f}, images were acquired with a frame size of 1024x1024 pixels using a macro magnification of 1.6x at E18 and of 1.25x at P4, resulting in spatial resolution of 8.12

μm/pixel and 10.64 μm/pixel, respectively. Image frames were captured continuously at a rate of 3.33 frames per second (300 ms frame period) for *Emx1*^{GCaMP6f} with an average of 3 movies was acquired per animal.

In vivo mechanical stimulation of the whisker pad

We conducted somatosensory stimulations by touching the whisker pad and upper lip using a 0.16 g von Frey filament (TouchTest®, BIOSEB). Each animal was stimulated at least three times, with intervals of 5 minutes between each stimulus. Subsequently, we calculated the size of responses in the PMBSF and ALBSF elicited by whisker pad and upper lip stimulations.

Analysis of the evoked activity *in vivo*

For the assignment of cortical territories, the perimeters of the PMBSF and ALBSF were determined using the cortical responses elicited by mechanical stimulation of five sites on the whisker pad, as previously described (Antón-Bolaños et al., 2019; Guillamón-Vivancos et al., 2022) and two or three sites of the upper lip. At embryonic day (E)18, the perimeters were predicted by scaling down and superimposing the limits of the sensory territories observed in the TCA-GFP transgenic line (Mizuno et al., 2014) at P2, as previously detailed (Guillamón-Vivancos et al., 2022), and using the responses to whisker pad and upper lip stimulations as reference for PMBSF and ALBSF, respectively. Image analysis was performed with ImageJ. The mean fluorescence of five frames just prior to the stimulation established F0 (baseline fluorescence), and a ΔF/F0 time series was then generated from the raw data and subsequently transformed into 8-bit images before processing with a 2-pixel diameter Gaussian filter. A maximum intensity projection of all frames containing evoked responses was obtained. The boundaries of the response were defined using the wand tool, connecting pixels of the same intensity level within a 15-pixel range, and the area of each response was calculated using the measure tool in ImageJ. To measure the active fraction of PMBSF and ALBSF in embWPC mice at E18 and P4, the control side was used to delineate the PMBSF

and ALBSF territories following stimulation of the whisker pad or upper lip, respectively. On the WPC side, these areas were superimposed using the mirror image from the control side. The PMBSF and ALBSF active fractions were determined by measuring all elicited responses within each territory and calculating the percentage of the PMBSF and ALBSF theoretical areas occupied by these responses following whisker pad or upper lip stimulations. To quantify the percentage of overlap between responses following whisker pad and upper lip stimulations (% PMBSF-ALBSF overlap) at E18 and P4, the overlap between all elicited responses following whisker pad and those following upper lip stimulations was calculated. To quantify the percentage of overlap within PMBSF or ALBSF (% Responses overlap) in ctrl and embWPC, the overlap for two different stimuli on the whisker pad or two different stimuli on the upper lip was calculated.

To visualize the evoked stimuli in different colour profiles for the generation of supplementary movies, we utilized custom scripts developed in Matlab™. These scripts were adapted from the image analysis suite WholeBrainDX (referenced in the Data and code availability section). For each movie, frames containing movement artifacts, spontaneous activity, and calcium activity deemed as stimulation byproducts were excluded. Baseline correction was performed using the built-in Matlab function 'msbackadj' with a window size of 20 and a step size of 20. Subsequently, ΔF/F0 was computed using the median value of the corrected signal as F0. Movie segmentation and calcium event detection followed the method described (James et al., 2014). Image segmentation and generation of a binary movie involved Gaussian smoothing with an 80 μm distance and a signal intensity threshold. The binary movie was color-labeled using ImageJ software and customized with a Gaussian filter. Subsequently, the original movie and the color-coded binary movie were merged using the 'Image Calculator' function in ImageJ.

Microdissection and RNA isolation for RNA-seq

To capture gene expression changes during the critical period of somatosensory map plasticity, we collected tissue from the wpVPM and ulVPM territories of P0 ctrl and embWPC

pups. Pups were euthanized by decapitation, and their brains were dissected out under RNase-free conditions to prevent RNA degradation. The brains (five brains were pooled for each sample) were collected in ice-cold KREBS solution and sliced into 300 μm sections using a vibratome (VT1000S Leica). The wpVPM and ulVPM territories were rapidly microdissected under a stereo microscope. The bulk tissue was immediately transferred to lysis buffer of the Rneasy® Micro Kit (Qiagen, 74004) for total RNA extraction, following the manufacturer's instructions. RNA quality was measured for all samples using an Agilent Bioanalyzer 2100 system, and only samples with RNA Integrity Number (RIN) > 8 were used for library construction.

Library preparation and RNA sequencing

Library construction and sequencing were performed at Novogene Co. Ltd. Genomics core facility (Cambridge, UK). cDNA multiplex libraries were prepared using a custom Novogene NGS RNA Library Prep Set (PT042) kit. Briefly, mRNA was purified from total RNA using poly-T oligo-attached magnetic beads. After fragmentation, the first strand cDNA was synthesized using random hexamer primers followed by the second strand cDNA synthesis. The library was ready after end repair, A-tailing, adapter ligation, size selection, amplification, and purification.

The library was checked with Qubit and real-time PCR for quantification and bioanalyzer for size distribution detection. Libraries were pooled and sequenced in 2x150bp paired-end mode on a S4 flowcell in the Illumina Novaseq6000 platform. A minimum of 40 million reads were generated from each library.

Bioinformatic analysis of the RNA-seq

RNA-seq analysis were performed as previously described (Herrero-Navarro et al., 2021) with minor modifications: quality control of the raw data was performed with FastQC (v.0.11.9). RNA-seq reads were mapped to the Mouse genome (GRCm39) using STAR (v2.7.9a) (Dobin

et al., 2013) and SAM/BAM files were further processed using SAMtools (v1.15). Aligned reads were counted and assigned to genes using Ensembl release 104 gene annotation and FeatureCounts, Subread (v2.0.1). Normalization of read counts and differential expression analyses were performed using DESeq2 (v1.32) (Love et al., 2014), Bioconductor (v3.15) (Huber et al., 2015) in the R statistical computing and graphics platform (v4.2.2 "Innocent and Trusting").

In the analysis of wpVPM and ulVPM datasets (control and embWPC samples) generated for this study, significantly Differentially Expressed Genes (DEGs) were identified using a simultaneous statistical significance threshold (Benjamini-Hochberg (BH) adjusted P-value < 0.1) and absolute log2 fold change (log2FC) > 0.14 by shrunken log2FC using the adaptive T prior Bayesian shrinkage estimator "apeglm" (Zhu et al., 2019). Hierarchical clustering analysis was performed using "Euclidean" distance and "Complete" clustering methods metrics to visualize significantly upregulated and down-regulated genes. A linear support-vector machine (SVM) model for classifying RNA-seq samples was developed using the e1071 package (v1.7-14). This model was based on the gene expression profiles of the top 500 most variable genes in ulVPM and wpVPM control samples. Subsequently, the C-SVM model was utilized to predict the classification of ulVPM embWPC samples based on their transcriptomic profiles.

Functional enrichment analyses were performed using clusterProfiler (v4.4.4) (Gu et al., 2023) under org.Mm.eg.db package (v3.15) for better annotation data. All enriched terms were considered significant at adjusted P-values by 'BH' < 0.1, in the Gene Ontology (GO) Over-Representation Analysis. Enrichment results were further clustered and simplified using the simplifyEnrichment package (version 1.11.1) (Yu et al., 2012).

Ex vivo calcium imaging

At E16, embryos were retrieved from the dam's uterus by cesarean section, their brains were rapidly dissected out and they were submerged in an ice-cold slicing solution containing (in mM): 2.5 KCl, 7 $MgSO_4$, 0.5 $CaCl_2$, 1 NaH_2PO_4, 26 Na_2HCO_3, 11 glucose and 228 sucrose.

Coronal slices (350 μm thick) were obtained using a vibratome (VT1200S Leica) and they were left to recover for at least 30 minutes at room temperature in standard artificial cerebrospinal fluid (ACSF) containing (in mM): 119 NaCl, 5 KCl, 1.3 $MgSO_4$, 2.4 $CaCl_2$, 1 NaH_2PO_4, 26 Na_2HCO_3 and 11 glucose. All extracellular solutions were continuously bubbled with a 95% O_2 and 5% CO_2 gas mixture. Slices were loaded with the calcium indicator Cal520TM (AAT Bioquest) as previously described (Moreno-Juan et al., 2017; Antón-Bolaños et al., 2019), transferred to a submersion-type recording chamber and perfused with warm ACSF (32-34 ºC) at a rate of 1.8 ml/min. Images were acquired with a digital charge-coupled device (CCD) camera (ORCA-R2 C10600-10B, Hamamatsu) coupled to an upright microscope (DM-LFSA, Leica) and using a 5x objective. For recordings of spontaneous calcium activity, frames were acquired with an exposure time of 150 ms, an interframe interval of 300 ms, a frame size of 672x512 pixel and a spatial resolution of 2.5 μm/pixel. With each slice, 1 to 5 epochs of 15 mins (3000 frames) were recorded.

Analysis of fluorescence spontaneous activity

Analysis of spontaneous thalamic calcium activity was conducted using custom software developed in Matlab™, which was adapted from the CalciumDX toolbox (indexed in the Data and code availability section). For each movie, VPM was delineated, and the two prospective areas (wpVPM and ulVPM) were subdivided into a grid of 6x6 pixels where each small square is a region of interest (ROI). Calcium activity events were detected based on the average calcium signal of each ROI over time, employing threshold-based algorithms modified from CalciumDX. To identify significant synchronous activity and discard ROI co-activation that resulting from random temporal coincidence of calcium events, we generated surrogated calcium events sequences for each experiment using Matlab™. The alternative dataset was built by randomly shuffling the original temporal intervals between calcium transients in every ROI while preserving the spiking frequency and temporal structure of the calcium activity. Subsequently, the maximum value of co-activation from shuffled data was calculated. Through 1000 iterations, we established a synchronicity threshold as the 95th

percentile of the maximum values of co-activation obtained from the shuffled dataset. In each experiment, only activity super passing the synchronicity threshold was used for calculations and visualization. The onset of a synchronic event was defined as the frame in which co-activation overpass the threshold, while the end was determined as the frame in which co-activation reached 25% of peak synchronicity.

Behavioural Testing

Twenty-three mice (9 males, 14 females) from four litters were bred for behavioural testing in adulthood (4 months old). Mice were housed in groups of 2-4 per cage. All behavioural testing was conducted during the light phase.

To evaluate tactile sensory processing, we used mice with bilateral (rather than unilateral) whisker pad cauterization at E14 (bi-embWPC group), enabling a more precise assessment of whisker-dependent processing by eliminating potential compensatory input in response to vibrissae driven sensory stimuli from the intact contralateral side of the snout in unilateral cauterized mice. Wild type littermates with intact whiskers served as control mice, while an additional control group of wild type littermates underwent acute whisker trimming to assess texture discrimination in the absence of mystacial vibrissae input. Whisker trimming occurred on day 2, three hours after the second habituation session (see protocol below). All groups of mice were anaesthetized with 5% isoflurane for induction and maintained on 2% isoflurane for 10 minutes. In the trimmed group, precise trimming to the fur level was achieved using micro spring scissors and a surgical microscope, carefully sparing upper-lip whiskers.

Mice were habituated to handling and the testing room over 5-7 days, with dim lighting (20-30 lux) before testing. Behavioural testing arena was a black methacrylate box (40 x 40 x 40 cm) with no visual cues, and illumination was kept low (3-5 lux) to minimize visual information. Target objects consisted of 3D-printed cylinders (4 cm diameter, 9 cm height) covered with sandpaper of either 80 or 180 grit (P80 or P180) using double-sided tape. Six sets of textured covers were prepared a week prior to testing to minimize residual odors; each

set contained four covers (three P180 and one P80), avoiding repetitive use and minimizing olfactory interference.

We used a modified whisker-dependent texture discrimination task based on established protocols (Wu et al., 2013; Benamer et al., 2020; Balasco et al., 2022). This three-day paradigm takes advantage of mice´s innate preference for novelty. During days 1 and 2 (habituation sessions), mice freely explored the empty arena for 5 minutes each day. On day 3 (testing sessions), two identical P180 sandpaper-covered cylinders were placed diagonally within the arena (12 cm from walls, 15 cm apart) during the sample session (t_1). Mice explored these objects for 5 minutes before being returned to their home cages for a 2-minute inter-trial interval (ITI). During this interval, the arena and objects were cleaned with 70% ethanol, one P180 cover was replaced with a P80 sandpaper to create a novel texture and the other P180 cover was replaced by a new P180 cover. The short ITI minimized the influence of hippocampal processes on texture discrimination. During the test session (t_2), mice were returned to the arena to explore both the familiar (P180) and novel (P80) textures for 5 minutes. Mice were acclimated to the testing room for 30-60 minutes prior to each session.

Data analyses were performed offline using custom Matlab scripts to track and analyze locomotor and exploratory behaviours. Texture discrimination was assessed using the discrimination index (DI), calculated as the proportion of time spent exploring the novel texture relative to the total exploration time, according to the formula:

$$DI = \frac{Tnew}{Tnew + Tfamiliar}$$

where T_{new} refers to the time spent exploring the novel texture (P80) and $T_{familiar}$ is the time spent on the familiar texture (P180). In sample session (t_1), T_{new} refers to the texture that will be replaced in the following test session (t_2). DI values range from 0 to 1, with a value of 0.5 indicating no preference, and values above 0.5 indicating a preference for the novel texture.

Statistical analysis

Data were analysed using Prism 9 (GraphPad). A Kolmogorov-Smirnov normality test was conducted on all datasets. For independent data that conforming to a normal distribution, an unpaired two-tailed Student's *t*-test was employed to compare two groups. In cases where independent data that did not follow a normal distribution, a Mann-Whitney *U*-Test two-tailed test was used for comparison. For analyses involving more than two groups and one factor, one-way ANOVA was applied, followed by a Tukey *post hoc* analysis when data exhibited a normal distribution. For more than two groups and two factors, two-way ANOVA was conducted, followed by a Tukey *post hoc* analysis for normally distributed data. When data did not conform to a normal distribution, a Kruskal-Wallis test was performed, followed by Dunn's multiple comparisons without any correction. Results are presented as mean ± standard error of mean (SEM) with the n value for each dataset. Statistically significant effects and n numbers are detailed in the corresponding figure legend or Methods. The significance threshold was set at 0.05, two-tailed (not significant, ns, $p > 0.05$; *$p < 0.05$; **$p < 0.01$; ***$p < 0.001$). In the bioinformatical analysis, DEGs were identified using a statistical significance threshold (BH-adjusted p value < 0.1) and set as follows: *adj. $p < 0.1$, **adj. $p < 0.01$, and ***adj. $p < 0.001$. No data exclusion was performed. Data for RNA-seq were processed according to the description in the Methods sections, and statistical details are explained in the results and corresponding figure legends.

Quantifications

Main Figures

In Fig. 1b: Whisker pad volume, unpaired two-tailed Student *t*-test. **$p < 0.01$. Upper lip volume, unpaired two-tailed Student *t*-test. ns, $p= 0.11$. Upper lip area, unpaired two-tailed Student *t*-test. ns, $p= 0.32$. 9 follicles volume, two-tailed Mann-Whitney *U*-test. *$p < 0.05$. ns, $p= 0.73$. Upper lip number of follicles, unpaired two-tailed Student *t*-test. ns, $p= 0.78$. In Fig. 1d: unpaired two-tailed Student *t*-test. PMBSF, ***$p < 0.0001$, ALBSF, ***$p= 0.0002$.

In Fig. 1f: unpaired two-tailed Student *t*-test. DiI, ***p= 0.0002, DiA, ***p < 0.0001. In Fig. 1h: unpaired two-tailed Student *t*-test. ns, PMBSF, p= 0.55, ALBSF, p= 0.30. In Fig. 1j: unpaired two-tailed Student *t*-test. ns, p= 0.09. **p < 0.01.

In Fig. 2c: unpaired two-tailed Student *t*-test. PMBSF active fraction after wps, *p= 0.0198, PMBSF active fraction after uls, ***p= 0.0001, ALBSF active fraction after wps, **p= 0.0037, ALBSF active fraction after uls, **p= 0.0014. In Fig. 2e: PMBSF active fraction, unpaired two-tailed Student *t*-test. **p < 0.01. ALBSF active fraction, two-tailed Mann-Whitney *U*-test. ns, p= 0.06. *p < 0.05. In Fig. 2f: Kruskal-Wallis test, ***p <0.001. Dunn's multiple comparison test post-hoc analysis, ctrl E18 vs embWPC E18 ns, p= 0.37; ctrl E18 vs ctrl P4, ***p= 0.0009; ctrl E18 vs embWPC P4, ***p < 0.0001; embWPC E18 vs ctrl P4 ns, p= 0.77; embWPC E18 vs embWPC P4 ns, p= 0.14; ctrl P4 vs embWPC P4 ns, p > 0.999.

In Fig. 3d: Kruskal-Wallis test, ***p <0.001. Dunn's multiple comparison test post-hoc analysis, wpVPM ctrl vs wpVPM embWPC ns, p= 0.14; wpVPM ctrl vs ulVPM embWPC ns, p= 0.32; wpVPM embWPC vs ulVPM embWPC ns, p >0.99. wpVPM ctrl vs ulVPM ctrl, *p= 0.04. ulVPM ctrl vs ulVPM embWPC, ***p < 0.0001. In Fig. 3f: Thalamus, wpVPM, Two-way ANOVA test: ***p <0.001. Tukey's multiple comparison test post-hoc analysis, ns, p= 0.98. ***p < 0.0001; ulVPM, Kruskal-Wallis test, ***p= 0.0005. Dunn's multiple comparison test post-hoc analysis, ns, p >0.99. **p= 0.0019. Cortex, PMBSF, Two-way ANOVA test: ***p < 0.0001. Tukey's multiple comparison test post-hoc analysis, ns, p= 0.99. ***p < 0.0001; ALBSF, Two-way ANOVA test: ***p <0.0001. Tukey's multiple comparison test post-hoc analysis, ns, p= 0.52. ***p= 0.0002. In Fig. 3h: DiI, two-tailed Mann-Whitney *U*-test. ns, p= 0.7; DiA, unpaired two-tailed Student *t*-test. ns, 0.76.

In Fig. 4b: One-way ANOVA test: ***p <0.0001. Tukey's multiple comparison test post-hoc analysis, ns, p= 0.056, ***p <0.0001. In Fig. 4i: Negative binomial generalized linear model (GLM) analysis, p-values calculated using a two-tailed Wald's test. Adjusted p-values were obtained using the Benjamini-Hochberg (BH) method for multiple comparisons, with a

significance threshold of adjusted p-value < 0.1. *Ror*α wpVPM-ctrl vs ulVPM-ctrl, ***adj. p < 0.0001; *Ror*α wpVPM-ctrl vs ulVPM-embWPC ns, adj. p= 0.98; *Ror*α ulVPM-ctrl vs ulVPM-embWPC, **adj. p= 0.002; *Hs6st2* wpVPM-ctrl vs ulVPM-ctrl, ***adj. p < 0.0001; *Hs6st2* wpVPM-ctrl vs ulVPM-embWPC, *adj. p= 0.04; *Hs6st2* ulVPM-ctrl vs ulVPM-embWPC, ***adj. p < 0.0001; *Pou2f2* wpVPM-ctrl vs ulVPM-ctrl, ***adj. p < 0.0001; *Pou2f2* wpVPM-ctrl vs ulVPM-embWPC, *adj. p= 0.07; *Pou2f2* ulVPM-ctrl vs ulVPM-embWPC, ***adj. p= 0.0003; *Epha4* wpVPM-ctrl vs ulVPM-ctrl, ***adj. p= 0.0008; *Epha4* wpVPM-ctrl vs ulVPM-embWPC ns, adj. p= 0.79; *Epha4* ulVPM-ctrl vs ulVPM-embWPC, *adj. p= 0.08; *Plxna2* wpVPM-ctrl vs ulVPM-ctrl, ***adj. p < 0.0001; *Plxna2* wpVPM-ctrl vs ulVPM-embWPC, *adj. p= 0.06; *Plxna2* ulVPM-ctrl vs ulVPM-embWPC, ***adj. p < 0.0001; *Cdh9* wpVPM-ctrl vs ulVPM-ctrl, ***adj. p < 0.0001; *Cdh9* wpVPM-ctrl vs ulVPM-embWPC ns, adj. p= 0.98; *Cdh9* ulVPM-ctrl vs ulVPM-embWPC, ***adj. p < 0.0001.

In Fig. 5b: Barrels average area (34 barrels), Two-way ANOVA test: ***p <0.0001. Tukey's multiple comparison test post-hoc analysis, ns, p= 0.88. ***p < 0.0001. Average area of 4 barrels per three caudal-to-rostral levels, Two-way ANOVA test: ***p <0.0001. Tukey's multiple comparison test post-hoc analysis, level 1 ALBSF-ctrl vs ALBSF-embWPC, ***p < 0.0001; level 2 ALBSF-ctrl vs ALBSF-embWPC, ***p < 0.0001; level 3 ALBSF-ctrl vs ALBSF-embWPC, ns, p= 0.21; level 1 ALBSF-ctrl vs level 2 ALBSF-ctrl, ns, p > 0.99; level 1 ALBSF-ctrl vs level 3 ALBSF-ctrl, ns, p= 0.88; level 2 ALBSF-ctrl vs level 3 ALBSF-ctrl, ns, p= 0.92; level 1 ALBSF-embWPC vs level 2 ALBSF-embWPC, **p= 0.0023; level 1 ALBSF-embWPC vs level 3 ALBSF-embWPC, ***p < 0.0001; level 2 ALBSF-embWPC vs level 3 ALBSF-embWPC, **p= 0.0027. In Fig. 5c: barrel/septum fluorescence ratio (ΔFb/Fs), Two-way ANOVA test: ***p <0.0001. Tukey's multiple comparison test post-hoc analysis, PMBSF-ctrl vs ALBSF-embWPC ns, p= 0.80; ALBSF-ctrl vs ALBSF-P0WPC ns, p= 0.35; PMBSF-ctrl vs ALBSF-ctrl, ***p <0.0001; ALBSF-ctrl vs ALBSF-embWPC, ***p <0.0001; PMBSF-ctrl vs ALBSF-P0WPC, ***p <0.0001; ALBSF-embWPC vs ALBSF-P0WPC, ***p <0.0001. Gray value fluorescence intensity in a barrel, One-way ANOVA test: ***p= 0.0002. Tukey's multiple comparison test post-hoc analysis, ns, p= 0.99. PMBSF-ctrl

vs ALBSF-embWPC ns, p= 0.99; ALBSF-ctrl vs ALBSF-P0WPC ns, p= 0.99; ALBSF-ctrl vs ALBSF-embWPC, *p= 0.01; PMBSF-ctrl vs ALBSF-ctrl, **p= 0.005; ALBSF-embWPC vs ALBSF-P0WPC, **p= 0.005; PMBSF-ctrl vs ALBSF-P0WPC, **p= 0.0023. In Fig. 5e: One-way ANOVA test: *p= 0.01. Tukey's multiple comparison test post-hoc analysis, PMBSF ctrl vs ALBSF-embWPC ns, p= 0.75; ALBSF-ctrl vs PMBSF-ctrl, *p= 0.048; ALBSF-ctrl vs ALBSF-embWPC, *p= 0.013. In Fig. 5g: PV+ cells in barrels P8, One-way ANOVA test: ***p <0.0001. Tukey's multiple comparison test post-hoc analysis, PMBSF-ctrl vs ALBSF-embWPC ns, p= 0.98; PMBSF-ctrl vs ALBSF-ctrl, ***p= 0.0003; ALBSF-embWPC vs ALBSF-ctrl, ***p= 0.0002. PV+ cells in septa P8, One-way ANOVA test: ***p <0.0001. Tukey's multiple comparison test post-hoc analysis, PMBSF-ctrl vs ALBSF-embWPC ns, p > 0.99; PMBSF-ctrl vs ALBSF-ctrl, ***p < 0.0001; ALBSF-embWPC vs ALBSF-ctrl, ***p < 0.0001.

In Fig. 6c: One-way ANOVA test: ***p <0.0001. Tukey's multiple comparison test post-hoc analysis, ns, p= 0.18. ***p < 0.0001. In Fig. 6f: PMBSF, unpaired two-tailed Student *t*-test. ***p <0.0001; ALBSF, two-tailed Mann-Whitney *U*-test. ***p= 0.0002. In Fig. 6j: Total time of exploration, Two-way ANOVA test: **p= 0.0023. Tukey's multiple comparison test post-hoc analysis, t1 ctrl vs bi-embWPC, *p= 0.05; t1 ctrl vs trimmed, **p= 0.001, t1 bi-embWPC vs trimmed ns, p= 0.42; t2 ctrl vs bi-embWPC, *p= 0.029; t2 ctrl vs trimmed, *p= 0.029, t2 bi-embWPC vs trimmed ns, p= 0.997. Discrimination Index, Two-way ANOVA test: **p= 0.002. Bonferroni's multiple comparison post-hoc test; t1 ctrl vs t2 ctrl, *p= 0.035; t1 bi-embWPC vs t2 bi-embWPC, **p= 0.009; t1 trimmed vs t2 trimmed ns, p> 0.999.

Data availability

RNAseq datasets have been deposited at the National Center for Biotechnology Information (NCBI) Gene Expression Omnibus (GEO) as GEO: GSE260865 (https://www.ncbi.nlm.nih.gov/geo/query/acc.cgi?acc=GSE260865) and are publicly available as of the date of publication.

The remaining data are available within the Article, Supplementary Information, or Source data file. Source data are provided with this paper. Any additional information required to reanalyze the data reported in this work paper is available from the lead contact upon request.

Code availability

This study did not generate original code. For *ex vivo* experiments analysis, calcium imaging code previously reported[21] and deposited at https://github.com/ackman678/CalciumDX. For *in vivo* calcium imaging experiments, the code from WholeBrainDX repository (James et al., 2014) (available at https://github.com/ackman678/wholeBrainDX) was employed to prepared the supplementary videos. For behavioural experiments, video recordings were processed using custom codes developed with Matlab's Image Processing Toolbox.

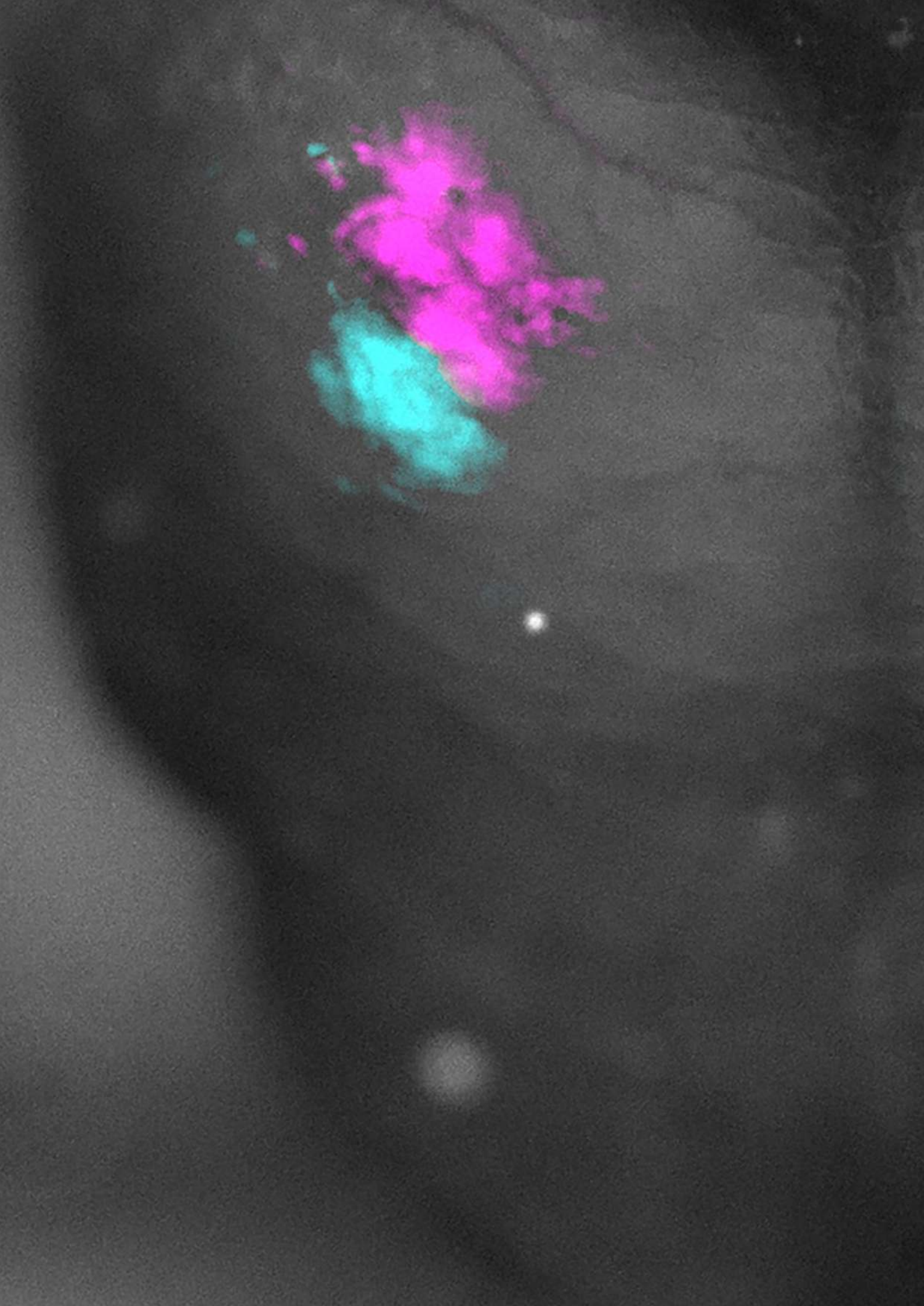

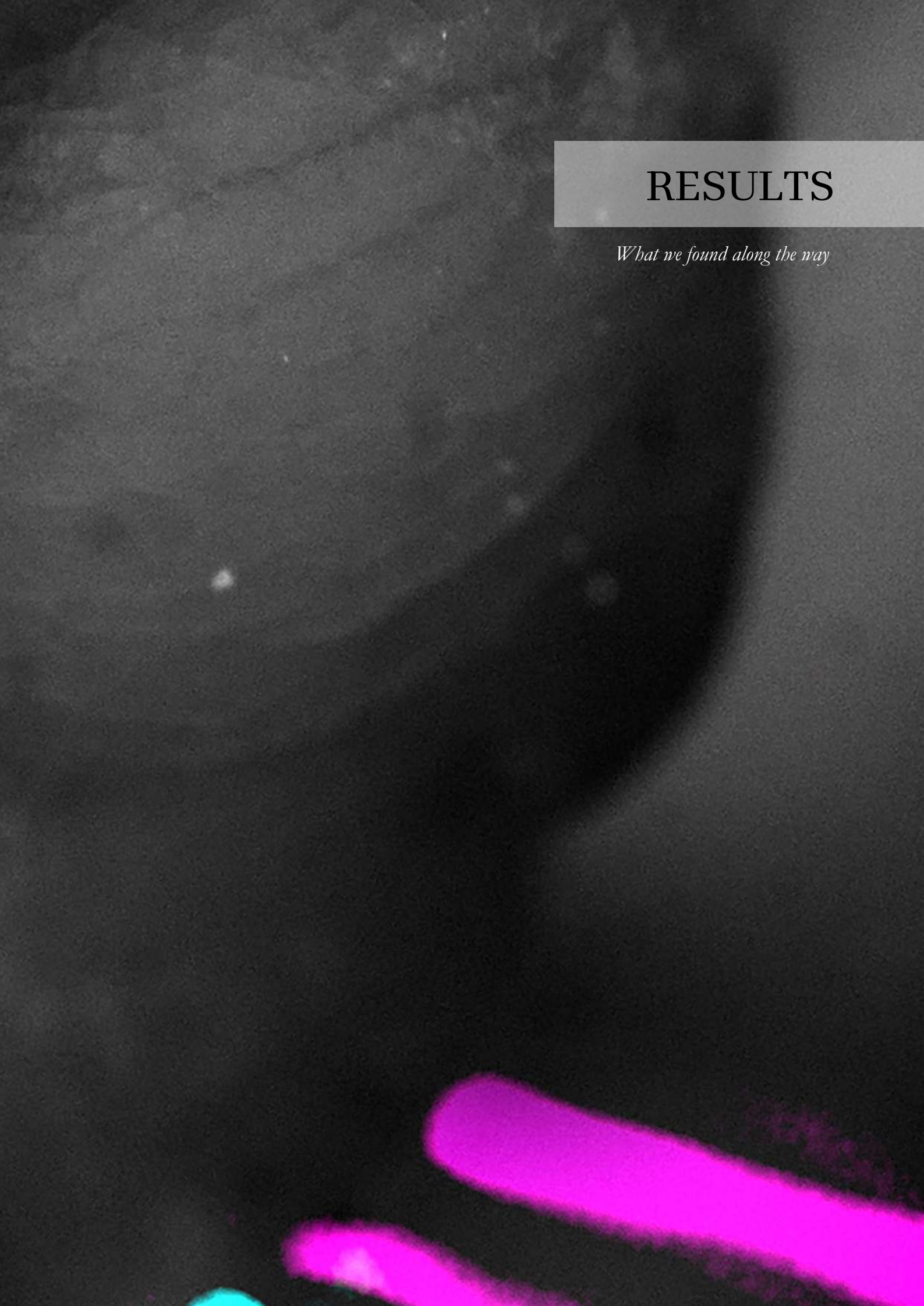

RESULTS

What we found along the way

RESULTS

The results of this thesis are published in *Nature Communications*, in the annexed paper titled "**A prenatal window for enhancing spatial resolution of cortical barrel maps**", where I am the sole first author. This work was conducted in collaboration with members of my laboratory and researchers from other institutions, and the specific contributions of each co-author are outlined below: Guillermina López-Bendito and Mar Aníbal-Martínez designed the experiments. Mar Aníbal-Martínez performed the surgeries, conducted histological experiments, dye tracings, *ex vivo* and *in vivo* calcium imaging experiments, and analyzed the data. Mar Aníbal-Martínez collected tissue for RNAseq and Lorenzo Puche-Aroca performed all bioinformatic analyses of the massively parallel sequencing data. Elena Pérez-Montoyo and Mar Aníbal-Martínez carried out behavioural experiments. M. Pilar Madrigal performed iDISCO+ experiments, processed the images, and analyzed the resulting data. Luis M. Rodríguez-Malmierca conducted *in situ* hybridization validation of the RNAseq. Gabriele Pumo and Filippo M. Rijli provided data of *Krox20*^{ZsGreen}*::r2*^{mCherry} triple transgenic mice. Francisco J. Martini reviewed and edited the manuscript. Guillermina López-Bendito acquired funding. Finally, the manuscript was jointly written by Mar Aníbal-Martínez and Guillermina López-Bendito.

A prenatal window for enhancing spatial resolution of cortical barrel maps

Mar Aníbal-Martínez[1], Lorenzo Puche-Aroca[1], Elena Pérez-Montoyo[1], Gabriele Pumo[2,3], M. Pilar Madrigal[4], Luis M. Rodríguez-Malmierca[1], Francisco J. Martini[1], Filippo M. Rijli[2,3], Guillermina López-Bendito[1,*]

[1]Instituto de Neurociencias de Alicante, Universidad Miguel Hernández-Consejo Superior de Investigaciones Científicas (UMH-CSIC), San Juan de Alicante, Alicante, Spain.
[2] Friedrich Miescher Institute for Biomedical Research, Fabrikstrasse 24, 4056 Basel, Switzerland.
[3]University of Basel, Basel, Switzerland.
[4]Departamento de Histología y Anatomía, Facultad de Medicina, Universidad Miguel Hernández (UMH), San Juan de Alicante, Alicante, Spain.

*Correspondence: g.lbendito@umh.es (G.L-B)

Nature Communications March 2025: 16, no. 1955. DOI: 10.1038/s41467-025-57052-w. https://www.nature.com/articles/s41467-025-57052-w

Abstract

Precise mapping of peripheral inputs onto cortical areas is essential for accurate sensory processing. In the mouse primary somatosensory cortex, mystacial whiskers correspond to large, well-defined barrels, while upper lip whiskers form smaller, less distinct barrels. These differences are traditionally attributed to variations in whisker input type and receptor density, but prenatal activity and transcriptional programs also impact somatosensory map development independently of sensory experience. Here, we demonstrate that prenatal ablation of mystacial whiskers leads to a remapping of cortical territories, enhancing the functional and anatomical definition of upper lip whisker barrels. This reorganization occurs without altering peripheral receptor types. Instead, thalamic neurons that receive upper lip inputs adopt a mystacial-like transcriptional profile. Our findings unveil a regulated prenatal mechanism in the thalamus that ensures sufficient cortical barrel size and spatial resolution for sensory processing, irrespective of peripheral receptor type or density, highlighting a critical developmental process in sensory mapping.

Introduction

Sensory systems are represented in the primary sensory areas of the brain, structured into both anatomical and functional maps[1-4]. The spatial precision of sensory maps varies among species according to the ethological relevance of the modality or the intra-modal sensory branch[5]. This precision is achieved through the accuracy of point-to-point innervation along the ascending sensory pathway. In rodents, which heavily rely on the somatosensory modality, a prominent cortical area is devoted to processing stimuli from facial whiskers. Within the mouse primary somatosensory cortex (S1), information from facial whiskers is processed in two juxtaposed subfields: the postero-medial barrel subfield (PMBSF) and the antero-lateral barrel subfield (ALBSF). The PMBSF receives input from the mystacial whiskers which provide diverse and specialized information to S1[6,7]. The ALBSF receives input from the upper lip whiskers which are considered to play a secondary role in sensory processing[8]. While each barrel corresponds to a single whisker in both regions, the degree of clustering of incoming thalamocortical axons varies, leading to notable anatomical distinctions between the two territories. While PMBSF barrels are characterized by their large size and sharp borders, ALBSF barrels are smaller and have poorly defined borders[9]. These differences in intra-modal map organization parallel the distinct morphological characteristics of mystacial and upper lip whiskers: mystacial whiskers are long with large follicles, whereas upper lip whiskers are comparatively short with small follicles, albeit more abundant. Despite their clear anatomical and functional differences, we still lack a complete understanding of the mechanism underlying the construction of these two distinct barrel maps and to what extent they rely on the type of sensory receptors (mystacial versus upper lip). Indeed, recent data demonstrated that sensory receptor-independent mechanisms can also influence cortical barrel size by altering the patterns of activity in subcortical stations. For instance, increasing thalamic waves in the developing somatosensory thalamus of early blind mice results in larger barrels in the PMBSF of S1, even before the onset of active whisking[10,11]. Thus, the size of a sensory barrel map may not only depend on the type and number of sensory receptors but may also be regulated by intrinsic programs during development. By embryonically ablating

mystacial whiskers and follicles, and the subsequent PMBSF representation, we generated mice in which the ALBSF barrels become larger and better-defined, without altering the size and number of upper lip follicles. This intra-modal reorganization of the barrel maps occurs within a restricted prenatal time window and is guided by transcriptional programs operating intra-modally in the thalamus. Interestingly, these reorganized ALBSF barrels resemble normal PMBSF barrels at the morphological, molecular and functional levels, showing an enhanced spatial resolution upon tactile stimulation.

Results

The size of barrel subfield areas can be adjusted prenatally

The size of the areas devoted to processing distinct whisker -mystacial versus upper lip- input information is thought to be determined by the corresponding type and density of sensory receptors on the mouse face[12,13]. We asked whether prenatal removal of a selected facial whisker type might have an impact on the cortical barrel areas and spatial distribution of the spared whiskers. We implemented a strategy whereby the mystacial whiskers in the whisker pad were cauterized unilaterally at embryonic day (E) 14 (named as embWPC), in both wild type and TCA-GFP mice[14], in which thalamocortical projections are labeled with green fluorescent protein (GFP). At this stage, trigeminal nerve axons have just begun to target the principal trigeminal sensory nucleus (PrV) in the brainstem (Supplementary Fig. 1a), but PrV neuron axons have not yet entered the ventral posteromedial (VPM) thalamic nucleus[15-19].

Analysis of the snout at E18 confirmed the specific ablation of the mystacial whiskers and follicles (Fig. 1a,b), with a strong reduction of whisker pad-innervating primary trigeminal sensory axons targeting the PrV (Supplementary Fig. 1b). At early postnatal stages, the total areas of PrV, thalamic ventral posterior nucleus (VPN) and S1, including other somatosensory body representations apart from the snout, did not exhibit significant differences in embWPC, as compared to control mice (Supplementary Fig. 2a-h). In contrast, the size of the areas corresponding to mystacial and upper lip whiskers significantly rescaled in embWPC mice at all levels of the pathway, suggesting intra-modal plasticity of connectivity. For example, in S1, we found a 54% decrease in the PMBSF territory, and a 34% expansion of the ALBSF territory, a phenomenon already observed at P4 (Fig. 1c,d; Supplementary Fig. 2i,j). Notably, we found no discernible differences in the total upper lip volume, nor in the volume and number of upper lip follicles between control and embWPC mice both at E18 and P8 (Fig.1a,b; Supplementary Movies 1,2). Dye depositions in the cortical PMBSF or ALBSF of P8 embWPC confirmed a similar intra-modal remapping of the corresponding whisker pad input-receiving VPM (wpVPM) or upper lip input-receiving VPM (ulVPM) areas in the thalamic VPM[20] (Fig. 1e,f). Moreover, retrogradely labeled

thalamocortical neurons within each VPM sub-territory maintained their expected point-to-point distribution, matching cortical topography (Supplementary Fig. 3).

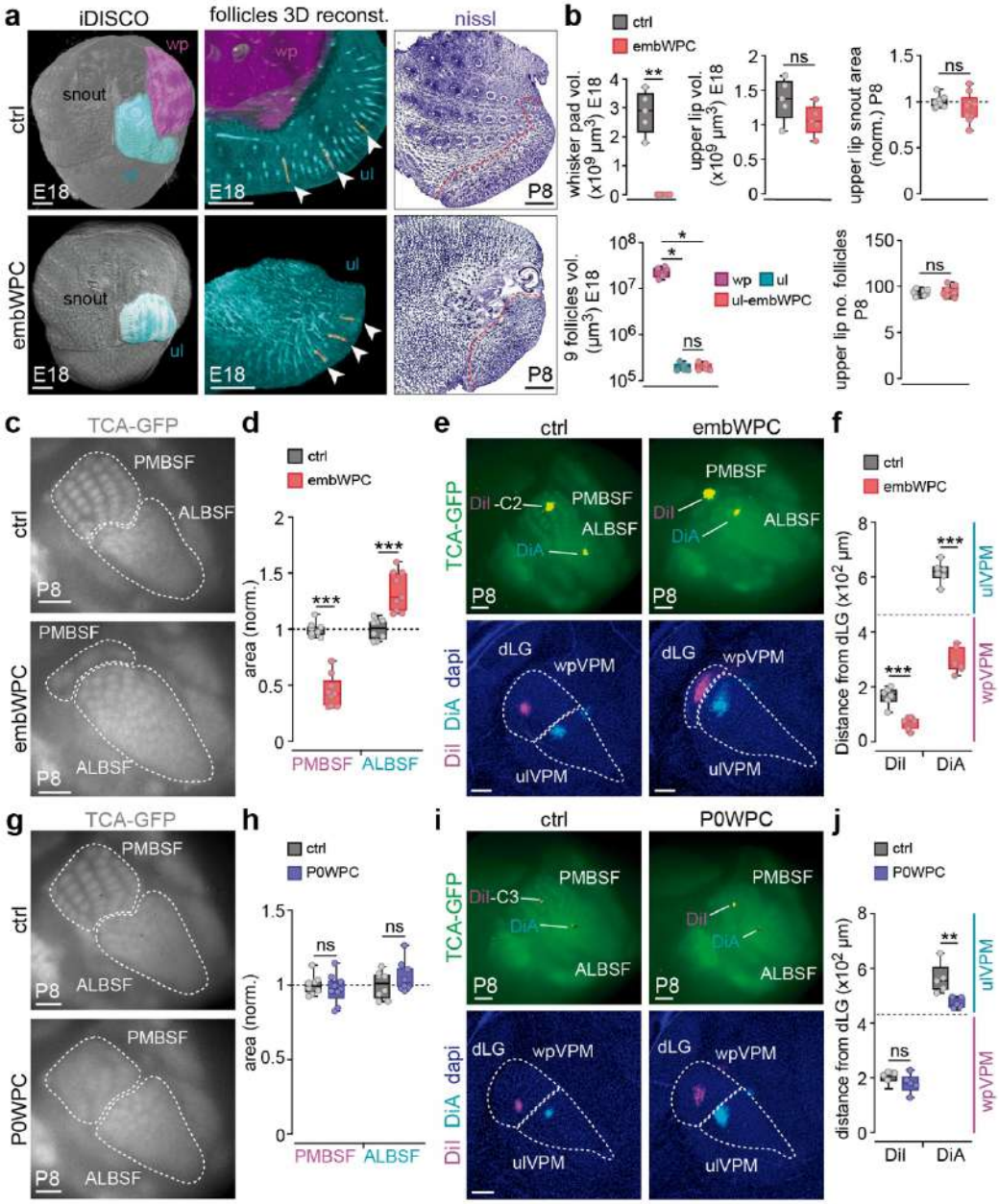

Figure 1. Whisker pad deprivation in embryos rescales barrel field areas and thalamocortical circuits. a Left and middle, iDISCO frontal snout views showing the whisker pad (magenta) and upper lip (cyan) areas, lateral 3D-reconstructions of the follicles (yellow) at E18. Right, Nissl stainings of the snout at P8, red dashed line delimits upper lip area. **b** Quantification (iDISCO E18, n= 5 ctrl, n= 5 embWPC. Nissl P8, n= 8 ctrl, n= 9 embWPC). **c** Surface view of thalamocortical terminals (TCA-GFP+) in the PMBSF and ALBSF at P8. **d** Quantification (n= 8 ctrl, n= 9 embWPC). **e** Upper panels, DiI and DiA crystal placements in the C2 PMBSF and in the ALBSF, respectively, at P8. Lower panels, backlabelled cells in the wpVPM and ulVPM. **f** Quantification of the position of backlabelled cells with respect to the

distance to the dLG nucleus. The gray horizontal dashed line represents the separation between wpVPM and ulVPM (n= 6 ctrl, n= 6 embWPC). **g** Surface view of TCA-GFP+ in the PMBSF and ALBSF at P8. **h** Quantification of the data (n= 8 ctrl, n= 9 P0WPC). **i** Upper panels, DiI and DiA crystal placements in the C3 PMBSF and in the ALBSF, respectively, at P8. Lower panels, backlabelled cells in the wpVPM and ulVPM. **j** Quantification of the position of backlabelled cells with respect to the distance to the dLG nucleus. The gray horizontal dashed line represents the separation between wpVPM and ulVPM (n= 5 ctrl, n= 5 P0WPC). Source data are provided as a Source data file. wp, whisker pad; ul, upper lip; E, embryonic; P, postnatal; embWPC, embryonic whisker pad cauterized; P0WPC, postnatal day 0 whisker pad cauterized; vol., volume; no., number; TCA-GFP, thalamocortical axons labelled with green fluorescent protein; norm., normalized. Scale bars: **a** (left), **c**, **e** (top), **g**, **i** (top) 500 μm; **a** (middle) 400 μm; **a** (right) 1000 μm; **e** (bottom) and **i** (bottom) 200 μm. Boxplots show the medians with the interquartile range (box) and range (whiskers). Bar graphs show the means ± SEM. ns, not significant. *p < 0.05, **p < 0.01, ***p < 0.001.

Importantly, the changes of the cortical barrel field sub-territories depended on mechanisms only present before birth, since cauterization of the whisker pad at postnatal day 0 (P0), referred to as P0WPC, revealed no significant territorial differences in the PMBSF and ALBSF between control and P0WPC across the somatosensory stations (Fig. 1g,h and Supplementary Fig. 4). As expected, there were no re-arrangements of the thalamocortical axons in the P0WPC (Fig. 1i,j; Supplementary Fig. 5). Notably, barrels in PMBSF exhibited a diminished degree of definition and structure, with blurred point-to-point topography, highlighting the enduring effects of early sensory deprivation on cortical organization (Supplementary Fig. 5c,d). Thus, there is a critical window in which the cortical ALBSF area can be significantly adjusted without altering upper lip receptors, suggesting that after this timepoint plasticity might arise from a different strategy to compensate for sensory loss.

Functional rescaling of ALBSF in embWPC mice occurs before birth

Whisker pad stimulation *in vivo* at E18 can elicit activity in the developing PMBSF[21,22], indicating that the periphery-to-cortex somatosensory pathway is already functional before birth. We asked whether the anatomical changes observed in embWPC at P8 were detectable at prenatal stages by assessing functional reorganizations. We carried out peripheral whisker pad and upper lip stimulations at E18 while recording cortical calcium activity in *Emx1*^{GCaMP6f} transgenic mice, expressing GCaMP6f in cortical glutamatergic neurons[22] and carrying

unilateral whisker pad cauterization (Fig. 2a). We also used non cauterized mice as additional controls.

Stimulations of either the whisker pad or the upper lip in control mice or in the control side of embWPC mice at E18 elicited responses from clusters of cortical neurons corresponding to the putative territories of the PMBSF or ALBSF, respectively (Fig. 2b,c; Supplementary Fig. 6; Supplementary Movie 3). In contrast, whisker pad stimulations in the cauterized side of embWPC mice triggered very reduced responses in the caudal-most part of the expected contralateral PMBSF ("PMBSF"), confirming the anatomical reduction of this territory. Remarkably, stimulations of the upper lip in the cauterized side elicited misplaced responses in the expected ALBSF ("ALBSF") that notably expanded into the "PMBSF" (Fig. 2b,c; Supplementary Movie 4), as compared to the control side. This ectopic "PMBSF" activation was maintained at P4 when the size of responses to upper lip stimulation were already refined in the control side (Fig. 2d-g; Supplementary Movies 5,6). Thus, the anatomical rescaling of barrel field sub-territories seen in the postnatal embWPC can be functionally detected prior to birth.

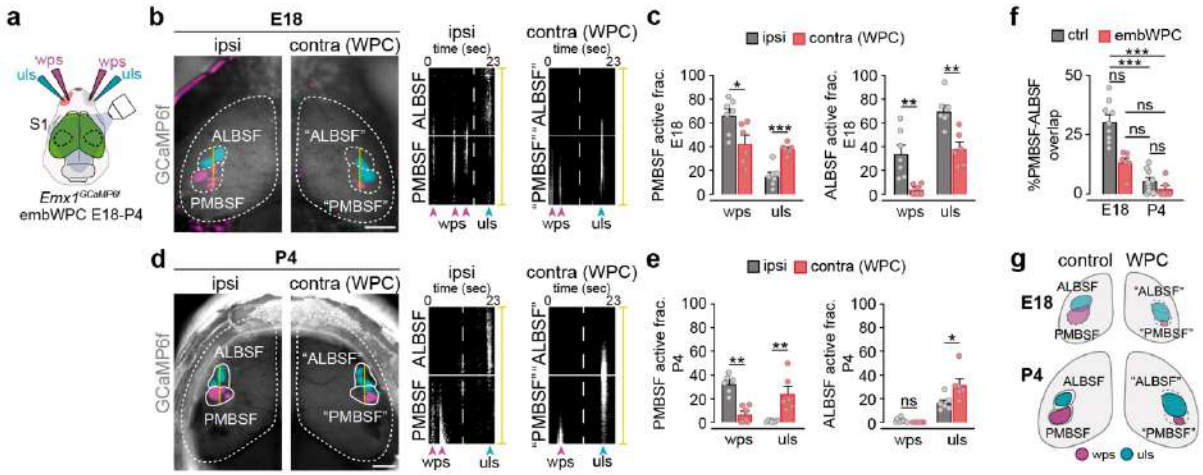

Figure 2. Functional rescaling of cortical barrel field territories in embWPC mice. a Schema representing the experimental paradigm. **b** Left, cortical evoked responses (GCaMP6f) to whisker pad (magenta) and upper lip (cyan) stimulations in control (ipsilateral) and whisker pad cauterized (WPC, contralateral) sides in embWPC mice at E18. Control PMBSF and ALBSF territories were translated to the WPC side for direct comparison and labelled as "PMBSF" and "ALBSF". Right, reslice of the yellow line in the left, representing responses elicited in PMBSF and ALBSF primordia by whisker pad stimulation (wps) or upper lip stimulations (uls). The white horizontal line delineates the boundaries between PMBSF

and ALBSF. The vertical dashed line divides the wps from the uls over time. The arrows label the stimulation times for whisker pad (magenta) and upper lip (cyan). **c** Quantification of the PMBSF and ALBSF active fraction to wps or uls (n= 7 ctrl, n= 6 WPC). **d** Left, cortical evoked responses (GCaMP6f) to whisker pad (magenta) and upper lip (cyan) stimulations in control (ipsilateral) and WPC (contralateral) sides in embWPC at P4. Right, reslice of the yellow line in the left, representing responses elicited in PMBSF or ALBSF by wps or uls. The white horizontal line delineates the boundaries between PMBSF and ALBSF. The vertical dashed line divides the wps from the uls over time. The arrows label the stimulation times for whisker pad (magenta) and upper lip (cyan). **e** Quantification of the PMBSF and ALBSF active fraction to wps and uls (n= 6 ctrl side, n= 6 WPC side). **f** Quantification of the percentage of overlap responses between the PMBSF and ALBSF territories at E18 and P4 (n= 9 ctrl E18, n= 6 embWPC E18, n= 9 ctrl P4, n= 6 embWPC P4). **g** Schema illustrating the results. Dashed lines delineate PMBSF and ALBSF putative evoked territories at E18. Source data are provided as a Source data file. S1, primary somatosensory cortex; GCaMP6f, calmodulin-based genetically encoded fluorescent calcium indicator 6–fast. Scale bars, 1000 μm. Bar graphs show the means ± SEM. ns, not significant. *$p < 0.05$, **$p < 0.01$, ***$p < 0.001$.

Silencing prenatal thalamic synchronous activity does not prevent the area rescaling of barrel field sub-territories

Thalamic neurons display waves of prenatal spontaneous activity that are crucial for the development of cortical barrel field maps[10,21]. Therefore, we investigated whether the rescaling of barrel field territories in embWPC embryos could be explained by changes in spontaneous activity of VPM neurons. Inputs from the whisker pad at E16 are carried by afferents from ventral portion of the PrV (vPrV), whereas inputs from the upper lip are carried by afferents from dorsal PrV (dPrV)[17-19]. While at this prenatal stage vPrV afferents topographically target the dorsolateral VPM (the prospective wpVPM), dPrV afferents target not only the ventromedial part (the prospective ulVPM) but cover most part of the VPM[17,19]. Thus, while whisker pad and upper lip inputs are segregated at the brainstem nuclei, dPrV and vPrV axons terminals prenatally overlap within the prospective wpVPM territory[17,19] (Fig. 3a,b and Supplementary Fig.7a-c). Remarkably, despite this axonal overlap, spontaneous activity patterns in the VPM thalamus at E16 were sub-territory specific. We detected a notable distinction in the frequency of spontaneous activity waves between the prospective wpVPM and ulVPM regions. While wpVPM exhibited a high frequency of waves, the prospective ulVPM showed significantly reduced frequency (Fig. 3c,d; Supplementary Movie 7). In embWPC, we observed a striking change in the spontaneous activity pattern, with a

significant increase in thalamic waves frequency within the prospective ulVPM, resembling the pattern observed in the control wpVPM primordium (Fig. 3c,d; Supplementary Movie 8). Interestingly, in embWPC VPM at P4, dPrV axon projections did not undergo normal developmental segregation but still targeted most of the dorsolateral VPM, unlike in controls, and covered the area normally occupied by vPrV input afferents (Supplementary Fig.7d,e). Thus, during prenatal development whisker input deprivation remaps spontaneous neuronal activity patterns in the future ulVPM territory.

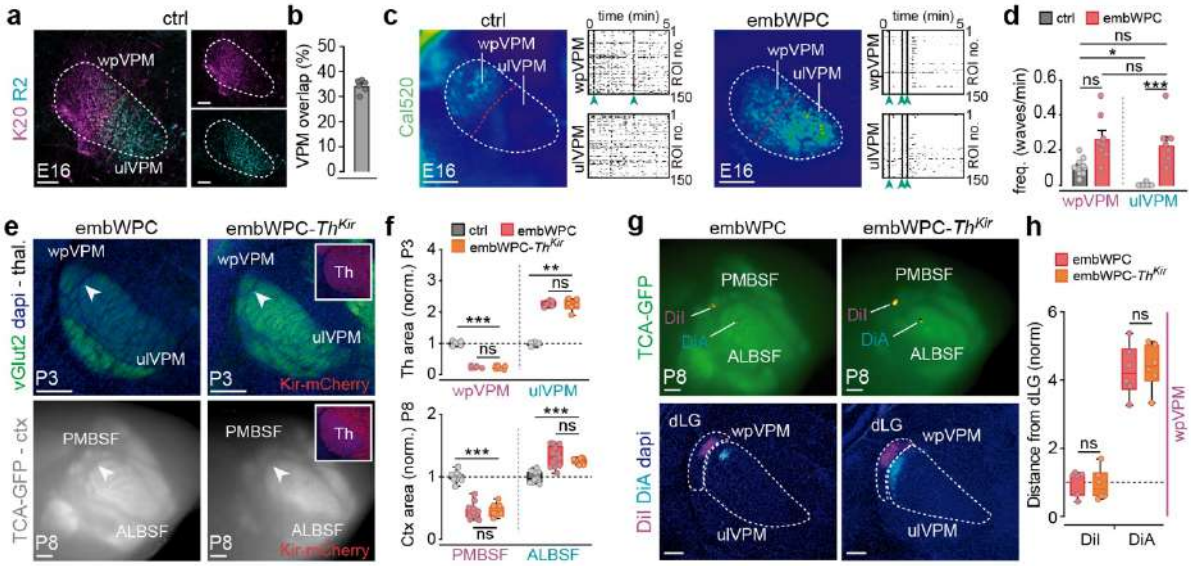

Figure 3. ALBSF rescaling is independent of thalamic patterned activity. a Coronal sections from the *Krox20-zsgreen::R2-mCherry* double transgenic mouse showing Krox20-labelled axons (magenta, vPrV) and R2-labelled axons (cyan, dPrV) at the VPM at E16. **b** Quantification of the percentage of overlap of labelled axons (n= 6). **c** Maximal projection of *ex vivo* spontaneous calcium activity in the prospective VPM sub-regions (wpVPM and ulVPM) in acute slices at E16. Raster plots of 5 minutes. The arrows label the calcium waves of synchronous activity. **d** Quantification of the frequency of waves activity in the VPM (n= 11 ctrl, n= 8 embWPC). **e** Upper panels, coronal sections of vGlut2 staining (green) in the wpVPM and ulVPM of embWPC and embWPC-*Th*^{Kir} mouse (Kir-mCherry positive) at P3. Lower panels, surface view of TCA-GFP+ terminals in the PMBSF and ALBSF in embWPC and embWPC-*Th*^{Kir} mice at P8. The arrows label the limits between wpVPM and ulVPM in the thalamus, and PMBSF and ALBSF in the cortex. **f** Quantification of the data (Thalamus, n= 5 ctrl, n= 5 embWPC, n= 6 embWPC-*Th*^{Kir}; Cortex, n= 10 ctrl, n= 13 embWPC, n= 7 embWPC-*Th*^{Kir}). **g** Upper panels, DiI and DiA crystal placements in the PMBSF and ALBSF, respectively. Lower panels, backlabelled cells at the thalamus show shifted positions within the ulVPM thalamic area in both embWPC and embWPC-*Th*^{Kir} mice at P8. **h** Quantification of the position of backlabelled cells with respect to the distance to the dLG nucleus. The gray horizontal dashed line in the graph represents the separation between wpVPM and ulVPM (n= 6 embWPC, n= 6 embWPC-*Th*^{Kir}). Source data are provided as a Source data file. Scale bars, **a** 100 μm; **c**, **g** (bottom) 200 μm; **e** (top) 250 μm, **e** (bottom), **g** (top) 500 μm. Boxplots show the medians with the interquartile range (box) and

range (whiskers). Bar graphs show the means ± SEM. ns, not significant. *p < 0.05, **p < 0.01, ***p < 0.001.

Next, we asked whether the embryonic increased activity in the prospective ulVPM might influence the functional and anatomical rescaling of the ALBSF territory. Thus, we tested this possibility and conducted embryonic whisker pad cauterization in a mouse in which the synchronous spontaneous activity of the thalamus is embryonically disrupted (referred to as embWPC-*Th*^{Kir})[21]. Briefly, we used a tamoxifen-dependent *Gbx2*^{CreERT2} mouse with a floxed line expressing the inward rectifier potassium channel 2.1 (*Kcnj2*) fused to the mCherry reporter in thalamic neurons (referred to as *Th*^{Kir}). Our data revealed that thalamic and cortical territories in embWPC-*Th*^{Kir} mice exhibited a spatial reorganization similar to that observed in embWPC mice. In both mice, the wpVPM and PMBSF territories virtually disappeared, and the ulVPM and ALBSF expanded as compared to the control (Fig. 3e). Consistent to previous studies in the *Th*^{Kir} mouse[21], manipulating thalamic activity patterns in the embWPC mice (embWPC-*Th*^{Kir}) resulted in the absence of thalamic waves (Supplementary Fig. 8a,b) and, the complete loss of barrels, evidenced by a total lack of TCA clustering, in both PMBSF and ALBSF territories (Fig. 3e,g). Rescaling of thalamic and cortical territories, along with thalamocortical circuits, was still observed in the embWPC-*Th*^{Kir} mouse but was virtually absent in the *Th*^{Kir} mouse alone, as shown by anatomical and dye tracing analyses (Fig. 3e-h; and Supplementary Fig. 8c-g). In sum, our results demonstrate that the patterns of spontaneous activity in prenatal VPM neurons are dispensable for intra-modal thalamic and cortical sub-territories rescaling to input deprivation.

Upper lip input-receiving thalamic neurons adopt a similar transcriptional profile to mystacial input-receiving neurons

Cross-modal and intra-modal changes in the transcriptional programs of thalamic neurons have been shown to generate thalamocortical circuit re-organizations and cortical adaptations, as shown in early blind pups or in mice with an early postnatal ablation of the VPM nucleus[10,23,24]. Therefore, we examined whether the anatomical and functional circuit

expansion of the ALBSF in embWPC might be influenced by changes in the transcriptional program of VPM neurons. To assess this, we dissected tissue, at similar distances from the dorsal lateral geniculate (dLG) nucleus, from wpVPM and ulVPM in control and embWPC mice at P0 (Fig. 4a,b) and compared their transcriptional profiles by bulk RNA-sequencing (RNA-seq). Principal component analysis (PCA) revealed that the transcriptomes from wpVPM and ulVPM cells in control mice clustered separately already at P0 (Supplementary Fig. 9a). Differential Expression Analysis (DEA) further revealed 377 Differentially Expressed Genes (DEGs) enriched in the wpVPM as opposed to 365 in the ulVPM cells. Among the DEGs enriched in each population, we found genes previously identified as being involved in somatosensory development such as *Epha3, Sox2, Hs6st2, Cdh8* or *Rorα* enriched in wpVPM[25-29] or *Rorβ*, *Slitrk6, Foxp2, Calb1* or *Lhx2*[10,30-33] enriched in the ulVPM (Supplementary Fig. 9b,c; Supplementary Data 1).

Then, we compared control versus embWPC transcriptional programs in the VPM. Remarkably, PCA analysis from ulVPM cells in embWPC mouse indicated that these neurons grouped more closely with control wpVPM than control ulVPM (Fig. 4c and Supplementary Fig. 9d). This transcriptional shift was appreciated when the expression pattern of the upper lip and whisker-pad DEGs was plotted in the ulVPM of the embWPC (Fig. 4d). To investigate this effect, we trained a Support Vector Machine classifier (C-SVM) using differentially expressed genes and compared the results with the ulVPM-embWPC. This machine learning approach predicted that the cauterized model would be classified as the wpVPM control in 70% of cases, compared to 30% for the ulVPM control (Fig. 4e). Additionally, DEA against the wpVPM control revealed a much lower number of differentially expressed genes (93 DEGs) compared to the ulVPM control (268 DEGs) (Fig. 4f).

In total, 150 region-specific DEGs from ulVPM and wpVPM where significantly changed by the embWPC (Fig. 4g). Namely, in the ulVPM of the embWPC mouse, we observed an upregulation of approximately 17% of the DEGs normally expressed in the control wpVPM and a downregulation of about 23% of control ulVPM DEGs, respectively

(Fig. 4g and Supplementary Fig. 9e; Supplementary Data 2). Notably, genes such as *Rorα, Epha4, Hs6st2, Cdh9,* or *Plxna2*, involved in axon guidance, thalamocortical mapping and wpVPM development[26,34], exhibited a wpVPM-like pattern in the ulVPM of embWPC mice (Fig. 4h,i and Supplementary Fig. 9f), also corroborated by *in situ* hybridization (Fig. 4j and Supplementary Fig. 9g). Next, we performed a Gene Ontology (GO) functional enrichment analysis of the genes with expression changes in the ulVPM of the embWPC and identified 11 clusters of GO-Terms enriched in Biological Processes (BP) and Molecular Functions (MF) (Supplementary Fig. 10; Supplementary Data 3). The top ranked cluster included 99 genes (46.8%) enriched in BP involved in dendrite development or synapse assembly (e.g. *Robo1, Flrt3*), and 12 genes (18.8%) enriched in MF involved in voltage-gated channel activity (e.g. *Kcnc2, Kcnab1*).

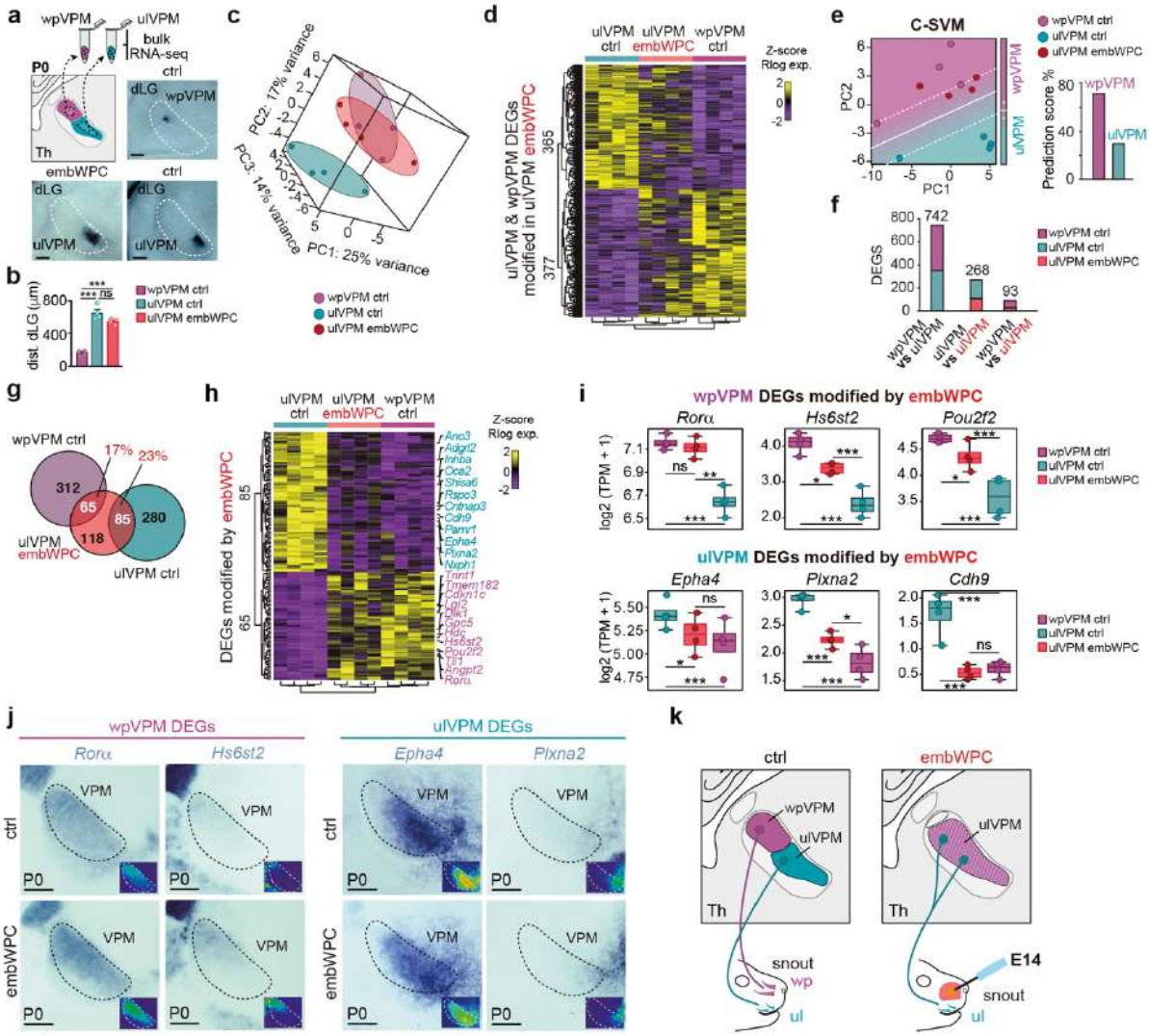

Figure 4. Upper-lip recipient thalamic neurons switch their transcriptional program to that of whisker-pad neurons. a Top left, schema representing the paradigm. Top right and bottom, coronal images showing the dissected thalamic territories for sequencing. **b** Quantification of the dissected area with respect to the distance to the dLG nucleus (n= 4 wpVPM ctrl slices, n= 4 ulVPM ctrl slices, and n= 4 ulWPC embWPC slices, 4 mice per condition). **c** Principal Component Analysis (PCA) of wpVPM ctrl (n= 4), ulVPM ctrl (n= 4) and ulVPM embWPC (n= 4) at P0. **d** Heatmap of the normalized regularized logarithm (Rlog) Z-score of expression and unbiased clustering of region-specific DEGs showing their expression profiled in the ulVPM of the embWPC at P0. The color-code (yellow, high expression; purple, low expression) corresponds to the log2FC. **e** Left, C-support vector machine (C-SVM) analysis identifies the optimal demarcation plane between wpVPM (magenta dots) and ulVPM population (cyan dots). The ulVPM embWPC samples are identified as wpVPM control based on its gene expression pattern (red dots). Right, Prediction score value of ulVPM embWPC classified as wpVPM (70%) or ulVPM (30%) controls. **f** Number of Differentially Expressed Genes (DEGs) obtained in their respective differential expression analysis. **g** Venn Diagram shows the number of genes modified by embWPC in ulVPM overlapped in every subset of region specific DEGs. **h** Heatmap of the normalized regularized logarithm (Rlog) Z-score of expression and unbiased clustering of region-specific DEGs whose expression was modified by embWPC in the ulVPM at P0. The color-code (yellow, high expression; purple, low expression) corresponds to the log2FC. **i** Boxplots showing TPM expression levels of selected wpVPM-specific and ulVPM-specific DEGs modified by embWPC in the ulVPM. Boxplots show the medians with the interquartile range (box) and range (whiskers). **j** Coronal sections showing *in situ* hybridization of wpVPM and ulVPM DEGS at P0 (n= 5 ctrl, n= 5 embWPC, for each probe). **k** Schema illustrating the results. Source data are provided as a Source data file. VPM, ventroposterior medial nucleus. Scale bars, 200 μm. *adj. $p < 0.1$, **adj. $p < 0.01$, and ***adj. $p < 0.001$.

Since the lack of spontaneous thalamic waves in embWPC-Th^{Kir} mice did not prevent the ALBSF reorganization, we investigated whether the changes in ulVPM transcriptome are still observed in embWPC-Th^{Kir} VPM. We conducted *in situ* hybridization for probes that we identified as wpVPM markers upregulated in the ulVPM of embWPC mice such as *Hs6st2, Rorα,* and *Pou2f2*, or markers downregulated in the ulVPM of embWPC mice such as *Epha4*. Our results show a similar shift in the expression pattern for these genes in both embWPC and embWPC-Th^{Kir} mouse (Supplementary Fig. 11) reinforcing that the transcriptomic changes in VPM territories are mainly independent of thalamic waves activity. In summary, the spatial rescaling of cortical ALBSF territory in embWPC correlates with transcriptomic changes observed in upper lip thalamic input neurons, which shift towards a molecular signature resembling that of whisker pad input neurons (Fig. 4k).

Increase of barrel size and functional spatial resolution of the cortical ALBSF map

We investigated whether upper lip-recipient thalamic neurons that acquire a whisker pad transcriptional profile during perinatal development might develop additional PMBSF characteristics later in life. At P8, PMBSF and ALBSF cortical areas differ in the average size of their barrels and the extent of clustering of thalamocortical axons. Remarkably, we observed that, in addition to the overall increase in the cortical area occupied by the ALBSF, the average size of the cortical individual barrels in the ALBSF of the embWPC was significantly larger compared to the ALBSF control (Fig. 5a,b). This change appears to follow a gradient, with the largest ALBSF barrels located nearest to the remaining PMBSF (Fig. 5b). Furthermore, the cortical map of the expanded ALBSF gained definition and contrast as thalamocortical terminals appeared more clustered within each barrel, and less innervating the barrel septa, resembling the control PMBSF (Fig. 5c-e). These differences in barrel size and contrast in the ALBSF map of the embWPC where not detected in P0WPC mice (Fig. 5a-c).

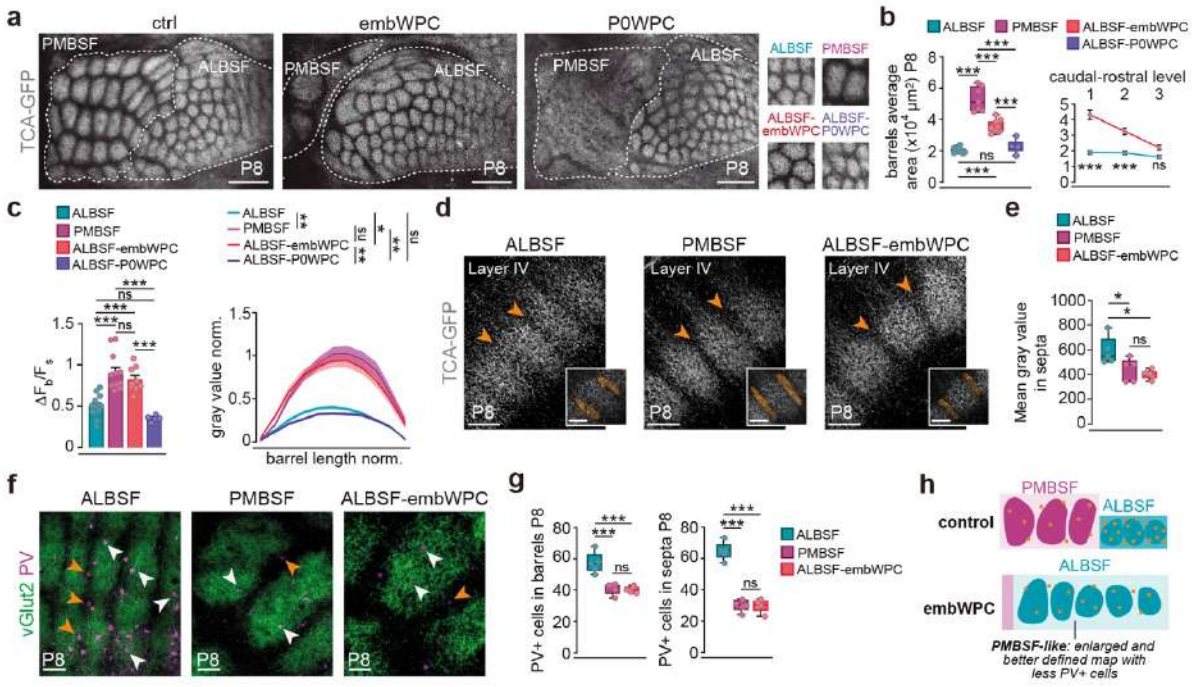

Figure 5. ALBSF barrels acquire PMBSF cortical features. a Cortical flattened tangential sections showing thalamocortical terminals (TCA-GFP+) in the PMBSF and ALBSF in control, embWPC and P0WPC mice at P8. Insets show in detail the clustering of TCAs in each condition. **b** Left, quantification of the average area of 34 barrels (n= 7 ctrl PMBSF, n= 9 ctrl ALBSF, n= 9 embWPC ALBSF, n= 5

P0WPC ALBSF). Right, quantification of the average area of 4 barrels per three caudal-to-rostral levels (n= 9 ctrl ALBSF, n= 9 embWPC ALBSF). **c** Left, quantification of the barrel/septum fluorescence ratio (ΔFb/Fs) (n= 12 ctrl PMBSF, n= 13 ctrl ALBSF, n= 9 embWPC ALBSF, n= 5 P0WPC ALBSF). Right, quantification of the gray value fluorescence intensity in a barrel (n= 66 ctrl PMBSF barrels, n= 65 ctrl ALBSF barrels, n= 42 embWPC ALBSF barrels, n= 25 P0WPC ALBSF barrels). **d** Coronal sections showing thalamocortical terminals in layer IV in the ALBSF and PMBSF of control, and ALBSF of embWPC mice. Insets showing the septa volume analyzed. **e** Quantification of the EGFP expression from TCA in septa of three barrels per animal (orange arrowheads in d) (n= 5 ctrl ALBSF, n= 5 ctrl PMBSF, n= 5 embWPC ALBSF). **f** Cortical flattened tangential sections showing thalamocortical terminals (vGlut2+) and parvalbumin (PV) expression in barrel core (white arrowheads) and septa (orange arrowheads) in the ALBSF and PMBSF of control, and ALBSF of embWPC mice at P8. **g** Quantification of PV+ cells in 4 barrels and septa (n= 5 ctrl ALBSF, n= 5 ctrl PMBSF, n= 5 embWPC ALBSF). **h** Schema illustrating the results. Source data are provided as a Source data file. Scale bars, **a** 500 μm, **d** and **f** 100 μm, **d** (insets) 80 μm. Boxplots show the medians with the interquartile range (box) and range (whiskers). Bar graphs show the means ± SEM. ns, not significant. *$p < 0.05$, **$p < 0.01$, ***$p < 0.001$.

Since thalamocortical input is a primary regulator of region-specific cortical features, we next investigated whether other cortical characteristics, besides barrel size and thalamocortical clustering, had also changed in the ALBSF cortex of the embWPC. The postnatal PMBSF is known to contain fewer parvalbumin (PV) expressing interneurons in layer IV compared to the ALBSF[35]. Like in the PMBSF, we found significantly fewer PV-positive interneurons both in barrels and septa in layer IV of the ALBSF in the embWPC as compared to the ALBSF control (Fig. 5f,g). Hence, our findings demonstrate that, irrespective of receiving input from upper lip peripheral receptors, the VPM territory in embWPC adopts a molecular identity akin to that of a territory receiving input from mystacial whiskers. Consequently, it gains specific features of that circuit, including increased barrel size, better anatomical map definition, and fewer layer IV PV interneurons (Fig. 5h).

Next, we tested whether these anatomical reorganizations might have a functional correlate, as for example an enhanced topographical spatial resolution to upper lip stimulation. Thus, we carried out multi-point stimulations within the whisker pad or upper lip on both control and embWPC mice at P4 (Fig. 6a). On the control mice, cortical evoked responses confirmed a topographic organization of both PMBSF and ALBSF responses; however, while the PMBSF responses exhibited a well-defined and precise organization with virtually non-overlapping responses, those of the ALBSF were broader and less refined in

comparison (Fig. 6b,c; Supplementary Movie 9). Thus, beyond their anatomical idiosyncrasies, cortical barrel sub-fields also have a distinct degree of functional map definition as they emerge during perinatal development. Interestingly, stimulations from distinct locations of the upper lip of embWPC mice resulted in significantly less overlapping responses within the ALBSF (Fig. 6b,c; Supplementary Movie 10), suggesting an enhanced spatial discrimination in the ALBSF of embWPC akin to that seen in the control PMBSF map.

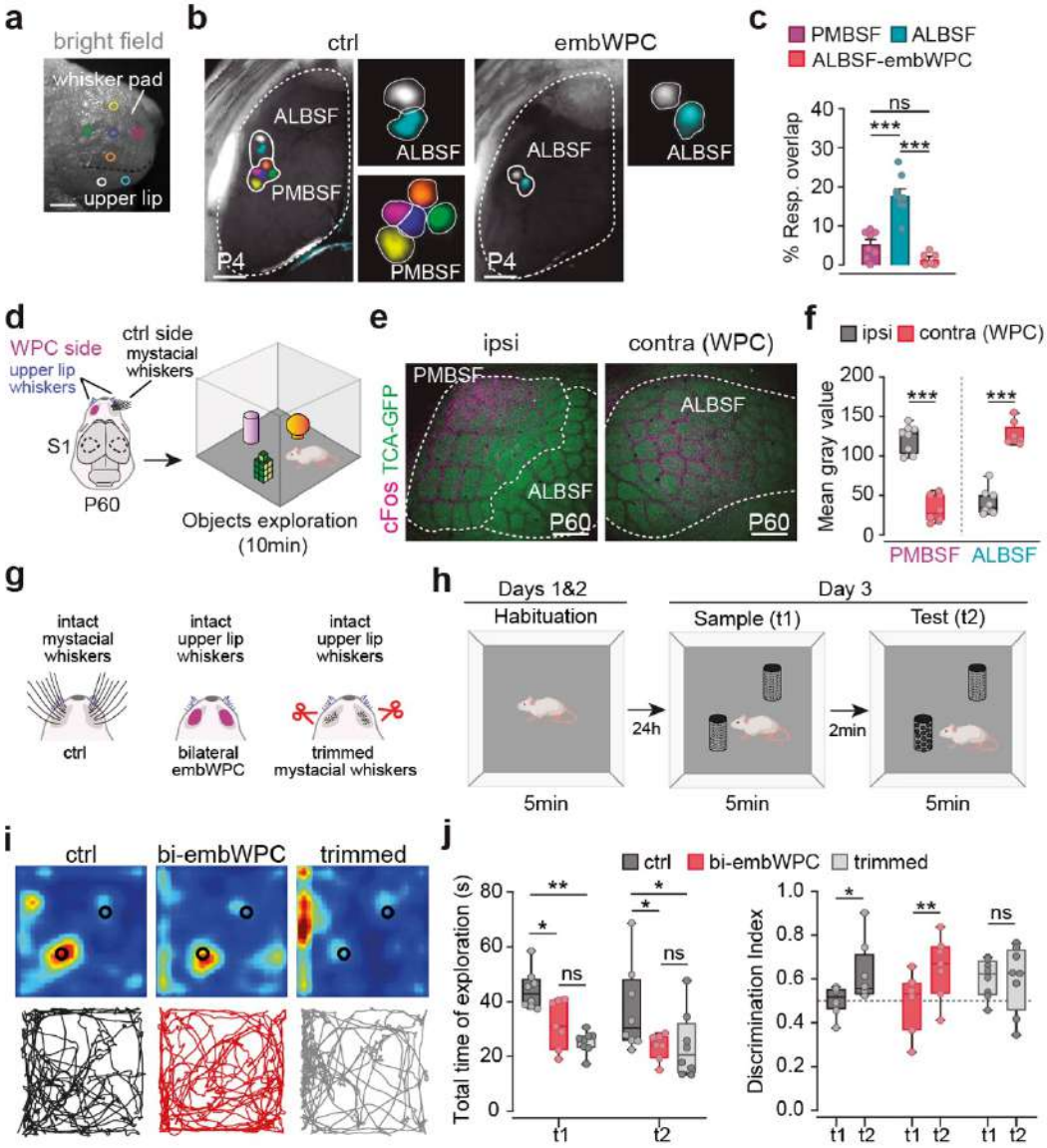

Figure 6. Enhance ALBSF functional map in the postnatal embWPC mice. a Schema representing the experimental paradigm. **b** Cortical evoked responses (GCaMP6f) within the PMBSF and ALBSF to five distinct wps and two distinct uls in control and embWPC mice at P4. Dashed lines define the cortical

hemisphere, and continuous lines indicate the territory covered by elicited responses. **c** Quantification of the percentage of overlap between two distinct PMBSF and two distinct ALBSF responses at P4 (n= 8 ctrl for PMBSF responses, n= 9 ctrl for ALBSF responses, n= 6 embWPC for ALBSF responses). **d** Schema representing the experimental paradigm. **e** Cortical flattened tangential sections showing thalamocortical terminals and cFOS expression in cortical ipsilateral (control) and contralateral (WPC) sides of P60 mice. **f** Quantification of the mean gray value of cFOS expression (n= 8 embWPC ipsi PMBSF, n= 8 embWPC ipsi ALBSF, n= 8 embWPC contra (WPC) PMBSF, n= 8 embWPC contra (WPC) ALBSF). **g** Schematic representation of the three experimental groups involved in the behavioural paradigm: mice with intact whiskers (ctrl n= 8); mice with bilateral whisker pad cauterization at E14 and intact upper-lip whiskers (bi-embWPC n= 7) and mice with trimmed mystacial whiskers and intact upper-lip whiskers (trimmed n= 8). **h** Schema representing the texture discrimination task protocol. **i** Representative heatmaps showing the distribution of snout positions during a 5-minute test session for individual mice from each group (top), along with corresponding centroid trajectories (bottom). Warmer colors in the heatmaps denote regions with higher snout position frequency, highlighting areas of increased exploratory interest. **j** Left, boxplots comparing the total time that control, bi-embWPC and trimmed mice spent exploring textured objects across t_1 and t_2 sessions. Right, evaluation of texture discrimination performance comparing the discrimination index for each session. Source data are provided as a Source data file. Scale bars, **a** 1000 μm and **e** 500 μm. Bar graphs show the means ± SEM. ns, not significant. *p < 0.05, **p < 0.01, ***p < 0.001. Mouse images were created in BioRender. Martini, F. (2025) https://BioRender.com/l19k613

Lastly, we investigated whether the rescaled ALBSF with enhanced resolution of in the embWPC mice takes on PMBSF functions during somatosensory behaviour in adulthood. To do this, we first conducted cFOS staining to label stimulated neurons in the ipsilateral and contralateral barrel sub-fields of embWPC mice after 10 minutes of exploring an enriched environment at P60 (Fig. 6d). Our immunostaining for cFOS revealed that, whereas in the ipsilateral (control) side the ALBSF was barely activated as compared to the PMBSF, the ALBSF was the predominantly activated region in the contralateral (cauterized) side after exploration (Fig. 6e,f). Therefore, we hypothesized that the rescaled ALBSF neurons of the embWPC mouse play a prominent role in vibrissae-driven sensory behaviour in the adult. We conducted a texture discrimination test to evaluate tactile sensory processing, requiring adult mice to distinguish between novel and familiar textures (Fig. 6g,h). We used control mice, bilateral embWPC mice, and an additional control group where mystacial whiskers were bilaterally trimmed prior to testing. Our findings showed that embWPC mice discriminated textures as effectively as controls, while the trimmed group could not discriminate the new texture using only the remaining upper lip whiskers (Fig. 6i,j;

Supplementary Fig. 12). These results suggest that the rescaled ALBSF cortex in embWPC mice can support complex tactile discrimination, a function typically mediated by PMBSF neurons in adult mice under normal conditions.

Discussion

Our study underscores the existence of a prenatal temporal window during mouse brain development that allows for the tuning of the size and definition of somatosensory cortical representations. Before cortical barrel fields are anatomically apparent, the thalamic VPM sub-territories exhibit specific transcriptional signatures at birth. Our results suggest that these signatures contribute to the distinct intra-modal anatomical and functional circuitry features specific to PMBSF and ALBSF cortical sub-territories.

Furthermore, our findings suggest that modulations in these transcription programs might enable intra-modal plasticity changes independently of the type of peripheral receptors. In mice lacking the mystacial whiskers, VPM neurons receiving upper lip whisker input can shift their transcriptional features toward a whisker pad-like program, reconfiguring thalamocortical circuits and cortical features to resemble a PMBSF. These changes increase barrel size and functional spatial resolution, thereby enhancing spatial discrimination in regions such as the ALBSF, where cortical representations were otherwise less defined.

The developmental relationship between sensory receptors and somatosensory representations has been thoroughly examined in prior work involving mice and rats. Embryonic ablation of the forelimb in rats resulted in the expansion of S1 representation of the hindlimb without altering the sensory receptors of the spared peripheral region[36]. Moreover, deprivation of a single whisker or a row of whiskers during the first postnatal week, leads to the loss of the corresponding cortical barrels and enlargement of the surrounding barrels[37-42]. And remarkably, rewiring of ipsilateral trigeminal input from mystacial whiskers to the ipsilateral barrel field generates an ectopic barrel field within the normal barrel map[43]. Collectively, these studies highlight the sensitivity of somatosensory regions and barrel maps to manipulations in peripheral or sensory input but also questioned

a direct correlation between the size of cortical barrels and their corresponding peripheral sensory receptors. Our results in the embWPC model define a developmental window for an intra-modal barrel field reorganization, showing that only embryonic, and not postnatal, ablation of the whisker pad induces the ALBSF anatomical and functional enlargement. This reorganization capability is therefore temporally constrained during prenatal development and anticipates the closure of the critical time window for somatosensory circuits[39,44].

Thalamic spontaneous activity is key for the emergence of cortical somatosensory maps, as evidenced by the fact that suppressing this activity leads to mice that do not develop barrels despite having normal whiskers[21]. Moreover, in early blind pups, cross-modal changes in activity-dependent gene regulation in VPM neurons correlate to changes in barrel size[10]. Here, we observed a striking intra-modal prenatal reorganization of the frequency and pattern of thalamic waves between VPM sub-fields in embWPC mice. The ulVPM significantly increased the frequency of thalamic waves compared to control mice. This change in activity pattern might serve as a mechanism to enhance ulVPM barrel size and definition and, in turn, to map these activity-dependent features onto the cortical ALBSF during development. This hypothesis could not be directly tested, as thalamocortical axons in the embWPC-Th^{Kir} mice, in which spontaneous thalamic waves are blocked, fail to cluster in layer IV in both PMBSF and ALBSF, as previously described in Th^{Kir} mice[21].

Notably, using embWPC, we could show that the enlargement of the cortical ALBSF area is guided by the thalamus in an activity-independent manner. Indeed, in embWPC-Th^{Kir} mice, lacking synchronous thalamic activity, the rescaling of the ALBSF still occurs. Moreover, we show that the PrV input reorganizes in the embWPC VPM. Therefore, we propose that remapping within the PrV, initiated at E14 following whisker pad ablation, may significantly influence the development and organization of thalamocortical axons, subsequently affecting thalamic and cortical map reorganization.

Remarkably, our study revealed that thalamic neurons can shift their transcriptional profile intra-modally. We found that the transcriptional profile of ulVPM neurons in embWPC mice mirrors that of the wpVPM neurons in control mice. Crucial genes for

thalamocortical barrel field development, such as *Rorα* or *Epha4*[26,34], accordingly altered their expression pattern in the ulVPM neurons innervating the ALBSF. For instance, we observed an upregulation of *Rorα* in this region, suggesting a potential role in increasing the density and clustering of axonal terminals in layer IV in the ALBSF of the embWPC mice. An activity-dependent upregulation of *Rorβ*, a related orphan receptor, in VPM neurons has been shown to mediate an increased clustering of thalamic axons in S1[10]. ulVPM neurons adopting a region-specific wpVPM transcriptional profile might serve as an intrinsic mechanism to switch a PMBSF developmental program, ensuring an enhanced anatomical and functional definition of thalamocortical axons in the ALBSF cortical barrel map. Additionally, we identified alterations in genes directly associated with neuronal activity[45,46], including ion channels, which may contribute to or reflect the modified pattern of thalamic activity observed in the embWPC model. Yet, it remains to be determined whether the acquisition of wpVPM-like molecular identity by ulVPM neurons is dependent on thalamic spontaneous activity.

Large barrels in the PMBSF correspond to long mystacial whiskers[12,13], whereas ALBSF barrels relate to the short whiskers on the upper lip of the snout and are comparatively smaller, less defined and densely packed[9,47,48]. Moreover, although the average volume of a single barrel in the ALBSF is smaller than in the PMBSF, the numerical density of parvalbumin (PV)-positive interneurons is higher in ALBSF than in the PMBSF[35]. Somata of PV neurons in the barrels and septa of the ALBSF are reported to receive more vesicular glutamate transporter Type 2–labeled (vGlut2) boutons than those in the PMBSF, suggesting the presence of more potent feedforward inhibitory circuits in the ALBSF[35]. Behaviourally, mystacial vibrissae hold significant behavioural relevance for the animal, being the first ones used for search of objects and gaps, and to discern diverse tactile features such as object position, shape, or texture[49]. Although the function of upper lip shorter whiskers remains largely unexplored, they appear to primarily aid in object discrimination when the snout is near the object[8,50-52]. Given these anatomical and functional disparities, the PMBSF and ALBSF represent two distinct somatosensory subsystems. Consequently, we initially

expected minimal reorganization of the ALBSF upon deprivation of the whiskers corresponding to the PMBSF. However, our data from the embWPC mice revealed a notable anatomical reorganization within the ALBSF, leading to the formation of large and well-defined barrels and a decreased density of PV interneurons at the postnatal life. Additionally, our *in vivo* functional data revealed that this reorganization might contribute to enhance functional resolution of the ALBSF map to point-to-point peripheral stimulations. Our texture discrimination experiments demonstrated that embWPC adult mice, in which the small upper lip whiskers remain intact, can adopt specialized mystacial whiskers functions and discriminate between distinct textures as effectively as control mice.

Altogether, these findings highlight a decoupling of mechanisms governing the type, size, and density of sensory peripheral receptors from those influencing the size and definition of cortical representations that might involve adopting subcortical- and subregion-specific transcriptional programs. Specifically, we observed that the prenatal thalamus possesses plasticity mechanisms to drive the development of a barrel field with anatomical and functional features akin to the PMBSF, regardless of the type of peripheral receptor. Therefore, our findings indicate that the brain may still construct a barrel map capable of processing intricate tactile functions for the animal, even in scenarios involving the availability of only small receptors with subsidiary functions.

References

1. Rakic, P. (1988). Specification of cerebral cortical areas. Science *241*, 170-176. 10.1126/science.3291116.

2. O'Leary, D.D., and Sahara, S. (2008). Genetic regulation of arealization of the neocortex. Curr Opin Neurobiol *18*, 90-100. 10.1016/j.conb.2008.05.011.

3. O'Leary, D.D., Chou, S.J., and Sahara, S. (2007). Area patterning of the mammalian cortex. Neuron *56*, 252-269. 10.1016/j.neuron.2007.10.010.

4. Grove, E.A., and Fukuchi-Shimogori, T. (2003). Generating the cerebral cortical area map. Annu Rev Neurosci *26*, 355-380. 10.1146/annurev.neuro.26.041002.131137.

5. Harris, K.D., and Shepherd, G.M. (2015). The neocortical circuit: themes and variations. Nat Neurosci *18*, 170-181. 10.1038/nn.3917.

6. Welker, C. (1976). Receptive fields of barrels in the somatosensory neocortex of the rat. J Comp Neurol *166*, 173-189. 10.1002/cne.901660205.

7. Diamond, M.E., von Heimendahl, M., Knutsen, P.M., Kleinfeld, D., and Ahissar, E. (2008). 'Where' and 'what' in the whisker sensorimotor system. Nat Rev Neurosci *9*, 601-612. 10.1038/nrn2411.

8. Brecht, M., Preilowski, B., and Merzenich, M.M. (1997). Functional architecture of the mystacial vibrissae. Behav Brain Res *84*, 81-97. 10.1016/s0166-4328(97)83328-1.

9. Woolsey, T.A., and Van der Loos, H. (1970). The structural organization of layer IV in the somatosensory region (SI) of mouse cerebral cortex. The description of a cortical field composed of discrete cytoarchitectonic units. Brain Res *17*, 205-242. 10.1016/0006-8993(70)90079-x.

10. Moreno-Juan, V., Filipchuk, A., Anton-Bolanos, N., Mezzera, C., Gezelius, H., Andres, B., Rodriguez-Malmierca, L., Susin, R., Schaad, O., Iwasato, T., et al. (2017). Prenatal thalamic waves regulate cortical area size prior to sensory processing. Nat Commun *8*, 14172. 10.1038/ncomms14172.

11. Lopez-Bendito, G., Anibal-Martinez, M., and Martini, F.J. (2022). Cross-Modal Plasticity in Brains Deprived of Visual Input Before Vision. Annu Rev Neurosci *45*, 471-489. 10.1146/annurev-neuro-111020-104222.
12. Gaspar, P., and Erzurumlu, R. (2013). The Birth of the Barrels. Developmental Cell *27*, 3-4. 10.1016/j.devcel.2013.09.028.
13. Erzurumlu, R.S., and Gaspar, P. (2020). How the Barrel Cortex Became a Working Model for Developmental Plasticity: A Historical Perspective. The Journal of Neuroscience *40*, 6460-6473. 10.1523/jneurosci.0582-20.2020.
14. Mizuno, H., Luo, W., Tarusawa, E., Saito, Y.M., Sato, T., Yoshimura, Y., Itohara, S., and Iwasato, T. (2014). NMDAR-regulated dynamics of layer 4 neuronal dendrites during thalamocortical reorganization in neonates. Neuron *82*, 365-379. 10.1016/j.neuron.2014.02.026.
15. Laumonnerie, C., Bechara, A., Vilain, N., Kurihara, Y., Kurihara, H., and Rijli, F.M. (2015). Facial whisker pattern is not sufficient to instruct a whisker-related topographic map in the mouse somatosensory brainstem. Development *142*, 3704-3712. 10.1242/dev.128736.
16. Ozdinler, P.H., and Erzurumlu, R.S. (2002). Slit2, a branching-arborization factor for sensory axons in the Mammalian CNS. J Neurosci *22*, 4540-4549. 10.1523/JNEUROSCI.22-11-04540.2002.
17. Oury, F., Murakami, Y., Renaud, J.S., Pasqualetti, M., Charnay, P., Ren, S.Y., and Rijli, F.M. (2006). Hoxa2- and rhombomere-dependent development of the mouse facial somatosensory map. Science *313*, 1408-1413. 10.1126/science.1130042.
18. Kitazawa, T., and Rijli, F.M. (2018). Barrelette map formation in the prenatal mouse brainstem. Curr Opin Neurobiol *53*, 210-219. 10.1016/j.conb.2018.09.008.
19. Bechara, A., Laumonnerie, C., Vilain, N., Kratochwil, C.F., Cankovic, V., Maiorano, N.A., Kirschmann, M.A., Ducret, S., and Rijli, F.M. (2015). Hoxa2 Selects Barrelette Neuron Identity and Connectivity in the Mouse Somatosensory Brainstem. Cell Rep *13*, 783-797. 10.1016/j.celrep.2015.09.031.

20. Zembrzycki, A., Chou, S.J., Ashery-Padan, R., Stoykova, A., and O'Leary, D.D. (2013). Sensory cortex limits cortical maps and drives top-down plasticity in thalamocortical circuits. Nat Neurosci *16*, 1060-1067. 10.1038/nn.3454.

21. Anton-Bolanos, N., Sempere-Ferrandez, A., Guillamon-Vivancos, T., Martini, F.J., Perez-Saiz, L., Gezelius, H., Filipchuk, A., Valdeolmillos, M., and Lopez-Bendito, G. (2019). Prenatal activity from thalamic neurons governs the emergence of functional cortical maps in mice. Science *364*, 987-990. 10.1126/science.aav7617.

22. Guillamon-Vivancos, T., Anibal-Martinez, M., Puche-Aroca, L., Moreno-Bravo, J.A., Valdeolmillos, M., Martini, F.J., and Lopez-Bendito, G. (2022). Input-dependent segregation of visual and somatosensory circuits in the mouse superior colliculus. Science *377*, 845-850. 10.1126/science.abq2960.

23. Frangeul, L., Pouchelon, G., Telley, L., Lefort, S., Luscher, C., and Jabaudon, D. (2016). A cross-modal genetic framework for the development and plasticity of sensory pathways. Nature *538*, 96-98. 10.1038/nature19770.

24. Pouchelon, G., Gambino, F., Bellone, C., Telley, L., Vitali, I., Luscher, C., Holtmaat, A., and Jabaudon, D. (2014). Modality-specific thalamocortical inputs instruct the identity of postsynaptic L4 neurons. Nature *511*, 471-474. 10.1038/nature13390.

25. Ono, K., Clavairoly, A., Nomura, T., Gotoh, H., Uno, A., Armant, O., Takebayashi, H., Zhang, Q., Shimamura, K., Itohara, S., et al. (2014). Development of the prethalamus is crucial for thalamocortical projection formation and is regulated by Olig2. Development *141*, 2075-2084. 10.1242/dev.097790.

26. Vitalis, T., Dauphinot, L., Gressens, P., Potier, M.C., Mariani, J., and Gaspar, P. (2018). RORalpha Coordinates Thalamic and Cortical Maturation to Instruct Barrel Cortex Development. Cereb Cortex *28*, 3994-4007. 10.1093/cercor/bhx262.

27. Gezelius, H., and Lopez-Bendito, G. (2017). Thalamic neuronal specification and early circuit formation. Dev Neurobiol *77*, 830-843. 10.1002/dneu.22460.

28. Rubenstein, J., Anderson, S., Shi, L., Miyashita-Lin, E., Bulfone, A., and Hevner, R. (1999). Genetic control of cortical regionalization and connectivity. Cereb Cortex *9*, 524-532.

29. Mercurio, S., Serra, L., Motta, A., Gesuita, L., Sanchez-Arrones, L., Inverardi, F., Foglio, B., Barone, C., Kaimakis, P., Martynoga, B., et al. (2019). Sox2 Acts in Thalamic Neurons to Control the Development of Retina-Thalamus-Cortex Connectivity. iScience *15*, 257-273. 10.1016/j.isci.2019.04.030.

30. Nakagawa, Y., and O'Leary, D.D. (2003). Dynamic patterned expression of orphan nuclear receptor genes RORalpha and RORbeta in developing mouse forebrain. Dev Neurosci *25*, 234-244. 10.1159/000072271.

31. Yuge, K., Kataoka, A., Yoshida, A.C., Itoh, D., Aggarwal, M., Mori, S., Blackshaw, S., and Shimogori, T. (2011). Region-specific gene expression in early postnatal mouse thalamus. J Comp Neurol *519*, 544-561. 10.1002/cne.22532.

32. Ebisu, H., Iwai-Takekoshi, L., Fujita-Jimbo, E., Momoi, T., and Kawasaki, H. (2017). Foxp2 Regulates Identities and Projection Patterns of Thalamic Nuclei During Development. Cereb Cortex *27*, 3648-3659. 10.1093/cercor/bhw187.

33. Puelles, L., Sanchez, M.P., Spreafico, R., and Fairen, A. (1992). Prenatal development of calbindin immunoreactivity in the dorsal thalamus of the rat. Neuroscience *46*, 135-147. 10.1016/0306-4522(92)90013-r.

34. Dufour, A., Seibt, J., Passante, L., Depaepe, V., Ciossek, T., Frisen, J., Kullander, K., Flanagan, J., Polleux, F., and Vanderhaeghen, P. (2003). Area specificity and topography of thalamocortical projections are controlled by ephrin/Eph genes. Neuron *39*, 453-465. S0896627303004409 [pii].

35. Shigematsu, N., Miyamoto, Y., Esumi, S., and Fukuda, T. (2024). The Anterolateral Barrel Subfield Differs from the Posteromedial Barrel Subfield in the Morphology and Cell Density of Parvalbumin-Positive GABAergic Interneurons. eNeuro *11*. 10.1523/ENEURO.0518-22.2024.

36. Killackey, H.P., and Dawson, D.R. (1989). Expansion of the Central Hindpaw Representation Following Fetal Forelimb Removal in the Rat. Eur J Neurosci *1*, 210-221. 10.1111/j.1460-9568.1989.tb00790.x.
37. Van der Loos, H., and Woolsey, T.A. (1973). Somatosensory cortex: structural alterations following early injury to sense organs. Science *179*, 395-398. 10.1126/science.179.4071.395.
38. Killackey, H.P., and Belford, G.R. (1979). The formation of afferent patterns in the somatosensory cortex of the neonatal rat. J Comp Neurol *183*, 285-303. 10.1002/cne.901830206.
39. Woolsey, T.A., Anderson, J.R., Wann, J.R., and Stanfield, B.B. (1979). Effects of early vibrissae damage on neurons in the ventrobasal (VB) thalamus of the mouse. J Comp Neurol *184*, 363-380. 10.1002/cne.901840210.
40. Belford, G.R., and Killackey, H.P. (1979). The development of vibrissae representation in subcortical trigeminal centers of the neonatal rat. J Comp Neurol *188*, 63-74. 10.1002/cne.901880106.
41. Woolsey, T.A., and Wann, J.R. (1976). Areal changes in mouse cortical barrels following vibrissal damage at different postnatal ages. J Comp Neurol *170*, 53-66. 10.1002/cne.901700105.
42. Killackey, H.P., Belford, G., Ryugo, R., and Ryugo, D.K. (1976). Anomalous organization of thalamocortical projections consequent to vibrissae removal in the newborn rat and mouse. Brain Res *104*, 309-315. 10.1016/0006-8993(76)90623-5.
43. Renier, N., Dominici, C., Erzurumlu, R.S., Kratochwil, C.F., Rijli, F.M., Gaspar, P., and Chedotal, A. (2017). A mutant with bilateral whisker to barrel inputs unveils somatosensory mapping rules in the cerebral cortex. Elife *6*. 10.7554/eLife.23494.
44. Belford, G.R., and Killackey, H.P. (1980). The sensitive period in the development of the trigeminal system of the neonatal rat. J Comp Neurol *193*, 335-350. 10.1002/cne.901930203.

45. Martini, F.J., Guillamon-Vivancos, T., Moreno-Juan, V., Valdeolmillos, M., and Lopez-Bendito, G. (2021). Spontaneous activity in developing thalamic and cortical sensory networks. Neuron *109*, 2519-2534. 10.1016/j.neuron.2021.06.026.

46. Mire, E., Mezzera, C., Leyva-Díaz, E., Paternain, A.V., Squarzoni, P., Bluy, L., Castillo-Paterna, M., López, M.J., Peregrín, S., Tessier-Lavigne, M., et al. (2012). Spontaneous activity regulates Robo1 transcription to mediate a switch in thalamocortical axon growth. Nat Neurosci *15*, 1134-1143. 10.1038/nn.3160.

47. Land, P.W., and Simons, D.J. (1985). Cytochrome oxidase staining in the rat SmI barrel cortex. J Comp Neurol *238*, 225-235. 10.1002/cne.902380209.

48. Jan, T.A., Lu, L., Li, C.X., Williams, R.W., and Waters, R.S. (2008). Genetic analysis of posterior medial barrel subfield (PMBSF) size in somatosensory cortex (SI) in recombinant inbred strains of mice. BMC Neurosci *9*, 3. 10.1186/1471-2202-9-3.

49. Kleinfeld, D., Ahissar, E., and Diamond, M.E. (2006). Active sensation: insights from the rodent vibrissa sensorimotor system. Curr Opin Neurobiol *16*, 435-444. 10.1016/j.conb.2006.06.009.

50. Grant, R.A., Sperber, A.L., and Prescott, T.J. (2012). The role of orienting in vibrissal touch sensing. Front Behav Neurosci *6*, 39. 10.3389/fnbeh.2012.00039.

51. Kuruppath, P., Gugig, E., and Azouz, R. (2014). Microvibrissae-based texture discrimination. J Neurosci *34*, 5115-5120. 10.1523/JNEUROSCI.4217-13.2014.

52. Morita, T., Kang, H., Wolfe, J., Jadhav, S.P., and Feldman, D.E. (2011). Psychometric curve and behavioral strategies for whisker-based texture discrimination in rats. PLoS One *6*, e20437. 10.1371/journal.pone.0020437.

53. Gorski, J.A., Talley, T., Qiu, M., Puelles, L., Rubenstein, J.L., and Jones, K.R. (2002). Cortical excitatory neurons and glia, but not GABAergic neurons, are produced in the Emx1-expressing lineage. J Neurosci *22*, 6309-6314. 10.1523/JNEUROSCI.22-15-06309.2002.

54. Chen, L., Guo, Q., and Li, J. (2009). Transcription factor Gbx2 acts cell-nonautonomously to regulate the formation of lineage-restriction boundaries of the thalamus. Development *136*, 1317-1326. 10.1242/dev.030510.

55. Franco, S.J., Gil-Sanz, C., Martinez-Garay, I., Espinosa, A., Harkins-Perry, S.R., Ramos, C., and Muller, U. (2012). Fate-restricted neural progenitors in the mammalian cerebral cortex. Science *337*, 746-749. 10.1126/science.1223616.

56. Voiculescu, O., Charnay, P., and Schneider-Maunoury, S. (2000). Expression pattern of a Krox-20/Cre knock-in allele in the developing hindbrain, bones, and peripheral nervous system. Genesis *26*, 123-126. 10.1002/(sici)1526-968x(200002)26:2<123::aid-gene7>3.0.co;2-o.

57. Madisen, L., Garner, A.R., Shimaoka, D., Chuong, A.S., Klapoetke, N.C., Li, L., van der Bourg, A., Niino, Y., Egolf, L., Monetti, C., et al. (2015). Transgenic mice for intersectional targeting of neural sensors and effectors with high specificity and performance. Neuron *85*, 942-958. 10.1016/j.neuron.2015.02.022.

58. Renier, N., Wu, Z., Simon, D.J., Yang, J., Ariel, P., and Tessier-Lavigne, M. (2014). iDISCO: a simple, rapid method to immunolabel large tissue samples for volume imaging. Cell *159*, 896-910. 10.1016/j.cell.2014.10.010.

59. Renier, N., Adams, E.L., Kirst, C., Wu, Z., Azevedo, R., Kohl, J., Autry, A.E., Kadiri, L., Umadevi Venkataraju, K., Zhou, Y., et al. (2016). Mapping of Brain Activity by Automated Volume Analysis of Immediate Early Genes. Cell *165*, 1789-1802. 10.1016/j.cell.2016.05.007.

60. Madisen, L., Zwingman, T.A., Sunkin, S.M., Oh, S.W., Zariwala, H.A., Gu, H., Ng, L.L., Palmiter, R.D., Hawrylycz, M.J., Jones, A.R., et al. (2010). A robust and high-throughput Cre reporting and characterization system for the whole mouse brain. Nat Neurosci *13*, 133-140. 10.1038/nn.2467.

61. James B. Ackman, H.Z., Michael C. Crair (2014). Structured dynamics of neural activity across developing neocortex. Preprint at bioRxiv. 10.1101/012237.

62. Herrero-Navarro, A., Puche-Aroca, L., Moreno-Juan, V., Sempere-Ferrandez, A., Espinosa, A., Susin, R., Torres-Masjoan, L., Leyva-Diaz, E., Karow, M., Figueres-Onate, M., et al. (2021). Astrocytes and neurons share region-specific transcriptional signatures that confer regional identity to neuronal reprogramming. Sci Adv *7*. 10.1126/sciadv.abe8978.

63. Dobin, A., Davis, C.A., Schlesinger, F., Drenkow, J., Zaleski, C., Jha, S., Batut, P., Chaisson, M., and Gingeras, T.R. (2013). STAR: ultrafast universal RNA-seq aligner. Bioinformatics *29*, 15-21. 10.1093/bioinformatics/bts635.

64. Love, M.I., Huber, W., and Anders, S. (2014). Moderated estimation of fold change and dispersion for RNA-seq data with DESeq2. Genome Biol *15*, 550. 10.1186/s13059-014-0550-8.

65. Huber, W., Carey, V.J., Gentleman, R., Anders, S., Carlson, M., Carvalho, B.S., Bravo, H.C., Davis, S., Gatto, L., Girke, T., et al. (2015). Orchestrating high-throughput genomic analysis with Bioconductor. Nat Methods *12*, 115-121. 10.1038/nmeth.3252.

66. Zhu, A., Srivastava, A., Ibrahim, J.G., Patro, R., and Love, M.I. (2019). Nonparametric expression analysis using inferential replicate counts. Nucleic Acids Res *47*, e105. 10.1093/nar/gkz622.

67. Gu, Z., and Hubschmann, D. (2023). simplifyEnrichment: A Bioconductor Package for Clustering and Visualizing Functional Enrichment Results. Genomics Proteomics Bioinformatics *21*, 190-202. 10.1016/j.gpb.2022.04.008.

68. Yu, G., Wang, L.G., Han, Y., and He, Q.Y. (2012). clusterProfiler: an R package for comparing biological themes among gene clusters. OMICS *16*, 284-287. 10.1089/omi.2011.0118.

69. Wu, H.P., Ioffe, J.C., Iverson, M.M., Boon, J.M., and Dyck, R.H. (2013). Novel, whisker-dependent texture discrimination task for mice. Behav Brain Res *237*, 238-242. 10.1016/j.bbr.2012.09.044.

70. Benamer, N., Vidal, M., Balia, M., and Angulo, M.C. (2020). Myelination of parvalbumin interneurons shapes the function of cortical sensory inhibitory circuits. Nat Commun *11*, 5151. 10.1038/s41467-020-18984-7.

71. Balasco, L., Pagani, M., Pangrazzi, L., Chelini, G., Viscido, F., Chama, A.G.C., Galbusera, A., Provenzano, G., Gozzi, A., and Bozzi, Y. (2022). Somatosensory cortex hyperconnectivity and impaired whisker-dependent responses in Cntnap2(-/-) mice. Neurobiol Dis *169*, 105742. 10.1016/j.nbd.2022.105742.

Acknowledgements

We thank Belén Andrés and María Aurelia Torregrosa for their technical support. We thank Teresa Guillamón-Vivancos and Miguel Valdeolmillos for their comments and input on the manuscript and other members of López-Bendito's laboratory for stimulating discussions. This work was supported by grants from the Swiss National Science Foundation (31003A_175776 and 310030_219370) and the Novartis Research Foundation to F.M.R., and by grants from the European Research Council (ERC) under the European Union's Horizon 2020 research and innovation programme (ERC-2021-ADG-101054313 SPONTSENSE), PID2021-127112NB-I00 from the MCIN/AEI /10.13039/501100011033/ and ERDF A way to make Europe, and Generalitat Valenciana, Conselleria d'Educació, Universitats, i Ocupació (PROMETEO 2021/052) to G.L.-B.

Author contributions

Conceptualization, M.A-M. and G.L-B.; methodology, M.A-M., E.P-M., G.P., MP.M. and LM.R-M; data curation, M.A-M., E.P-M., G.P., MP.M. and L.P.; transcriptomic analysis, L.P.; writing – original draft, M.A-M., and G.L-B.; writing – review & editing, M.A-M., L.P., E.P-M., G.P., FJ.M., FM.R., and G.L-B.; funding acquisition, FM.R., and G.L-B.; resources, FM.R., and G.L-B.; supervision, FJ.M., FM.R., and G.L-B.

Competing interests

The authors declare no competing interests.

Supplementary Information

A prenatal window for enhancing spatial resolution of cortical barrel maps

Mar Aníbal-Martínez[1], Lorenzo Puche-Aroca[1], Elena Pérez-Montoyo[1], Gabriele Pumo[2,3], M. Pilar Madrigal[4], Luis M. Rodríguez-Malmierca[1], Francisco J. Martini[1], Filippo M. Rijli[2,3], Guillermina López-Bendito[1,*]

[1]Instituto de Neurociencias de Alicante, Universidad Miguel Hernández-Consejo Superior de Investigaciones Científicas (UMH-CSIC), San Juan de Alicante, Alicante, Spain.
[2] Friedrich Miescher Institute for Biomedical Research, Fabrikstrasse 24, 4056 Basel, Switzerland.
[3]University of Basel, Basel, Switzerland.
[4]Departamento de Histología y Anatomía, Facultad de Medicina, Universidad Miguel Hernández (UMH), San Juan de Alicante, Alicante, Spain.

*Correspondence: g.lbendito@umh.es (G.L-B)

Nature Communications March 2025: 16, no. 1955. DOI: 10.1038/s41467-025-57052-w. https://www.nature.com/articles/s41467-025-57052-w

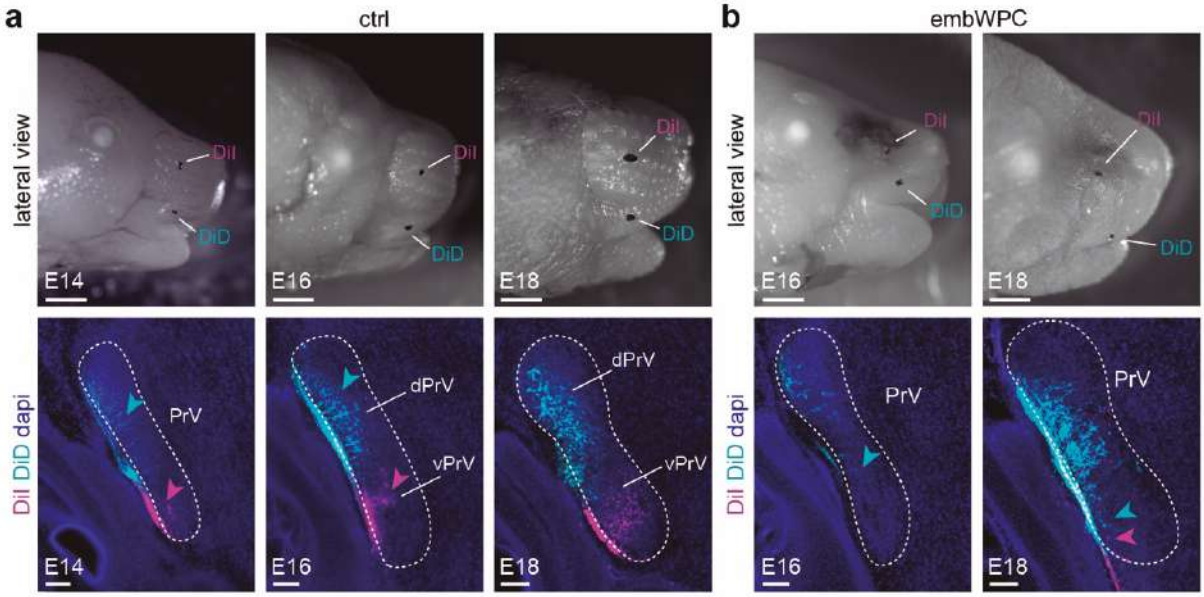

Supplementary Fig. 1. Early reorganization of peripheral axons at the trigeminal nucleus. a Upper panels, lateral views of control mouse heads showing DiI and DiD crystal placements in the whisker pad and upper lip, respectively, at distinct developmental stages (E14, E16 and E18). Lower panels, coronal sections showing labelled axons at the vPrV (magenta, arrowheads) and dPrV (cyan, arrowheads) (n= 6 mice at E14, n= 9 mice at E16, n= 6 mice at E18). **b** Upper panels, lateral views of embWPC mouse heads showing DiI and DiD crystal placements in the whisker pad and upper lip, respectively, at distinct developmental stages (E16 and E18). Lower panels, coronal sections showing displaced upper lip axons at the vPrV (cyan, arrowheads) and a few axons from the whisker pad scar sparsely innervating the vPrV (magenta, arrowheads) (n= 9 embWPC at E16, n= 5 embWPC at E18). E, embryonic; embWPC, embryonic whisker pad cauterized; PrV, principal nucleus; vPrV, ventral principal nucleus; dPrV, dorsal principal nucleus; DiI, 1,1'-dioctadecyl 3,3,3',3'-tetramethylindocarbocyanine perchlorate; DiD, 1,1'-Dioctadecyl-3,3,3',3'-Tetramethylindodicarbocyanine, 4-Chlorobenzenesulfonate. Scale bars, **a** (top) and **b** (top) 1000 μm; **a** (bottom) and **b** (bottom) 100 μm.

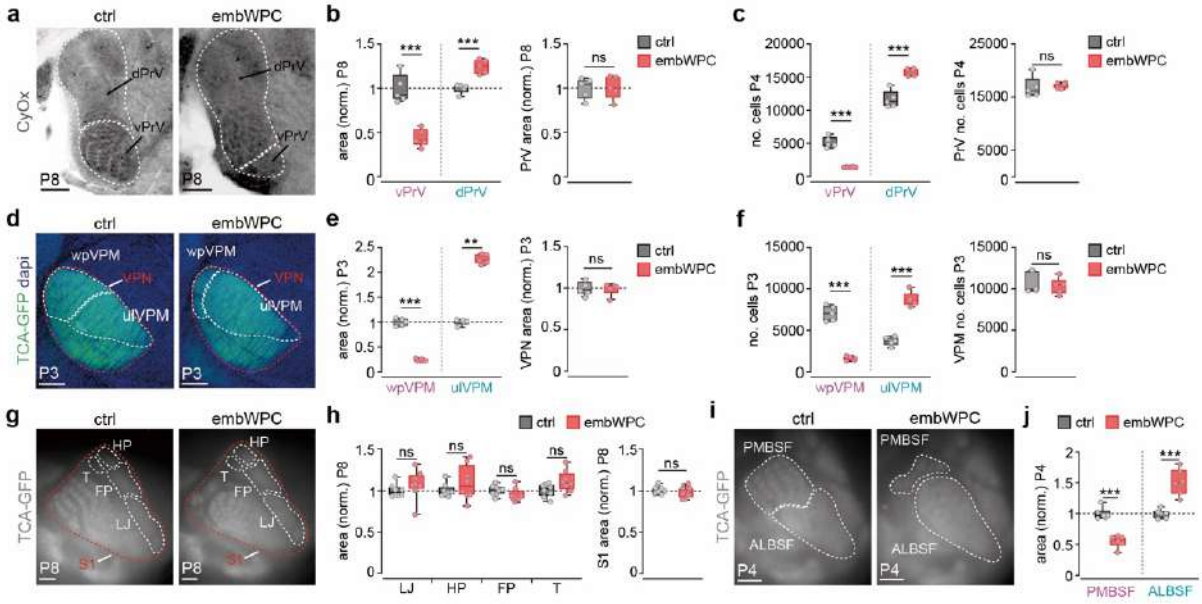

Supplementary Fig. 2. Intra-modal rescaling of facial whiskers representations in cortical and subcortical territories in embWPC mice. a Coronal sections of the trigeminal PrV nucleus stained with CyOx at P8. **b** Quantification of the data (n= 5 ctrl, n= 5 embWPC, vPrV and dPrV areas, unpaired two-tailed Student *t*-test; PrV area, unpaired two-tailed Student *t*-test. ns, $p > 0.9$). **c** Quantification of the number of cells in PrV at P4 (n= 5 ctrl, n= 5 embWPC, vPrV and dPrV areas, unpaired two-tailed Student *t*-test; PrV area, unpaired two-tailed Student *t*-test. ns, p= 0.66). **d** Coronal sections showing TCA-GFP labelling in the PMBSF, ALBSF and VPN at P3. **e** Quantification of the data (n= 5 ctrl, n= 5 embWPC, PMBSF, unpaired two-tailed Student *t*-test. ALBSF, two-tailed Mann-Whitney *U*-test; VPN at P3, n= 5 ctrl, n= 5 embWPC, two-tailed Mann-Whitney *U*-test. ns, $p > 0.99$). **f** Quantification of the number of cells in VPM at P3 (n= 5 ctrl, n= 5 embWPC, wpVPM and ulVPM areas, unpaired two-tailed Student *t*-test; VPM area, unpaired two-tailed Student *t*-test. ns, p= 0.57). **g** Surface view of thalamocortical terminals (TCA-GFP+) in the PMBSF and ALBSF at P8. **h** Quantification of the data (n= 8 ctrl, n= 8 embWPC, unpaired two-tailed Student *t*-test. ns, $p > 0.05$. S1 area, n= 8 ctrl, n= 9 embWPC, unpaired two-tailed Student *t*-test. ns, p= 0.29). **i** Surface view of thalamocortical terminals (TCA-GFP+) in the PMBSF and ALBSF at P4. **j** Quantification of the data (n= 6 ctrl, n= 6 embWPC, unpaired two-tailed Student *t*-test; ***$p < 0.001$). Source data are provided as a Source data file. CyOx, Cytochrome oxidase; P, postnatal; wpVPM, whisker pad recipient ventral posteromedial nucleus; ulVPM, upper lip recipient ventral posteromedial nucleus; VPN, ventroposterior nucleus; TCA-GFP, thalamocortical axons labelled with green fluorescent protein; S1, primary somatosensory cortex; HP, hindpaw; FP, forepaw; LJ, lowerjaw; T, trunk; PMBSF, postero-medial barrel subfield; ALBSF, antero-lateral barrel subfield; norm., normalized. Scale bars, **a** and **d** 200 μm; **g** and **i** 500 μm. Boxplots show the medians with the interquartile range (box) and range (whiskers). ns, not significant. **$p < 0.01$, ***$p < 0.001$.

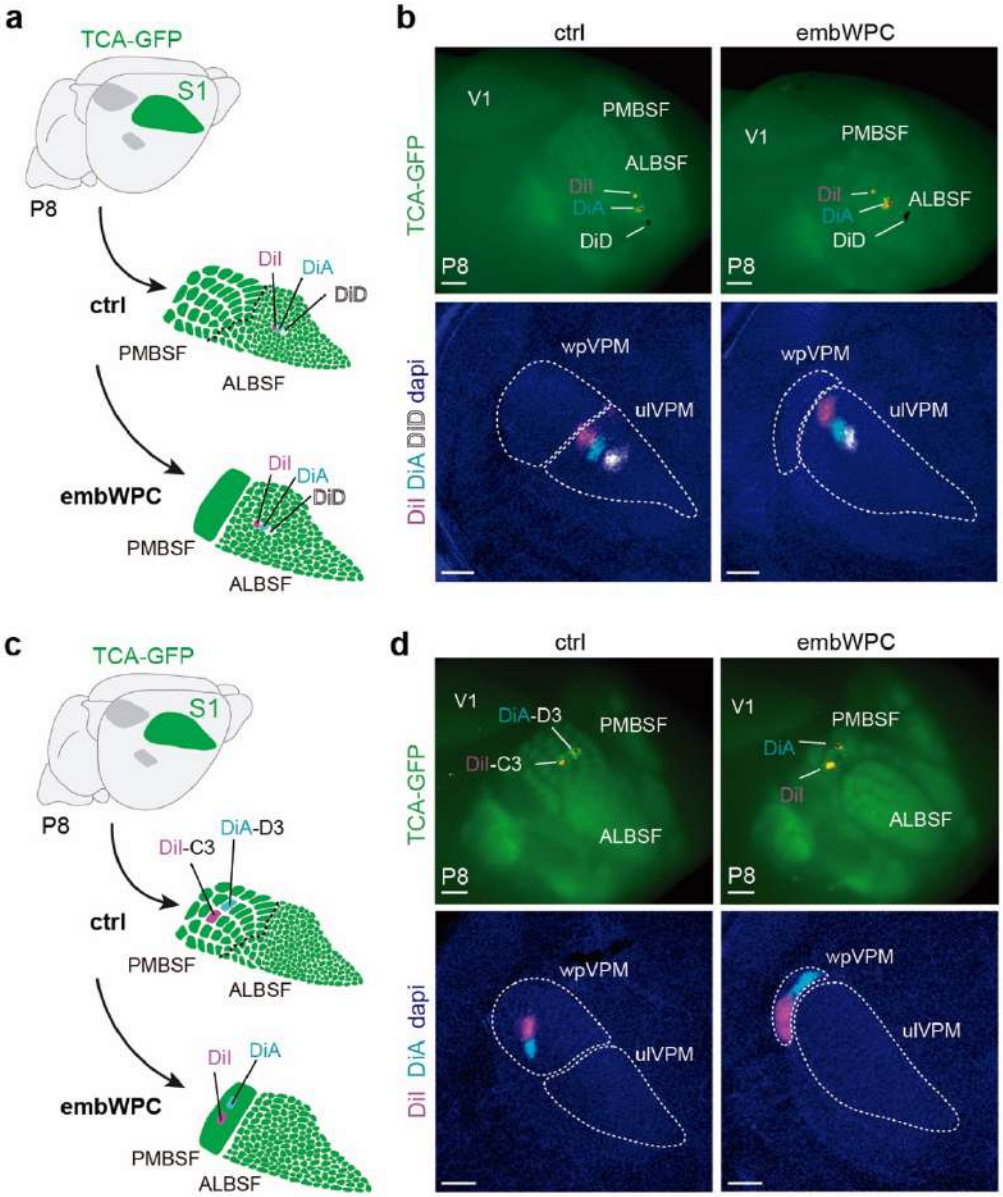

Supplementary Fig. 3. Thalamocortical point-to-point topography in embWPC mice. a Schema representing the experimental paradigm. **b** Upper panels, DiI, DiA and DiD crystal placements subsequent non-overlapping points in the ALBSF in control and embWPC at P8. Lower panels, backlabelled cells at the ulVPM showed a shifted relative displacement toward the wpVPM in embWPC mice (n= 8 ctrl, n= 8 embWPC). **c** Schema representing the experimental paradigm. **d** Upper panels, DiI and DiA crystal placements in the C3 and D3 cortical barrels, respectively, in PMBSF control and in the remaining territory of the PMBSF in embWPC at P8. Lower panels, backlabelled cells maintain their point-to-point distribution at the wpVPM both in control and embWPC mice (n= 9 ctrl, n= 9 mice). V1, primary visual cortex; DiA, 4-[4-(dihexadecylamino) styryl]-N-methylpyridinium iodide. Scale bars, **b** and **d** (top) 500 μm; **b** and **d** (bottom) 200 μm.

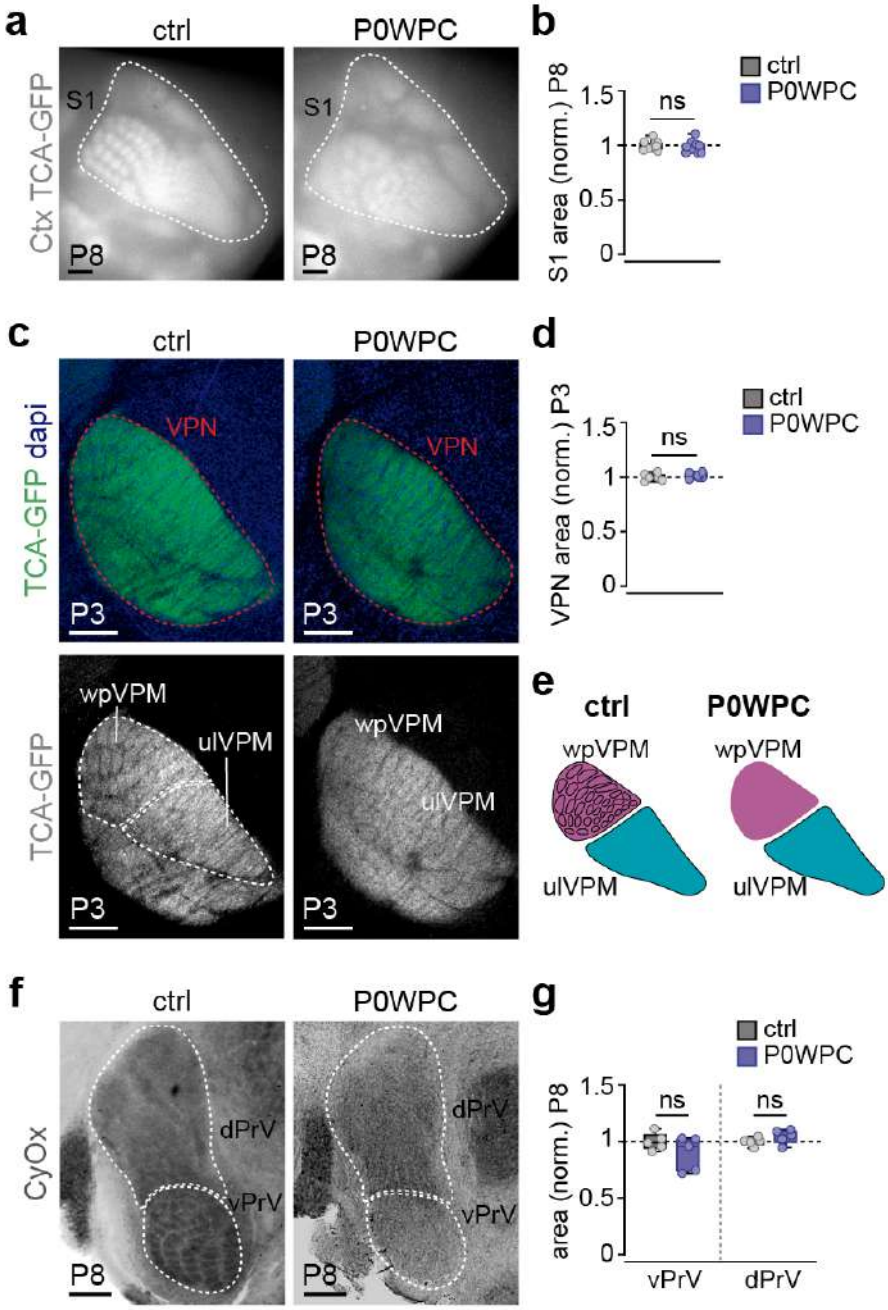

Supplementary Fig. 4. Cortical and subcortical areas for facial whiskers representations remained unchanged in P0WPC mice. a Surface view of thalamocortical terminals (TCA-GFP+) in the cortical S1 in control and P0WPC mice at P8. **b** Quantification of the total S1 area (n= 8 ctrl, n= 9 P0WPC, unpaired two-tailed Student *t*-test. ns, p= 0.66). **c** Coronal sections showing TCA-GFP labelling in the wpVPM, ulVPM and VPN of the thalamus in control and P0WPC at P3. **d** Quantification of the VPN area (n= 8 ctrl, n= 9 P0WPC, unpaired two-tailed Student *t*-test. ns, p= 0.39). **e** schema representing the results. **f** Coronal sections of the trigeminal PrV nucleus stained with CyOx in control and P0WPC at P8. **g** Quantification of the vPrV and dPrV area (n= 5 ctrl, n= 5 P0WPC, unpaired two-tailed Student *t*-test. ns, p> 0.20). Source data are provided as a Source data file. P0WPC, postnatal day 0 whisker pad cauterized. Scale bars, **a** 500 μm; **c** and **f** 200 μm. Boxplots show the medians with the interquartile range (box) and range (whiskers). ns, not significant.

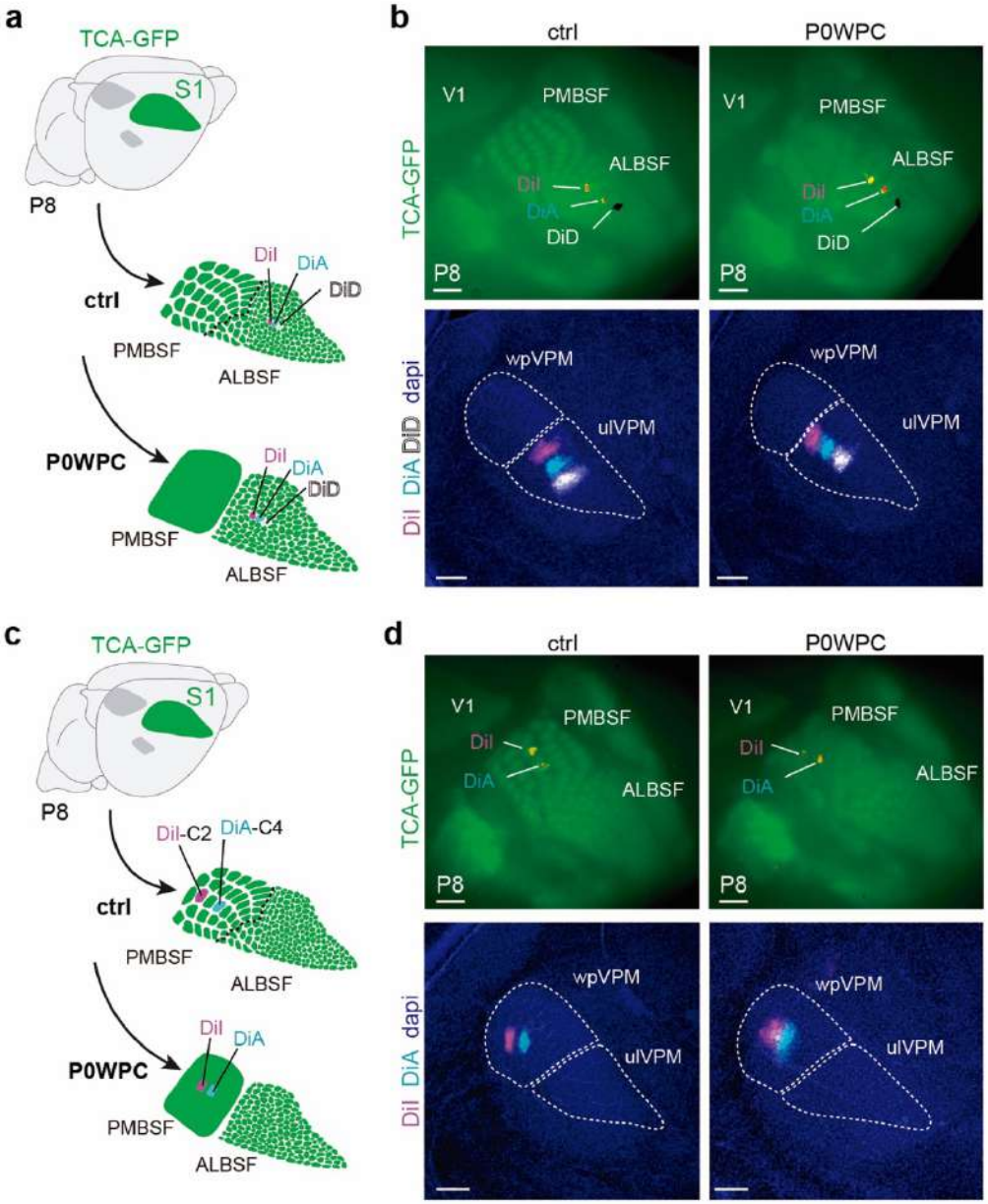

Supplementary Fig. 5. Thalamocortical point-to-point topography in P0WPC mice. a Schema representing the experimental paradigm. **b** Upper panels, DiI, DiA and DiD crystal placements subsequent non-overlapping positions in the ALBSF in control and P0WPC at P8. Lower panels, backlabelled cells at the ulVPM (n= 7 ctrl, n= 7 P0WPC). **c** Schema representing the experimental paradigm. **d** Upper panels, DiI and DiA crystal placements in the C2 and C4 cortical barrels, respectively, in control and in the deprived PMBSF territory in P0WPC at P8. Lower panels, backlabelled cells showing their point-to-point distribution at the wpVPM in control and P0WPC mice (n= 7 ctrl, n= 7 P0WPC). Scale bars, **b** (top) and **d** (top) 500 μm; **b** (bottom) and **d** (bottom) 200 μm.

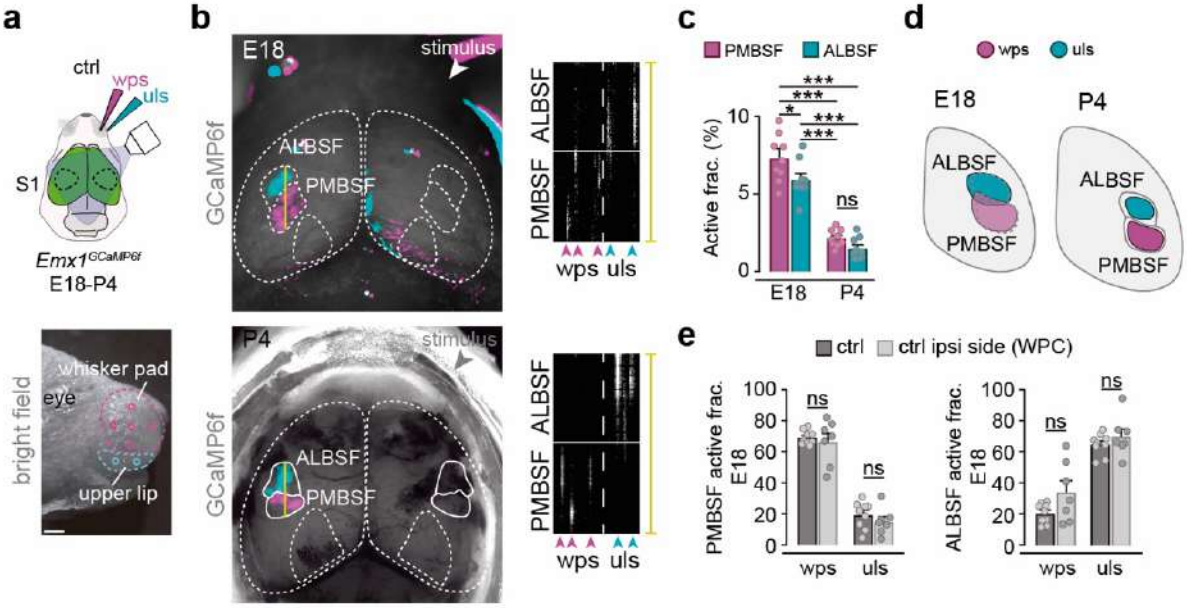

Supplementary Fig. 6. Intra-modal responses in control mice after whisker pad and upper-lip stimulations. a Top, schema representing the experimental paradigm. Bottom, Image of a mouse snout denoting the stimulations sites**. b** Left panels, cortical evoked responses (GCaMP6f) to whisker pad (magenta) and upper lip (cyan) stimulations in control mice at E18 and P4. Right, reslices of the yellow line in the left, representing responses elicited in PMBSF and ALBSF by whisker pad stimulation (wps) or upper lip stimulations (uls). The white horizontal line delineates the boundaries between PMBSF and ALBSF, while the vertical dashed line divides the wps from the uls over time. The arrows label the stimulation times for whisker pad (magenta) and upper lip (cyan). **c** Quantification of the cortical hemisphere active fraction evoked to wps (PMBSF) or uls (ALBSF) (n= 9 ctrl at E18, n= 9 ctrl at P4, Two-way ANOVA test: ***p <0.001. Tukey's multiple comparison test post-hoc analysis, ns, p= 0.55). **d** Schema illustrating the results found. **e** Quantification of the PMBSF and ALBSF active fraction to wps and uls comparing control mice and the control ipsilateral side from embWPC mice (n= 9 ctrl, n= 7 ctrl ipsi side from embWPC mice, PMBSF active fraction, unpaired two-tailed Student *t*-test; ALBSF active fraction, unpaired two-tailed Student *t*-test). Source data are provided as a Source data file. S1, primary somatosensory cortex; wps, whisker pad stimulation; uls, upper lip stimulation; GCaMP6f, calmodulin-based genetically encoded fluorescent calcium indicator 6–fast. Scale bars, 1000 μm. Bar graphs show the means ± SEM. ns, not significant. *p < 0.05, **p < 0.01, ***p < 0.001.

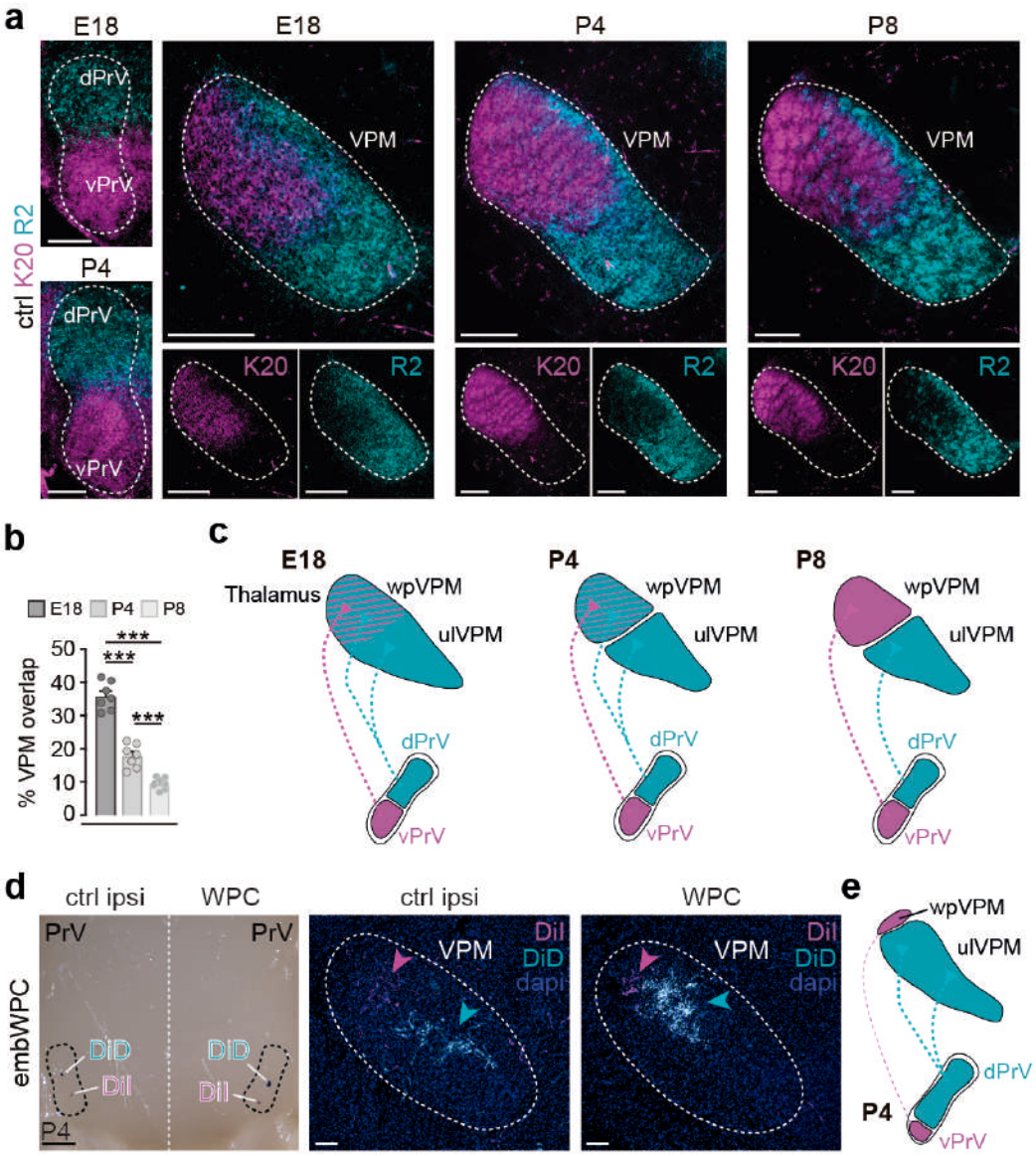

Supplementary Fig. 7. Developmental progression of trigemino-thalamic axons. a Coronal sections from the *Krox20-zsgreen::R2-mCherry* double transgenic mouse showing cells expressing Krox20 (magenta) at the vPrV and R2 (cyan) at the dPrV at E18 and P4 (n= 7 E18, n= 7 P4). Coronal sections from the *Krox20-zsgreen::R2-mCherry* double transgenic mice showing Krox20-labelled axons (magenta) and R2-labelled axons (cyan) at the VPM of the thalamus at E18, P4 and P8. **b** Quantification of the percentage of developmental overlap between vPrV and dPrV axons at the thalamus (n= 7 E18, n= 7 P4, n= 8 P8, Two-way ANOVA test: ***p <0.001. Tukey's multiple comparison test post-hoc analysis). **c** Schemas representing the results found. **d** Left, DiI and DiD crystal placements in the vPrV and dPrV areas, respectively. Right, backlabelled cells at the thalamus show shifted positions within the ulVPM thalamic area in the WPC side as compared to ctrl ipsilateral side at P4 (n= 5). **e** Schema representing the results**.** Source data are provided as a Source data file. Scale bars, **a** and **b** 200 μm; **d** (left) 500 μm; (right) 100 μm**.** Bar graphs show the means ± SEM. ***p <0.001.

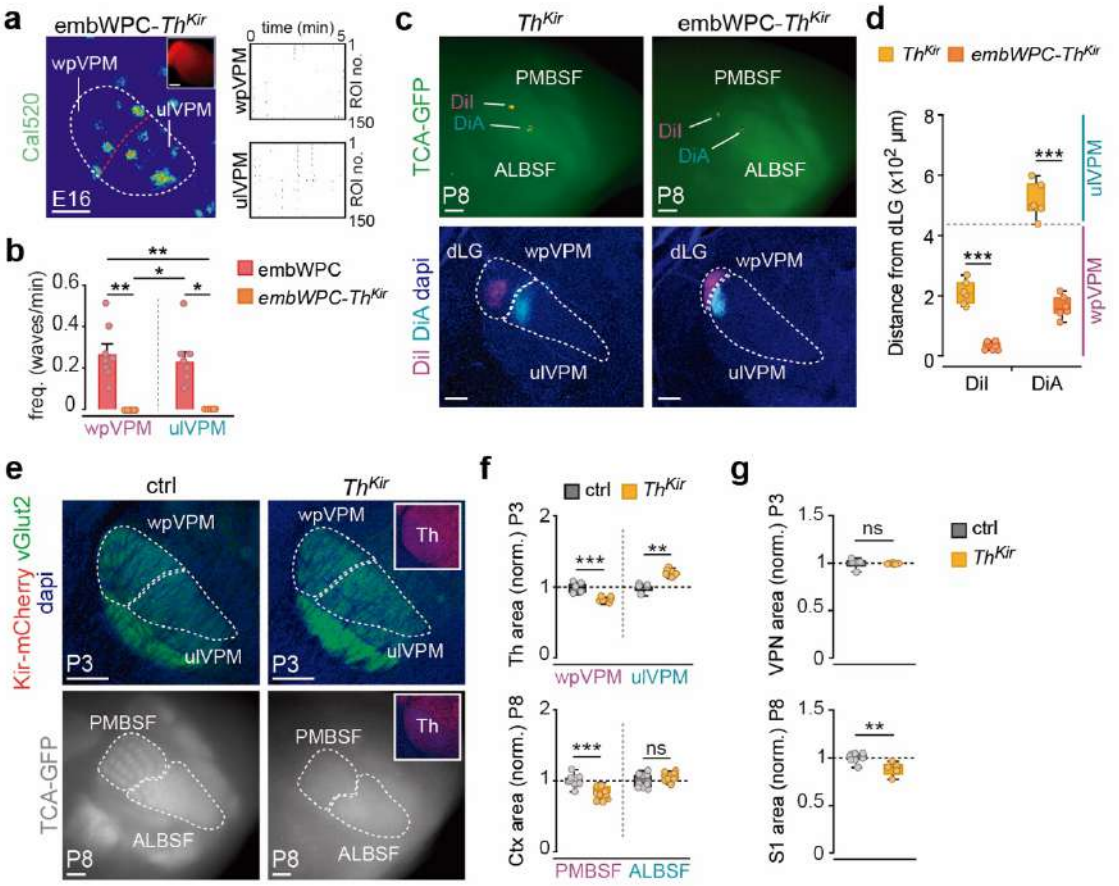

Supplementary Fig. 8. Thalamocortical point-to-point topography is shifted in embWPC-*Th*^{Kir} but not in *Th*^{Kir} mouse. a Maximal projection of *ex vivo* spontaneous calcium activity in the prospective VPM sub-regions (wpVPM, wp input-receiving neurons, and ulVPM, ul input-receiving neurons) of the thalamus in acute slices at E16. Raster plots of 5 minutes. **b** Quantification of the frequency of waves activity in the VPM in both embWPC and embWPC-*Th*^{Kir} mice (n= 8 embWPC, n= 5 embWPC-*Th*^{Kir}, Kruskal-Wallis test, ***p <0.001. Dunn's multiple comparison test post-hoc analysis). **c** Upper panels, DiI and DiA crystal placements in the cortical PMBSF and ALBSF areas, respectively. Lower panels, backlabelled cells at the thalamus show shifted positions within the ulVPM thalamic area in the embWPC-*Th*^{Kir} mice as compared to *Th*^{Kir} at P8. **d** Quantification of the position of backlabelled cells with respect to the distance to the dLG nucleus. The gray horizontal dashed line in the graph represents the separation between wpVPM and ulVPM (n= 6 *Th*^{Kir}, n= 6 embWPC-*Th*^{Kir}, unpaired two-tailed Student *t*-test). **e** Upper panels, coronal sections of vGlut2 staining (green) showing the size of the wpVPM and ulVPM in the thalamus of ctrl and *Th*^{Kir} mouse (Kir-mCherry positive) at P3. Lower panels, surface view of thalamocortical terminals (TCA-GFP+) in the cortical PMBSF and ALBSF in ctrl and *Th*^{Kir} mice at P8. **f** Quantification of the data (Thalamus, n= 5 ctrl, n= 6 *Th*^{Kir}, wpVPM, unpaired two-tailed Student *t*-test; ulVPM, two-tailed Mann-Whitney *U*-test. Cortex, n= 10 ctrl, n= 10 *Th*^{Kir}, PMBSF, unpaired two-tailed Student *t*-test; ALBSF, unpaired two-tailed Student *t*-test. ns, p< 0.1). **g** Top, quantification of the VPN area (n= 5 ctrl, n= 6 *Th*^{Kir}, unpaired two-tailed Student *t*-test. ns, p= 0.84). Bottom, quantification of the total S1 area (n= 8 ctrl, n= 5 *Th*^{Kir}, unpaired two-tailed Student *t*-test). Source data are provided as a Source data file. Scale bars, **a** and **c** (bottom) 200 µm; **e** (top) 250 µm; **c** (top) and **e** (bottom) 500 µm. Bar graphs show the means ± SEM. *p < 0.05, **p < 0.01, ***p < 0.001.

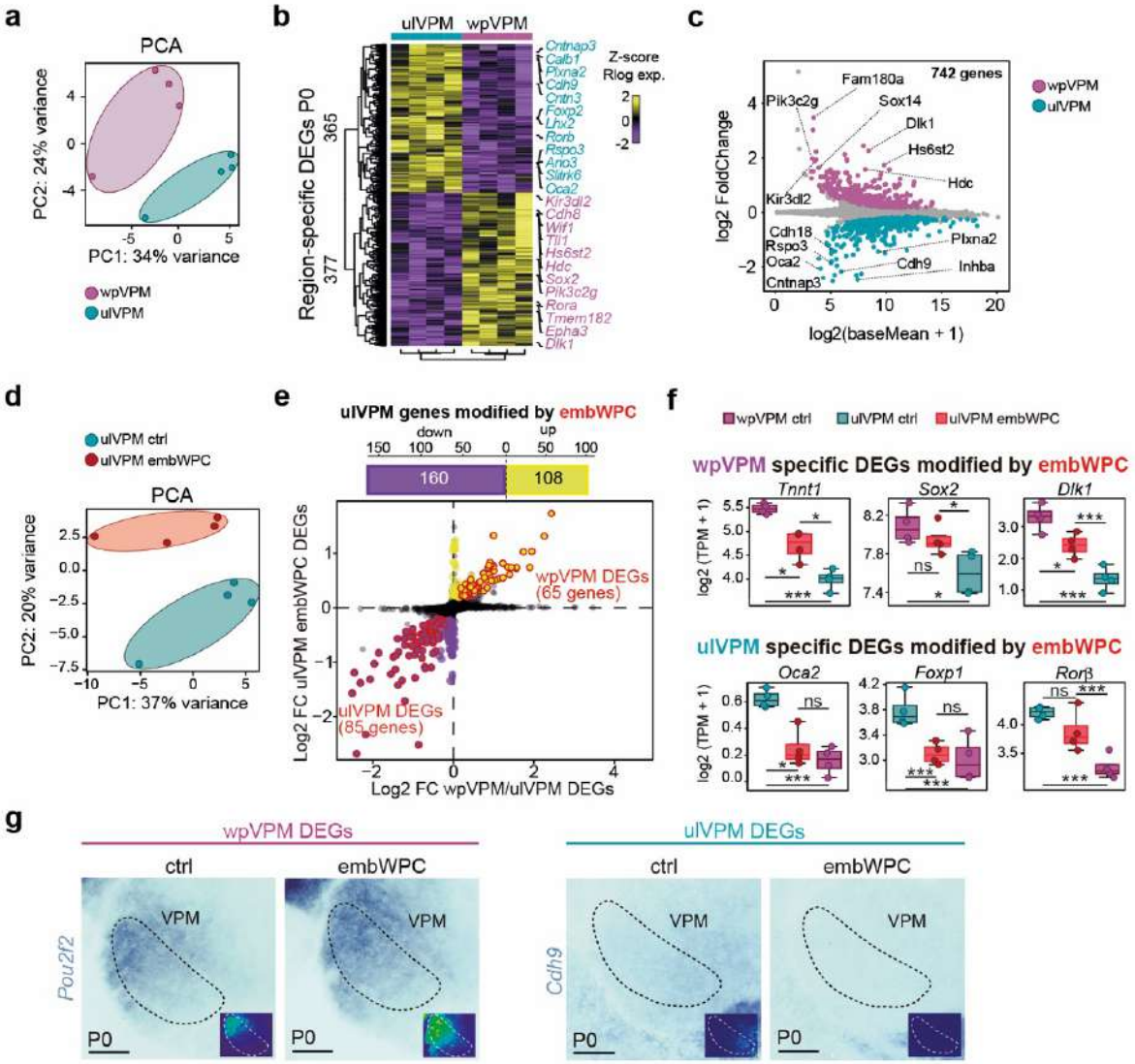

Supplementary Fig. 9. Region-specific transcriptional signatures in the thalamic VPM sub-regions in control and embWPC mice at P0. a Principal Component Analysis (PCA) of wpVPM (n= 4) and ulVPM (n= 4) control mice at P0. **b** Heatmap of normalized regularized logarithm (Rlog) Z-score of expression and unbiased clustering of ulVPM- and wpVPM-specific Differentially Expressed Genes (DEGs) at P0. The color-code (yellow, high expression; purple, low expression) corresponds to the log2FC. **c** MA plot showing the log2 FoldChange and the mean expression distribution of DEGs. The magenta and cyan dots represent wpVPM and ulVPM DEGs, respectively, with the top 7 protein coding genes listed in every region. **d** Principal Component Analysis (PCA) of thalamic control ulVPM (n= 4) and embWPC ulVPM (n= 4) mice at P0. **e** Top, histogram showing ulVPM DEGs that are up- and downregulated by embWPC at P0. Bottom, scatterplot of log2Foldchange between ulVPM DEGs modified by embWPC and wpVPM versus ulVPM region-specific DEGs. **f** Boxplots displaying TPM expression levels of selected wpVPM DEGs and ulVPM DEGs modified in the ulVPM of the embWPC mice. Boxplots show the medians with the interquartile range (box) and range (whiskers). **g** Coronal sections showing by *in situ* hybridization the change in the pattern of expression of additional wpVPM and ulVPM DEGs in the embWPC mouse at P0 (n= 5 ctrl, n= 5 embWPC, for each probe). Scale bars, 200 µm. *adj. $p < 0.1$, **adj. $p < 0.01$, and ***adj. $p < 0.001$.

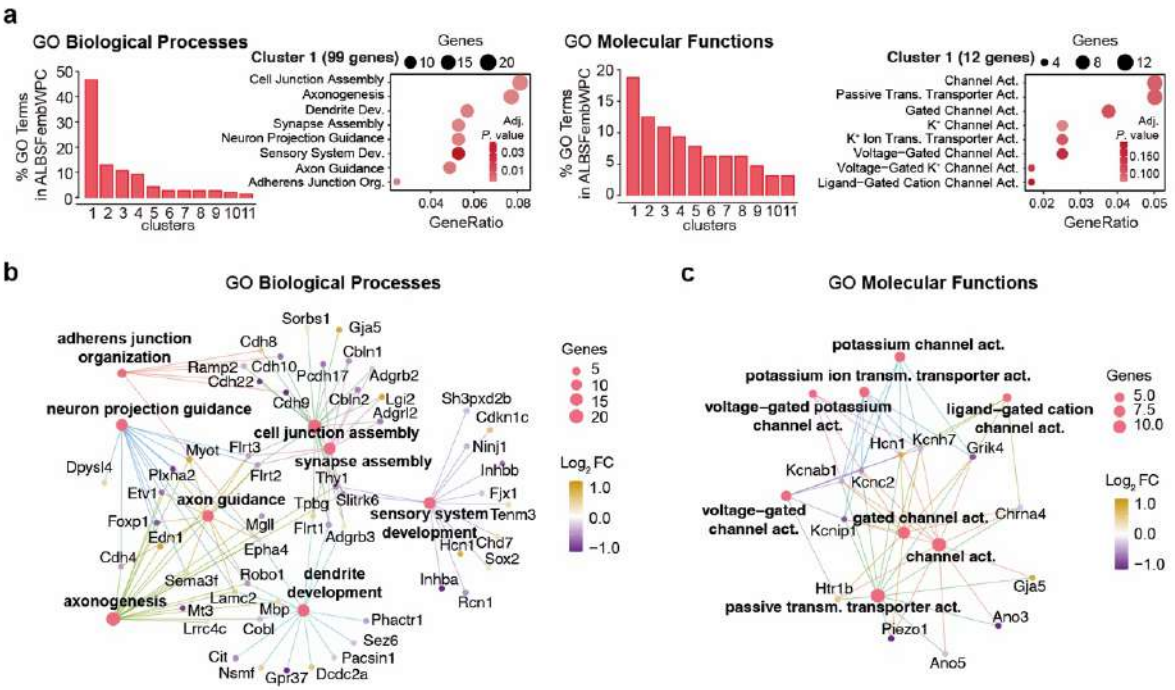

Supplementary Fig. 10. Gene Ontology analysis of region-specific genes modified in embWPC mice. a Gene Ontology (GO) functional analysis (Biological Processes, left; and Molecular Functions, right) showing the top ranked clusters of GO terms enriched in the region-specific gene-set modified in embWPC-ulVPM. **b** Gene ontology (GO) biological process (BP) enrichment analysis of wpVPM and ulVPM DEGs modified by embWPC in ulVPM. **c** Gene ontology (GO) molecular function (MF) enrichment analysis of wpVPM and ulVPM DEGs modified by embWPC in ulVPM. The size of every node (enriched term) in the gene networks represents the number of genes enriched and the color-code (yellow, high expression; purple, low expression) corresponds to the log2FC in the wpVPM vs ulVPM Differential expression analysis (DEA).

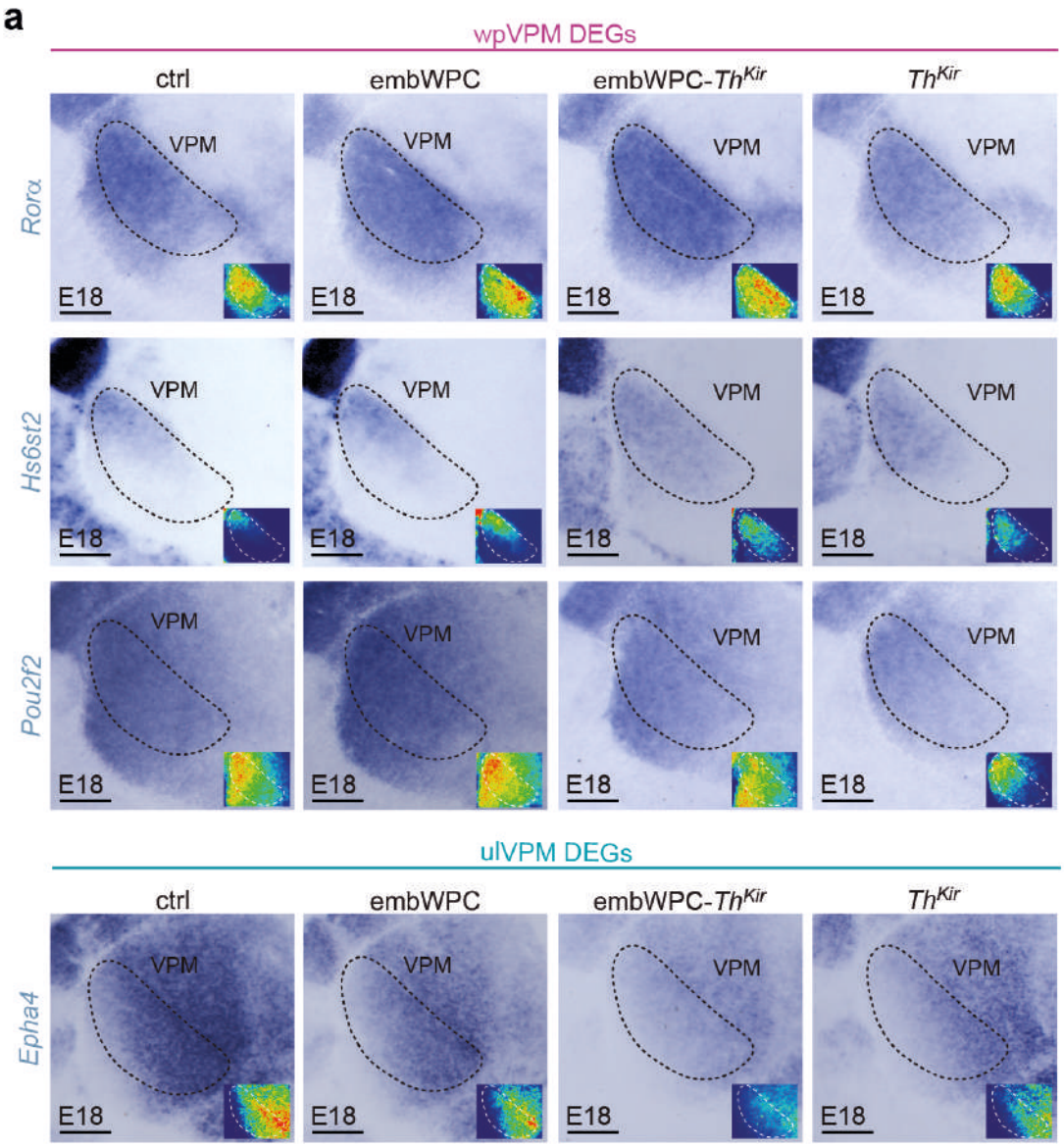

Supplementary Fig. 11. Region-specific transcriptional signatures in the thalamic VPM sub-regions are similarly shifted in embWPC-*Th*^{Kir} and embWPC mice. a Coronal sections showing by *in situ* hybridization the change in the pattern of expression of wpVPM and ulVPM DEGs in embWPC and embWPC-*Th*^{Kir} at E18 (n= 5 ctrl, n= 5 embWPC, n=5 embWPC-*Th*^{Kir} and n=5 *Th*^{Kir}, for each probe). Scale bars, 200 μm.

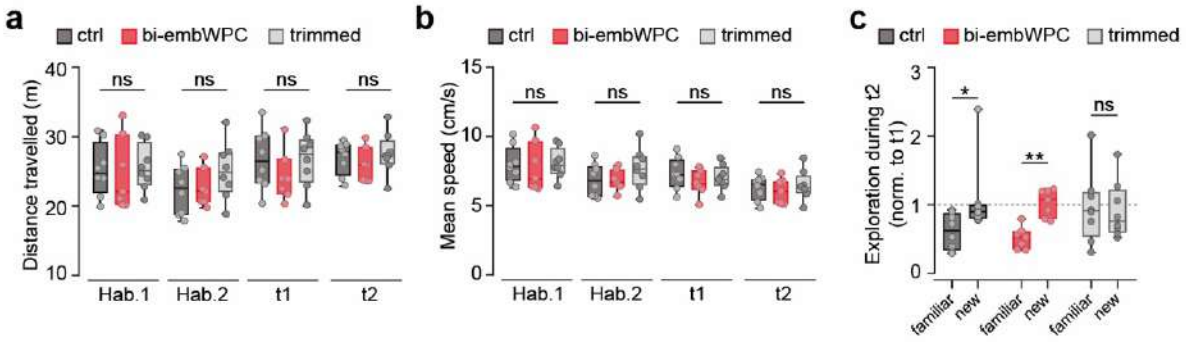

Supplementary Fig. 12. Analysis of locomotor and exploratory activity during the texture discrimination task. a Total distance travelled across each 5-minute session for three experimental groups (n=8 ctrl, n=7 bi-embWPC and n=8 trimmed, Two-way ANOVA test indicates no significant differences between groups on the distance travelled in any of the sessions, ns, p=0.4329). **b** Mean speed of movement (velocity) during each 5-minute session for control, bi-embWPC and trimmed mice (Two-way ANOVA test shows no significant differences across groups, ns, p=0.6191). **c** Boxplots showing the relative time that mice spent exploring familiar versus novel textures during the test session (t_2), normalized to exploration times in the sample session (t_1), where both textures were identical (Ctrl, Wilcoxon matched-pairs signed rank nonparametric test, *p=0.0391; bi-embWPC, paired two-tailed Student's *t*-test. **p=0.0045; trimmed, paired two-tailed Student's *t*-test. ns, p=0.7527). Source data are provided as a Source data file. Boxplots depict median values with interquartile ranges (box) and full range (whiskers). Statistical significance is indicated as follows: ns, not significant. *p < 0.05, **p < 0.01.

Legends for Supplementary Movies

Supplementary Movie 1. iDISCO 3D reconstruction of E18 control mouse. Volume of the whisker pad and upper lip areas in magenta and cyan, respectively. Volume of nice whisker pad and nine upper lip follicles in yellow. Related to Fig. 1 and Supplementary Fig. 1.

Supplementary Movie 2. iDISCO 3D reconstruction of E18 embWPC mouse. Volume of the whisker pad and upper lip areas in magenta and cyan, respectively. Volume of nice whisker pad and nine upper lip follicles in yellow. Related to Fig. 1 and Supplementary Fig. 1.

Supplementary Movie 3. *In vivo* cortical evoked responses in the control side (ipsilateral to cauterization) of embWPC mouse at E18. Stimulations of the whisker pad (magenta) and upper lip (cyan). Dashed lines delineate cortical hemisphere, PMBSF and ALBSF putative cortical territories. Speed x2. Related to Fig. 2.

Supplementary Movie 4. *In vivo* cortical evoked responses in the whisker pad cauterized (WPC) side (contralateral to cauterization) of embWPC mouse at E18. Stimulations of the whisker pad (magenta) and upper lip (cyan). Dashed lines delineate cortical hemisphere, PMBSF and ALBSF putative cortical territories translated from control side stimulations ("PMBSF" and "ALBSF"). Speed x2. Related to Fig. 2.

Supplementary Movie 5. *In vivo* cortical evoked responses in the control side (ipsilateral to cauterization) of embWPC mouse at P4. Stimulations of the whisker pad (magenta) and upper lip (cyan). Dashed lines delineate cortical hemisphere, PMBSF and ALBSF cortical territories. Speed x2. Related to Fig. 2.

Supplementary Movie 6. *In vivo* cortical evoked responses in the whisker pad cauterized (WPC) side (contralateral to cauterization) of embWPC mouse at P4. Stimulations of the whisker pad (magenta) and upper lip (cyan). Dashed lines delineate cortical hemisphere, PMBSF and ALBSF cortical territories translated from control side stimulations ("PMBSF" and "ALBSF"). Speed x2. Related to Fig. 2.

Supplementary Movie 7. Spontaneous thalamic activity in the prospective VPM regions (wpVPM and ulVPM) in an acute slice of control mice at E16. Dashed lines delineate dLG (dorsolateral geniculate) nucleus, prospective wpVPM and ulVPM regions. Speed x15. Related to Fig. 3.

Supplementary Movie 8. Spontaneous thalamic activity in the prospective VPM regions (wpVPM" and ulVPM) in an acute slice of embWPC mice at E16. Dashed lines delineate dLG

(dorsolateral geniculate) nucleus, prospective wpVPM and ulVPM regions. Speed x15. Related to Fig. 3.

Supplementary Movie 9. Topographic representations in the cortex of *in vivo* evoked responses in control mouse at P4. Stimulations of the whisker pad (magenta, blue, green, yellow and orange) and upper lip (cyan and white). Dashed lines delineate cortical hemisphere, PMBSF and ALBSF evoked cortical territories. Speed x2. Related to Fig. 6.

Supplementary Movie 10. Topographic representations in the cortex of *in vivo* evoked responses in embWPC mouse at P4. Stimulations of the upper lip (cyan and white). Dashed lines delineate cortical hemisphere and ALBSF evoked cortical territory. Speed x2. Related to Fig. 6.

Legends for Supplementary Data

Supplementary Data 1. Differential expression analysis of wpVPM vs ulVPM control samples from bulk RNA-seq. Related to Fig. 4 and Supplementary Fig. 9.

Supplementary Data 2. Differential expression analysis of EmbWPC vs control-ulVPM samples from bulk RNA-seq. Related to Fig. 4 and Supplementary Fig. 9.

Supplementary Data 3. Enrichment analysis of EmbWPC and control-ulVPM samples from bulk RNA-seq. Related to Fig. 4 and Supplementary Fig. 10.

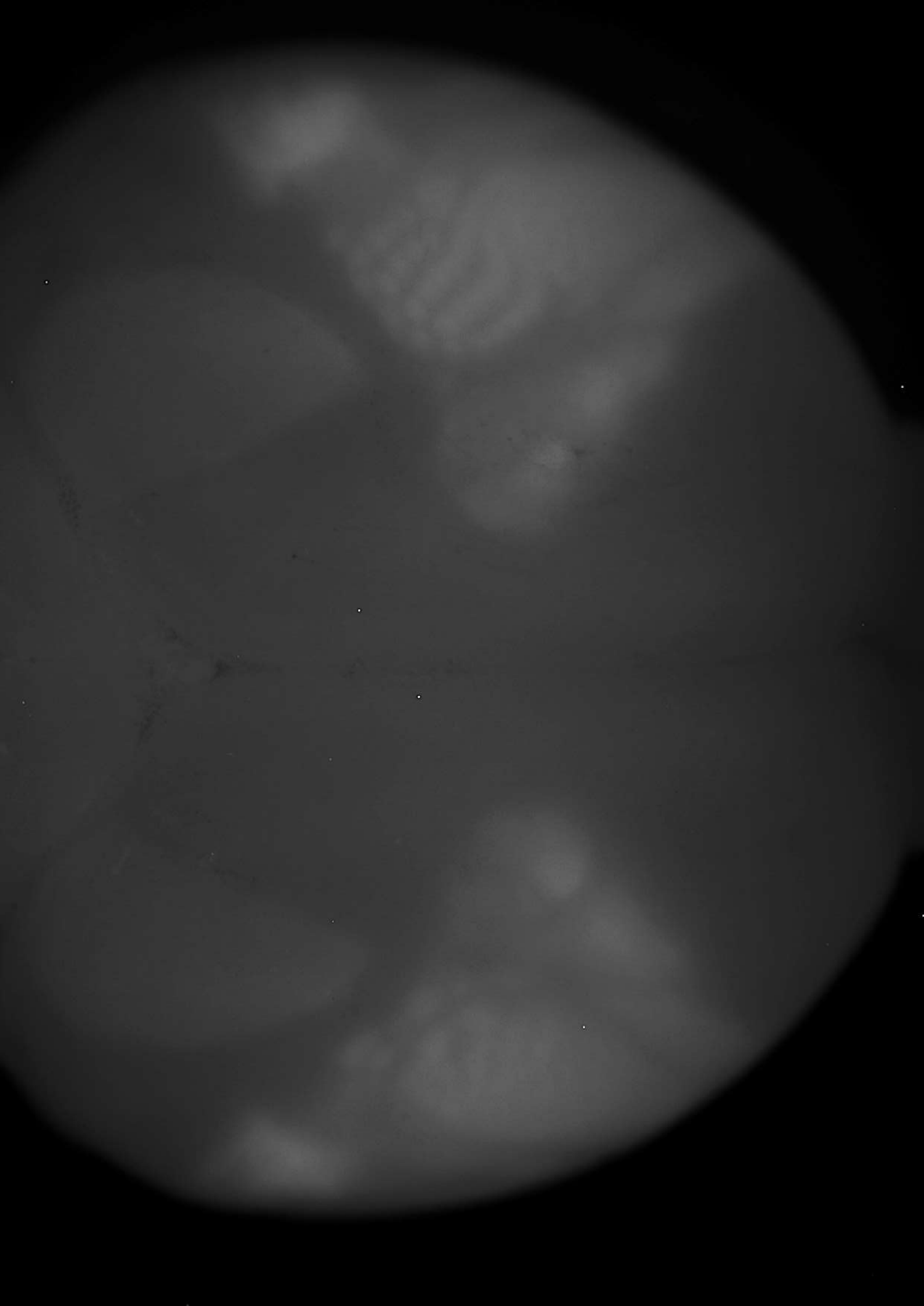

DISCUSSION

Piecing the puzzle together

DISCUSSION

Specialized sensory maps in the neocortex are essential for processing and integrating sensory information. While intracortical transcriptional programs predominantly govern the basic cytoarchitecture of sensory cortical areas (Rakic et al., 2009), subcortical structures such as the thalamus also play a key role in shaping these maps and determining their size (Moreno-Juan et al., 2017). During embryonic development, TCAs establish their first synaptic connections with SPNs while cortical layers remain immature (Luhmann et al., 2018). At this stage, thalamic sensory nuclei are already compartmentalized and well-defined (Angevine, 1970). TCAs navigate topographically to specific cortical regions, carrying positional and sensory-modality information in a process that occurs prior to birth and independently of sensory experience (López-Bendito & Molnár, 2003).

The spatial organization of central brain structures is inherited from peripheral sensory organs such as the retina, cochlea or whisker pad. Neighbor connectivity, driven by peripheral neuronal activity, consolidates topographic mapping (Hanganu-Opatz, 2010; Bednar & Wilson, 2016). While intrinsic genetic factors lay the foundational framework, functional maps are refined postnatally through peripheral input (Woolsey & Wann 1976; Killackey et al. 1978; Hensch 2004; Renier et al., 2017; Tiriac et al. 2018; Gaspar & Renier 2018). Alterations in sensory inputs, such as the removal of a single whisker or an entire row of whiskers during the first postnatal week, result in the loss of corresponding cortical barrels and an expansion of adjacent barrels (Van der Loos & Woolsey, 1973; Woolsey & Wann, 1976; Killackey et al., 1976; Killackey & Belford, 1979; Woolsey et al., 1979; Belford & Killackey, 1979). These observations underscore the sensitivity of somatosensory maps to peripheral input and challenge the assumption that cortical barrel size directly corresponds to the size or type of peripheral sensory receptors.

A prenatal window for intra-modal plasticity in the somatosensory pathway

Classical studies of intra-modal plasticity within the somatosensory system suggested that cortical adaptations following sensory deprivation are primarily experience-dependent and occur postnatally through compensatory growth of intact sensory regions (Killackey et al., 1976; Woolsey & Wann, 1976; Belford & Killackey, 1979; Woolsey et al., 1979; Killackey & Dawson, 1989; Erzurumlu & Gaspar, 2012). However, cross-modal plasticity studies have shown that adaptations in the somatosensory cortex after visual deprivation arise well before sensory experience begins (Fetter-Pruneda et al., 2013; Abbott et al., 2015; Moreno-Juan et al., 2017). These studies suggest that experience-independent mechanisms, such as embryonic thalamic calcium waves, may trigger cortical plasticity (Moreno-Juan et al., 2017).

To explore whether experience-independent mechanisms influence the size of somatosensory cortical maps intra-modally, we developed a mouse model in which whiskers input was deprived at E14 (embWPC). The embryonic ablation of mystacial whiskers induced intra-modal plasticity, leading to a profound reorganization of barrel-field territories within the somatosensory system prior to birth. We found an enlargement of ALBSF cortical territory occupying the space previously associated with the PMBSF, as demonstrated by *in vivo* recordings at E18. Evoked activity from upper lip stimulations revealed columnar responses that precede the formation of cytoarchitectural sensory maps. Although anatomical cortical columns are absent at embryonic stages (Agmon et al., 1995), functional precolumnar patterns delineating cortical barrel fields are already apparent. Prenatal peripheral stimulations support the existence of functional cortical maps, indicating that the somatosensory system is capable of transmitting topographic information even before birth. These results align with previous neonatal studies showing that early postnatal cortical activity, both spontaneous and evoked, is already organized topographically (Yang et al. 2013; Mitrukhina et al. 2015; Mizuno et al. 2018a; Antón-Bolaños et al., 2019).

Unlike the cross-modal plasticity observed in early blind models, where sensory cortical adaptations span different modalities (Moreno-Juan et al., 2017), our findings highlight the specificity of intra-modal reorganization. The mechanisms driving this

reorganization are tightly constrained to preserve functional fidelity within the affected sensory modality.

Our data also demonstrates the existence of a critical prenatal temporal window during which somatosensory cortical maps are established, as the rearrangements observed in embWPC mice are absent when whiskers input is deprived at birth (P0). This aligns with prior studies showing that manipulations outside this critical window do not lead to significant cortical reorganization (Erzurumlu, 2010; Erzurumlu & Gaspar, 2012; Iwasato & Erzurumlu, 2018).

Independence from peripheral receptor properties

Traditionally, the barrel field representation in the cortex has been thought to reflect the characteristics of peripheral sensory receptors—e.g., larger whisker follicles driving the formation of larger barrels in the PMBSF (Gaspar & Erzurumlu, 2013; Erzurumlu & Gaspar, 2020), while smaller upper lip whiskers correspond to smaller, less defined ALBSF barrels (Woolsey & Van der Loos, 1970; Land & Simons, 1985; Jan et al., 2008). However, previous research demonstrated that altering sensory inputs can reshape cortical maps without modifying receptor properties (Killackey & Dawson, 1989). Consistent with this, we found that the size of cortical barrels is not correlated with peripheral receptor size in embWPC mice. Despite the expansion of the ALBSF cortical territory and individual barrels, the size of upper lip follicles and their associated area remained unchanged. This suggests that mechanisms beyond peripheral receptor features regulate barrel field size and organization, raising further questions about the intrinsic and subcortical factors driving the establishment and refinement of these cortical territories.

Role of spontaneous thalamic activity in map formation

Previous work from our lab demonstrated that the thalamus can generate intrinsic spontaneous calcium waves, which serve as a cross-modal communication mechanism among sensory systems to maintain homeostatic regulation of cortical areal size after sensory loss

(Moreno-Juan et al. 2017). This was the first evidence identifying spontaneous thalamic activity as a regulatory element in cortical development. Later, Antón-Bolaños et al. (2019) found that embryonic thalamic calcium waves are essential for barrel map development in the somatosensory cortex, independent of external input. However, the precise contribution of peripheral input and spontaneous activity in central brain structures, as well as their interaction in shaping sensory circuits remains largely unclear.

Our data show that the rescaling of the ALBSF in embWPC mice occurs independently of these activity patterns. The preserved point-to-point topography in embWPC and embWPC-*Th*^{Kir} mice further supports the robustness of these results. These findings suggest a dual mechanism in which transcriptional programs drive large-scale reorganization, while thalamic activity is necessary for fine-tuning barrel field territories, emphasizing the complexity of sensory map formation.

Specific thalamic cues in VPM sub-territories guiding somatosensory maps development

We demonstrated that by E16, thalamic sub-regions in the VPM receiving input from mystacial whiskers or upper lip whiskers exhibit distinct spontaneous calcium waves frequencies. The wpVPM region displays high-frequency activity, whereas the ulVPM does not exhibit such activity. By P0, before cortical barrel fields are anatomically evident, thalamic VPM sub-territories express distinct transcriptional profiles. wpVPM and ulVPM regions are distinguishable by DEGs that are region specific. Thus, these molecular profiles may guide the functional and anatomical differentiation of PMBSF and ALBSF, supporting the establishment of precise intra-modal somatosensory maps. The enlargement of ALBSF maps in embWPC mice is mediated by thalamic transcriptional programs. Genes such as *Rora* and *Epha4*, essential for thalamocortical barrel field development (Vitalis et al., 2018; Dufour et al., 2003), are upregulated in ulVPM neurons, aligning their transcriptional profiles with those of wpVPM neurons. This transcriptional shift likely drives the anatomical transformation of the ALBSF, independent of the periphery.

The barrel field cortical territories exhibit distinct structural characteristics, with the PMBSF containing large, well-defined barrels, while the ALBSF is composed of smaller, less distinct barrels (Woolsey & Van der Loos, 1970; Land & Simons, 1985; Erzurumlu & Gaspar, 2020). Interestingly, the ALBSF also has a higher density of PV+ interneurons compared to the PMBSF, suggesting the presence of more potent feedforward inhibitory circuits (Shigematsu et al., 2024). When intra-modal plasticity is induced using the embWPC model, the reorganized ALBSF territory acquires anatomical properties resembling those of the PMBSF, including larger and more sharply defined barrels, and lower density of PV+ interneurons. Notably, the ulVPM territory in these mice mirrors the transcriptional signatures and activity patterns of the wpVPM territory, suggesting that these specific transcriptional profiles and activity patterns drive the acquisition of PMBSF-like features.

Our findings reveal a critical prenatal window during which sensory maps exhibit high plasticity, enabling the establishment of their size and definition through thalamic signaling.

Functional and behavioural outcomes of intra-modal plasticity

The reorganized ALBSF map in embWPC mice acquires functional properties typically associated with the PMBSF, including enhanced spatial resolution and the ability to discriminate textures (Kleinfeld et al., 2006). In control mice, mechanical stimulation of the whisker pad at early postnatal stages (P4) elicits more defined and higher-resolution responses in the PMBSF compared to upper lip stimulation in the ALBSF. In embWPC mice, upper lip stimulations evoked refined responses in the ALBSF comparable to those observed in the PMBSF of control mice. This intra-modal adaptation suggests that the spatial resolution in the ALBSF map was enhanced. Additionally, embWPC mice used the upper lip comparably to how control mice used the whisker pad, as evidenced by cFos expression levels, which are similar in the ALBSF of embWPC mice and the PMBSF of control mice. Notably, despite the absence of mystacial whiskers, embWPC mice displayed behavioural recovery through the enhanced ALBSF map, achieving texture discrimination capabilities comparable to control mice. This demonstrates the functional relevance of intra-modal plasticity in

maintaining behavioural adaptability, that do not only reshape cortical representations but also supports functional recovery. Consistent with prior studies showing that sensory maps adapt to preserve critical behavioural functions even under altered developmental conditions (Simons & Land, 1987).

Concluding remarks

Our findings highlight the developmental plasticity of the somatosensory system, revealing that intra-modal mechanisms enable robust cortical adaptations during a critical prenatal window. These adaptations are mediated by the interplay of thalamic specific transcriptional programs and, to a lesser extent, thalamic calcium waves. The discovery that intra-modal reorganization can reshape cortical maps and preserve functionality emphasizes the importance of intrinsic mechanisms in sensory development. By elucidating the principles governing somatosensory map formation, this study contributes to our understanding of cortical development and opens new avenues for exploring therapeutic strategies to enhance sensory function in injury contexts.

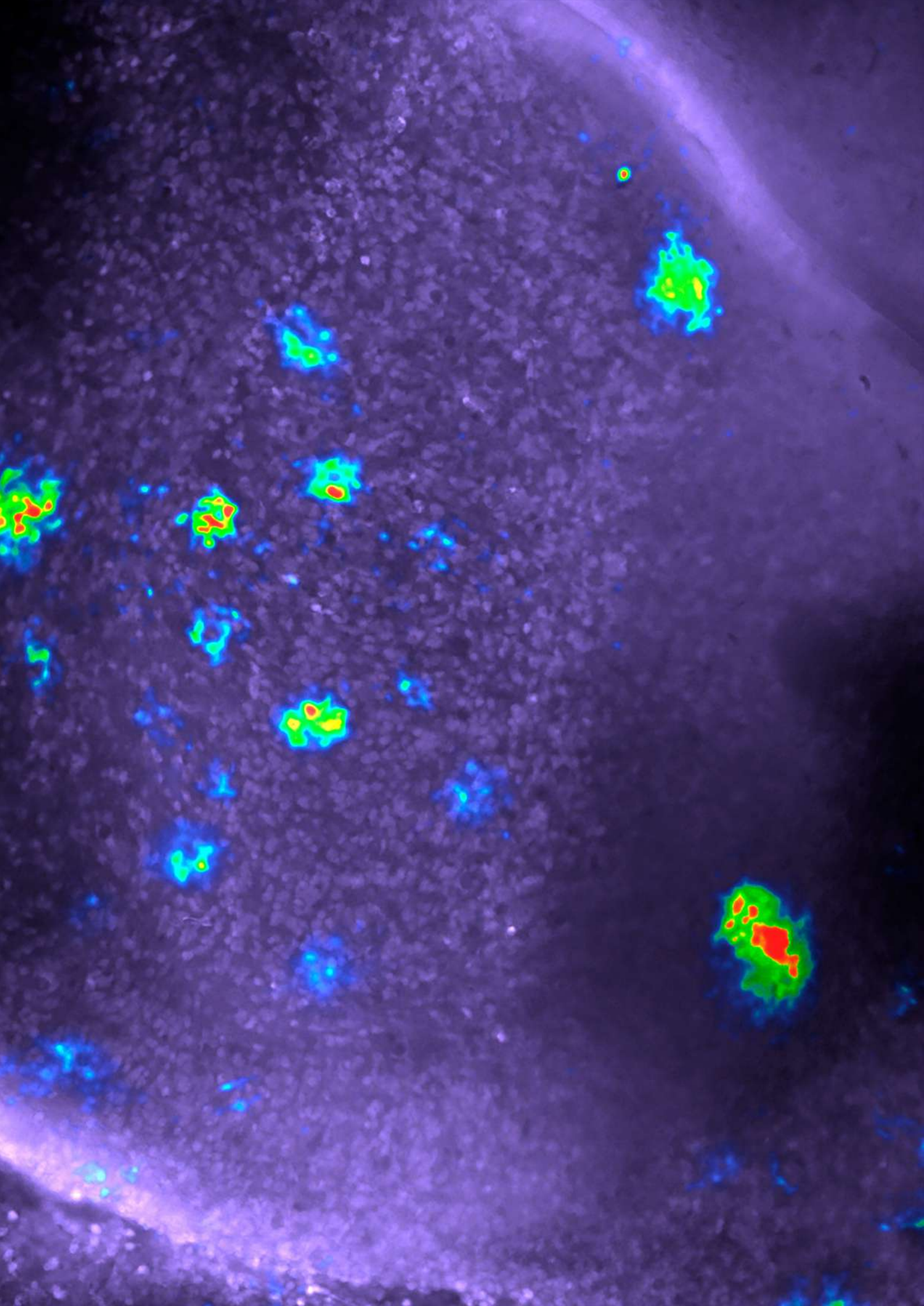

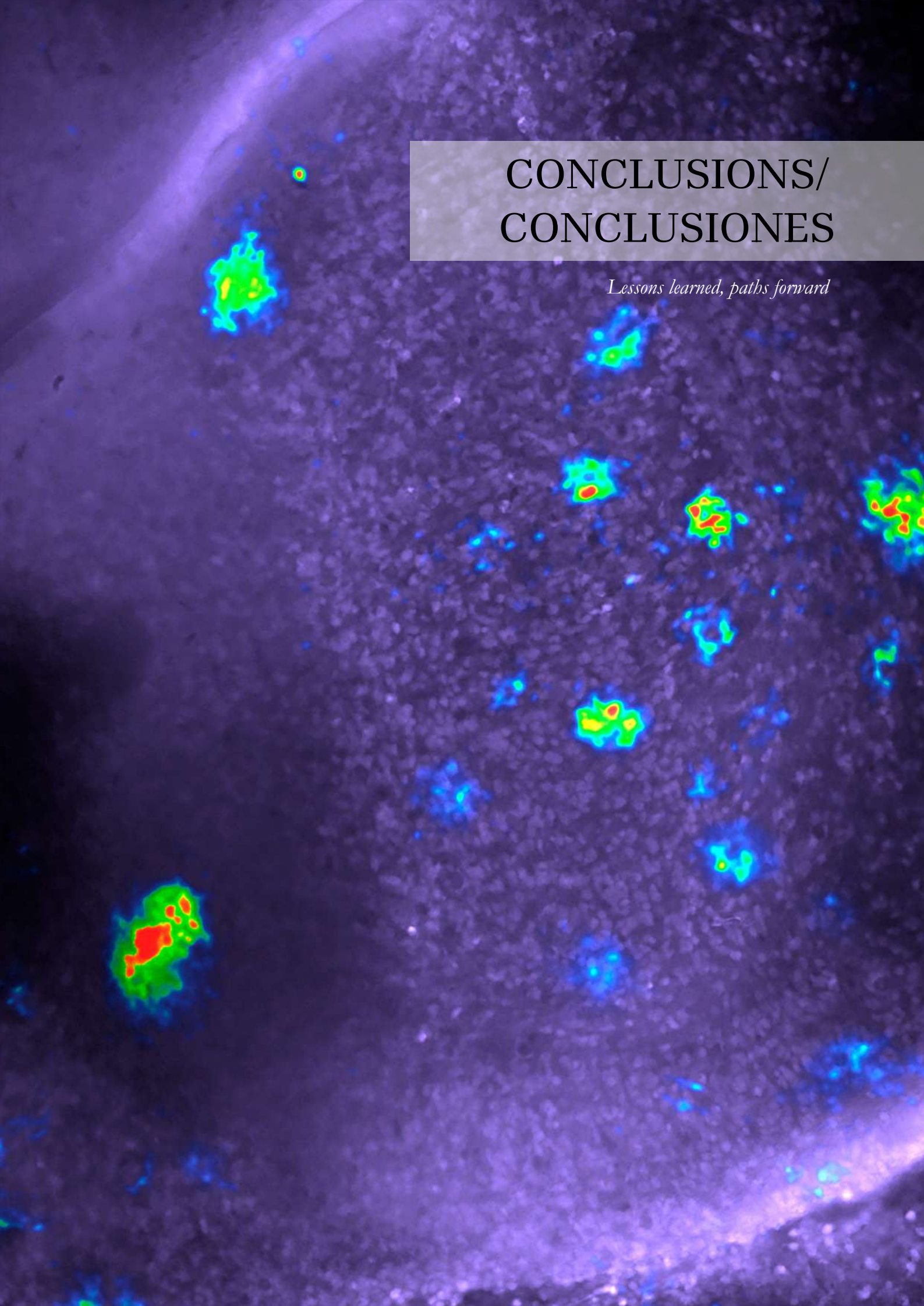

CONCLUSIONS/ CONCLUSIONES

Lessons learned, paths forward

CONCLUSIONS

1. Somatosensory territories are established within a brief embryonic window and are functionally segregated before birth.
2. Embryonic whiskers input deprivation induces intra-modal plasticity within the somatosensory system rather than cross-modal plasticity involving other sensory systems.
3. Barrel field sizes can be adjusted prenatally, with functional reorganization of territories evident before birth.
4. The point-to-point topography is preserved in reorganized maps of embWPC mice.
5. Functional rearrangements in barrel field territories are accompanied by thalamic calcium waves during development.
6. Blocking thalamic calcium waves does not prevent the reorganization of somatosensory territories under input-deprived conditions.
7. The segregation of somatosensory territories is primarily driven by the input.
8. The VPM sub-territories exhibit unique transcriptional profiles and specific spontaneous activity patterns, each corresponding to different barrel field maps.
9. Whiskers input deprivation modifies territory-specific genes associated with axon guidance and activity, mimicking the molecular profiles and thalamic spontaneous activity patterns of the deprived territory.
10. The rescaling of the ALBSF map incorporates features of the PMBSF, including increased barrel size, sharper definition, and enhanced spatial resolution.
11. Cortical barrel field features are independent of peripheral receptor characteristics.
12. Thalamic spontaneous activity regulates somatosensory map resolution during prenatal development.
13. The reorganized ALBSF map acquires functional properties typically associated with the PMBSF, enabling texture discrimination.

CONCLUSIONES

1. Los territorios somatosensoriales se establecen durante una breve ventana embrionaria y están funcionalmente segregados antes del nacimiento.
2. La privación de los bigotes durante el desarrollo embrionario genera plasticidad intra-modal dentro del sistema somatosensorial, en lugar de plasticidad cross-modal que involucre a otros sistemas sensoriales.
3. El tamaño de los territorios de barriles puede ajustarse durante el desarrollo prenatal, y su reorganización funcional es evidente antes del nacimiento.
4. La topografía se conserva en los mapas reorganizados de los ratones embWPC.
5. Las reorganizaciones funcionales en los territorios de barriles están acompañadas por ondas de calcio talámicas durante el desarrollo.
6. El bloqueo de las ondas de calcio talámicas no impide la reorganización de los territorios somatosensoriales en condiciones de privación de estímulos.
7. La segregación de los mapas somatosensoriales está mediada por la entrada sensorial.
8. Los subterritorios del VPM presentan perfiles transcripcionales únicos y patrones de actividad espontánea específicos, asociados a diferentes mapas de barriles.
9. La privación de los bigotes modifica genes específicos de territorio relacionados con guía axonal y actividad, imitando los perfiles moleculares y patrones de actividad espontánea talámica del territorio privado.
10. La reorganización del mapa ALBSF incorpora características del PMBSF, como un mayor tamaño de los barriles, una mayor definición y una mejor resolución espacial.
11. Las características de los territorios de barriles corticales son independientes de las propiedades de los receptores sensoriales periféricos.
12. La actividad espontánea talámica regula la resolución de los mapas somatosensoriales durante el desarrollo embrionario.
13. El mapa reorganizado del ALBSF adquiere funciones propias del PMBSF, como la discriminación de texturas.

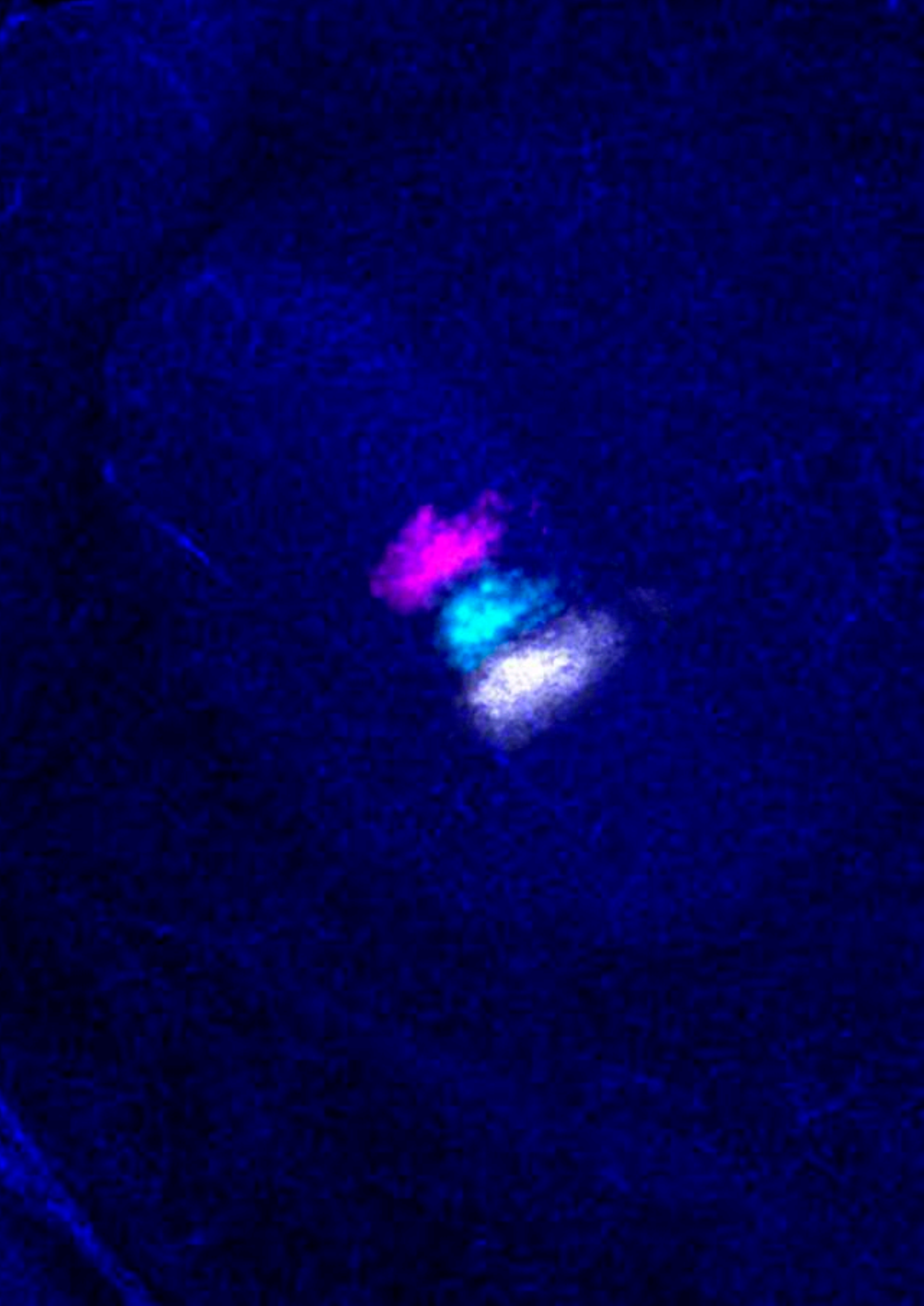

REFERENCES

Standing on the shoulders of giants

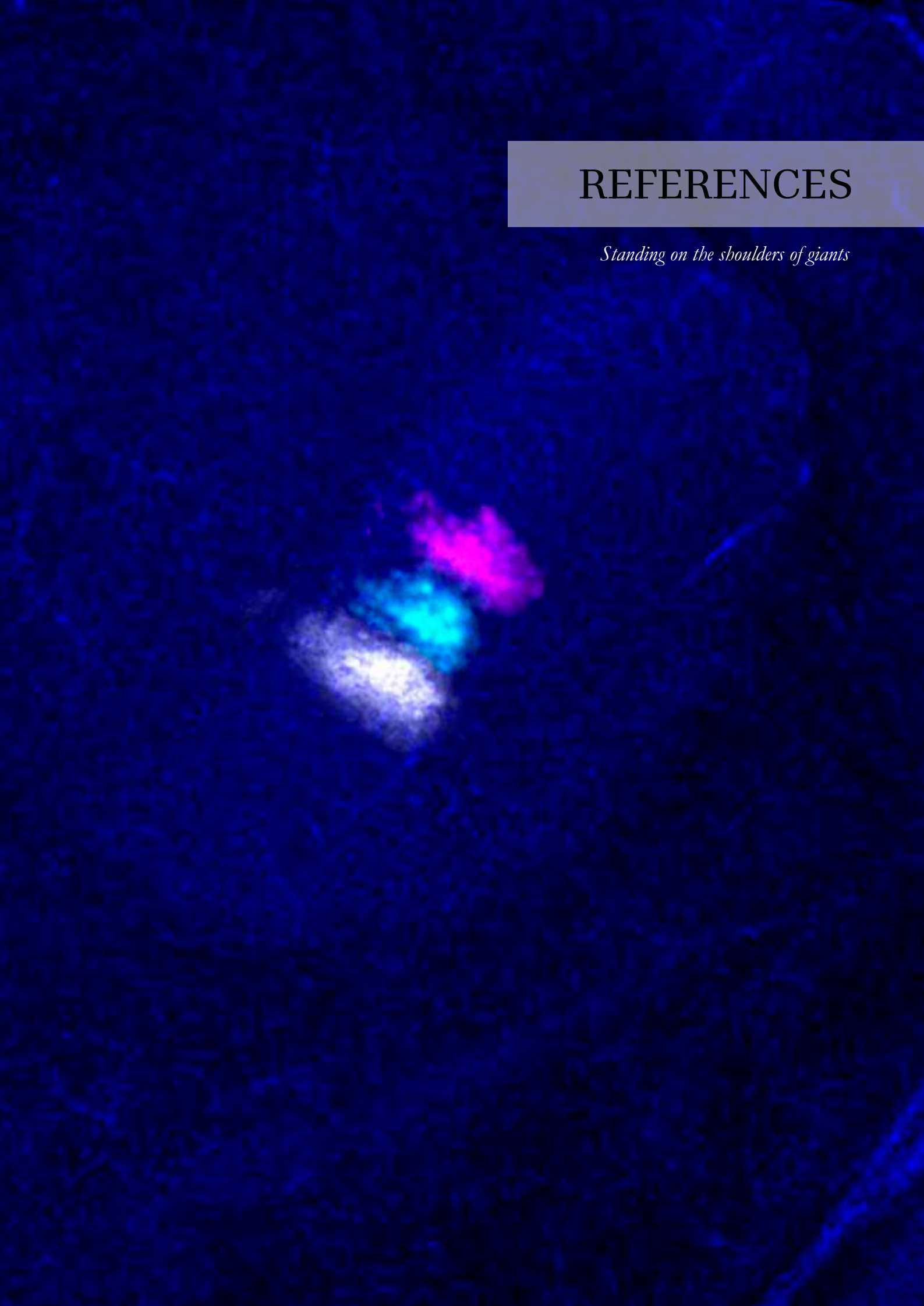

REFERENCES

Abbott CW, Kozanian OO, Huffman KJ. The effects of lifelong blindness on murine neuroanatomy and gene expression. Front Aging Neurosci. 2015 Jul 24;7:144. doi: 10.3389/fnagi.2015.00144. PMID: 26257648; PMCID: PMC4513570.

Abdel-Majid RM, Leong WL, Schalkwyk LC, Smallman DS, Wong ST, Storm DR, Fine A, Dobson MJ, Guernsey DL, Neumann PE. Loss of adenylyl cyclase I activity disrupts patterning of mouse somatosensory cortex. Nat Genet. 1998 Jul;19(3):289-91. doi: 10.1038/980. PMID: 9662407.

Ackman JB, Burbridge TJ, Crair MC. Retinal waves coordinate patterned activity throughout the developing visual system. Nature. 2012 Oct 11;490(7419):219-25. doi: 10.1038/nature11529. PMID: 23060192; PMCID: PMC3962269.

Ackman JB, Crair MC. Role of emergent neural activity in visual map development. Curr Opin Neurobiol. 2014 Feb;24(1):166-75. doi: 10.1016/j.conb.2013.11.011. Epub 2013 Dec 22. PMID: 24492092; PMCID: PMC3957181.

Agmon A, Yang LT, Jones EG, O'Dowd DK. Topological precision in the thalamic projection to neonatal mouse barrel cortex. J Neurosci. 1995 Jan;15(1 Pt 2):549-61. doi: 10.1523/JNEUROSCI.15-01-00549.1995. PMID: 7823163; PMCID: PMC6578331.

Agmon A, Yang LT, O'Dowd DK, Jones EG. Organized growth of thalamocortical axons from the deep tier of terminations into layer IV of developing mouse barrel cortex. J Neurosci. 1993 Dec;13(12):5365-82. doi: 10.1523/JNEUROSCI.13-12-05365.1993. PMID: 8254380; PMCID: PMC6576404.

Akerman CJ, Smyth D, Thompson ID. Visual experience before eye-opening and the development of the retinogeniculate pathway. Neuron. 2002 Dec 5;36(5):869-79. doi: 10.1016/s0896-6273(02)01010-3. PMID: 12467590.

Akhmetshina D, Nasretdinov A, Zakharov A, Valeeva G, Khazipov R. The Nature of the Sensory Input to the Neonatal Rat Barrel Cortex. J Neurosci. 2016 Sep 21;36(38):9922-32. doi: 10.1523/JNEUROSCI.1781-16.2016. PMID: 27656029; PMCID: PMC6705573.

Alencar CDC, Butler BE, Lomber SG. What and How the Deaf Brain Sees. J Cogn Neurosci. 2019 Aug;31(8):1091-1109. doi: 10.1162/jocn_a_01425. Epub 2019 May 21. PMID: 31112472.

Allen CB, Celikel T, Feldman DE. Long-term depression induced by sensory deprivation during cortical map plasticity in vivo. Nat Neurosci. 2003 Mar;6(3):291-9. doi: 10.1038/nn1012. PMID: 12577061.

Allendoerfer KL, Shatz CJ. The subplate, a transient neocortical structure: its role in the development of connections between thalamus and cortex. Annu Rev Neurosci. 1994;17:185-218. doi: 10.1146/annurev.ne.17.030194.001153. PMID: 8210173.

Alonso, J-M and Swadlow, H.A. Thalamocortical interactions for sensory processing. Oxford Research Encyclopedia of Neuroscience, 1-29, Oxford University Press, USA, April. 2017. doi: 10.1093/acrefore/9780190264086.013.112.

Angevine JB Jr. Time of neuron origin in the diencephalon of the mouse. An autoradiographic study. J Comp Neurol. 1970 Jun;139(2):129-87. doi: 10.1002/cne.901390202. PMID: 5463599.

Angevine JB Jr, Sidman RL. Autoradiographic study of cell migration during histogenesis of cerebral cortex in the mouse. Nature. 1961 Nov 25;192:766-8. doi: 10.1038/192766b0. PMID: 17533671.

Antón-Bolaños N, Espinosa A, López-Bendito G. Developmental interactions between thalamus and cortex: a true love reciprocal story. Curr Opin Neurobiol. 2018 Oct;52:33-41. doi: 10.1016/j.conb.2018.04.018. Epub 2018 Apr 25. PMID: 29704748; PMCID: PMC7611016.

Antón-Bolaños N, Sempere-Ferràndez A, Guillamón-Vivancos T, Martini FJ, Pérez-Saiz L, Gezelius H, Filipchuk A, Valdeolmillos M, López-Bendito G. Prenatal activity from thalamic neurons governs the emergence of functional cortical maps in mice. Science. 2019 Jun 7;364(6444):987-990. doi: 10.1126/science.aav7617. Epub 2019 May 2. PMID: 31048552; PMCID: PMC7611000.

Arai Y, Pierani A. Development and evolution of cortical fields. Neurosci Res. 2014 Sep;86:66-76. doi: 10.1016/j.neures.2014.06.005. Epub 2014 Jun 28. PMID: 24983875.

Arakawa H, Akkentli F, Erzurumlu RS. Region-Specific Disruption of Adenylate Cyclase Type 1 Gene Differentially Affects Somatosensorimotor Behaviors in Mice(1,2,3). eNeuro. 2014a Nov 12;1(1):ENEURO.0007-14.2014. doi: 10.1523/ENEURO.0007-14.2014. PMID: 26464960; PMCID: PMC4596139.

Arakawa H, Suzuki A, Zhao S, Tsytsarev V, Lo FS, Hayashi Y, Itohara S, Iwasato T, Erzurumlu RS. Thalamic NMDA receptor function is necessary for patterning of the thalamocortical somatosensory map and for sensorimotor behaviors. J Neurosci. 2014b Sep 3;34(36):12001-14. doi: 10.1523/JNEUROSCI.1663-14.2014. PMID: 25186746; PMCID: PMC4152605.

Armentano M, Chou SJ, Tomassy GS, Leingärtner A, O'Leary DD, Studer M. COUP-TFI regulates the balance of cortical patterning between frontal/motor and sensory areas. Nat Neurosci. 2007 Oct;10(10):1277-86. doi: 10.1038/nn1958. Epub 2007 Sep 9. PMID: 17828260.

Ashmore J, Avan P, Brownell WE, Dallos P, Dierkes K, Fettiplace R, Grosh K, Hackney CM, Hudspeth AJ, Jülicher F, Lindner B, Martin P, Meaud J, Petit C, Santos-Sacchi J, Sacchi JR, Canlon B. The remarkable cochlear amplifier. Hear Res. 2010 Jul;266(1-2):1-17. doi: 10.1016/j.heares.2010.05.001. Erratum in: Hear Res. 2011 Oct;280(1-2):245. Sacchi, J R Santos [corrected to Santos-Sacchi, J]. PMID: 20541061; PMCID: PMC6366996.

Assali A, Le Magueresse C, Bennis M, Nicol X, Gaspar P, Rebsam A. RIM1/2 in retinal ganglion cells are required for the refinement of ipsilateral axons and eye-specific segregation. Sci Rep. 2017 Jun 12;7(1):3236. doi: 10.1038/s41598-017-03361-0. PMID: 28607399; PMCID: PMC5468276.

Assimacopoulos S, Kao T, Issa NP, Grove EA. Fibroblast growth factor 8 organizes the neocortical area map and regulates sensory map topography. J Neurosci. 2012 May 23;32(21):7191-201. doi: 10.1523/JNEUROSCI.0071-12.2012. PMID: 22623663; PMCID: PMC3466079.

Auer ET Jr, Bernstein LE, Sungkarat W, Singh M. Vibrotactile activation of the auditory cortices in deaf versus hearing adults. Neuroreport. 2007 May 7;18(7):645-8. doi: 10.1097/WNR.0b013e3280d943b9. PMID: 17426591; PMCID: PMC1934619.

Auladell C, Pérez-Sust P, Supèr H, Soriano E. The early development of thalamocortical and corticothalamic projections in the mouse. Anat Embryol (Berl). 2000 Mar;201(3):169-79. doi: 10.1007/pl00008238. PMID: 10664178.

Babola TA, Li S, Gribizis A, Lee BJ, Issa JB, Wang HC, Crair MC, Bergles DE. Homeostatic Control of Spontaneous Activity in the Developing Auditory System. Neuron. 2018 Aug 8;99(3):511-524.e5. doi: 10.1016/j.neuron.2018.07.004. Epub 2018 Aug 1. PMID: 30077356; PMCID: PMC6100752.

Babola TA, Li S, Wang Z, Kersbergen CJ, Elgoyhen AB, Coate TM, Bergles DE. Purinergic Signaling Controls Spontaneous Activity in the Auditory System throughout Early Development. J Neurosci. 2021 Jan 27;41(4):594-612. doi: 10.1523/JNEUROSCI.2178-20.2020. Epub 2020 Dec 10. PMID: 33303678; PMCID: PMC7842760.

Baden T, Berens P, Franke K, Román Rosón M, Bethge M, Euler T. The functional diversity of retinal ganglion cells in the mouse. Nature. 2016 Jan 21;529(7586):345-50. doi: 10.1038/nature16468. Epub 2016 Jan 6. PMID: 26735013; PMCID: PMC4724341.

Bagri A, Marín O, Plump AS, Mak J, Pleasure SJ, Rubenstein JL, Tessier-Lavigne M. Slit proteins prevent midline crossing and determine the dorsoventral position of major axonal pathways in the mammalian forebrain. Neuron. 2002 Jan 17;33(2):233-48. doi: 10.1016/s0896-6273(02)00561-5. PMID: 11804571.

Balasco L, Pagani M, Pangrazzi L, Chelini G, Viscido F, Chama AGC, Galbusera A, Provenzano G, Gozzi A, Bozzi Y. Somatosensory cortex hyperconnectivity and impaired whisker-dependent responses in Cntnap2-/- mice. Neurobiol Dis. 2022 Jul;169:105742. doi: 10.1016/j.nbd.2022.105742. Epub 2022 Apr 26. PMID: 35483565.

Ballester-Rosado CJ, Albright MJ, Wu CS, Liao CC, Zhu J, Xu J, Lee LJ, Lu HC. mGluR5 in cortical excitatory neurons exerts both cell-autonomous and -nonautonomous influences on cortical somatosensory circuit formation. J Neurosci. 2010 Dec 15;30(50):16896-909. doi: 10.1523/JNEUROSCI.2462-10.2010. PMID: 21159961; PMCID: PMC3008407.

Ballester-Rosado CJ, Sun H, Huang JY, Lu HC. mGluR5 Exerts Cell-Autonomous Influences on the Functional and Anatomical Development of Layer IV Cortical Neurons in the Mouse Primary Somatosensory Cortex. J Neurosci. 2016 Aug 24;36(34):8802-14. doi: 10.1523/JNEUROSCI.1224-16.2016. PMID: 27559164; PMCID: PMC4995298.

Bansal A, Singer JH, Hwang BJ, Xu W, Beaudet A, Feller MB. Mice lacking specific nicotinic acetylcholine receptor subunits exhibit dramatically altered spontaneous activity patterns and reveal a limited role for retinal waves in forming ON and OFF circuits in the inner retina. J Neurosci. 2000 Oct 15;20(20):7672-81. doi: 10.1523/JNEUROSCI.20-20-07672.2000. PMID: 11027228; PMCID: PMC6772851.

Bavelier D, Hirshorn EA. I see where you're hearing: how cross-modal plasticity may exploit homologous brain structures. Nat Neurosci. 2010 Nov;13(11):1309-11. doi: 10.1038/nn1110-1309. PMID: 20975752.

Bavelier D, Neville HJ. Cross-modal plasticity: where and how? Nat Rev Neurosci. 2002 Jun;3(6):443-52. doi: 10.1038/nrn848. PMID: 12042879.

Bechara A, Laumonnerie C, Vilain N, Kratochwil CF, Cankovic V, Maiorano NA, Kirschmann MA, Ducret S, Rijli FM. Hoxa2 Selects Barrelette Neuron Identity and Connectivity in the Mouse Somatosensory Brainstem. Cell Rep. 2015 Oct 27;13(4):783-797. doi: 10.1016/j.celrep.2015.09.031. Epub 2015 Oct 17. PMID: 26489473.

Bednar JA, Wilson SP. Cortical Maps. Neuroscientist. 2016 Dec;22(6):604-617. doi: 10.1177/1073858415597645. Epub 2015 Aug 19. PMID: 26290447.

Belford GR, Killackey HP. Anatomical correlates of the forelimb in the ventrobasal complex and the cuneate nucleus of the neonatal rat. Brain Res. 1978 Dec 15;158(2):450-5. doi: 10.1016/0006-8993(78)90688-1. PMID: 81706.

Belford GR, Killackey HP. The development of vibrissae representation in subcortical trigeminal centers of the neonatal rat. J Comp Neurol. 1979 Nov 1;188(1):63-74. doi: 10.1002/cne.901880106. PMID: 500854.

Benamer N, Vidal M, Balia M, Angulo MC. Myelination of parvalbumin interneurons shapes the function of cortical sensory inhibitory circuits. Nat Commun. 2020 Oct 13;11(1):5151. doi: 10.1038/s41467-020-18984-7. PMID: 33051462; PMCID: PMC7555533.

Bender VA, Bender KJ, Brasier DJ, Feldman DE. Two coincidence detectors for spike timing-dependent plasticity in somatosensory cortex. J Neurosci. 2006 Apr 19;26(16):4166-77. doi: 10.1523/JNEUROSCI.0176-06.2006. PMID: 16624937; PMCID: PMC3071735.

Benoit LJ, Holt ES, Posani L, Fusi S, Harris AZ, Canetta S, Kellendonk C. Adolescent thalamic inhibition leads to long-lasting impairments in prefrontal cortex function. Nat Neurosci. 2022 Jun;25(6):714-725. doi: 10.1038/s41593-022-01072-y. Epub 2022 May 19. PMID: 35590075; PMCID: PMC9202412.

Berglund AM, Ryugo DK. Hair cell innervation by spiral ganglion neurons in the mouse. J Comp Neurol. 1987 Jan 22;255(4):560-70. doi: 10.1002/cne.902550408. PMID: 3819031.

Bickford ME. Thalamic Circuit Diversity: Modulation of the Driver/Modulator Framework. Front Neural Circuits. 2016 Jan 12;9:86. doi: 10.3389/fncir.2015.00086. PMID: 26793068; PMCID: PMC4709853.

Bickford ME, Slusarczyk A, Dilger EK, Krahe TE, Kucuk C, Guido W. Synaptic development of the mouse dorsal lateral geniculate nucleus. J Comp Neurol. 2010 Mar 1;518(5):622-35. doi: 10.1002/cne.22223. PMID: 20034053; PMCID: PMC4278806.

Bickford ME, Zhou N, Krahe TE, Govindaiah G, Guido W. Retinal and Tectal "Driver-Like" Inputs Converge in the Shell of the Mouse Dorsal Lateral Geniculate Nucleus. J Neurosci. 2015 Jul 22;35(29):10523-34. doi: 10.1523/JNEUROSCI.3375-14.2015. PMID: 26203147; PMCID: PMC4510292.

Bicknese AR, Sheppard AM, O'Leary DD, Pearlman AL. Thalamocortical axons extend along a chondroitin sulfate proteoglycan-enriched pathway coincident with the neocortical subplate and distinct from the efferent path. J Neurosci. 1994 Jun;14(6):3500-10. doi: 10.1523/JNEUROSCI.14-06-03500.1994. PMID: 8207468; PMCID: PMC6576951.

Bielle F, Marcos-Mondejar P, Keita M, Mailhes C, Verney C, Nguyen Ba-Charvet K, Tessier-Lavigne M, Lopez-Bendito G, Garel S. Slit2 activity in the migration of guidepost neurons shapes thalamic projections during development and evolution. Neuron. 2011 Mar 24;69(6):1085-98. doi: 10.1016/j.neuron.2011.02.026. PMID: 21435555.

Blakemore C, Molnár Z. Factors involved in the establishment of specific interconnections between thalamus and cerebral cortex. Cold Spring Harb Symp Quant Biol. 1990;55:491-504. doi: 10.1101/sqb.1990.055.01.048. PMID: 2132833.

Blankenship AG, Feller MB. Mechanisms underlying spontaneous patterned activity in developing neural circuits. Nat Rev Neurosci. 2010 Jan;11(1):18-29. doi: 10.1038/nrn2759. Epub 2009 Dec 2. PMID: 19953103; PMCID: PMC2902252.

Blankenship AG, Ford KJ, Johnson J, Seal RP, Edwards RH, Copenhagen DR, Feller MB. Synaptic and extrasynaptic factors governing glutamatergic retinal waves. Neuron. 2009 Apr 30;62(2):230-41. doi: 10.1016/j.neuron.2009.03.015. PMID: 19409268; PMCID: PMC2807181.

Blumberg MS, Coleman CM, Gerth AI, McMurray B. Spatiotemporal structure of REM sleep twitching reveals developmental origins of motor synergies. Curr Biol. 2013 Nov 4;23(21):2100-9. doi: 10.1016/j.cub.2013.08.055. Epub 2013 Oct 17. PMID: 24139739; PMCID: PMC3823644.

Blumberg MS, Dooley JC. Phantom Limbs, Neuroprosthetics, and the Developmental Origins of Embodiment. Trends Neurosci. 2017 Oct;40(10):603-612. doi: 10.1016/j.tins.2017.07.003. PMID: 28843655; PMCID: PMC5623093.

Bokor H, Acsády L, Deschênes M. Vibrissal responses of thalamic cells that project to the septal columns of the barrel cortex and to the second somatosensory area. J Neurosci. 2008 May 14;28(20):5169-77. doi: 10.1523/JNEUROSCI.0490-08.2008. PMID: 18480273; PMCID: PMC2631158.

Borello U, Madhavan M, Vilinsky I, Faedo A, Pierani A, Rubenstein J, Campbell K. Sp8 and COUP-TF1 reciprocally regulate patterning and Fgf signaling in cortical progenitors. Cereb Cortex. 2014 Jun;24(6):1409-21. doi: 10.1093/cercor/bhs412. Epub 2013 Jan 10. PMID: 23307639; PMCID: PMC4014177.

Bosman LW, Houweling AR, Owens CB, Tanke N, Shevchouk OT, Rahmati N, Teunissen WH, Ju C, Gong W, Koekkoek SK, De Zeeuw CI. Anatomical pathways involved in generating and sensing rhythmic whisker movements. Front Integr Neurosci. 2011 Oct 4;5:53. doi: 10.3389/fnint.2011.00053. PMID: 22065951; PMCID: PMC3207327.

Braisted JE, Ringstedt T, O'Leary DD. Slits are chemorepellents endogenous to hypothalamus and steer thalamocortical axons into ventral telencephalon. Cereb Cortex. 2009 Jul;19 Suppl 1(Suppl 1):i144-51. doi: 10.1093/cercor/bhp035. Epub 2009 May 11. PMID: 19435711; PMCID: PMC2693534.

Braisted JE, Tuttle R, O'leary DD. Thalamocortical axons are influenced by chemorepellent and chemoattractant activities localized to decision points along their path. Dev Biol. 1999 Apr 15;208(2):430-40. doi: 10.1006/dbio.1999.9216. PMID: 10191056.

Brecht M, Preilowski B, Merzenich MM. Functional architecture of the mystacial vibrissae. Behav Brain Res. 1997 Mar;84(1-2):81-97. doi: 10.1016/s0166-4328(97)83328-1. PMID: 9079775.

Brecht M, Sakmann B. Dynamic representation of whisker deflection by synaptic potentials in spiny stellate and pyramidal cells in the barrels and septa of layer 4 rat somatosensory cortex. J Physiol. 2002 Aug 15;543(Pt 1):49-70. doi: 10.1113/jphysiol.2002.018465. PMID: 12181281; PMCID: PMC2290465.

Briggs F, Usrey WM. Emerging views of corticothalamic function. Curr Opin Neurobiol. 2008 Aug;18(4):403-7. doi: 10.1016/j.conb.2008.09.002. Epub 2008 Oct 6. PMID: 18805486; PMCID: PMC2626162.

Bronchti G, Heil P, Sadka R, Hess A, Scheich H, Wollberg Z. Auditory activation of "visual" cortical areas in the blind mole rat (Spalax ehrenbergi). Eur J Neurosci. 2002 Jul;16(2):311-29. doi: 10.1046/j.1460-9568.2002.02063.x. PMID: 12169112.

Brooks JM, Su J, Levy C, Wang JS, Seabrook TA, Guido W, Fox MA. A molecular mechanism regulating the timing of corticogeniculate innervation. Cell Rep. 2013 Nov 14;5(3):573-81. doi: 10.1016/j.celrep.2013.09.041. Epub 2013 Oct 31. PMID: 24183669; PMCID: PMC3849812.

Brown A, Yates PA, Burrola P, Ortuño D, Vaidya A, Jessell TM, Pfaff SL, O'Leary DD, Lemke G. Topographic mapping from the retina to the midbrain is controlled by relative but not absolute levels of EphA receptor signaling. Cell. 2000 Jul 7;102(1):77-88. doi: 10.1016/s0092-8674(00)00012-x. PMID: 10929715.

Bruno RM, Sakmann B. Cortex is driven by weak but synchronously active thalamocortical synapses. Science. 2006 Jun 16;312(5780):1622-7. doi: 10.1126/science.1124593. PMID: 16778049.

Burbridge TJ, Xu HP, Ackman JB, Ge X, Zhang Y, Ye MJ, Zhou ZJ, Xu J, Contractor A, Crair MC. Visual circuit development requires patterned activity mediated by retinal acetylcholine receptors. Neuron. 2014 Dec 3;84(5):1049-64. doi: 10.1016/j.neuron.2014.10.051. Epub 2014 Nov 20. PMID: 25466916; PMCID: PMC4258148.

Bureau I, von Saint Paul F, Svoboda K. Interdigitated paralemniscal and lemniscal pathways in the mouse barrel cortex. PLoS Biol. 2006 Nov;4(12):e382. doi: 10.1371/journal.pbio.0040382. Erratum in: PLoS Biol. 2007 Jan;5(1):e28. PMID: 17121453; PMCID: PMC1637129.

Butler AB. Evolution of the thalamus: a morphological and functional review. Thalamus & Related Systems. 2008;4(1):35-58. doi:10.1017/S1472928808000356

Cabelli RJ, Shelton DL, Segal RA, Shatz CJ. Blockade of endogenous ligands of trkB inhibits formation of ocular dominance columns. Neuron. 1997 Jul;19(1):63-76. doi: 10.1016/s0896-6273(00)80348-7. PMID: 9247264.

Cadwell CR, Bhaduri A, Mostajo-Radji MA, Keefe MG, Nowakowski TJ. Development and Arealization of the Cerebral Cortex. Neuron. 2019 Sep 25;103(6):980-1004. doi: 10.1016/j.neuron.2019.07.009. PMID: 31557462; PMCID: PMC9245854.

Callejas-Marin A, Moreno-Bravo JA, Company V, Madrigal MP, Almagro-García F, Martínez S, Puelles E. Gli2-Mediated Shh Signaling Is Required for Thalamocortical Projection Guidance. Front Neuroanat. 2022 Feb 10;16:830758. doi: 10.3389/fnana.2022.830758. PMID: 35221935; PMCID: PMC8866834.

Cang J, Feldheim DA. Developmental mechanisms of topographic map formation and alignment. Annu Rev Neurosci. 2013 Jul 8;36:51-77. doi: 10.1146/annurev-neuro-062012-170341. Epub 2013 Apr 29. PMID: 23642132.

Cardon G, Sharma A. Somatosensory Cross-Modal Reorganization in Adults With Age-Related, Early-Stage Hearing Loss. Front Hum Neurosci. 2018 May 3;12:172. doi: 10.3389/fnhum.2018.00172. PMID: 29773983; PMCID: PMC5943502.

Cases O, Vitalis T, Seif I, De Maeyer E, Sotelo C, Gaspar P. Lack of barrels in the somatosensory cortex of monoamine oxidase A-deficient mice: role of a serotonin excess during the critical period. Neuron. 1996 Feb;16(2):297-307. doi: 10.1016/s0896-6273(00)80048-3. PMID: 8789945.

Castillo-Paterna M, Moreno-Juan V, Filipchuk A, Rodríguez-Malmierca L, Susín R, López-Bendito G. DCC functions as an accelerator of thalamocortical axonal growth downstream of spontaneous thalamic activity. EMBO Rep. 2015 Jul;16(7):851-62. doi: 10.15252/embr.201439882. Epub 2015 May 6. PMID: 25947198; PMCID: PMC4515124.

Caviness VS Jr, Frost DO. Tangential organization of thalamic projections to the neocortex in the mouse. J Comp Neurol. 1980 Nov 15;194(2):335-67. doi: 10.1002/cne.901940205. PMID: 7440805.

Chabot N, Charbonneau V, Laramée ME, Tremblay R, Boire D, Bronchti G. Subcortical auditory input to the primary visual cortex in anophthalmic mice. Neurosci Lett. 2008 Mar 12;433(2):129-34. doi: 10.1016/j.neulet.2008.01.003. Epub 2008 Jan 10. PMID: 18276073.

Chabot N, Robert S, Tremblay R, Miceli D, Boire D, Bronchti G. Audition differently activates the visual system in neonatally enucleated mice compared with anophthalmic mutants. Eur J Neurosci. 2007 Oct;26(8):2334-48. doi: 10.1111/j.1460-9568.2007.05854.x. PMID: 17953622.

Charbonneau V, Laramée ME, Boucher V, Bronchti G, Boire D. Cortical and subcortical projections to primary visual cortex in anophthalmic, enucleated and sighted mice. Eur J Neurosci. 2012 Oct;36(7):2949-63. doi: 10.1111/j.1460-9568.2012.08215.x. Epub 2012 Jul 11. PMID: 22780435.

Chatterjee M, Guo Q, Weber S, Scholpp S, Li JY. Pax6 regulates the formation of the habenular nuclei by controlling the temporospatial expression of Shh in the diencephalon in vertebrates. BMC Biol. 2014 Feb 14;12:13. doi: 10.1186/1741-7007-12-13. PMID: 24528677; PMCID: PMC3996077.

Chatterjee M, Li JY. Patterning and compartment formation in the diencephalon. Front Neurosci. 2012 May 11;6:66. doi: 10.3389/fnins.2012.00066. PMID: 22593732; PMCID: PMC3349951.

Che A, Babij R, Iannone AF, Fetcho RN, Ferrer M, Liston C, Fishell G, De Marco García NV. Layer I Interneurons Sharpen Sensory Maps during Neonatal Development. Neuron. 2018 Jul 11;99(1):98-116.e7. doi: 10.1016/j.neuron.2018.06.002. Epub 2018 Jun 21. PMID: 29937280; PMCID: PMC6152945.

Chen L, Guo Q, Li JY. Transcription factor Gbx2 acts cell-nonautonomously to regulate the formation of lineage-restriction boundaries of the thalamus. Development. 2009 Apr;136(8):1317-26. doi: 10.1242/dev.030510. Epub 2009 Mar 11. PMID: 19279136; PMCID: PMC2687463.

Chen Y, Magnani D, Theil T, Pratt T, Price DJ. Evidence that descending cortical axons are essential for thalamocortical axons to cross the pallial-subpallial boundary in the embryonic forebrain. PLoS One. 2012;7(3):e33105. doi: 10.1371/journal.pone.0033105. Epub 2012 Mar 8. PMID: 22412988; PMCID: PMC3297629.

Chen S, Rahn RM, Bice AR, Bice SH, Padawer-Curry JA, Hengen KB, Dougherty JD, Culver JP. Visual Deprivation during Mouse Critical Period Reorganizes Network-Level Functional Connectivity. J Neurosci. 2024 May 8;44(19):e1019232024. doi: 10.1523/JNEUROSCI.1019-23.2024. PMID: 38538145; PMCID: PMC11079959.

Chou SJ, Babot Z, Leingärtner A, Studer M, Nakagawa Y, O'Leary DD. Geniculocortical input drives genetic distinctions between primary and higher-order visual areas. Science. 2013 Jun 7;340(6137):1239-42. doi: 10.1126/science.1232806. PMID: 23744949; PMCID: PMC3851411.

Clark WE. A MORPHOLOGICAL STUDY OF THE LATERAL GENICULATE BODY. Br J Ophthalmol. 1932 May;16(5):264-84. doi: 10.1136/bjo.16.5.264. PMID: 18169029; PMCID: PMC511418.

Clascá F, Angelucci A, Sur M. Layer-specific programs of development in neocortical projection neurons. Proc Natl Acad Sci U S A. 1995 Nov 21;92(24):11145-9. doi: 10.1073/pnas.92.24.11145. PMID: 7479954; PMCID: PMC40588.

Coate TM, Scott MK, Gurjar M. Current concepts in cochlear ribbon synapse formation. Synapse. 2019 May;73(5):e22087. doi: 10.1002/syn.22087. Epub 2019 Feb 18. PMID: 30592086; PMCID: PMC6573016.

Craddock R, Vasalauskaite A, Ranson A, Sengpiel F. Experience dependent plasticity of higher visual cortical areas in the mouse. Cereb Cortex. 2023 Jul 24;33(15):9303-9312. doi: 10.1093/cercor/bhad203. PMID: 37279562; PMCID: PMC10393491.

Cramer KS. Eph proteins and the assembly of auditory circuits. Hear Res. 2005 Aug;206(1-2):42-51. doi: 10.1016/j.heares.2004.11.024. PMID: 16080997.

Crandall SR, Patrick SL, Cruikshank SJ, Connors BW. Infrabarrels Are Layer 6 Circuit Modules in the Barrel Cortex that Link Long-Range Inputs and Outputs. Cell Rep. 2017 Dec 12;21(11):3065-3078. doi: 10.1016/j.celrep.2017.11.049. PMID: 29241536; PMCID: PMC5736017.

Datwani A, Iwasato T, Itohara S, Erzurumlu RS. NMDA receptor-dependent pattern transfer from afferents to postsynaptic cells and dendritic differentiation in the barrel cortex. Mol Cell Neurosci. 2002 Nov;21(3):477-92. doi: 10.1006/mcne.2002.1195. PMID: 12498788; PMCID: PMC3564661.

Dawson DR, Killackey HP. The organization and mutability of the forepaw and hindpaw representations in the somatosensory cortex of the neonatal rat. J Comp Neurol. 1987 Feb 8;256(2):246-56. doi: 10.1002/cne.902560205. PMID: 3558880.

De Carlos JA, O'Leary DD. Growth and targeting of subplate axons and establishment of major cortical pathways. J Neurosci. 1992 Apr;12(4):1194-211. doi: 10.1523/JNEUROSCI.12-04-01194.1992. Erratum in: J Neurosci 1993 Mar;13(3):followi. PMID: 1556593; PMCID: PMC6575791.

De Marco García NV, Priya R, Tuncdemir SN, Fishell G, Karayannis T. Sensory inputs control the integration of neurogliaform interneurons into cortical circuits. Nat Neurosci. 2015 Mar;18(3):393-401. doi: 10.1038/nn.3946. Epub 2015 Feb 9. PMID: 25664912; PMCID: PMC4624196.

Deck M, Lokmane L, Chauvet S, Mailhes C, Keita M, Niquille M, Yoshida M, Yoshida Y, Lebrand C, Mann F, Grove EA, Garel S. Pathfinding of corticothalamic axons relies on a rendezvous with thalamic projections. Neuron. 2013 Feb 6;77(3):472-84. doi: 10.1016/j.neuron.2012.11.031. PMID: 23395374; PMCID: PMC3756696.

Dehay C, Giroud P, Berland M, Killackey H, Kennedy H. Contribution of thalamic input to the specification of cytoarchitectonic cortical fields in the primate: effects of bilateral enucleation in the fetal monkey on the boundaries, dimensions, and gyrification of striate and

extrastriate cortex. J Comp Neurol. 1996 Mar 25;367(1):70-89. doi: 10.1002/(SICI)1096-9861(19960325)367:1<70::AID-CNE6>3.0.CO;2-G. PMID: 8867284.

Del Río JA, Martínez A, Auladell C, Soriano E. Developmental history of the subplate and developing white matter in the murine neocortex. Neuronal organization and relationship with the main afferent systems at embryonic and perinatal stages. Cereb Cortex. 2000 Aug;10(8):784-801. doi: 10.1093/cercor/10.8.784. PMID: 10920050.

Delogu A, Sellers K, Zagoraiou L, Bocianowska-Zbrog A, Mandal S, Guimera J, Rubenstein JL, Sugden D, Jessell T, Lumsden A. Subcortical visual shell nuclei targeted by ipRGCs develop from a Sox14+-GABAergic progenitor and require Sox14 to regulate daily activity rhythms. Neuron. 2012 Aug 23;75(4):648-62. doi: 10.1016/j.neuron.2012.06.013. PMID: 22920256.

Deschênes, M. & Urbain, N. (2009) Vibrissal afferents from trigeminus to cortices. Scholarpedia, 4, 7454.

Di Bella DJ, Habibi E, Stickels RR, Scalia G, Brown J, Yadollahpour P, Yang SM, Abbate C, Biancalani T, Macosko EZ, Chen F, Regev A, Arlotta P. Molecular logic of cellular diversification in the mouse cerebral cortex. Nature. 2021 Jul;595(7868):554-559. doi: 10.1038/s41586-021-03670-5. Epub 2021 Jun 23. Erratum in: Nature. 2021 Aug;596(7873):E11. doi: 10.1038/s41586-021-03797-5. PMID: 34163074; PMCID: PMC9006333.

Diamond IT, Jones EG, Powell TP. The projection of the auditory cortex upon the diencephalon and brain stem in the cat. Brain Res. 1969 Oct;15(2):305-40. doi: 10.1016/0006-8993(69)90160-7. PMID: 5344373.

Diamond ME, von Heimendahl M, Knutsen PM, Kleinfeld D, Ahissar E. 'Where' and 'what' in the whisker sensorimotor system. Nat Rev Neurosci. 2008 Aug;9(8):601-12. doi: 10.1038/nrn2411. Erratum in: Nat Rev Neurosci. 2008 Sep;9(9):709. PMID: 18641667.

Ding YQ, Yin J, Xu HM, Jacquin MF, Chen ZF. Formation of whisker-related principal sensory nucleus-based lemniscal pathway requires a paired homeodomain transcription factor, Drg11. J Neurosci. 2003 Aug 13;23(19):7246-54. doi: 10.1523/JNEUROSCI.23-19-07246.2003. PMID: 12917357; PMCID: PMC6740446.

Dobin A, Davis CA, Schlesinger F, Drenkow J, Zaleski C, Jha S, Batut P, Chaisson M, Gingeras TR. STAR: ultrafast universal RNA-seq aligner. Bioinformatics. 2013 Jan

1;29(1):15-21. doi: 10.1093/bioinformatics/bts635. Epub 2012 Oct 25. PMID: 23104886; PMCID: PMC3530905.

Dooley JC, Glanz RM, Sokoloff G, Blumberg MS. Self-Generated Whisker Movements Drive State-Dependent Sensory Input to Developing Barrel Cortex. Curr Biol. 2020 Jun 22;30(12):2404-2410.e4. doi: 10.1016/j.cub.2020.04.045. Epub 2020 May 14. PMID: 32413304; PMCID: PMC7314650.

Dräger UC, Olsen JF. Origins of crossed and uncrossed retinal projections in pigmented and albino mice. J Comp Neurol. 1980 Jun;191(3):383-412. doi: 10.1002/cne.901910306. PMID: 7410600.

Dufour A, Seibt J, Passante L, Depaepe V, Ciossek T, Frisén J, Kullander K, Flanagan JG, Polleux F, Vanderhaeghen P. Area specificity and topography of thalamocortical projections are controlled by ephrin/Eph genes. Neuron. 2003 Jul 31;39(3):453-65. doi: 10.1016/s0896-6273(03)00440-9. PMID: 12895420.

Dupont E, Hanganu IL, Kilb W, Hirsch S, Luhmann HJ. Rapid developmental switch in the mechanisms driving early cortical columnar networks. Nature. 2006 Jan 5;439(7072):79-83. doi: 10.1038/nature04264. Epub 2005 Dec 4. PMID: 16327778.

Dye CA, Abbott CW, Huffman KJ. Bilateral enucleation alters gene expression and intraneocortical connections in the mouse. Neural Dev. 2012 Jan 30;7:5. doi: 10.1186/1749-8104-7-5. PMID: 22289655; PMCID: PMC3347983.

Eckrich T, Blum K, Milenkovic I, Engel J. Fast Ca2+ Transients of Inner Hair Cells Arise Coupled and Uncoupled to Ca2+ Waves of Inner Supporting Cells in the Developing Mouse Cochlea. Front Mol Neurosci. 2018 Jul 30;11:264. doi: 10.3389/fnmol.2018.00264. PMID: 30104958; PMCID: PMC6077211.

Egger V, Nevian T, Bruno RM. Subcolumnar dendritic and axonal organization of spiny stellate and star pyramid neurons within a barrel in rat somatosensory cortex. Cereb Cortex. 2008 Apr;18(4):876-89. doi: 10.1093/cercor/bhm126. Epub 2007 Jul 26. PMID: 17656622.

El-Danaf RN, Huberman AD. Sub-topographic maps for regionally enhanced analysis of visual space in the mouse retina. J Comp Neurol. 2019 Jan 1;527(1):259-269. doi: 10.1002/cne.24457. Epub 2018 Dec 19. PMID: 29675855; PMCID: PMC6506235.

Ellsworth CA, Lyckman AW, Feldheim DA, Flanagan JG, Sur M. Ephrin-A2 and -A5 influence patterning of normal and novel retinal projections to the thalamus: conserved mapping mechanisms in visual and auditory thalamic targets. J Comp Neurol. 2005 Jul 25;488(2):140-51. doi: 10.1002/cne.20602. PMID: 15924339.

Erskine L, Herrera E. Connecting the retina to the brain. ASN Neuro. 2014 Dec 12;6(6):1759091414562107. doi: 10.1177/1759091414562107. PMID: 25504540; PMCID: PMC4720220.

Erzurumlu RS. Critical period for the whisker-barrel system. Exp Neurol. 2010 Mar;222(1):10-2. doi: 10.1016/j.expneurol.2009.12.025. Epub 2010 Jan 4. PMID: 20045409; PMCID: PMC3700571.

Erzurumlu RS, Gaspar P. Development and critical period plasticity of the barrel cortex. Eur J Neurosci. 2012 May;35(10):1540-53. doi: 10.1111/j.1460-9568.2012.08075.x. PMID: 22607000; PMCID: PMC3359866.

Erzurumlu RS, Gaspar P. How the Barrel Cortex Became a Working Model for Developmental Plasticity: A Historical Perspective. J Neurosci. 2020 Aug 19;40(34):6460-6473. doi: 10.1523/JNEUROSCI.0582-20.2020. PMID: 32817388; PMCID: PMC7486654.

Erzurumlu RS, Jhaveri S. Emergence of connectivity in the embryonic rat parietal cortex. Cereb Cortex. 1992 Jul-Aug;2(4):336-52. doi: 10.1093/cercor/2.4.336. PMID: 1422091.

Erzurumlu RS, Killackey HP. Development of order in the rat trigeminal system. J Comp Neurol. 1983 Feb 1;213(4):365-80. doi: 10.1002/cne.902130402. PMID: 6601119.

Fagard J, Esseily R, Jacquey L, O'Regan K, Somogyi E. Fetal Origin of Sensorimotor Behavior. Front Neurorobot. 2018 May 23;12:23. doi: 10.3389/fnbot.2018.00023. PMID: 29875649; PMCID: PMC5974044.

Fariñas I, Jones KR, Tessarollo L, Vigers AJ, Huang E, Kirstein M, de Caprona DC, Coppola V, Backus C, Reichardt LF, Fritzsch B. Spatial shaping of cochlear innervation by temporally regulated neurotrophin expression. J Neurosci. 2001 Aug 15;21(16):6170-80. doi: 10.1523/JNEUROSCI.21-16-06170.2001. PMID: 11487640; PMCID: PMC2710117.

Feldman DE, Brecht M. Map plasticity in somatosensory cortex. Science. 2005 Nov 4;310(5749):810-5. doi: 10.1126/science.1115807. PMID: 16272113.

Feldmeyer D. Excitatory neuronal connectivity in the barrel cortex. Front Neuroanat. 2012 Jul 11;6:24. doi: 10.3389/fnana.2012.00024. PMID: 22798946; PMCID: PMC3394394.

Feldmeyer D, Lübke J, Silver RA, Sakmann B. Synaptic connections between layer 4 spiny neurone-layer 2/3 pyramidal cell pairs in juvenile rat barrel cortex: physiology and anatomy of interlaminar signalling within a cortical column. J Physiol. 2002 Feb 1;538(Pt 3):803-22. doi: 10.1113/jphysiol.2001.012959. PMID: 11826166; PMCID: PMC2290091.

Feller MB, Wellis DP, Stellwagen D, Werblin FS, Shatz CJ. Requirement for cholinergic synaptic transmission in the propagation of spontaneous retinal waves. Science. 1996 May 24;272(5265):1182-7. doi: 10.1126/science.272.5265.1182. PMID: 8638165.

Fernandez LM, Vantomme G, Osorio-Forero A, Cardis R, Béard E, Lüthi A. Thalamic reticular control of local sleep in mouse sensory cortex. Elife. 2018 Dec 25;7:e39111. doi: 10.7554/eLife.39111. PMID: 30583750; PMCID: PMC6342525.

Ferran JL, de Oliveira ED, Merchán P, Sandoval JE, Sánchez-Arrones L, Martínez-De-La-Torre M, Puelles L. Genoarchitectonic profile of developing nuclear groups in the chicken pretectum. J Comp Neurol. 2009 Dec 1;517(4):405-51. doi: 10.1002/cne.22115. PMID: 19790262.

Fetter-Pruneda I, Geovannini-Acuña H, Santiago C, Ibarrarán-Viniegra AS, Martínez-Martínez E, Sandoval-Velasco M, Uribe-Figueroa L, Padilla-Cortés P, Mercado-Célis G, Gutiérrez-Ospina G. Shifts in developmental timing, and not increased levels of experience-dependent neuronal activity, promote barrel expansion in the primary somatosensory cortex of rats enucleated at birth. PLoS One. 2013;8(1):e54940. doi: 10.1371/journal.pone.0054940. Epub 2013 Jan 25. PMID: 23372796; PMCID: PMC3556040.

Firth SI, Wang CT, Feller MB. Retinal waves: mechanisms and function in visual system development. Cell Calcium. 2005 May;37(5):425-32. doi: 10.1016/j.ceca.2005.01.010. PMID: 15820390.

Fishell G, Kriegstein AR. Neurons from radial glia: the consequences of asymmetric inheritance. Curr Opin Neurobiol. 2003 Feb;13(1):34-41. doi: 10.1016/s0959-4388(03)00013-8. PMID: 12593980.

Foeller E, Feldman DE. Synaptic basis for developmental plasticity in somatosensory cortex. Curr Opin Neurobiol. 2004 Feb;14(1):89-95. doi: 10.1016/j.conb.2004.01.011. PMID: 15018943.

Ford KJ, Félix AL, Feller MB. Cellular mechanisms underlying spatiotemporal features of cholinergic retinal waves. J Neurosci. 2012 Jan 18;32(3):850-63. doi: 10.1523/JNEUROSCI.5309-12.2012. PMID: 22262883; PMCID: PMC3311224.

Fox K, Schlaggar BL, Glazewski S, O'Leary DD. Glutamate receptor blockade at cortical synapses disrupts development of thalamocortical and columnar organization in somatosensory cortex. Proc Natl Acad Sci U S A. 1996 May 28;93(11):5584-9. doi: 10.1073/pnas.93.11.5584. PMID: 8643619; PMCID: PMC39290.

Fox K, Wong RO. A comparison of experience-dependent plasticity in the visual and somatosensory systems. Neuron. 2005 Nov 3;48(3):465-77. doi: 10.1016/j.neuron.2005.10.013. PMID: 16269363.

Fox, K. & Woolsey, T., 2009. Anatomical pathways. In Barrel Cortex. Cambridge: Cambridge University Press, pp. 14–48.

Franco SJ, Gil-Sanz C, Martinez-Garay I, Espinosa A, Harkins-Perry SR, Ramos C, Müller U. Fate-restricted neural progenitors in the mammalian cerebral cortex. Science. 2012 Aug 10;337(6095):746-9. doi: 10.1126/science.1223616. PMID: 22879516; PMCID: PMC4287277.

Frangeul L, Pouchelon G, Telley L, Lefort S, Luscher C, Jabaudon D. A cross-modal genetic framework for the development and plasticity of sensory pathways. Nature. 2016 Oct 6;538(7623):96-98. doi: 10.1038/nature19770. Epub 2016 Sep 26. PMID: 27669022.

Fries P. Neuronal gamma-band synchronization as a fundamental process in cortical computation. Annu Rev Neurosci. 2009;32:209-24. doi: 10.1146/annurev.neuro.051508.135603. PMID: 19400723.

Frost DO, Caviness VS Jr. Radial organization of thalamic projections to the neocortex in the mouse. J Comp Neurol. 1980 Nov 15;194(2):369-93. doi: 10.1002/cne.901940206. PMID: 7440806.

Froud KE, Wong AC, Cederholm JM, Klugmann M, Sandow SL, Julien JP, Ryan AF, Housley GD. Type II spiral ganglion afferent neurons drive medial olivocochlear reflex suppression of the cochlear amplifier. Nat Commun. 2015 May 12;6:7115. doi: 10.1038/ncomms8115. PMID: 25965946; PMCID: PMC4432632.

Fukuchi-Shimogori T, Grove EA. Neocortex patterning by the secreted signaling molecule FGF8. Science. 2001 Nov 2;294(5544):1071-4. doi: 10.1126/science.1064252. Epub 2001 Sep 20. PMID: 11567107.

Gao P, Postiglione MP, Krieger TG, Hernandez L, Wang C, Han Z, Streicher C, Papusheva E, Insolera R, Chugh K, Kodish O, Huang K, Simons BD, Luo L, Hippenmeyer S, Shi SH. Deterministic progenitor behavior and unitary production of neurons in the neocortex. Cell. 2014 Nov 6;159(4):775-88. doi: 10.1016/j.cell.2014.10.027. PMID: 25417155; PMCID: PMC4225456.

Garel S, López-Bendito G. Inputs from the thalamocortical system on axon pathfinding mechanisms. Curr Opin Neurobiol. 2014 Aug;27:143-50. doi: 10.1016/j.conb.2014.03.013. Epub 2014 Apr 17. PMID: 24742382.

Garel S, Rubenstein JL. Intermediate targets in formation of topographic projections: inputs from the thalamocortical system. Trends Neurosci. 2004 Sep;27(9):533-9. doi: 10.1016/j.tins.2004.06.014. PMID: 15331235.

Gaspar P, Erzurumlu R. The birth of the barrels. Dev Cell. 2013 Oct 14;27(1):3-4. doi: 10.1016/j.devcel.2013.09.028. PMID: 24135227; PMCID: PMC6044471.

Gaspar P, Renier N. Constraints on somatosensory map development: mutants lead the way. Curr Opin Neurobiol. 2018 Dec;53:43-49. doi: 10.1016/j.conb.2018.04.028. Epub 2018 May 10. PMID: 29753205.

Geal-Dor M, Freeman S, Li G, Sohmer H. Development of hearing in neonatal rats: air and bone conducted ABR thresholds. Hear Res. 1993 Sep;69(1-2):236-42. doi: 10.1016/0378-5955(93)90113-f. PMID: 8226345.

Gezelius H, López-Bendito G. Thalamic neuronal specification and early circuit formation. Dev Neurobiol. 2017 Jul;77(7):830-843. doi: 10.1002/dneu.22460. Epub 2016 Nov 4. PMID: 27739248.

Gezelius H, Moreno-Juan V, Mezzera C, Thakurela S, Rodríguez-Malmierca LM, Pistolic J, Benes V, Tiwari VK, López-Bendito G. Genetic Labeling of Nuclei-Specific Thalamocortical Neurons Reveals Putative Sensory-Modality Specific Genes. Cereb Cortex. 2017 Nov 1;27(11):5054-5069. doi: 10.1093/cercor/bhw290. PMID: 27655933; PMCID: PMC7610997.

Gheorghita F, Kraftsik R, Dubois R, Welker E. Structural basis for map formation in the thalamocortical pathway of the barrelless mouse. J Neurosci. 2006 Sep 27;26(39):10057-67. doi: 10.1523/JNEUROSCI.1263-06.2006. PMID: 17005869; PMCID: PMC6674479.

Glowatzki E, Fuchs PA. Transmitter release at the hair cell ribbon synapse. Nat Neurosci. 2002 Feb;5(2):147-54. doi: 10.1038/nn796. PMID: 11802170.

Godement P, Salaün J, Imbert M. Prenatal and postnatal development of retinogeniculate and retinocollicular projections in the mouse. J Comp Neurol. 1984 Dec 20;230(4):552-75. doi: 10.1002/cne.902300406. PMID: 6520251.

Goldreich D, Kanics IM. Performance of blind and sighted humans on a tactile grating detection task. Percept Psychophys. 2006 Nov;68(8):1363-71. doi: 10.3758/bf03193735. PMID: 17378422.

Golshani P, Gonçalves JT, Khoshkhoo S, Mostany R, Smirnakis S, Portera-Cailliau C. Internally mediated developmental desynchronization of neocortical network activity. J Neurosci. 2009 Sep 2;29(35):10890-9. doi: 10.1523/JNEUROSCI.2012-09.2009. PMID: 19726647; PMCID: PMC2771734.

Gorski JA, Talley T, Qiu M, Puelles L, Rubenstein JL, Jones KR. Cortical excitatory neurons and glia, but not GABAergic neurons, are produced in the Emx1-expressing lineage. J Neurosci. 2002 Aug 1;22(15):6309-14. doi: 10.1523/JNEUROSCI.22-15-06309.2002. PMID: 12151506; PMCID: PMC6758181.

Grant E, Hoerder-Suabedissen A, Molnár Z. Development of the corticothalamic projections. Front Neurosci. 2012 May 4;6:53. doi: 10.3389/fnins.2012.00053. PMID: 22586359; PMCID: PMC3343305.

Grant E, Hoerder-Suabedissen A, Molnár Z. The Regulation of Corticofugal Fiber Targeting by Retinal Inputs. Cereb Cortex. 2016 Mar;26(3):1336-1348. doi: 10.1093/cercor/bhv315. Epub 2016 Jan 6. PMID: 26744542; PMCID: PMC4737616.

Greig LC, Woodworth MB, Galazo MJ, Padmanabhan H, Macklis JD. Molecular logic of neocortical projection neuron specification, development and diversity. Nat Rev Neurosci. 2013 Nov;14(11):755-69. doi: 10.1038/nrn3586. Epub 2013 Oct 9. PMID: 24105342; PMCID: PMC3876965.

Greig LC, Woodworth MB, Greppi C, Macklis JD. Ctip1 Controls Acquisition of Sensory Area Identity and Establishment of Sensory Input Fields in the Developing Neocortex. Neuron. 2016 Apr 20;90(2):261-77. doi: 10.1016/j.neuron.2016.03.008. PMID: 27100196; PMCID: PMC4873772.

Gribizis A, Ge X, Daigle TL, Ackman JB, Zeng H, Lee D, Crair MC. Visual Cortex Gains Independence from Peripheral Drive before Eye Opening. Neuron. 2019 Nov 20;104(4):711-723.e3. doi: 10.1016/j.neuron.2019.08.015. Epub 2019 Sep 24. PMID: 31561919; PMCID: PMC6872942.

Grove EA, Fukuchi-Shimogori T. Generating the cerebral cortical area map. Annu Rev Neurosci. 2003;26:355-80. doi: 10.1146/annurev.neuro.26.041002.131137. PMID: 14527269.

Gu Z, Hübschmann D. simplifyEnrichment: A Bioconductor Package for Clustering and Visualizing Functional Enrichment Results. Genomics Proteomics Bioinformatics. 2023 Feb;21(1):190-202. doi: 10.1016/j.gpb.2022.04.008. Epub 2022 Jun 6. PMID: 35680096; PMCID: PMC10373083.

Guillamón-Vivancos T, Aníbal-Martínez M, Puche-Aroca L, Moreno-Bravo JA, Valdeolmillos M, Martini FJ, López-Bendito G. Input-dependent segregation of visual and somatosensory circuits in the mouse superior colliculus. Science. 2022 Aug 19;377(6608):845-850. doi: 10.1126/science.abq2960. Epub 2022 Aug 18. PMID: 35981041; PMCID: PMC7614159.

Guillery RW. Patterns of fiber degeneration in the dorsal lateral geniculate nucleus of the cat following lesions in the visual cortex. J Comp Neurol. 1967 Jul;130(3):197-221. doi: 10.1002/cne.901300303. PMID: 6036110.

Guillery RW. Retinal representations. Science. 1995 Feb 17;267(5200):1038. doi: 10.1126/science.7863333. PMID: 7863333.

Guillery RW, Sherman SM (2002) The thalamus as a monitor of motor outputs. Philosophical Transactions of the Royal Society B: Biological Sciences 357:1809–1821.

Guillery RW, Sherman SM. The thalamus as a monitor of motor outputs. Philos Trans R Soc Lond B Biol Sci. 2002 Dec 29;357(1428):1809-21. doi: 10.1098/rstb.2002.1171. PMID: 12626014; PMCID: PMC1693090.

Guo C, Eckler MJ, McKenna WL, McKinsey GL, Rubenstein JL, Chen B. Fezf2 expression identifies a multipotent progenitor for neocortical projection neurons, astrocytes, and oligodendrocytes. Neuron. 2013 Dec 4;80(5):1167-74. doi: 10.1016/j.neuron.2013.09.037. PMID: 24314728; PMCID: PMC3857588.

Hagihara KM, Murakami T, Yoshida T, Tagawa Y, Ohki K. Neuronal activity is not required for the initial formation and maturation of visual selectivity. Nat Neurosci. 2015 Dec;18(12):1780-8. doi: 10.1038/nn.4155. Epub 2015 Nov 2. PMID: 26523644.

Hamasaki T, Leingärtner A, Ringstedt T, O'Leary DD. EMX2 regulates sizes and positioning of the primary sensory and motor areas in neocortex by direct specification of cortical progenitors. Neuron. 2004 Aug 5;43(3):359-72. doi: 10.1016/j.neuron.2004.07.016. PMID: 15294144.

Hamburger V, Narayanan CH. Effects of the deafferentation of the trigeminal area on the motility of the chick embryo. J Exp Zool. 1969 Apr;170(4):411-26. doi: 10.1002/jez.1401700404. PMID: 5804915.

Hamburger, V., Wenger, E., and Oppenheim, R. (1966). Motility in the chick embryo in the absence of sensory input. J. Exp. Zool. 1966 July;162, 133–159. doi: 10.1002/jez.1401620202.

Hannan AJ, Blakemore C, Katsnelson A, Vitalis T, Huber KM, Bear M, Roder J, Kim D, Shin HS, Kind PC. PLC-beta1, activated via mGluRs, mediates activity-dependent differentiation in cerebral cortex. Nat Neurosci. 2001 Mar;4(3):282-8. doi: 10.1038/85132. PMID: 11224545.

Hanganu-Opatz IL. Between molecules and experience: role of early patterns of coordinated activity for the development of cortical maps and sensory abilities. Brain Res Rev. 2010 Sep;64(1):160-76. doi: 10.1016/j.brainresrev.2010.03.005. Epub 2010 Apr 8. PMID: 20381527.

Hanson MG, Landmesser LT. Normal patterns of spontaneous activity are required for correct motor axon guidance and the expression of specific guidance molecules. Neuron. 2004 Sep 2;43(5):687-701. doi: 10.1016/j.neuron.2004.08.018. PMID: 15339650.

Harrus AG, Ceccato JC, Sendin G, Bourien J, Puel JL, Nouvian R. Spiking Pattern of the Mouse Developing Inner Hair Cells Is Mostly Invariant Along the Tonotopic Axis. Front Cell Neurosci. 2018 Nov 14;12:407. doi: 10.3389/fncel.2018.00407. PMID: 30524238; PMCID: PMC6262317.

Hensch TK. Critical period mechanisms in developing visual cortex. Curr Top Dev Biol. 2005;69:215-37. doi: 10.1016/S0070-2153(05)69008-4. PMID: 16243601.

Hensch TK. Critical period regulation. Annu Rev Neurosci. 2004;27:549-79. doi: 10.1146/annurev.neuro.27.070203.144327. PMID: 15217343.

Herrera CG, Tarokh L. A Thalamocortical Perspective on Sleep Spindle Alterations in Neurodevelopmental Disorders. Curr Sleep Med Rep. 2024;10(2):103-118. doi: 10.1007/s40675-024-00284-x. Epub 2024 Mar 11. PMID: 38764858; PMCID: PMC11096120.

Herrero-Navarro Á, Puche-Aroca L, Moreno-Juan V, Sempere-Ferràndez A, Espinosa A, Susín R, Torres-Masjoan L, Leyva-Díaz E, Karow M, Figueres-Oñate M, López-Mascaraque L, López-Atalaya JP, Berninger B, López-Bendito G. Astrocytes and neurons share region-specific transcriptional signatures that confer regional identity to neuronal reprogramming. Sci Adv. 2021 Apr 7;7(15):eabe8978. doi: 10.1126/sciadv.abe8978. PMID: 33827819; PMCID: PMC8026135.

Herrmann K, Shatz CJ. Blockade of action potential activity alters initial arborization of thalamic axons within cortical layer 4. Proc Natl Acad Sci U S A. 1995 Nov 21;92(24):11244-8. doi: 10.1073/pnas.92.24.11244. PMID: 7479973; PMCID: PMC40608.

Hodge LK, Klassen MP, Han BX, Yiu G, Hurrell J, Howell A, Rousseau G, Lemaigre F, Tessier-Lavigne M, Wang F. Retrograde BMP signaling regulates trigeminal sensory neuron identities and the formation of precise face maps. Neuron. 2007 Aug 16;55(4):572-86. doi: 10.1016/j.neuron.2007.07.010. PMID: 17698011.

Hoerder-Suabedissen A, Hayashi S, Upton L, Nolan Z, Casas-Torremocha D, Grant E, Viswanathan S, Kanold PO, Clasca F, Kim Y, Molnár Z. Subset of Cortical Layer 6b Neurons Selectively Innervates Higher Order Thalamic Nuclei in Mice. Cereb Cortex. 2018 May 1;28(5):1882-1897. doi: 10.1093/cercor/bhy036. PMID: 29481606; PMCID: PMC6018949.

Hoerder-Suabedissen A, Molnár Z. Development, evolution and pathology of neocortical subplate neurons. Nat Rev Neurosci. 2015 Mar;16(3):133-46. doi: 10.1038/nrn3915. PMID: 25697157.

Hoogland PV, Welker E, Van der Loos H. Organization of the projections from barrel cortex to thalamus in mice studied with Phaseolus vulgaris-leucoagglutinin and HRP. Exp Brain Res. 1987;68(1):73-87. doi: 10.1007/BF00255235. PMID: 2826209.

Hooks BM, Chen C. Critical periods in the visual system: changing views for a model of experience-dependent plasticity. Neuron. 2007 Oct 25;56(2):312-26. doi: 10.1016/j.neuron.2007.10.003. PMID: 17964248.

Hooks BM, Chen C. Distinct roles for spontaneous and visual activity in remodeling of the retinogeniculate synapse. Neuron. 2006 Oct 19;52(2):281-91. doi: 10.1016/j.neuron.2006.07.007. PMID: 17046691.

Hooks BM, Hires SA, Zhang YX, Huber D, Petreanu L, Svoboda K, Shepherd GM. Laminar analysis of excitatory local circuits in vibrissal motor and sensory cortical areas. PLoS Biol. 2011 Jan 4;9(1):e1000572. doi: 10.1371/journal.pbio.1000572. PMID: 21245906; PMCID: PMC3014926.

Hubel DH, Wiesel TN. Receptive fields, binocular interaction and functional architecture in the cat's visual cortex. J Physiol. 1962 Jan;160(1):106-54. doi: 10.1113/jphysiol.1962.sp006837. PMID: 14449617; PMCID: PMC1359523.

HUBEL DH, WIESEL TN. RECEPTIVE FIELDS OF CELLS IN STRIATE CORTEX OF VERY YOUNG, VISUALLY INEXPERIENCED KITTENS. J Neurophysiol. 1963 Nov;26:994-1002. doi: 10.1152/jn.1963.26.6.994. PMID: 14084171.

Huber W, Carey VJ, Gentleman R, Anders S, Carlson M, Carvalho BS, Bravo HC, Davis S, Gatto L, Girke T, Gottardo R, Hahne F, Hansen KD, Irizarry RA, Lawrence M, Love MI, MacDonald J, Obenchain V, Oleś AK, Pagès H, Reyes A, Shannon P, Smyth GK, Tenenbaum D, Waldron L, Morgan M. Orchestrating high-throughput genomic analysis with Bioconductor. Nat Methods. 2015 Feb;12(2):115-21. doi: 10.1038/nmeth.3252. PMID: 25633503; PMCID: PMC4509590.

Huberman AD. Mechanisms of eye-specific visual circuit development. Curr Opin Neurobiol. 2007 Feb;17(1):73-80. doi: 10.1016/j.conb.2007.01.005. Epub 2007 Jan 24. PMID: 17254766.

Huberman AD, Feller MB, Chapman B. Mechanisms underlying development of visual maps and receptive fields. Annu Rev Neurosci. 2008a;31:479-509. doi: 10.1146/annurev.neuro.31.060407.125533. PMID: 18558864; PMCID: PMC2655105.

Huberman AD, Manu M, Koch SM, Susman MW, Lutz AB, Ullian EM, Baccus SA, Barres BA. Architecture and activity-mediated refinement of axonal projections from a mosaic of genetically identified retinal ganglion cells. Neuron. 2008b Aug 14;59(3):425-38. doi: 10.1016/j.neuron.2008.07.018. PMID: 18701068; PMCID: PMC8532044.

Huberman AD, Murray KD, Warland DK, Feldheim DA, Chapman B. Ephrin-As mediate targeting of eye-specific projections to the lateral geniculate nucleus. Nat Neurosci. 2005 Aug;8(8):1013-21. doi: 10.1038/nn1505. Epub 2005 Jul 17. PMID: 16025110; PMCID: PMC2652399.

Huberman AD, Speer CM, Chapman B. Spontaneous retinal activity mediates development of ocular dominance columns and binocular receptive fields in v1. Neuron. 2006 Oct 19;52(2):247-54. doi: 10.1016/j.neuron.2006.07.028. PMID: 17046688; PMCID: PMC2647846.

Huffman KJ, Cramer KS. EphA4 misexpression alters tonotopic projections in the auditory brainstem. Dev Neurobiol. 2007 Oct;67(12):1655-68. doi: 10.1002/dneu.20535. PMID: 17577206.

Inácio AR, Nasretdinov A, Lebedeva J, Khazipov R. Sensory feedback synchronizes motor and sensory neuronal networks in the neonatal rat spinal cord. Nat Commun. 2016 Oct 7;7:13060. doi: 10.1038/ncomms13060. PMID: 27713428; PMCID: PMC5494195.

Inan M, Lu HC, Albright MJ, She WC, Crair MC. Barrel map development relies on protein kinase A regulatory subunit II beta-mediated cAMP signaling. J Neurosci. 2006 Apr 19;26(16):4338-49. doi: 10.1523/JNEUROSCI.3745-05.2006. PMID: 16624954; PMCID: PMC6674004.

Iwasato T, Datwani A, Wolf AM, Nishiyama H, Taguchi Y, Tonegawa S, Knöpfel T, Erzurumlu RS, Itohara S. Cortex-restricted disruption of NMDAR1 impairs neuronal patterns in the barrel cortex. Nature. 2000 Aug 17;406(6797):726-31. doi: 10.1038/35021059. PMID: 10963597; PMCID: PMC3558691.

Iwasato T, Erzurumlu RS. Development of tactile sensory circuits in the CNS. Curr Opin Neurobiol. 2018 Dec;53:66-75. doi: 10.1016/j.conb.2018.06.001. Epub 2018 Jun 13. PMID: 29908482; PMCID: PMC6242754.

Iwasato T, Erzurumlu RS, Huerta PT, Chen DF, Sasaoka T, Ulupinar E, Tonegawa S. NMDA receptor-dependent refinement of somatotopic maps. Neuron. 1997 Dec;19(6):1201-10. doi: 10.1016/s0896-6273(00)80412-2. PMID: 9427244.

Iwasato T, Inan M, Kanki H, Erzurumlu RS, Itohara S, Crair MC. Cortical adenylyl cyclase 1 is required for thalamocortical synapse maturation and aspects of layer IV barrel development. J Neurosci. 2008 Jun 4;28(23):5931-43. doi: 10.1523/JNEUROSCI.0815-08.2008. PMID: 18524897; PMCID: PMC2733830.

Jabaudon D. Fate and freedom in developing neocortical circuits. Nat Commun. 2017 Jul 3;8:16042. doi: 10.1038/ncomms16042. PMID: 28671189; PMCID: PMC5500875.

Jacobs EC, Campagnoni C, Kampf K, Reyes SD, Kalra V, Handley V, Xie YY, Hong-Hu Y, Spreur V, Fisher RS, Campagnoni AT. Visualization of corticofugal projections during early cortical development in a tau-GFP-transgenic mouse. Eur J Neurosci. 2007 Jan;25(1):17-30. doi: 10.1111/j.1460-9568.2006.05258.x. PMID: 17241263.

Jagger DJ, Housley GD. Membrane properties of type II spiral ganglion neurones identified in a neonatal rat cochlear slice. J Physiol. 2003 Oct 15;552(Pt 2):525-33. doi: 10.1111/j.1469-7793.2003.00525.x. PMID: 14561834; PMCID: PMC2343372.

James B. Ackman, H.Z., Michael C. Crair (2014). Structured dynamics of neural activity across developing neocortex. Preprint at bioRxiv. 10.1101/012237.

Jan TA, Lu L, Li CX, Williams RW, Waters RS. Genetic analysis of posterior medial barrel subfield (PMBSF) size in somatosensory cortex (SI) in recombinant inbred strains of mice. BMC Neurosci. 2008 Jan 7;9:3. doi: 10.1186/1471-2202-9-3. PMID: 18179704; PMCID: PMC2254631.

Jaubert-Miazza L, Green E, Lo FS, Bui K, Mills J, Guido W. Structural and functional composition of the developing retinogeniculate pathway in the mouse. Vis Neurosci. 2005 Sep-Oct;22(5):661-76. doi: 10.1017/S0952523805225154. PMID: 16332277.

Jensen KF, Killackey HP. Terminal arbors of axons projecting to the somatosensory cortex of the adult rat. I. The normal morphology of specific thalamocortical afferents. J Neurosci. 1987 Nov;7(11):3529-43. doi: 10.1523/JNEUROSCI.07-11-03529.1987. PMID: 3316525; PMCID: PMC6569018.

Jhaveri S, Erzurumlu RS, Crossin K. Barrel construction in rodent neocortex: role of thalamic afferents versus extracellular matrix molecules. Proc Natl Acad Sci U S A. 1991 May 15;88(10):4489-93. doi: 10.1073/pnas.88.10.4489. PMID: 1709743; PMCID: PMC51686.

Johnson SL, Eckrich T, Kuhn S, Zampini V, Franz C, Ranatunga KM, Roberts TP, Masetto S, Knipper M, Kros CJ, Marcotti W. Position-dependent patterning of spontaneous action potentials in immature cochlear inner hair cells. Nat Neurosci. 2011 Jun;14(6):711-7. doi: 10.1038/nn.2803. Epub 2011 May 15. PMID: 21572434; PMCID: PMC3103712.

Jones, E.G., 1985. Descriptions of the Thalamus in Representative Mammals. In E. G. Jones, ed. The Thalamus. Boston, MA: Springer US, pp. 45–84.

Jones EG. Thalamic circuitry and thalamocortical synchrony. Philos Trans R Soc Lond B Biol Sci. 2002 Dec 29;357(1428):1659-73. doi: 10.1098/rstb.2002.1168. PMID: 12626002; PMCID: PMC1693077.

Jones EG, Powell TP. The projection of the somatic sensory cortex upon the thalamus in te cat. Brain Res. 1968 Sep;10(3):369-91. doi: 10.1016/0006-8993(68)90206-0. PMID: 4176807.

Jones EG, Rockel AJ. The synaptic organization in the medial geniculate body of afferent fibres ascending from the inferior colliculus. Z Zellforsch Mikrosk Anat. 1971;113(1):44-66. doi: 10.1007/BF00331201. PMID: 5545217.

Jones EG, Wise SP. Size, laminar and columnar distribution of efferent cells in the sensory-motor cortex of monkeys. J Comp Neurol. 1977 Oct 15;175(4):391-438. doi: 10.1002/cne.901750403. PMID: 410849.

Kähne M, Rüdiger S, Kihara AH, Lindner B. Gap junctions set the speed and nucleation rate of stage I retinal waves. PLoS Comput Biol. 2019 Apr 29;15(4):e1006355. doi: 10.1371/journal.pcbi.1006355. PMID: 31034472; PMCID: PMC6508742.

Kandler K, Clause A, Noh J. Tonotopic reorganization of developing auditory brainstem circuits. Nat Neurosci. 2009 Jun;12(6):711-7. doi: 10.1038/nn.2332. Epub 2009 May 10. PMID: 19471270; PMCID: PMC2780022.

Kanold PO, Deng R, Meng X. The Integrative Function of Silent Synapses on Subplate Neurons in Cortical Development and Dysfunction. Front Neuroanat. 2019 Apr 16;13:41. doi: 10.3389/fnana.2019.00041. PMID: 31040772; PMCID: PMC6476909.

Kanold PO, Luhmann HJ. The subplate and early cortical circuits. Annu Rev Neurosci. 2010;33:23-48. doi: 10.1146/annurev-neuro-060909-153244. PMID: 20201645.

Karlen SJ, Kahn DM, Krubitzer L. Early blindness results in abnormal corticocortical and thalamocortical connections. Neuroscience. 2006 Oct 27;142(3):843-58. doi: 10.1016/j.neuroscience.2006.06.055. Epub 2006 Aug 24. PMID: 16934941.

Karlsson KA, Gall AJ, Mohns EJ, Seelke AM, Blumberg MS. The neural substrates of infant sleep in rats. PLoS Biol. 2005 May;3(5):e143. doi: 10.1371/journal.pbio.0030143. Epub 2005 Apr 19. PMID: 15826218; PMCID: PMC1079781.

Kataoka A, Shimogori T. Fgf8 controls regional identity in the developing thalamus. Development. 2008 Sep;135(17):2873-81. doi: 10.1242/dev.021618. Epub 2008 Jul 24. PMID: 18653561.

Katz LC, Shatz CJ. Synaptic activity and the construction of cortical circuits. Science. 1996 Nov 15;274(5290):1133-8. doi: 10.1126/science.274.5290.1133. PMID: 8895456.

Kennedy HJ. New developments in understanding the mechanisms and function of spontaneous electrical activity in the developing mammalian auditory system. J Assoc Res Otolaryngol. 2012 Aug;13(4):437-45. doi: 10.1007/s10162-012-0325-4. Epub 2012 Apr 17. PMID: 22526733; PMCID: PMC3387308.

Kerschensteiner D. Glutamatergic Retinal Waves. Front Neural Circuits. 2016 May 10;10:38. doi: 10.3389/fncir.2016.00038. PMID: 27242446; PMCID: PMC4861735.

Khazipov R, Luhmann HJ. Early patterns of electrical activity in the developing cerebral cortex of humans and rodents. Trends Neurosci. 2006 Jul;29(7):414-418. doi: 10.1016/j.tins.2006.05.007. Epub 2006 May 19. PMID: 16713634.

Khazipov R, Minlebaev M, Valeeva G. Early gamma oscillations. Neuroscience. 2013 Oct 10;250:240-52. doi: 10.1016/j.neuroscience.2013.07.019. Epub 2013 Jul 17. PMID: 23872391.

Khazipov R, Sirota A, Leinekugel X, Holmes GL, Ben-Ari Y, Buzsáki G. Early motor activity drives spindle bursts in the developing somatosensory cortex. Nature. 2004 Dec 9;432(7018):758-61. doi: 10.1038/nature03132. PMID: 15592414.

Kilb W, Kirischuk S, Luhmann HJ. Electrical activity patterns and the functional maturation of the neocortex. Eur J Neurosci. 2011 Nov;34(10):1677-86. doi: 10.1111/j.1460-9568.2011.07878.x. PMID: 22103424.

Killackey HP, Belford GR. The formation of afferent patterns in the somatosensory cortex of the neonatal rat. J Comp Neurol. 1979 Jan 15;183(2):285-303. doi: 10.1002/cne.901830206. PMID: 762260.

Killackey HP, Belford G, Ryugo R, Ryugo DK. Anomalous organization of thalamocortical projections consequent to vibrissae removal in the newborn rat and mouse. Brain Res. 1976 Mar 12;104(2):309-15. doi: 10.1016/0006-8993(76)90623-5. PMID: 1260427.

Killackey HP, Dawson DR. Expansion of the Central Hindpaw Representation Following Fetal Forelimb Removal in the Rat. Eur J Neurosci. 1989 May;1(3):210-221. doi: 10.1111/j.1460-9568.1989.tb00790.x. PMID: 12106153.

Killackey HP, Fleming K. The role of the principal sensory nucleus in central trigeminal pattern formation. Brain Res. 1985 Sep;354(1):141-5. doi: 10.1016/0165-3806(85)90077-x. PMID: 4041914.

Killackey HP, Ivy GO, Cunningham TJ. Anomalous organization of SMI somatotopic map consequent to vibrissae removal in the newborn rat. Brain Res. 1978 Oct 20;155(1):136-40. doi: 10.1016/0006-8993(78)90314-1. PMID: 688006.

Killackey HP, Rhoades RW, Bennett-Clarke CA. The formation of a cortical somatotopic map. Trends Neurosci. 1995 Sep;18(9):402-7. doi: 10.1016/0166-2236(95)93937-s. PMID: 7482806.

Kim GJ, Shatz CJ, McConnell SK. Morphology of pioneer and follower growth cones in the developing cerebral cortex. J Neurobiol. 1991 Sep;22(6):629-42. doi: 10.1002/neu.480220608. PMID: 1919567.

Kirischuk S, Sinning A, Blanquie O, Yang JW, Luhmann HJ, Kilb W. Modulation of Neocortical Development by Early Neuronal Activity: Physiology and Pathophysiology. Front Cell Neurosci. 2017 Nov 29;11:379. doi: 10.3389/fncel.2017.00379. PMID: 29238291; PMCID: PMC5712676.

Kitazawa T, Rijli FM. Barrelette map formation in the prenatal mouse brainstem. Curr Opin Neurobiol. 2018 Dec;53:210-219. doi: 10.1016/j.conb.2018.09.008. Epub 2018 Oct 17. PMID: 30342228.

Kivrak BG, Erzurumlu RS. Development of the principal nucleus trigeminal lemniscal projections in the mouse. J Comp Neurol. 2013 Feb 1;521(2):299-311. doi: 10.1002/cne.23183. PMID: 22791623; PMCID: PMC3492550.

Kleinfeld D, Ahissar E, Diamond ME. Active sensation: insights from the rodent vibrissa sensorimotor system. Curr Opin Neurobiol. 2006 Aug;16(4):435-44. doi: 10.1016/j.conb.2006.06.009. Epub 2006 Jul 11. PMID: 16837190.

Koundakjian EJ, Appler JL, Goodrich LV. Auditory neurons make stereotyped wiring decisions before maturation of their targets. J Neurosci. 2007 Dec 19;27(51):14078-88. doi: 10.1523/JNEUROSCI.3765-07.2007. PMID: 18094247; PMCID: PMC6673527.

Kozanian OO, Abbott CW, Huffman KJ. Rapid Changes in Cortical and Subcortical Brain Regions after Early Bilateral Enucleation in the Mouse. PLoS One. 2015 Oct 9;10(10):e0140391. doi: 10.1371/journal.pone.0140391. Erratum in: PLoS One. 2015 Nov 04;10(11):e0142461. doi: 10.1371/journal.pone.0142461. PMID: 26452243; PMCID: PMC4599918.

Kreider JC, Blumberg MS. Mesopontine contribution to the expression of active 'twitch' sleep in decerebrate week-old rats. Brain Res. 2000 Jul 28;872(1-2):149-59. doi: 10.1016/s0006-8993(00)02518-x. PMID: 10924687.

Kros CJ, Ruppersberg JP, Rüsch A. Expression of a potassium current in inner hair cells during development of hearing in mice. Nature. 1998 Jul 16;394(6690):281-4. doi: 10.1038/28401. PMID: 9685158.

Krug K, Akerman CJ, Thompson ID. Responses of neurons in neonatal cortex and thalamus to patterned visual stimulation through the naturally closed lids. J Neurophysiol. 2001 Apr;85(4):1436-43. doi: 10.1152/jn.2001.85.4.1436. PMID: 11287467.

Land PW, Simons DJ. Cytochrome oxidase staining in the rat SmI barrel cortex. J Comp Neurol. 1985 Aug 8;238(2):225-35. doi: 10.1002/cne.902380209. PMID: 2413086.

Landers M, Philip Zeigler H. Development of rodent whisking: trigeminal input and central pattern generation. Somatosens Mot Res. 2006 Mar-Jun;23(1-2):1-10. doi: 10.1080/08990220600700768. PMID: 16846954.

Larsen DD, Callaway EM. Development of layer-specific axonal arborizations in mouse primary somatosensory cortex. J Comp Neurol. 2006 Jan 20;494(3):398-414. doi: 10.1002/cne.20754. PMID: 16320250; PMCID: PMC4651208.

Laumonnerie C, Bechara A, Vilain N, Kurihara Y, Kurihara H, Rijli FM. Facial whisker pattern is not sufficient to instruct a whisker-related topographic map in the mouse

somatosensory brainstem. Development. 2015 Nov 1;142(21):3704-12. doi: 10.1242/dev.128736. Epub 2015 Sep 28. PMID: 26417040.

Lee LJ, Iwasato T, Itohara S, Erzurumlu RS. Exuberant thalamocortical axon arborization in cortex-specific NMDAR1 knockout mice. J Comp Neurol. 2005 May 16;485(4):280-92. doi: 10.1002/cne.20481. PMID: 15803506; PMCID: PMC3560856.

Lee CC, Lam YW, Sherman SM. Intracortical convergence of layer 6 neurons. Neuroreport. 2012 Aug 22;23(12):736-40. doi: 10.1097/WNR.0b013e328356c1aa. PMID: 22776905; PMCID: PMC3462588.

Lee CC, Sherman SM. Topography and physiology of ascending streams in the auditory tectothalamic pathway. Proc Natl Acad Sci U S A. 2010 Jan 5;107(1):372-7. doi: 10.1073/pnas.0907873107. Epub 2009 Dec 15. PMID: 20018757; PMCID: PMC2806784.

Lefort S, Tomm C, Floyd Sarria JC, Petersen CC. The excitatory neuronal network of the C2 barrel column in mouse primary somatosensory cortex. Neuron. 2009 Jan 29;61(2):301-16. doi: 10.1016/j.neuron.2008.12.020. PMID: 19186171.

Leighton AH, Lohmann C. The Wiring of Developing Sensory Circuits-From Patterned Spontaneous Activity to Synaptic Plasticity Mechanisms. Front Neural Circuits. 2016 Sep 5;10:71. doi: 10.3389/fncir.2016.00071. PMID: 27656131; PMCID: PMC5011135.

Leyva-Díaz E, del Toro D, Menal MJ, Cambray S, Susín R, Tessier-Lavigne M, Klein R, Egea J, López-Bendito G. FLRT3 is a Robo1-interacting protein that determines Netrin-1 attraction in developing axons. Curr Biol. 2014 Mar 3;24(5):494-508. doi: 10.1016/j.cub.2014.01.042. Epub 2014 Feb 20. PMID: 24560577.

Li Y, Erzurumlu RS, Chen C, Jhaveri S, Tonegawa S. Whisker-related neuronal patterns fail to develop in the trigeminal brainstem nuclei of NMDAR1 knockout mice. Cell. 1994 Feb 11;76(3):427-37. doi: 10.1016/0092-8674(94)90108-2. PMID: 8313466.

Li H, Fertuzinhos S, Mohns E, Hnasko TS, Verhage M, Edwards R, Sestan N, Crair MC. Laminar and columnar development of barrel cortex relies on thalamocortical neurotransmission. Neuron. 2013 Sep 4;79(5):970-86. doi: 10.1016/j.neuron.2013.06.043. PMID: 24012009; PMCID: PMC3768017.

Li K, Zhang J, Li JY. Gbx2 plays an essential but transient role in the formation of thalamic nuclei. PLoS One. 2012;7(10):e47111. doi: 10.1371/journal.pone.0047111. Epub 2012 Oct 4. PMID: 23056596; PMCID: PMC3464241.

Lickiss T, Cheung AF, Hutchinson CE, Taylor JS, Molnár Z. Examining the relationship between early axon growth and transcription factor expression in the developing cerebral cortex. J Anat. 2012 Mar;220(3):201-11. doi: 10.1111/j.1469-7580.2011.01466.x. Epub 2012 Jan 3. PMID: 22212101; PMCID: PMC3381615.

Lim DJ, Anniko M. Developmental morphology of the mouse inner ear. A scanning electron microscopic observation. Acta Otolaryngol Suppl. 1985;422:1-69. PMID: 3877398.

Little GE, López-Bendito G, Rünker AE, García N, Piñon MC, Chédotal A, Molnár Z, Mitchell KJ. Specificity and plasticity of thalamocortical connections in Sema6A mutant mice. PLoS Biol. 2009 Apr 28;7(4):e98. doi: 10.1371/journal.pbio.1000098. PMID: 19402755; PMCID: PMC2672616.

Llorca A, Ciceri G, Beattie R, Wong FK, Diana G, Serafeimidou-Pouliou E, Fernández-Otero M, Streicher C, Arnold SJ, Meyer M, Hippenmeyer S, Maravall M, Marin O. A stochastic framework of neurogenesis underlies the assembly of neocortical cytoarchitecture. Elife. 2019 Nov 18;8:e51381. doi: 10.7554/eLife.51381. PMID: 31736464; PMCID: PMC6968929.

Lodato S, Arlotta P. Generating neuronal diversity in the mammalian cerebral cortex. Annu Rev Cell Dev Biol. 2015;31:699-720. doi: 10.1146/annurev-cellbio-100814-125353. Epub 2015 Sep 11. PMID: 26359774; PMCID: PMC4778709.

Lokmane L, Garel S. Map transfer from the thalamus to the neocortex: inputs from the barrel field. Semin Cell Dev Biol. 2014 Nov;35:147-55. doi: 10.1016/j.semcdb.2014.07.005. Epub 2014 Jul 11. PMID: 25020201.

Lokmane L, Proville R, Narboux-Nême N, Györy I, Keita M, Mailhes C, Léna C, Gaspar P, Grosschedl R, Garel S. Sensory map transfer to the neocortex relies on pretarget ordering of thalamic axons. Curr Biol. 2013 May 6;23(9):810-6. doi: 10.1016/j.cub.2013.03.062. Epub 2013 Apr 25. PMID: 23623550.

Lomber SG, Meredith MA, Kral A. Cross-modal plasticity in specific auditory cortices underlies visual compensations in the deaf. Nat Neurosci. 2010 Nov;13(11):1421-7. doi: 10.1038/nn.2653. Epub 2010 Oct 10. PMID: 20935644.

López-Bendito G. Development of the Thalamocortical Interactions: Past, Present and Future. Neuroscience. 2018 Aug 10;385:67-74. doi: 10.1016/j.neuroscience.2018.06.020. Epub 2018 Jun 20. PMID: 29932982; PMCID: PMC7611009.

López-Bendito G, Aníbal-Martínez M, Martini FJ. Cross-Modal Plasticity in Brains Deprived of Visual Input Before Vision. Annu Rev Neurosci. 2022 Jul 8;45:471-489. doi: 10.1146/annurev-neuro-111020-104222. PMID: 35803589.

López-Bendito G, Cautinat A, Sánchez JA, Bielle F, Flames N, Garratt AN, Talmage DA, Role LW, Charnay P, Marín O, Garel S. Tangential neuronal migration controls axon guidance: a role for neuregulin-1 in thalamocortical axon navigation. Cell. 2006 Apr 7;125(1):127-42. doi: 10.1016/j.cell.2006.01.042. PMID: 16615895; PMCID: PMC2365888.

López-Bendito G, Flames N, Ma L, Fouquet C, Di Meglio T, Chedotal A, Tessier-Lavigne M, Marín O. Robo1 and Robo2 cooperate to control the guidance of major axonal tracts in the mammalian forebrain. J Neurosci. 2007 Mar 28;27(13):3395-407. doi: 10.1523/JNEUROSCI.4605-06.2007. PMID: 17392456; PMCID: PMC6672128.

López-Bendito G, Molnár Z. Thalamocortical development: how are we going to get there? Nat Rev Neurosci. 2003 Apr;4(4):276-89. doi: 10.1038/nrn1075. Erratum in: Nat Rev Neurosci. 2003 May;4(5):422. PMID: 12671644.

Love MI, Huber W, Anders S. Moderated estimation of fold change and dispersion for RNA-seq data with DESeq2. Genome Biol. 2014;15(12):550. doi: 10.1186/s13059-014-0550-8. PMID: 25516281; PMCID: PMC4302049.

Lu HC, Butts DA, Kaeser PS, She WC, Janz R, Crair MC. Role of efficient neurotransmitter release in barrel map development. J Neurosci. 2006 Mar 8;26(10):2692-703. doi: 10.1523/JNEUROSCI.3956-05.2006. PMID: 16525048; PMCID: PMC6675166.

Lu HC, She WC, Plas DT, Neumann PE, Janz R, Crair MC. Adenylyl cyclase I regulates AMPA receptor trafficking during mouse cortical 'barrel' map development. Nat Neurosci. 2003 Sep;6(9):939-47. doi: 10.1038/nn1106. PMID: 12897788.

Luhmann HJ. Review of imaging network activities in developing rodent cerebral cortex in vivo. Neurophotonics. 2017 Jul;4(3):031202. doi: 10.1117/1.NPh.4.3.031202. Epub 2016 Nov 23. PMID: 27921066; PMCID: PMC5120148.

Luhmann HJ, Khazipov R. Neuronal activity patterns in the developing barrel cortex. Neuroscience. 2018 Jan 1;368:256-267. doi: 10.1016/j.neuroscience.2017.05.025. Epub 2017 May 19. PMID: 28528963.

Luhmann HJ, Kirischuk S, Kilb W. The Superior Function of the Subplate in Early Neocortical Development. Front Neuroanat. 2018 Nov 14;12:97. doi: 10.3389/fnana.2018.00097. PMID: 30487739; PMCID: PMC6246655.

Luhmann HJ, Sinning A, Yang JW, Reyes-Puerta V, Stüttgen MC, Kirischuk S, Kilb W. Spontaneous Neuronal Activity in Developing Neocortical Networks: From Single Cells to Large-Scale Interactions. Front Neural Circuits. 2016 May 24;10:40. doi: 10.3389/fncir.2016.00040. PMID: 27252626; PMCID: PMC4877528.

Luskin MB, Pearlman AL, Sanes JR. Cell lineage in the cerebral cortex of the mouse studied in vivo and in vitro with a recombinant retrovirus. Neuron. 1988 Oct;1(8):635-47. doi: 10.1016/0896-6273(88)90163-8. PMID: 3272182.

Lyckman AW, Jhaveri S, Feldheim DA, Vanderhaeghen P, Flanagan JG, Sur M. Enhanced plasticity of retinothalamic projections in an ephrin-A2/A5 double mutant. J Neurosci. 2001 Oct 1;21(19):7684-90. doi: 10.1523/JNEUROSCI.21-19-07684.2001. PMID: 11567058; PMCID: PMC6762904.

Ma PM, Woolsey TA. Cytoarchitectonic correlates of the vibrissae in the medullary trigeminal complex of the mouse. Brain Res. 1984 Jul 23;306(1-2):374-9. doi: 10.1016/0006-8993(84)90390-1. PMID: 6205721.

Madisen L, Garner AR, Shimaoka D, Chuong AS, Klapoetke NC, Li L, van der Bourg A, Niino Y, Egolf L, Monetti C, Gu H, Mills M, Cheng A, Tasic B, Nguyen TN, Sunkin SM, Benucci A, Nagy A, Miyawaki A, Helmchen F, Empson RM, Knöpfel T, Boyden ES, Reid RC, Carandini M, Zeng H. Transgenic mice for intersectional targeting of neural sensors and effectors with high specificity and performance. Neuron. 2015 Mar 4;85(5):942-58. doi: 10.1016/j.neuron.2015.02.022. PMID: 25741722; PMCID: PMC4365051.

Madisen L, Zwingman TA, Sunkin SM, Oh SW, Zariwala HA, Gu H, Ng LL, Palmiter RD, Hawrylycz MJ, Jones AR, Lein ES, Zeng H. A robust and high-throughput Cre reporting and characterization system for the whole mouse brain. Nat Neurosci. 2010 Jan;13(1):133-40. doi: 10.1038/nn.2467. Epub 2009 Dec 20. PMID: 20023653; PMCID: PMC2840225.

Majdan M, Shatz CJ. Effects of visual experience on activity-dependent gene regulation in cortex. Nat Neurosci. 2006 May;9(5):650-9. doi: 10.1038/nn1674. Epub 2006 Apr 2. PMID: 16582906.

Mallamaci A, Stoykova A. Gene networks controlling early cerebral cortex arealization. Eur J Neurosci. 2006 Feb;23(4):847-56. doi: 10.1111/j.1460-9568.2006.04634.x. PMID: 16519650.

Mallika C, Guo Q, Li JY. Gbx2 is essential for maintaining thalamic neuron identity and repressing habenular characters in the developing thalamus. Dev Biol. 2015 Nov 1;407(1):26-39. doi: 10.1016/j.ydbio.2015.08.010. Epub 2015 Aug 20. PMID: 26297811; PMCID: PMC4641819.

Malmierca MS, Ryugo DK. Auditory System. In The Mouse Nervous System. Elsevier Inc. 2012. p. 607-645 doi: 10.1016/B978-0-12-369497-3.10024-X

Mann ZF, Kelley MW. Development of tonotopy in the auditory periphery. Hear Res. 2011 Jun;276(1-2):2-15. doi: 10.1016/j.heares.2011.01.011. Epub 2011 Jan 27. PMID: 21276841.

Manuel M, Georgala PA, Carr CB, Chanas S, Kleinjan DA, Martynoga B, Mason JO, Molinek M, Pinson J, Pratt T, Quinn JC, Simpson TI, Tyas DA, van Heyningen V, West JD, Price DJ. Controlled overexpression of Pax6 in vivo negatively autoregulates the Pax6 locus, causing cell-autonomous defects of late cortical progenitor proliferation with little effect on cortical arealization. Development. 2007 Feb;134(3):545-55. doi: 10.1242/dev.02764. Epub 2007 Jan 3. PMID: 17202185; PMCID: PMC2386558.

Marcos-Mondéjar P, Peregrín S, Li JY, Carlsson L, Tole S, López-Bendito G. The lhx2 transcription factor controls thalamocortical axonal guidance by specific regulation of robo1 and robo2 receptors. J Neurosci. 2012 Mar 28;32(13):4372-85. doi: 10.1523/JNEUROSCI.5851-11.2012. PMID: 22457488; PMCID: PMC6622047.

Marques-Smith A, Lyngholm D, Kaufmann AK, Stacey JA, Hoerder-Suabedissen A, Becker EB, Wilson MC, Molnár Z, Butt SJ. A Transient Translaminar GABAergic Interneuron Circuit Connects Thalamocortical Recipient Layers in Neonatal Somatosensory Cortex. Neuron. 2016 Feb 3;89(3):536-49. doi: 10.1016/j.neuron.2016.01.015. PMID: 26844833; PMCID: PMC4742537.

Martínez S, Puelles E, Puelles L, and Echevarria D. Chapter 1 -molecular regionalization of the developing neural tube. In Charles Watson, George Paxi-nos, and Luis Puelles, editors, The Mouse Nervous System, pages 2–18. Academic Press, San Diego, January 2012.

Martinez-Ferre A, Martinez S. Molecular regionalization of the diencephalon. Front Neurosci. 2012 May 25;6:73. doi: 10.3389/fnins.2012.00073. PMID: 22654731; PMCID: PMC3360461.

Martinez-Ferre A, Martinez S. The development of the thalamic motor learning area is regulated by Fgf8 expression. J Neurosci. 2009 Oct 21;29(42):13389-400. doi: 10.1523/JNEUROSCI.2625-09.2009. PMID: 19846726; PMCID: PMC6665203.

Martini FJ, Guillamón-Vivancos T, Moreno-Juan V, Valdeolmillos M, López-Bendito G. Spontaneous activity in developing thalamic and cortical sensory networks. Neuron. 2021 Aug 18;109(16):2519-2534. doi: 10.1016/j.neuron.2021.06.026. Epub 2021 Jul 21. PMID: 34293296; PMCID: PMC7611560.

Martini FJ, Moreno-Juan V, Filipchuk A, Valdeolmillos M, López-Bendito G. Impact of thalamocortical input on barrel cortex development. Neuroscience. 2018 Jan 1;368:246-255. doi: 10.1016/j.neuroscience.2017.04.005. Epub 2017 Apr 13. PMID: 28412498; PMCID: PMC7610996.

Masland RH. The neuronal organization of the retina. Neuron. 2012 Oct 18;76(2):266-80. doi: 10.1016/j.neuron.2012.10.002. Epub 2012 Oct 17. PMID: 23083731; PMCID: PMC3714606.

McConnell SK, Ghosh A, Shatz CJ. Subplate neurons pioneer the first axon pathway from the cerebral cortex. Science. 1989 Sep 1;245(4921):978-82. doi: 10.1126/science.2475909. PMID: 2475909.

McLaughlin T, Hindges R, O'Leary DD. Regulation of axial patterning of the retina and its topographic mapping in the brain. Curr Opin Neurobiol. 2003 Feb;13(1):57-69. doi: 10.1016/s0959-4388(03)00014-x. PMID: 12593983.

McVea DA, Mohajerani MH, Murphy TH. Voltage-sensitive dye imaging reveals dynamic spatiotemporal properties of cortical activity after spontaneous muscle twitches in the newborn rat. J Neurosci. 2012 Aug 8;32(32):10982-94. doi: 10.1523/JNEUROSCI.1322-12.2012. PMID: 22875932; PMCID: PMC6621025.

Meng X, Solarana K, Bowen Z, Liu J, Nagode DA, Sheikh A, Winkowski DE, Kao JPY, Kanold PO. Transient Subgranular Hyperconnectivity to L2/3 and Enhanced Pairwise Correlations During the Critical Period in the Mouse Auditory Cortex. Cereb Cortex. 2020 Mar 14;30(3):1914-1930. doi: 10.1093/cercor/bhz213. PMID: 31667495; PMCID: PMC7132924.

Merzenich MM, Knight PL, Roth GL. Representation of cochlea within primary auditory cortex in the cat. J Neurophysiol. 1975 Mar;38(2):231-49. doi: 10.1152/jn.1975.38.2.231. PMID: 1092814.

Metzis V, Steinhauser S, Pakanavicius E, Gouti M, Stamataki D, Ivanovitch K, Watson T, Rayon T, Mousavy Gharavy SN, Lovell-Badge R, Luscombe NM, Briscoe J. Nervous System Regionalization Entails Axial Allocation before Neural Differentiation. Cell. 2018 Nov 1;175(4):1105-1118.e17. doi: 10.1016/j.cell.2018.09.040. Epub 2018 Oct 18. PMID: 30343898; PMCID: PMC6218657.

Meyer AC, Frank T, Khimich D, Hoch G, Riedel D, Chapochnikov NM, Yarin YM, Harke B, Hell SW, Egner A, Moser T. Tuning of synapse number, structure and function in the cochlea. Nat Neurosci. 2009 Apr;12(4):444-53. doi: 10.1038/nn.2293. Epub 2009 Mar 8. PMID: 19270686.

Meyer HS, Wimmer VC, Hemberger M, Bruno RM, de Kock CP, Frick A, Sakmann B, Helmstaedter M. Cell type-specific thalamic innervation in a column of rat vibrissal cortex. Cereb Cortex. 2010 Oct;20(10):2287-303. doi: 10.1093/cercor/bhq069. Epub 2010 Jun 9. PMID: 20534783; PMCID: PMC2936808.

Mezzera C, López-Bendito G. Cross-modal plasticity in sensory deprived animal models: From the thalamocortical development point of view. J Chem Neuroanat. 2016 Sep;75(Pt A):32-40. doi: 10.1016/j.jchemneu.2015.09.005. Epub 2015 Oct 13. PMID: 26459021.

Miller B, Chou L, Finlay BL. The early development of thalamocortical and corticothalamic projections. J Comp Neurol. 1993 Sep 1;335(1):16-41. doi: 10.1002/cne.903350103. PMID: 8408772.

Minlebaev M, Colonnese M, Tsintsadze T, Sirota A, Khazipov R. Early γ oscillations synchronize developing thalamus and cortex. Science. 2011 Oct 14;334(6053):226-9. doi: 10.1126/science.1210574. PMID: 21998388.

Mire E, Mezzera C, Leyva-Díaz E, Paternain AV, Squarzoni P, Bluy L, Castillo-Paterna M, López MJ, Peregrín S, Tessier-Lavigne M, Garel S, Galcerán J, Lerma J, López-Bendito G. Spontaneous activity regulates Robo1 transcription to mediate a switch in thalamocortical axon growth. Nat Neurosci. 2012 Jul 8;15(8):1134-43. doi: 10.1038/nn.3160. PMID: 22772332.

Mitrovic N, Mohajeri H, Schachner M. Effects of NMDA receptor blockade in the developing rat somatosensory cortex on the expression of the glia-derived extracellular matrix

glycoprotein tenascin-C. Eur J Neurosci. 1996 Sep;8(9):1793-802. doi: 10.1111/j.1460-9568.1996.tb01323.x. PMID: 8921270.

Mitrukhina O, Suchkov D, Khazipov R, Minlebaev M. Imprecise Whisker Map in the Neonatal Rat Barrel Cortex. Cereb Cortex. 2015 Oct;25(10):3458-67. doi: 10.1093/cercor/bhu169. Epub 2014 Aug 6. PMID: 25100857.

Mizuno H, Ikezoe K, Nakazawa S, Sato T, Kitamura K, Iwasato T. Patchwork-Type Spontaneous Activity in Neonatal Barrel Cortex Layer 4 Transmitted via Thalamocortical Projections. Cell Rep. 2018a Jan 2;22(1):123-135. doi: 10.1016/j.celrep.2017.12.012. PMID: 29298415.

Mizuno H, Luo W, Tarusawa E, Saito YM, Sato T, Yoshimura Y, Itohara S, Iwasato T. NMDAR-regulated dynamics of layer 4 neuronal dendrites during thalamocortical reorganization in neonates. Neuron. 2014 Apr 16;82(2):365-79. doi: 10.1016/j.neuron.2014.02.026. Epub 2014 Mar 27. PMID: 24685175.

Mizuno H, Nakazawa S, Iwasato T. In Vivo Two-photon Imaging of Cortical Neurons in Neonatal Mice. J Vis Exp. 2018b Oct 18;(140):58340. doi: 10.3791/58340. PMID: 30394388; PMCID: PMC6235557.

Molnár Z, Cordery P. Connections between cells of the internal capsule, thalamus, and cerebral cortex in embryonic rat. J Comp Neurol. 1999 Oct 11;413(1):1-25. doi: 10.1002/(sici)1096-9861(19991011)413:1<1::aid-cne1>3.0.co;2-5. PMID: 10464367.

Molnár Z, Garel S, López-Bendito G, Maness P, Price DJ. Mechanisms controlling the guidance of thalamocortical axons through the embryonic forebrain. Eur J Neurosci. 2012 May;35(10):1573-85. doi: 10.1111/j.1460-9568.2012.08119.x. PMID: 22607003; PMCID: PMC4370206.

Molnár Z, Higashi S, López-Bendito G. Choreography of early thalamocortical development. Cereb Cortex. 2003 Jun;13(6):661-9. doi: 10.1093/cercor/13.6.661. PMID: 12764042.

Molnár Z, Luhmann HJ, Kanold PO. Transient cortical circuits match spontaneous and sensory-driven activity during development. Science. 2020 Oct 16;370(6514):eabb2153. doi: 10.1126/science.abb2153. PMID: 33060328; PMCID: PMC8050953.

Molyneaux BJ, Arlotta P, Menezes JR, Macklis JD. Neuronal subtype specification in the cerebral cortex. Nat Rev Neurosci. 2007 Jun;8(6):427-37. doi: 10.1038/nrn2151. PMID: 17514196.

Monko T, Rebertus J, Stolley J, Salton SR, Nakagawa Y. Thalamocortical axons regulate neurogenesis and laminar fates in the early sensory cortex. Proc Natl Acad Sci U S A. 2022 May 31;119(22):e2201355119. doi: 10.1073/pnas.2201355119. Epub 2022 May 25. PMID: 35613048; PMCID: PMC9295754.

Mooney R, Penn AA, Gallego R, Shatz CJ. Thalamic relay of spontaneous retinal activity prior to vision. Neuron. 1996 Nov;17(5):863-74. doi: 10.1016/s0896-6273(00)80218-4. PMID: 8938119.

Moreno-Juan V, Filipchuk A, Antón-Bolaños N, Mezzera C, Gezelius H, Andrés B, Rodríguez-Malmierca L, Susín R, Schaad O, Iwasato T, Schüle R, Rutlin M, Nelson S, Ducret S, Valdeolmillos M, Rijli FM, López-Bendito G. Prenatal thalamic waves regulate cortical area size prior to sensory processing. Nat Commun. 2017 Feb 3;8:14172. doi: 10.1038/ncomms14172. PMID: 28155854; PMCID: PMC5296753.

Mountcastle VB. The columnar organization of the neocortex. Brain. 1997 Apr;120 (Pt 4):701-22. doi: 10.1093/brain/120.4.701. PMID: 9153131.

Muir-Robinson G, Hwang BJ, Feller MB. Retinogeniculate axons undergo eye-specific segregation in the absence of eye-specific layers. J Neurosci. 2002 Jul 1;22(13):5259-64. doi: 10.1523/JNEUROSCI.22-13-05259.2002. PMID: 12097474; PMCID: PMC6758243.

Murata Y, Colonnese MT. An excitatory cortical feedback loop gates retinal wave transmission in rodent thalamus. Elife. 2016 Oct 11;5:e18816. doi: 10.7554/eLife.18816. PMID: 27725086; PMCID: PMC5059135.

Murata Y, Colonnese MT. Thalamic inhibitory circuits and network activity development. Brain Res. 2019 Mar 1;1706:13-23. doi: 10.1016/j.brainres.2018.10.024. Epub 2018 Oct 23. PMID: 30366019; PMCID: PMC6363901.

Murata Y, Colonnese MT. Thalamus Controls Development and Expression of Arousal States in Visual Cortex. J Neurosci. 2018 Oct 10;38(41):8772-8786. doi: 10.1523/JNEUROSCI.1519-18.2018. Epub 2018 Aug 27. PMID: 30150360; PMCID: PMC6181317.

Nakagawa Y. Development of the thalamus: From early patterning to regulation of cortical functions. Wiley Interdiscip Rev Dev Biol. 2019 Sep;8(5):e345. doi: 10.1002/wdev.345. Epub 2019 Apr 29. PMID: 31034163.

Nakagawa Y, O'Leary DD. Combinatorial expression patterns of LIM-homeodomain and other regulatory genes parcellate developing thalamus. J Neurosci. 2001 Apr 15;21(8):2711-25. doi: 10.1523/JNEUROSCI.21-08-02711.2001. PMID: 11306624; PMCID: PMC6762518.

Nakagawa Y, Shimogori T. Diversity of thalamic progenitor cells and postmitotic neurons. Eur J Neurosci. 2012 May;35(10):1554-62. doi: 10.1111/j.1460-9568.2012.08089.x. PMID: 22607001.

Narayanan RT, Udvary D, Oberlaender M. Cell Type-Specific Structural Organization of the Six Layers in Rat Barrel Cortex. Front Neuroanat. 2017 Oct 13;11:91. doi: 10.3389/fnana.2017.00091. PMID: 29081739; PMCID: PMC5645532.

Narboux-Nême N, Evrard A, Ferezou I, Erzurumlu RS, Kaeser PS, Lainé J, Rossier J, Ropert N, Südhof TC, Gaspar P. Neurotransmitter release at the thalamocortical synapse instructs barrel formation but not axon patterning in the somatosensory cortex. J Neurosci. 2012 May 2;32(18):6183-96. doi: 10.1523/JNEUROSCI.0343-12.2012. PMID: 22553025; PMCID: PMC3526954.

Noctor SC, Flint AC, Weissman TA, Dammerman RS, Kriegstein AR. Neurons derived from radial glial cells establish radial units in neocortex. Nature. 2001 Feb 8;409(6821):714-20. doi: 10.1038/35055553. PMID: 11217860.

Noctor SC, Martínez-Cerdeño V, Ivic L, Kriegstein AR. Cortical neurons arise in symmetric and asymmetric division zones and migrate through specific phases. Nat Neurosci. 2004 Feb;7(2):136-44. doi: 10.1038/nn1172. Epub 2004 Jan 4. PMID: 14703572.

Nowakowski TJ, Bhaduri A, Pollen AA, Alvarado B, Mostajo-Radji MA, Di Lullo E, Haeussler M, Sandoval-Espinosa C, Liu SJ, Velmeshev D, Ounadjela JR, Shuga J, Wang X, Lim DA, West JA, Leyrat AA, Kent WJ, Kriegstein AR. Spatiotemporal gene expression trajectories reveal developmental hierarchies of the human cortex. Science. 2017 Dec 8;358(6368):1318-1323. doi: 10.1126/science.aap8809. PMID: 29217575; PMCID: PMC5991609.

Oberlaender M, de Kock CP, Bruno RM, Ramirez A, Meyer HS, Dercksen VJ, Helmstaedter M, Sakmann B. Cell type-specific three-dimensional structure of thalamocortical circuits in a

column of rat vibrissal cortex. Cereb Cortex. 2012 Oct;22(10):2375-91. doi: 10.1093/cercor/bhr317. Epub 2011 Nov 16. PMID: 22089425; PMCID: PMC3432239.

Oberst P, Agirman G, Jabaudon D. Principles of progenitor temporal patterning in the developing invertebrate and vertebrate nervous system. Curr Opin Neurobiol. 2019 Jun;56:185-193. doi: 10.1016/j.conb.2019.03.004. Epub 2019 Apr 15. PMID: 30999235.

O'Donnell P, Grace AA. Dysfunctions in multiple interrelated systems as the neurobiological bases of schizophrenic symptom clusters. Schizophr Bull. 1998;24(2):267-83. doi: 10.1093/oxfordjournals.schbul.a033325. PMID: 9613625.

Ohtaka-Maruyama C, Okamoto M, Endo K, Oshima M, Kaneko N, Yura K, Okado H, Miyata T, Maeda N. Synaptic transmission from subplate neurons controls radial migration of neocortical neurons. Science. 2018 Apr 20;360(6386):313-317. doi: 10.1126/science.aar2866. PMID: 29674592.

Olcese U, Iurilli G, Medini P. Cellular and synaptic architecture of multisensory integration in the mouse neocortex. Neuron. 2013 Aug 7;79(3):579-93. doi: 10.1016/j.neuron.2013.06.010. Epub 2013 Jul 11. PMID: 23850594.

O'Leary DD. Do cortical areas emerge from a protocortex? Trends Neurosci. 1989 Oct;12(10):400-6. doi: 10.1016/0166-2236(89)90080-5. PMID: 2479138.

O'Leary DD, Nakagawa Y. Patterning centers, regulatory genes and extrinsic mechanisms controlling arealization of the neocortex. Curr Opin Neurobiol. 2002 Feb;12(1):14-25. doi: 10.1016/s0959-4388(02)00285-4. PMID: 11861160.

O'Leary DD, Sahara S. Genetic regulation of arealization of the neocortex. Curr Opin Neurobiol. 2008 Feb;18(1):90-100. doi: 10.1016/j.conb.2008.05.011. Epub 2008 Jun 2. PMID: 18524571; PMCID: PMC2677555.

Olsen SR, Bortone DS, Adesnik H, Scanziani M. Gain control by layer six in cortical circuits of vision. Nature. 2012 Feb 22;483(7387):47-52. doi: 10.1038/nature10835. PMID: 22367547; PMCID: PMC3636977.

Oury F, Murakami Y, Renaud JS, Pasqualetti M, Charnay P, Ren SY, Rijli FM. Hoxa2- and rhombomere-dependent development of the mouse facial somatosensory map. Science. 2006 Sep 8;313(5792):1408-13. doi: 10.1126/science.1130042. Epub 2006 Aug 10. PMID: 16902088.

Pal S, Dwivedi D, Pramanik T, Godbole G, Iwasato T, Jabaudon D, Bhalla US, Tole S. An Early Cortical Progenitor-Specific Mechanism Regulates Thalamocortical Innervation. J Neurosci. 2021 Aug 11;41(32):6822-6835. doi: 10.1523/JNEUROSCI.0226-21.2021. Epub 2021 Jun 30. PMID: 34193558; PMCID: PMC8360687.

Park H, Poo MM. Neurotrophin regulation of neural circuit development and function. Nat Rev Neurosci. 2013 Jan;14(1):7-23. doi: 10.1038/nrn3379. PMID: 23254191.

Pasternak JR, Woolsey TA. The number, size and spatial distribution of neurons in lamina IV of the mouse SmI neocortex. J Comp Neurol. 1975 Apr 1;160(3):291-306. doi: 10.1002/cne.901600303. PMID: 1112926.

Penn AA, Riquelme PA, Feller MB, Shatz CJ. Competition in retinogeniculate patterning driven by spontaneous activity. Science. 1998 Mar 27;279(5359):2108-12. doi: 10.1126/science.279.5359.2108. PMID: 9516112.

Persico AM, Mengual E, Moessner R, Hall FS, Revay RS, Sora I, Arellano J, DeFelipe J, Gimenez-Amaya JM, Conciatori M, Marino R, Baldi A, Cabib S, Pascucci T, Uhl GR, Murphy DL, Lesch KP, Keller F. Barrel pattern formation requires serotonin uptake by thalamocortical afferents, and not vesicular monoamine release. J Neurosci. 2001 Sep 1;21(17):6862-73. doi: 10.1523/JNEUROSCI.21-17-06862.2001. Erratum in: J Neurosci 2001 Oct 1;21(19):1a. Hall SF [corrected to Hall FS]. PMID: 11517274; PMCID: PMC6763105.

Petersen CC. The functional organization of the barrel cortex. Neuron. 2007 Oct 25;56(2):339-55. doi: 10.1016/j.neuron.2007.09.017. PMID: 17964250.

Petersen CC, Sakmann B. Functionally independent columns of rat somatosensory barrel cortex revealed with voltage-sensitive dye imaging. J Neurosci. 2001 Nov 1;21(21):8435-46. doi: 10.1523/JNEUROSCI.21-21-08435.2001. PMID: 11606632; PMCID: PMC6762780.

Petreanu L, Huber D, Sobczyk A, Svoboda K. Channelrhodopsin-2-assisted circuit mapping of long-range callosal projections. Nat Neurosci. 2007 May;10(5):663-8. doi: 10.1038/nn1891. Epub 2007 Apr 15. PMID: 17435752.

Petreanu L, Mao T, Sternson SM, Svoboda K. The subcellular organization of neocortical excitatory connections. Nature. 2009 Feb 26;457(7233):1142-5. doi: 10.1038/nature07709. PMID: 19151697; PMCID: PMC2745650.

Pfeiffenberger C, Cutforth T, Woods G, Yamada J, Rentería RC, Copenhagen DR, Flanagan JG, Feldheim DA. Ephrin-As and neural activity are required for eye-specific patterning during retinogeniculate mapping. Nat Neurosci. 2005 Aug;8(8):1022-7. doi: 10.1038/nn1508. Epub 2005 Jul 17. PMID: 16025107; PMCID: PMC1352169.

Pfeiffenberger C, Yamada J, Feldheim DA. Ephrin-As and patterned retinal activity act together in the development of topographic maps in the primary visual system. J Neurosci. 2006 Dec 13;26(50):12873-84. doi: 10.1523/JNEUROSCI.3595-06.2006. PMID: 17167078; PMCID: PMC3664553.

Pierret T, Lavallée P, Deschênes M. Parallel streams for the relay of vibrissal information through thalamic barreloids. J Neurosci. 2000 Oct 1;20(19):7455-62. doi: 10.1523/JNEUROSCI.20-19-07455.2000. PMID: 11007905; PMCID: PMC6772772.

Pouchelon G, Frangeul L, Rijli FM, Jabaudon D. Patterning of pre-thalamic somatosensory pathways. Eur J Neurosci. 2012 May;35(10):1533-9. doi: 10.1111/j.1460-9568.2012.08059.x. PMID: 22606999.

Pouchelon G, Gambino F, Bellone C, Telley L, Vitali I, Lüscher C, Holtmaat A, Jabaudon D. Modality-specific thalamocortical inputs instruct the identity of postsynaptic L4 neurons. Nature. 2014 Jul 24;511(7510):471-4. doi: 10.1038/nature13390. Epub 2014 May 14. PMID: 24828045.

Price DJ, Kennedy H, Dehay C, Zhou L, Mercier M, Jossin Y, Goffinet AM, Tissir F, Blakey D, Molnár Z. The development of cortical connections. Eur J Neurosci. 2006 Feb;23(4):910-20. doi: 10.1111/j.1460-9568.2006.04620.x. PMID: 16519656.

Provine RR, Sharma SC, Sandel TT, Hamburger V. Electrical activity in the spinal cord of the chick embryo, in situ. Proc Natl Acad Sci U S A. 1970 Mar;65(3):508-15. doi: 10.1073/pnas.65.3.508. PMID: 5267135; PMCID: PMC282936.

Puelles L, Harrison M, Paxinos G, Watson C. A developmental ontology for the mammalian brain based on the prosomeric model. Trends Neurosci. 2013 Oct;36(10):570-8. doi: 10.1016/j.tins.2013.06.004. Epub 2013 Jul 18. PMID: 23871546.

Puelles L, Rubenstein JL. Forebrain gene expression domains and the evolving prosomeric model. Trends Neurosci. 2003 Sep;26(9):469-76. doi: 10.1016/S0166-2236(03)00234-0. PMID: 12948657.

Quintana-Urzainqui I, Hernández-Malmierca P, Clegg JM, Li Z, Kozić Z, Price DJ. The role of the diencephalon in the guidance of thalamocortical axons in mice. Development. 2020 Jun 26;147(12):dev184523. doi: 10.1242/dev.184523. PMID: 32541009; PMCID: PMC7327999.

Rakic P. Radial versus tangential migration of neuronal clones in the developing cerebral cortex. Proc Natl Acad Sci U S A. 1995 Dec 5;92(25):11323-7. doi: 10.1073/pnas.92.25.11323. PMID: 8524778; PMCID: PMC40392.

Rakic P. Specification of cerebral cortical areas. Science. 1988 Jul 8;241(4862):170-6. doi: 10.1126/science.3291116. PMID: 3291116.

Rakic P, Ayoub AE, Breunig JJ, Dominguez MH. Decision by division: making cortical maps. Trends Neurosci. 2009 May;32(5):291-301. doi: 10.1016/j.tins.2009.01.007. Epub 2009 Apr 18. PMID: 19380167; PMCID: PMC3601545.

Rakic P, Suñer I, Williams RW. A novel cytoarchitectonic area induced experimentally within the primate visual cortex. Proc Natl Acad Sci U S A. 1991 Mar 15;88(6):2083-7. doi: 10.1073/pnas.88.6.2083. PMID: 2006147; PMCID: PMC51173.

Ralston HJ 3rd. The synaptic organization of lemniscal projections to the ventrobasal thalamus of the cat. Brain Res. 1969 Jun;14(1):99-115. doi: 10.1016/0006-8993(69)90033-x. PMID: 5783118.

Rash BG, Grove EA. Area and layer patterning in the developing cerebral cortex. Curr Opin Neurobiol. 2006 Feb;16(1):25-34. doi: 10.1016/j.conb.2006.01.004. Epub 2006 Jan 19. PMID: 16426837.

Rauschecker JP, Korte M. Auditory compensation for early blindness in cat cerebral cortex. J Neurosci. 1993 Oct;13(10):4538-48. doi: 10.1523/JNEUROSCI.13-10-04538.1993. PMID: 8410202; PMCID: PMC6576362.

Rebsam A, Seif I, Gaspar P. Refinement of thalamocortical arbors and emergence of barrel domains in the primary somatosensory cortex: a study of normal and monoamine oxidase a knock-out mice. J Neurosci. 2002 Oct 1;22(19):8541-52. doi: 10.1523/JNEUROSCI.22-19-08541.2002. PMID: 12351728; PMCID: PMC6757778.

Reichova I, Sherman SM. Somatosensory corticothalamic projections: distinguishing drivers from modulators. J Neurophysiol. 2004 Oct;92(4):2185-97. doi: 10.1152/jn.00322.2004. Epub 2004 May 12. PMID: 15140908.

Renier N, Adams EL, Kirst C, Wu Z, Azevedo R, Kohl J, Autry AE, Kadiri L, Umadevi Venkataraju K, Zhou Y, Wang VX, Tang CY, Olsen O, Dulac C, Osten P, Tessier-Lavigne M. Mapping of Brain Activity by Automated Volume Analysis of Immediate Early Genes. Cell. 2016 Jun 16;165(7):1789-1802. doi: 10.1016/j.cell.2016.05.007. Epub 2016 May 26. PMID: 27238021; PMCID: PMC4912438.

Renier L, Cuevas I, Grandin CB, Dricot L, Plaza P, Lerens E, Rombaux P, De Volder AG. Right occipital cortex activation correlates with superior odor processing performance in the early blind. PLoS One. 2013 Aug 14;8(8):e71907. doi: 10.1371/journal.pone.0071907. PMID: 23967263; PMCID: PMC3743806.

Renier N, Dominici C, Erzurumlu RS, Kratochwil CF, Rijli FM, Gaspar P, Chédotal A. A mutant with bilateral whisker to barrel inputs unveils somatosensory mapping rules in the cerebral cortex. Elife. 2017 Mar 28;6:e23494. doi: 10.7554/eLife.23494. PMID: 28350297; PMCID: PMC5404921.

Renier N, Wu Z, Simon DJ, Yang J, Ariel P, Tessier-Lavigne M. iDISCO: a simple, rapid method to immunolabel large tissue samples for volume imaging. Cell. 2014 Nov 6;159(4):896-910. doi: 10.1016/j.cell.2014.10.010. Epub 2014 Oct 30. PMID: 25417164.

Renna JM, Weng S, Berson DM. Light acts through melanopsin to alter retinal waves and segregation of retinogeniculate afferents. Nat Neurosci. 2011 Jun 5;14(7):827-9. doi: 10.1038/nn.2845. PMID: 21642974; PMCID: PMC3125440.

Richards LJ, Koester SE, Tuttle R, O'Leary DD. Directed growth of early cortical axons is influenced by a chemoattractant released from an intermediate target. J Neurosci. 1997 Apr 1;17(7):2445-58. doi: 10.1523/JNEUROSCI.17-07-02445.1997. PMID: 9065505; PMCID: PMC6573499.

Robinson SR, Blumberg MS, Lane MS, Kreber LA. Spontaneous motor activity in fetal and infant rats is organized into discrete multilimb bouts. Behav Neurosci. 2000 Apr;114(2):328-36. doi: 10.1037//0735-7044.114.2.328. PMID: 10832794.

Rochefort NL, Narushima M, Grienberger C, Marandi N, Hill DN, Konnerth A. Development of direction selectivity in mouse cortical neurons. Neuron. 2011 Aug 11;71(3):425-32. doi: 10.1016/j.neuron.2011.06.013. PMID: 21835340.

Röder B, Teder-Sälejärvi W, Sterr A, Rösler F, Hillyard SA, Neville HJ. Improved auditory spatial tuning in blind humans. Nature. 1999 Jul 8;400(6740):162-6. doi: 10.1038/22106. PMID: 10408442.

Rouiller EM, Welker E. A comparative analysis of the morphology of corticothalamic projections in mammals. Brain Res Bull. 2000 Dec;53(6):727-41. doi: 10.1016/s0361-9230(00)00364-6. PMID: 11179837.

Rudhard Y, Kneussel M, Nassar MA, Rast GF, Annala AJ, Chen PE, Tigaret CM, Dean I, Roes J, Gibb AJ, Hunt SP, Schoepfer R. Absence of Whisker-related pattern formation in mice with NMDA receptors lacking coincidence detection properties and calcium signaling. J Neurosci. 2003 Mar 15;23(6):2323-32. doi: 10.1523/JNEUROSCI.23-06-02323.2003. PMID: 12657691; PMCID: PMC6742004.

Russell IJ, Sellick PM. Tuning properties of cochlear hair cells. Nature. 1977 Jun 30;267(5614):858-60. doi: 10.1038/267858a0. PMID: 895845.

Salichon N, Gaspar P, Upton AL, Picaud S, Hanoun N, Hamon M, De Maeyer E, Murphy DL, Mossner R, Lesch KP, Hen R, Seif I. Excessive activation of serotonin (5-HT) 1B receptors disrupts the formation of sensory maps in monoamine oxidase a and 5-ht transporter knock-out mice. J Neurosci. 2001 Feb 1;21(3):884-96. doi: 10.1523/JNEUROSCI.21-03-00884.2001. PMID: 11157075; PMCID: PMC6762299.

Sanes JR, Yamagata M. Many paths to synaptic specificity. Annu Rev Cell Dev Biol. 2009;25:161-95. doi: 10.1146/annurev.cellbio.24.110707.175402. PMID: 19575668.

Schlaggar BL, O'Leary DD. Early development of the somatotopic map and barrel patterning in rat somatosensory cortex. J Comp Neurol. 1994 Aug 1;346(1):80-96. doi: 10.1002/cne.903460106. PMID: 7962713.

Schubert D, Kötter R, Zilles K, Luhmann HJ, Staiger JF. Cell type-specific circuits of cortical layer IV spiny neurons. J Neurosci. 2003 Apr 1;23(7):2961-70. doi: 10.1523/JNEUROSCI.23-07-02961.2003. PMID: 12684483; PMCID: PMC6742105.

Seabrook TA, Burbridge TJ, Crair MC, Huberman AD. Architecture, Function, and Assembly of the Mouse Visual System. Annu Rev Neurosci. 2017 Jul 25;40:499-538. doi: 10.1146/annurev-neuro-071714-033842. PMID: 28772103.

Seidemann E, Zohary E, Newsome WT. Temporal gating of neural signals during performance of a visual discrimination task. Nature. 1998 Jul 2;394(6688):72-5. doi: 10.1038/27906. PMID: 9665129.

Sendin G, Bourien J, Rassendren F, Puel JL, Nouvian R. Spatiotemporal pattern of action potential firing in developing inner hair cells of the mouse cochlea. Proc Natl Acad Sci U S A. 2014 Feb 4;111(5):1999-2004. doi: 10.1073/pnas.1319615111. Epub 2014 Jan 15. PMID: 24429348; PMCID: PMC3918831.

Senft SL, Woolsey TA. Computer-aided analyses of thalamocortical afferent ingrowth. Cereb Cortex. 1991a Jul-Aug;1(4):336-47. doi: 10.1093/cercor/1.4.336. PMID: 1822739.

Senft SL, Woolsey TA. Growth of thalamic afferents into mouse barrel cortex. Cereb Cortex. 1991b Jul-Aug;1(4):308-35. doi: 10.1093/cercor/1.4.308. PMID: 1822738.

Shatz CJ, Stryker MP. Prenatal tetrodotoxin infusion blocks segregation of retinogeniculate afferents. Science. 1988 Oct 7;242(4875):87-9. doi: 10.1126/science.3175636. PMID: 3175636.

She WC, Quairiaux C, Albright MJ, Wang YC, Sanchez DE, Chang PS, Welker E, Lu HC. Roles of mGluR5 in synaptic function and plasticity of the mouse thalamocortical pathway. Eur J Neurosci. 2009 Apr;29(7):1379-96. doi: 10.1111/j.1460-9568.2009.06696.x. Epub 2009 Mar 23. PMID: 19519626; PMCID: PMC2714552.

Shen J, Colonnese MT. Development of Activity in the Mouse Visual Cortex. J Neurosci. 2016 Nov 30;36(48):12259-12275. doi: 10.1523/JNEUROSCI.1903-16.2016. PMID: 27903733; PMCID: PMC5148222.

Shepherd GM, Svoboda K. Laminar and columnar organization of ascending excitatory projections to layer 2/3 pyramidal neurons in rat barrel cortex. J Neurosci. 2005 Jun 15;25(24):5670-9. doi: 10.1523/JNEUROSCI.1173-05.2005. PMID: 15958733; PMCID: PMC6724876.

Sherman SM. Thalamus plays a central role in ongoing cortical functioning. Nat Neurosci. 2016 Apr;19(4):533-41. doi: 10.1038/nn.4269. PMID: 27021938.

Sherman SM, Guillery RW. On the actions that one nerve cell can have on another: distinguishing "drivers" from "modulators". Proc Natl Acad Sci U S A. 1998 Jun 9;95(12):7121-6. doi: 10.1073/pnas.95.12.7121. PMID: 9618549; PMCID: PMC22761.

Sherman SM, Guillery RW. The role of the thalamus in the flow of information to the cortex. Philos Trans R Soc Lond B Biol Sci. 2002 Dec 29;357(1428):1695-708. doi: 10.1098/rstb.2002.1161. PMID: 12626004; PMCID: PMC1693087.

Shi W, Xianyu A, Han Z, Tang X, Li Z, Zhong H, Mao T, Huang K, Shi SH. Ontogenetic establishment of order-specific nuclear organization in the mammalian thalamus. Nat Neurosci. 2017 Apr;20(4):516-528. doi: 10.1038/nn.4519. Epub 2017 Feb 27. PMID: 28250409; PMCID: PMC5374008.

Shigematsu N, Miyamoto Y, Esumi S, Fukuda T. The Anterolateral Barrel Subfield Differs from the Posteromedial Barrel Subfield in the Morphology and Cell Density of Parvalbumin-Positive GABAergic Interneurons. eNeuro. 2024 Mar 26;11(3):ENEURO.0518-22.2024. doi: 10.1523/ENEURO.0518-22.2024. PMID: 38438262; PMCID: PMC10965236.

Shimogori T, Grove EA. Fibroblast growth factor 8 regulates neocortical guidance of area-specific thalamic innervation. J Neurosci. 2005 Jul 13;25(28):6550-60. doi: 10.1523/JNEUROSCI.0453-05.2005. PMID: 16014716; PMCID: PMC6725424.

Siegel F, Heimel JA, Peters J, Lohmann C. Peripheral and central inputs shape network dynamics in the developing visual cortex in vivo. Curr Biol. 2012 Feb 7;22(3):253-8. doi: 10.1016/j.cub.2011.12.026. Epub 2012 Jan 19. PMID: 22264606.

Simi A, Studer M. Developmental genetic programs and activity-dependent mechanisms instruct neocortical area mapping. Curr Opin Neurobiol. 2018 Dec;53:96-102. doi: 10.1016/j.conb.2018.06.007. Epub 2018 Jul 10. PMID: 30005291.

Simons DJ, Land PW. Early experience of tactile stimulation influences organization of somatic sensory cortex. Nature. 1987 Apr 16-22;326(6114):694-7. doi: 10.1038/326694a0. PMID: 3561512.

Simpson TI, Pratt T, Mason JO, Price DJ. Normal ventral telencephalic expression of Pax6 is required for normal development of thalamocortical axons in embryonic mice. Neural Dev. 2009 Jun 5;4:19. doi: 10.1186/1749-8104-4-19. PMID: 19500363; PMCID: PMC2699344.

Sonntag M, Englitz B, Kopp-Scheinpflug C, Rübsamen R. Early postnatal development of spontaneous and acoustically evoked discharge activity of principal cells of the medial nucleus of the trapezoid body: an in vivo study in mice. J Neurosci. 2009 Jul 29;29(30):9510-20. doi: 10.1523/JNEUROSCI.1377-09.2009. PMID: 19641114; PMCID: PMC6666529.

Stroh A, Adelsberger H, Groh A, Rühlmann C, Fischer S, Schierloh A, Deisseroth K, Konnerth A. Making waves: initiation and propagation of corticothalamic Ca2+ waves in vivo. Neuron. 2013 Mar 20;77(6):1136-50. doi: 10.1016/j.neuron.2013.01.031. PMID: 23522048.

Sumser A, Mease RA, Sakmann B, Groh A. Organization and somatotopy of corticothalamic projections from L5B in mouse barrel cortex. Proc Natl Acad Sci U S A. 2017 Aug 15;114(33):8853-8858. doi: 10.1073/pnas.1704302114. Epub 2017 Aug 3. PMID: 28774955; PMCID: PMC5565434.

Sur M, Leamey CA. Development and plasticity of cortical areas and networks. Nat Rev Neurosci. 2001 Apr;2(4):251-62. doi: 10.1038/35067562. PMID: 11283748.

Sur M, Pallas SL, Roe AW. Cross-modal plasticity in cortical development: differentiation and specification of sensory neocortex. Trends Neurosci. 1990 Jun;13(6):227-33. doi: 10.1016/0166-2236(90)90165-7. PMID: 1694329.

Sur M, Rubenstein JL. Patterning and plasticity of the cerebral cortex. Science. 2005 Nov 4;310(5749):805-10. doi: 10.1126/science.1112070. PMID: 16272112.

Suzuki A, Lee LJ, Hayashi Y, Muglia L, Itohara S, Erzurumlu RS, Iwasato T. Thalamic adenylyl cyclase 1 is required for barrel formation in the somatosensory cortex. Neuroscience. 2015 Apr 2;290:518-29. doi: 10.1016/j.neuroscience.2015.01.043. Epub 2015 Jan 30. PMID: 25644422; PMCID: PMC5994750.

Syed MM, Lee S, He S, Zhou ZJ. Spontaneous waves in the ventricular zone of developing mammalian retina. J Neurophysiol. 2004 May;91(5):1999-2009. doi: 10.1152/jn.01129.2003. Epub 2003 Dec 17. PMID: 14681336.

Takahata T. Development of ocular dominance columns across rodents and other species: revisiting the concept of critical period plasticity. Front Neural Circuits. 2024 Jul 5;18:1402700. doi: 10.3389/fncir.2024.1402700. PMID: 39036421; PMCID: PMC11258045.

Takesian AE, Bogart LJ, Lichtman JW, Hensch TK. Inhibitory circuit gating of auditory critical-period plasticity. Nat Neurosci. 2018 Feb;21(2):218-227. doi: 10.1038/s41593-017-0064-2. Epub 2018 Jan 22. Erratum in: Nat Neurosci. 2018 Oct;21(10):1495. doi: 10.1038/s41593-018-0161-x. PMID: 29358666; PMCID: PMC5978727.

Telley L, Govindan S, Prados J, Stevant I, Nef S, Dermitzakis E, Dayer A, Jabaudon D. Sequential transcriptional waves direct the differentiation of newborn neurons in the mouse neocortex. Science. 2016 Mar 25;351(6280):1443-6. doi: 10.1126/science.aad8361. Epub 2016 Mar 3. PMID: 26940868.

Terreros G, Delano PH. Corticofugal modulation of peripheral auditory responses. Front Syst Neurosci. 2015 Sep 30;9:134. doi: 10.3389/fnsys.2015.00134. PMID: 26483647; PMCID: PMC4588004.

Theyel BB, Lee CC, Sherman SM. Specific and nonspecific thalamocortical connectivity in the auditory and somatosensory thalamocortical slices. Neuroreport. 2010 Sep 15;21(13):861-4. doi: 10.1097/WNR.0b013e32833d7cec. PMID: 20647961; PMCID: PMC2945241.

Thiers FA, Nadol JB Jr, Liberman MC. Reciprocal synapses between outer hair cells and their afferent terminals: evidence for a local neural network in the mammalian cochlea. J Assoc Res Otolaryngol. 2008 Dec;9(4):477-89. doi: 10.1007/s10162-008-0135-x. Epub 2008 Aug 8. PMID: 18688678; PMCID: PMC2580814.

Thomson AM. Neocortical layer 6, a review. Front Neuroanat. 2010 Mar 31;4:13. doi: 10.3389/fnana.2010.00013. PMID: 20556241; PMCID: PMC2885865.

Tiriac A, Blumberg MS. Gating of reafference in the external cuneate nucleus during self-generated movements in wake but not sleep. Elife. 2016 Aug 3;5:e18749. doi: 10.7554/eLife.18749. PMID: 27487470; PMCID: PMC4995095.

Tiriac A, Feller MB. Roles of visually evoked and spontaneous activity in the development of retinal direction selectivity maps. Trends Neurosci. 2022 Jul;45(7):529-538. doi: 10.1016/j.tins.2022.04.002. Epub 2022 Apr 29. PMID: 35491255.

Tiriac A, Smith BE, Feller MB. Light Prior to Eye Opening Promotes Retinal Waves and Eye-Specific Segregation. Neuron. 2018 Dec 5;100(5):1059-1065.e4. doi: 10.1016/j.neuron.2018.10.011. Epub 2018 Nov 1. PMID: 30392793; PMCID: PMC6283698.

Tiriac A, Uitermarkt BD, Fanning AS, Sokoloff G, Blumberg MS. Rapid whisker movements in sleeping newborn rats. Curr Biol. 2012 Nov 6;22(21):2075-80. doi: 10.1016/j.cub.2012.09.009. Epub 2012 Oct 18. PMID: 23084988; PMCID: PMC3494768.

Toldi J, Farkas T, Völgyi B. Neonatal enucleation induces cross-modal changes in the barrel cortex of rat. A behavioural and electrophysiological study. Neurosci Lett. 1994 Feb 14;167(1-2):1-4. doi: 10.1016/0304-3940(94)91014-6. PMID: 8177504.

Tolner EA, Sheikh A, Yukin AY, Kaila K, Kanold PO. Subplate neurons promote spindle bursts and thalamocortical patterning in the neonatal rat somatosensory cortex. J Neurosci. 2012 Jan 11;32(2):692-702. doi: 10.1523/JNEUROSCI.1538-11.2012. PMID: 22238105; PMCID: PMC3517992.

Toma K, Kumamoto T, Hanashima C. The timing of upper-layer neurogenesis is conferred by sequential derepression and negative feedback from deep-layer neurons. J Neurosci. 2014 Sep 24;34(39):13259-76. doi: 10.1523/JNEUROSCI.2334-14.2014. PMID: 25253869; PMCID: PMC6608336.

Torborg CL, Feller MB. Spontaneous patterned retinal activity and the refinement of retinal projections. Prog Neurobiol. 2005 Jul;76(4):213-35. doi: 10.1016/j.pneurobio.2005.09.002. Epub 2005 Nov 8. PMID: 16280194.

Tritsch NX, Bergles DE. Developmental regulation of spontaneous activity in the Mammalian cochlea. J Neurosci. 2010 Jan 27;30(4):1539-50. doi: 10.1523/JNEUROSCI.3875-09.2010. PMID: 20107081; PMCID: PMC2814371.

Tritsch NX, Yi E, Gale JE, Glowatzki E, Bergles DE. The origin of spontaneous activity in the developing auditory system. Nature. 2007 Nov 1;450(7166):50-5. doi: 10.1038/nature06233. PMID: 17972875.

Tsukano H, Horie M, Ohga S, Takahashi K, Kubota Y, Hishida R, Takebayashi H, Shibuki K. Reconsidering Tonotopic Maps in the Auditory Cortex and Lemniscal Auditory Thalamus in Mice. Front Neural Circuits. 2017 Feb 28;11:14. doi: 10.3389/fncir.2017.00014. Erratum in: Front Neural Circuits. 2017 May 31;11:39. doi: 10.3389/fncir.2017.00039. PMID: 28293178; PMCID: PMC5330090.

Tu DC, Zhang D, Demas J, Slutsky EB, Provencio I, Holy TE, Van Gelder RN. Physiologic diversity and development of intrinsically photosensitive retinal ganglion cells. Neuron. 2005 Dec 22;48(6):987-99. doi: 10.1016/j.neuron.2005.09.031. PMID: 16364902.

Tuncdemir SN, Wamsley B, Stam FJ, Osakada F, Goulding M, Callaway EM, Rudy B, Fishell G. Early Somatostatin Interneuron Connectivity Mediates the Maturation of Deep Layer Cortical Circuits. Neuron. 2016 Feb 3;89(3):521-35. doi: 10.1016/j.neuron.2015.11.020. PMID: 26844832; PMCID: PMC4861073.

Uemura M, Nakao S, Suzuki ST, Takeichi M, Hirano S. OL-Protocadherin is essential for growth of striatal axons and thalamocortical projections. Nat Neurosci. 2007 Sep;10(9):1151-9. doi: 10.1038/nn1960. Epub 2007 Aug 26. PMID: 17721516.

Uesaka N, Hayano Y, Yamada A, Yamamoto N. Interplay between laminar specificity and activity-dependent mechanisms of thalamocortical axon branching. J Neurosci. 2007 May 9;27(19):5215-23. doi: 10.1523/JNEUROSCI.4685-06.2007. PMID: 17494708; PMCID: PMC6672371.

Ueta Y, Miyata M. Functional and structural synaptic remodeling mechanisms underlying somatotopic organization and reorganization in the thalamus. Neurosci Biobehav Rev. 2023 Sep;152:105332. doi: 10.1016/j.neubiorev.2023.105332. Epub 2023 Jul 29. PMID: 37524138.

Uhlhaas, P.J., Roux, F. (2016). Thalamo-Cortical Interactions and Synchronous Oscillations in MEG Data. In: Palva, S. (eds) Multimodal Oscillation-based Connectivity Theory. Springer, Cham. https://doi.org/10.1007/978-3-319-32265-0_5

Valverde F. Structural changes in the area striata of the mouse after enucleation. Exp Brain Res. 1968;5(4):274-92. doi: 10.1007/BF00235903. PMID: 4889747.

Van der Bourg A, Yang JW, Reyes-Puerta V, Laurenczy B, Wieckhorst M, Stüttgen MC, Luhmann HJ, Helmchen F. Layer-Specific Refinement of Sensory Coding in Developing Mouse Barrel Cortex. Cereb Cortex. 2017 Oct 1;27(10):4835-4850. doi: 10.1093/cercor/bhw280. PMID: 27620976.

Van der Loos H. Barreloids in mouse somatosensory thalamus. Neurosci Lett. 1976 Mar;2(1):1-6. doi: 10.1016/0304-3940(76)90036-7. PMID: 19604804.

Van der Loos H, Woolsey TA. Somatosensory cortex: structural alterations following early injury to sense organs. Science. 1973 Jan 26;179(4071):395-8. doi: 10.1126/science.179.4071.395. PMID: 4682966.

Vanderhaeghen P, Lu Q, Prakash N, Frisén J, Walsh CA, Frostig RD, Flanagan JG. A mapping label required for normal scale of body representation in the cortex. Nat Neurosci. 2000 Apr;3(4):358-65. doi: 10.1038/73929. PMID: 10725925.

Viaene AN, Petrof I, Sherman SM. Properties of the thalamic projection from the posterior medial nucleus to primary and secondary somatosensory cortices in the mouse. Proc Natl

Acad Sci U S A. 2011 Nov 1;108(44):18156-61. doi: 10.1073/pnas.1114828108. Epub 2011 Oct 24. PMID: 22025694; PMCID: PMC3207656.

Vitali I, Fièvre S, Telley L, Oberst P, Bariselli S, Frangeul L, Baumann N, McMahon JJ, Klingler E, Bocchi R, Kiss JZ, Bellone C, Silver DL, Jabaudon D. Progenitor Hyperpolarization Regulates the Sequential Generation of Neuronal Subtypes in the Developing Neocortex. Cell. 2018 Aug 23;174(5):1264-1276.e15. doi: 10.1016/j.cell.2018.06.036. Epub 2018 Jul 26. PMID: 30057116; PMCID: PMC6545245.

Vitalis T, Dauphinot L, Gressens P, Potier MC, Mariani J, Gaspar P. RORα Coordinates Thalamic and Cortical Maturation to Instruct Barrel Cortex Development. Cereb Cortex. 2018 Nov 1;28(11):3994-4007. doi: 10.1093/cercor/bhx262. PMID: 29040410.

Viswanathan S, Bandyopadhyay S, Kao JP, Kanold PO. Changing microcircuits in the subplate of the developing cortex. J Neurosci. 2012 Feb 1;32(5):1589-601. doi: 10.1523/JNEUROSCI.4748-11.2012. PMID: 22302801; PMCID: PMC3517995.

Viswanathan S, Sheikh A, Looger LL, Kanold PO. Molecularly Defined Subplate Neurons Project Both to Thalamocortical Recipient Layers and Thalamus. Cereb Cortex. 2017 Oct 1;27(10):4759-4768. doi: 10.1093/cercor/bhw271. PMID: 27655928; PMCID: PMC6059176.

Voiculescu O, Charnay P, Schneider-Maunoury S. Expression pattern of a Krox-20/Cre knock-in allele in the developing hindbrain, bones, and peripheral nervous system. Genesis. 2000 Feb;26(2):123-6. doi: 10.1002/(sici)1526-968x(200002)26:2<123::aid-gene7>3.0.co;2-o. PMID: 10686605.

Voufo C, Chen AQ, Smith BE, Yan R, Feller MB, Tiriac A. Circuit mechanisms underlying embryonic retinal waves. Elife. 2023 Feb 15;12:e81983. doi: 10.7554/eLife.81983. PMID: 36790167; PMCID: PMC9988258.

Vue TY, Aaker J, Taniguchi A, Kazemzadeh C, Skidmore JM, Martin DM, Martin JF, Treier M, Nakagawa Y. Characterization of progenitor domains in the developing mouse thalamus. J Comp Neurol. 2007 Nov 1;505(1):73-91. doi: 10.1002/cne.21467. PMID: 17729296.

Vue TY, Bluske K, Alishahi A, Yang LL, Koyano-Nakagawa N, Novitch B, Nakagawa Y. Sonic hedgehog signaling controls thalamic progenitor identity and nuclei specification in mice. J Neurosci. 2009 Apr 8;29(14):4484-97. doi: 10.1523/JNEUROSCI.0656-09.2009. PMID: 19357274; PMCID: PMC2718849.

Vue TY, Lee M, Tan YE, Werkhoven Z, Wang L, Nakagawa Y. Thalamic control of neocortical area formation in mice. J Neurosci. 2013 May 8;33(19):8442-53. doi: 10.1523/JNEUROSCI.5786-12.2013. PMID: 23658181; PMCID: PMC3732791.

Wamsley B, Fishell G. Genetic and activity-dependent mechanisms underlying interneuron diversity. Nat Rev Neurosci. 2017 May;18(5):299-309. doi: 10.1038/nrn.2017.30. Epub 2017 Apr 6. PMID: 28381833.

Wang HC, Bergles DE. Spontaneous activity in the developing auditory system. Cell Tissue Res. 2015 Jul;361(1):65-75. doi: 10.1007/s00441-014-2007-5. Epub 2014 Oct 9. PMID: 25296716; PMCID: PMC7046314.

Watson RF, Abdel-Majid RM, Barnett MW, Willis BS, Katsnelson A, Gillingwater TH, McKnight GS, Kind PC, Neumann PE. Involvement of protein kinase A in patterning of the mouse somatosensory cortex. J Neurosci. 2006 May 17;26(20):5393-401. doi: 10.1523/JNEUROSCI.0750-06.2006. PMID: 16707791; PMCID: PMC6675315.

Weiler N, Wood L, Yu J, Solla SA, Shepherd GM. Top-down laminar organization of the excitatory network in motor cortex. Nat Neurosci. 2008 Mar;11(3):360-6. doi: 10.1038/nn2049. Epub 2008 Feb 3. PMID: 18246064; PMCID: PMC2748826.

Welker C. Receptive fields of barrels in the somatosensory neocortex of the rat. J Comp Neurol. 1976 Mar 15;166(2):173-89. doi: 10.1002/cne.901660205. PMID: 770516.

White LE, Coppola DM, Fitzpatrick D. The contribution of sensory experience to the maturation of orientation selectivity in ferret visual cortex. Nature. 2001 Jun 28;411(6841):1049-52. doi: 10.1038/35082568. PMID: 11429605.

Wijetunge LS, Till SM, Gillingwater TH, Ingham CA, Kind PC. mGluR5 regulates glutamate-dependent development of the mouse somatosensory cortex. J Neurosci. 2008 Dec 3;28(49):13028-37. doi: 10.1523/JNEUROSCI.2600-08.2008. PMID: 19052194; PMCID: PMC3844741.

Wilson SP, Bednar JA. What, if anything, are topological maps for? Dev Neurobiol. 2015 Jun;75(6):667-81. doi: 10.1002/dneu.22281. Epub 2015 Feb 18. PMID: 25683193.

Wimmer VC, Bruno RM, de Kock CP, Kuner T, Sakmann B. Dimensions of a projection column and architecture of VPM and POm axons in rat vibrissal cortex. Cereb Cortex. 2010

Oct;20(10):2265-76. doi: 10.1093/cercor/bhq068. Epub 2010 May 7. PMID: 20453248; PMCID: PMC2936807.

Wise SP, Jones EG. Cells of origin and terminal distribution of descending projections of the rat somatic sensory cortex. J Comp Neurol. 1977 Sep 15;175(2):129-57. doi: 10.1002/cne.901750202. PMID: 408380.

Wong FK, Bercsenyi K, Sreenivasan V, Portalés A, Fernández-Otero M, Marín O. Pyramidal cell regulation of interneuron survival sculpts cortical networks. Nature. 2018 May;557(7707):668-673. doi: 10.1038/s41586-018-0139-6. Epub 2018 May 30. PMID: 29849154; PMCID: PMC6207348.

Wong RO. Retinal waves and visual system development. Annu Rev Neurosci. 1999;22:29-47. doi: 10.1146/annurev.neuro.22.1.29. PMID: 10202531.

Woolsey TA. Some anatomical bases of cortical somatotopic organization. Brain Behav Evol. 1978;15(5-6):325-71. doi: 10.1159/000123786. PMID: 737526.

Woolsey TA, Anderson JR, Wann JR, Stanfield BB. Effects of early vibrissae damage on neurons in the ventrobasal (VB) thalamus of the mouse. J Comp Neurol. 1979 Mar 15;184(2):363-80. doi: 10.1002/cne.901840210. PMID: 762288.

Woolsey TA, Van der Loos H. The structural organization of layer IV in the somatosensory region (SI) of mouse cerebral cortex. The description of a cortical field composed of discrete cytoarchitectonic units. Brain Res. 1970 Jan 20;17(2):205-42. doi: 10.1016/0006-8993(70)90079-x. Erratum in: Brain Res. 2016 Nov 15;1651:121. doi: 10.1016/j.brainres.2016.09.008. PMID: 4904874.

Woolsey TA, Wann JR. Areal changes in mouse cortical barrels following vibrissal damage at different postnatal ages. J Comp Neurol. 1976 Nov 1;170(1):53-66. doi: 10.1002/cne.901700105. PMID: 977815.

Woolsey TA, Welker C, Schwartz RH. Comparative anatomical studies of the SmL face cortex with special reference to the occurrence of "barrels" in layer IV. J Comp Neurol. 1975 Nov 1;164(1):79-94. doi: 10.1002/cne.901640107. PMID: 809494.

Wu HP, Ioffe JC, Iverson MM, Boon JM, Dyck RH. Novel, whisker-dependent texture discrimination task for mice. Behav Brain Res. 2013 Jan 15;237:238-42. doi: 10.1016/j.bbr.2012.09.044. Epub 2012 Sep 28. PMID: 23026377.

Xu B, Zang K, Ruff NL, Zhang YA, McConnell SK, Stryker MP, Reichardt LF. Cortical degeneration in the absence of neurotrophin signaling: dendritic retraction and neuronal loss after removal of the receptor TrkB. Neuron. 2000 Apr;26(1):233-45. doi: 10.1016/s0896-6273(00)81153-8. PMID: 10798407.

Yaka R, Yinon U, Wollberg Z. Auditory activation of cortical visual areas in cats after early visual deprivation. Eur J Neurosci. 1999 Apr;11(4):1301-12. doi: 10.1046/j.1460-9568.1999.00536.x. PMID: 10103125.

Yamamoto N, López-Bendito G. Shaping brain connections through spontaneous neural activity. Eur J Neurosci. 2012 May;35(10):1595-604. doi: 10.1111/j.1460-9568.2012.08101.x. PMID: 22607005.

Yamashita T, Vavladeli A, Pala A, Galan K, Crochet S, Petersen SSA, Petersen CCH. Diverse Long-Range Axonal Projections of Excitatory Layer 2/3 Neurons in Mouse Barrel Cortex. Front Neuroanat. 2018 May 1;12:33. doi: 10.3389/fnana.2018.00033. PMID: 29765308; PMCID: PMC5938399.

Yang JW, An S, Sun JJ, Reyes-Puerta V, Kindler J, Berger T, Kilb W, Luhmann HJ. Thalamic network oscillations synchronize ontogenetic columns in the newborn rat barrel cortex. Cereb Cortex. 2013 Jun;23(6):1299-316. doi: 10.1093/cercor/bhs103. Epub 2012 May 16. PMID: 22593243.

Yang JW, Hanganu-Opatz IL, Sun JJ, Luhmann HJ. Three patterns of oscillatory activity differentially synchronize developing neocortical networks in vivo. J Neurosci. 2009 Jul 15;29(28):9011-25. doi: 10.1523/JNEUROSCI.5646-08.2009. PMID: 19605639; PMCID: PMC6665441.

Yang JW, Kilb W, Kirischuk S, Unichenko P, Stüttgen MC, Luhmann HJ. Development of the whisker-to-barrel cortex system. Curr Opin Neurobiol. 2018 Dec;53:29-34. doi: 10.1016/j.conb.2018.04.023. Epub 2018 May 5. PMID: 29738998.

Yu C, Derdikman D, Haidarliu S, Ahissar E. Parallel thalamic pathways for whisking and touch signals in the rat. PLoS Biol. 2006 May;4(5):e124. doi: 10.1371/journal.pbio.0040124. Epub 2006 Apr 18. PMID: 16605304; PMCID: PMC1436027.

Yu G, Wang LG, Han Y, He QY. clusterProfiler: an R package for comparing biological themes among gene clusters. OMICS. 2012 May;16(5):284-7. doi: 10.1089/omi.2011.0118. Epub 2012 Mar 28. PMID: 22455463; PMCID: PMC3339379.

Zhang-Hooks Y, Agarwal A, Mishina M, Bergles DE. NMDA Receptors Enhance Spontaneous Activity and Promote Neuronal Survival in the Developing Cochlea. Neuron. 2016 Jan 20;89(2):337-50. doi: 10.1016/j.neuron.2015.12.016. Epub 2016 Jan 7. Erratum in: Neuron. 2016 Feb 3;89(3):672. PMID: 26774161; PMCID: PMC4724245.

Zechel S, Nakagawa Y, Ibáñez CF. Thalamo-cortical axons regulate the radial dispersion of neocortical GABAergic interneurons. Elife. 2016 Dec 9;5:e20770. doi: 10.7554/eLife.20770. PMID: 27935475; PMCID: PMC5167520.

Zembrzycki A, Chou SJ, Ashery-Padan R, Stoykova A, O'Leary DD. Sensory cortex limits cortical maps and drives top-down plasticity in thalamocortical circuits. Nat Neurosci. 2013 Aug;16(8):1060-7. doi: 10.1038/nn.3454. Epub 2013 Jul 7. PMID: 23831966; PMCID: PMC3769112.

Zheng JJ, Lee S, Zhou ZJ. A developmental switch in the excitability and function of the starburst network in the mammalian retina. Neuron. 2004 Dec 2;44(5):851-64. doi: 10.1016/j.neuron.2004.11.015. PMID: 15572115.

Zhu A, Srivastava A, Ibrahim JG, Patro R, Love MI. Nonparametric expression analysis using inferential replicate counts. Nucleic Acids Res. 2019 Oct 10;47(18):e105. doi: 10.1093/nar/gkz622. PMID: 31372651; PMCID: PMC6765120.

Zimmermann M, Cusack R, Bedny M, Szwed M. Auditory areas are recruited for naturalistic visual meaning in early deaf people. Nat Commun. 2024 Sep 17;15(1):8035. doi: 10.1038/s41467-024-52383-6. PMID: 39289375; PMCID: PMC11408683.

Zong H, Espinosa JS, Su HH, Muzumdar MD, Luo L. Mosaic analysis with double markers in mice. Cell. 2005 May 6;121(3):479-92. doi: 10.1016/j.cell.2005.02.012. PMID: 15882628.

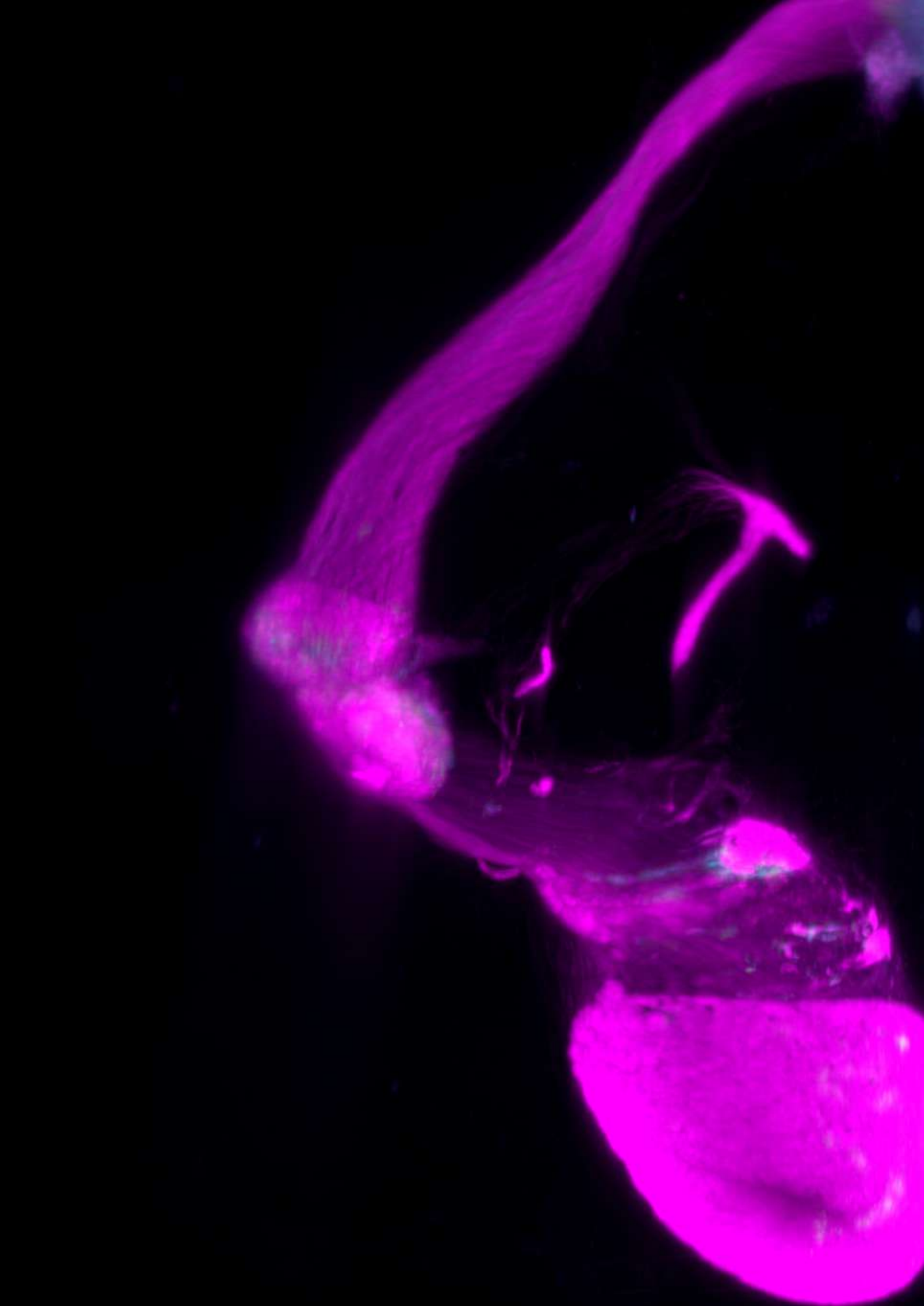

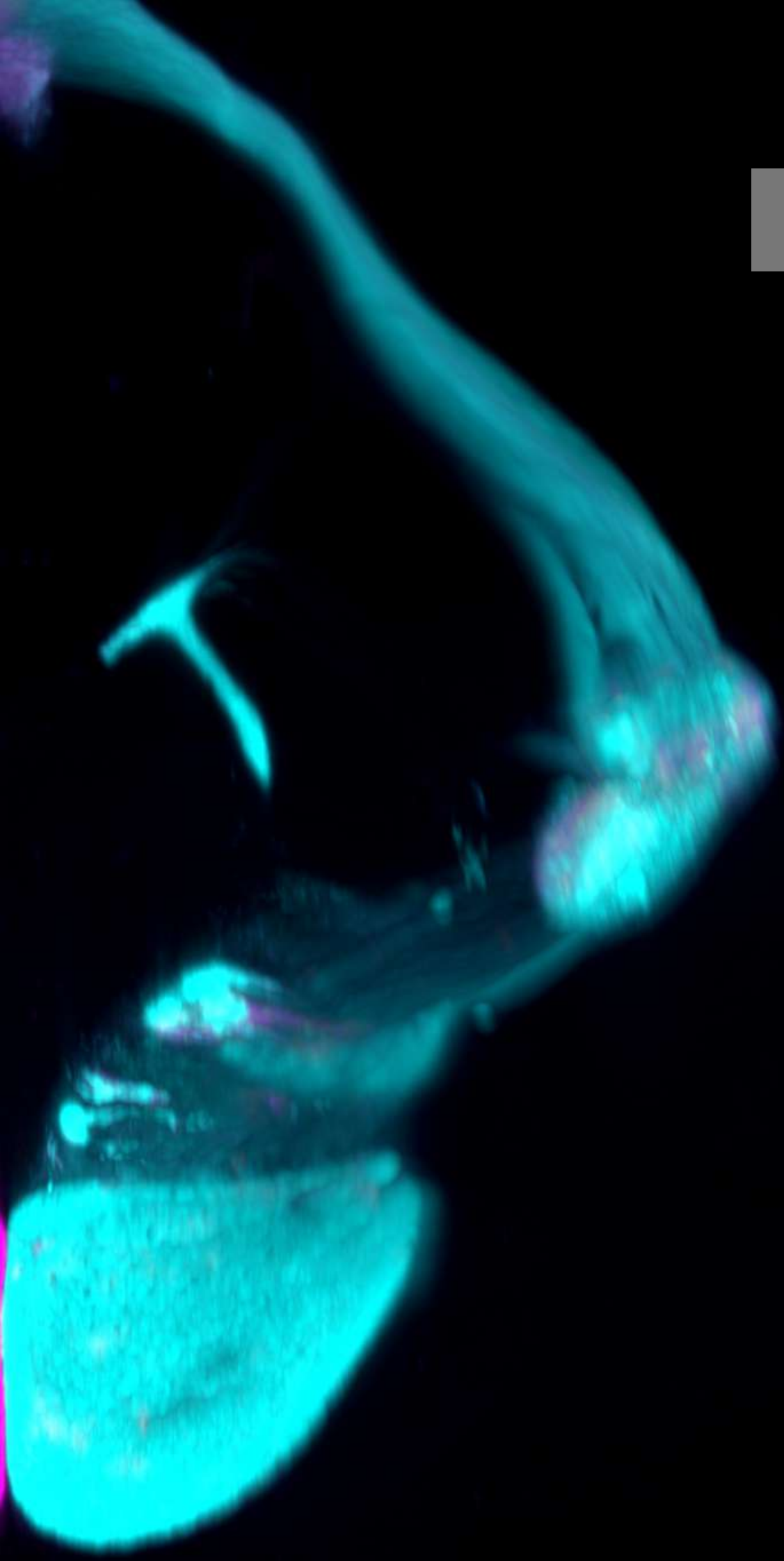

ANNEX

Side stories worth telling

A prenatal window for enhancing spatial resolution of cortical barrel maps

Mar Aníbal-Martínez[1], Lorenzo Puche-Aroca[1], Elena Pérez-Montoyo[1], Gabriele Pumo[2,3], M. Pilar Madrigal[4], Luis M. Rodríguez-Malmierca[1], Francisco J. Martini[1], Filippo M. Rijli[2,3], Guillermina López-Bendito[1,*]

[1]Instituto de Neurociencias de Alicante, Universidad Miguel Hernández-Consejo Superior de Investigaciones Científicas (UMH-CSIC), San Juan de Alicante, Alicante, Spain.
[2] Friedrich Miescher Institute for Biomedical Research, Fabrikstrasse 24, 4056 Basel, Switzerland.
[3]University of Basel, Basel, Switzerland.
[4]Departamento de Histología y Anatomía, Facultad de Medicina, Universidad Miguel Hernández (UMH), San Juan de Alicante, Alicante, Spain.

*Correspondence: g.lbendito@umh.es (G.L-B)

Nature Communications March 2025: 16, no. 1955. DOI: 10.1038/s41467-025-57052-w.

nature communications

Article

https://doi.org/10.1038/s41467-025-57052-w

A prenatal window for enhancing spatial resolution of cortical barrel maps

Received: 24 June 2024

Accepted: 5 February 2025

Published online: 06 March 2025

Check for updates

Mar Aníbal-Martínez[1], Lorenzo Puche-Aroca[1], Elena Pérez-Montoyo[1], Gabriele Pumo[2,3], M. Pilar Madrigal[4], Luis M. Rodríguez-Malmierca[1], Francisco J. Martini[1], Filippo M. Rijli[2,3] & Guillermina López-Bendito[1]

Precise mapping of peripheral inputs onto cortical areas is essential for accurate sensory processing. In the mouse primary somatosensory cortex, mystacial whiskers correspond to large, well-defined barrels, while upper lip whiskers form smaller, less distinct barrels. These differences are traditionally attributed to variations in whisker input type and receptor density, but prenatal activity and transcriptional programs also impact somatosensory map development independently of sensory experience. Here, we demonstrate that prenatal ablation of mystacial whiskers leads to a remapping of cortical territories, enhancing the functional and anatomical definition of upper lip whisker barrels. This reorganization occurs without altering peripheral receptor types. Instead, thalamic neurons that receive upper lip inputs adopt a mystacial-like transcriptional profile. Our findings unveil a regulated prenatal mechanism in the thalamus that ensures sufficient cortical barrel size and spatial resolution for sensory processing, irrespective of peripheral receptor type or density, highlighting a critical developmental process in sensory mapping.

Sensory systems are represented in the primary sensory areas of the brain, structured into both anatomical and functional maps[1–4]. The spatial precision of sensory maps varies among species according to the ethological relevance of the modality or the intra-modal sensory branch[5]. This precision is achieved through the accuracy of point-to-point innervation along the ascending sensory pathway. In rodents, which heavily rely on the somatosensory modality, a prominent cortical area is devoted to processing stimuli from facial whiskers. Within the mouse primary somatosensory cortex (S1), information from facial whiskers is processed in two juxtaposed subfields: the posteromedial barrel subfield (PMBSF) and the antero-lateral barrel subfield (ALBSF). The PMBSF receives input from the mystacial whiskers which provide diverse and specialized information to S1[6,7]. The ALBSF receives input from the upper lip whiskers which are considered to play a secondary role in sensory processing[8]. While each barrel corresponds to a single whisker in both regions, the degree of clustering of incoming thalamocortical axons varies, leading to notable anatomical distinctions between the two territories. While PMBSF barrels are characterized by their large size and sharp borders, ALBSF barrels are smaller and have poorly defined borders[9]. These differences in intra-modal map organization parallel the distinct morphological characteristics of mystacial and upper lip whiskers: mystacial whiskers are long with large follicles, whereas upper lip whiskers are comparatively short with small follicles, albeit more abundant. Despite their clear anatomical and functional differences, we still lack a complete understanding of the mechanism underlying the construction of these two distinct barrel maps and to what extent they rely on the type of sensory receptors (mystacial versus upper lip). Indeed, recent data demonstrated that sensory receptor-independent mechanisms can also influence cortical barrel size by altering the patterns of activity in subcortical stations. For instance, increasing thalamic waves in the developing somatosensory thalamus of early blind mice results in

[1]Instituto de Neurociencias de Alicante, Universidad Miguel Hernández-Consejo Superior de Investigaciones Científicas (UMH-CSIC), San Juan de Alicante, Alicante, Spain. [2]Friedrich Miescher Institute for Biomedical Research, Fabrikstrasse 24, 4056 Basel, Switzerland. [3]University of Basel, Basel, Switzerland. [4]Departamento de Histología y Anatomía, Facultad de Medicina, Universidad Miguel Hernández (UMH), San Juan de Alicante, Alicante, Spain.
e-mail: g.lbendito@umh.es

larger barrels in the PMBSF of S1, even before the onset of active whisking[10,11]. Thus, the size of a sensory barrel map may not only depend on the type and number of sensory receptors but may also be regulated by intrinsic programs during development. By embryonically ablating mystacial whiskers and follicles, and the subsequent PMBSF representation, we generated mice in which the ALBSF barrels become larger and better-defined, without altering the size and number of upper lip follicles. This intra-modal reorganization of the barrel maps occurs within a restricted prenatal time window and is guided by transcriptional programs operating intra-modally in the thalamus. Interestingly, these reorganized ALBSF barrels resemble normal PMBSF barrels at the morphological, molecular, and functional levels, showing an enhanced spatial resolution upon tactile stimulation.

Results

The size of barrel subfield areas can be adjusted prenatally

The size of the areas devoted to processing distinct whisker-mystacial versus upper lip input information is thought to be determined by the corresponding type and density of sensory receptors on the mouse face[12,13]. We asked whether prenatal removal of a selected facial whisker type might have an impact on the cortical barrel areas and spatial distribution of the spared whiskers. We implemented a strategy whereby the mystacial whiskers in the whisker pad were cauterized unilaterally at embryonic day (E) 14 (named as embWPC), in both wildtype and TCA-GFP mice[14], in which thalamocortical projections are labeled with green fluorescent protein (GFP). At this stage, trigeminal nerve axons have just begun to target the principal trigeminal sensory nucleus (PrV) in the brainstem (Supplementary Fig. 1a), but PrV neuron axons have not yet entered the ventral posteromedial (VPM) thalamic nucleus[15–19].

Analysis of the snout at E18 confirmed the specific ablation of the mystacial whiskers and follicles (Fig. 1a, b), with a strong reduction of whisker pad-innervating primary trigeminal sensory axons targeting the PrV (Supplementary Fig. 1b). At early postnatal stages, the total areas of PrV, thalamic ventral posterior nucleus (VPN) and S1, including other somatosensory body representations apart from the snout, did not exhibit significant differences in embWPC, as compared to control mice (Supplementary Fig. 2a–h). In contrast, the size of the areas corresponding to mystacial and upper lip whiskers was significantly rescaled in embWPC mice at all levels of the pathway, suggesting intra-modal plasticity of connectivity. For example, in S1, we found a 54% decrease in the PMBSF territory, and a 34% expansion of the ALBSF territory, a phenomenon already observed in P4 (Fig. 1c, d and Supplementary Fig. 2i, j). Notably, we found no discernible differences in the total upper lip volume, nor in the volume and number of upper lip follicles between control and embWPC mice both at E18 and P8 (Fig.1a, b and Supplementary Movies 1, 2). Dye depositions in the cortical PMBSF or ALBSF of P8 embWPC confirmed a similar intra-modal remapping of the corresponding whisker pad input-receiving VPM (wpVPM) or upper lip input-receiving VPM (ulVPM) areas in the thalamic VPM[20] (Fig. 1e, f). Moreover, retrogradely labeled thalamocortical neurons within each VPM sub-territory maintained their expected point-to-point distribution, matching cortical topography (Supplementary Fig. 3).

Importantly, the changes of the cortical barrel field sub-territories depended on mechanisms only present before birth, since cauterization of the whisker pad at postnatal day 0 (P0), referred to as P0WPC, revealed no significant territorial differences in the PMBSF and ALBSF between control and P0WPC across the somatosensory stations (Fig. 1g, h and Supplementary Fig. 4). As expected, there were no rearrangements of the thalamocortical axons in the P0WPC (Fig. 1i, j and Supplementary Fig. 5). Notably, barrels in PMBSF exhibited a diminished degree of definition and structure, with blurred point-to-point topography, highlighting the enduring effects of early sensory deprivation on the cortical organization (Supplementary Fig. 5c, d). Thus, there is a critical window in which the cortical ALBSF area can be significantly adjusted without altering upper lip receptors, suggesting that after this timepoint, plasticity might arise from a different strategy to compensate for sensory loss.

Functional rescaling of ALBSF in embWPC mice occurs before birth

Whisker pad stimulation in vivo at E18 can elicit activity in the developing PMBSF[21,22], indicating that the periphery-to-cortex somatosensory pathway is already functional before birth. We asked whether the anatomical changes observed in embWPC at P8 were detectable at prenatal stages by assessing functional reorganizations. We carried out peripheral whisker pad and upper lip stimulations at E18 while recording cortical calcium activity in *Emx1*^{GCaMP6f} transgenic mice, expressing GCaMP6f in cortical glutamatergic neurons[22] and carrying unilateral whisker pad cauterization (Fig. 2a). We also used non cauterized mice as additional controls.

Stimulations of either the whisker pad or the upper lip in control mice or in the control side of embWPC mice at E18 elicited responses from clusters of cortical neurons corresponding to the putative territories of the PMBSF or ALBSF, respectively (Fig. 2b, c, Supplementary Fig. 6, and Supplementary Movie 3). In contrast, whisker pad stimulations in the cauterized side of embWPC mice triggered very reduced responses in the caudal-most part of the expected contralateral PMBSF ("PMBSF"), confirming the anatomical reduction of this territory. Remarkably, stimulations of the upper lip in the cauterized side elicited misplaced responses in the expected ALBSF ("ALBSF") that notably expanded into the "PMBSF" (Fig. 2b, c and Supplementary Movie 4), as compared to the control side. This ectopic "PMBSF" activation was maintained at P4 when the size of responses to upper lip stimulation were already refined in the control side (Fig. 2d–g and Supplementary Movies 5, 6). Thus, the anatomical rescaling of barrel field sub-territories seen in the postnatal embWPC can be functionally detected prior to birth.

Silencing prenatal thalamic synchronous activity does not prevent the area rescaling of barrel subfields

Thalamic neurons display waves of prenatal spontaneous activity that are crucial for the development of cortical barrel field maps[10,21]. Therefore, we investigated whether the rescaling of barrel field territories in embWPC embryos could be explained by changes in the spontaneous activity of VPM neurons. Inputs from the whisker pad at E16 are carried by afferents from the ventral portion of the PrV (vPrV), whereas inputs from the upper lip are carried by afferents from dorsal PrV (dPrV)[17–19]. While at this prenatal stage, vPrV afferents topographically target the dorsolateral VPM (the prospective wpVPM), dPrV afferents target not only the ventromedial part (the prospective ulVPM) but cover most parts of the VPM[17,19]. Thus, while whisker pad and upper lip inputs are segregated at the brainstem nuclei, dPrV and vPrV axon terminals prenatally overlap within the prospective wpVPM territory[17,19] (Fig. 3a, b and Supplementary Fig. 7a–c). Remarkably, despite this axonal overlap, spontaneous activity patterns in the VPM thalamus at E16 were sub-territory specific. We detected a notable distinction in the frequency of spontaneous activity waves between the prospective wpVPM and ulVPM regions. While wpVPM exhibited a high frequency of waves, the prospective ulVPM showed significantly reduced frequency (Fig. 3c, d and Supplementary Movie 7). In embWPC, we observed a striking change in the spontaneous activity pattern, with a significant increase in thalamic wave frequency within the prospective ulVPM, resembling the pattern observed in the control wpVPM primordium (Fig. 3c, d and Supplementary Movie 8). Interestingly, in embWPC VPM at P4, dPrV axon projections did not undergo normal developmental segregation but still targeted most of the dorsolateral VPM, unlike in controls, and covered the area normally occupied by vPrV input afferents (Supplementary Fig. 7d, e).

https://doi.org/10.1038/s41467-025-57052-w

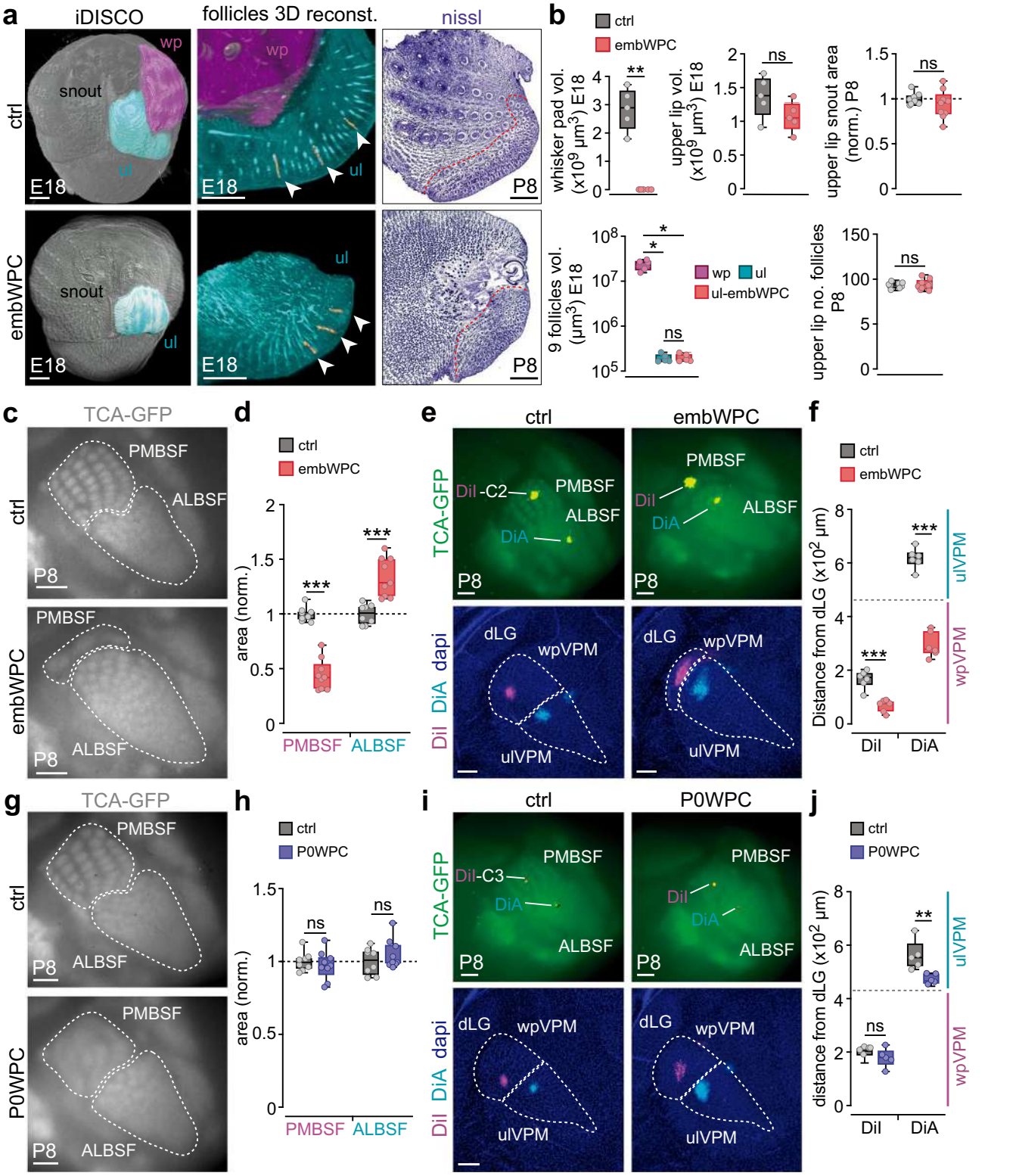

Thus, during prenatal development whisker input deprivation remaps spontaneous neuronal activity patterns in the future ulVPM territory.

Next, we asked whether the embryonic increased activity in the prospective ulVPM might influence the functional and anatomical rescaling of the ALBSF territory. Thus, we tested this possibility and conducted embryonic whisker pad cauterization in a mouse in which the synchronous spontaneous activity of the thalamus is embryonically disrupted (referred to as embWPC-Th^{Kir})[21]. Briefly, we used a tamoxifen-dependent $Gbx2^{CreERT2}$ mouse with a floxed line expressing the inward rectifier potassium channel 2.1 (*Kcnj2*) fused to the mCherry reporter in thalamic neurons (referred to as Th^{Kir}). Our data revealed that thalamic and cortical territories in embWPC-Th^{Kir} mice exhibited a spatial reorganization similar to that observed in embWPC mice. In both mice, the wpVPM and PMBSF territories virtually disappeared, and the ulVPM and ALBSF expanded as compared to the control (Fig. 3e). Consistent with

https://doi.org/10.1038/s41467-025-57052-w

Fig. 1 | Whisker pad deprivation in embryos rescales barrel field areas and thalamocortical circuits. a Left and middle, iDISCO frontal snout views showing the whisker pad (magenta) and upper lip (cyan) areas, lateral 3D-reconstructions of the follicles (yellow) at E18. Right, Nissl stainings of the snout at P8, red dashed line delimits upper lip area. **b** Quantification (iDISCO E18, $n = 5$ ctrl, $n = 5$ embWPC. Nissl P8, $n = 8$ ctrl, $n = 9$ embWPC). **c** Surface view of thalamocortical terminals (TCA-GFP+) in the PMBSF and ALBSF at P8. **d** Quantification ($n = 8$ ctrl, $n = 9$ embWPC). **e** Upper panels, DiI and DiA crystal placements in the C2 PMBSF and in the ALBSF, respectively, at P8. Lower panels, backlabelled cells in the wpVPM and ulVPM. **f** Quantification of the position of backlabelled cells with respect to the distance to the dLG nucleus. The gray horizontal dashed line represents the separation between wpVPM and ulVPM ($n = 6$ ctrl, $n = 6$ embWPC). **g** Surface view of TCA-GFP+ in the PMBSF and ALBSF at P8. **h** Quantification of the data ($n = 8$ ctrl, $n = 9$ P0WPC). **i** Upper panels, DiI and DiA crystal placements in the C3 PMBSF and in the ALBSF, respectively, at P8. Lower panels, backlabelled cells in the wpVPM and ulVPM. **j** Quantification of the position of backlabelled cells with respect to the distance to the dLG nucleus. The gray horizontal dashed line represents the separation between wpVPM and ulVPM ($n = 5$ ctrl, $n = 5$ P0WPC). Source data are provided as a Source data file. wp whisker pad, ul upper lip, E embryonic, P postnatal, embWPC embryonic whisker pad cauterized, P0WPC postnatal day 0 whisker pad cauterized, vol. volume, no. number, TCA-GFP thalamocortical axons labeled with a green fluorescent protein, norm. normalized. Scale bars: **a** (left), **c**, **e** (top), **g**, **i** (top) 500 µm; **a** (middle) 400 µm; **a** (right) 1000 µm; **e** (bottom), and **i** (bottom) 200 µm. Boxplots show the medians with the interquartile range (box) and range (whiskers). Bar graphs show the means ± SEM. ns not significant. $^{*}p < 0.05$, $^{**}p < 0.01$, $^{***}p < 0.001$.

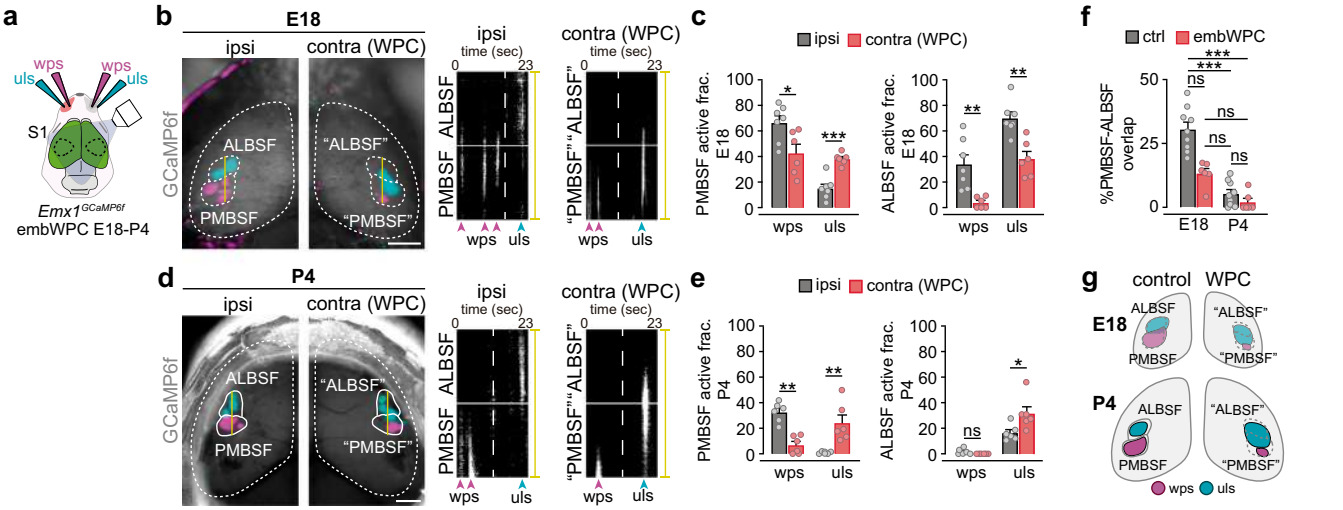

Fig. 2 | Functional rescaling of cortical barrel field territories in embWPC mice. a Schema representing the experimental paradigm. **b** Left, cortical evoked responses (GCaMP6f) to whisker pad (magenta) and upper lip (cyan) stimulations in control (ipsilateral) and whisker pad cauterized (WPC, contralateral) sides in embWPC mice at E18. Control PMBSF and ALBSF territories were translated to the WPC side for direct comparison and labeled as "PMBSF" and "ALBSF". Right, reslice of the yellow line in the left, representing responses elicited in PMBSF and ALBSF primordia by whisker pad stimulation (wps) or upper lip stimulations (uls). The white horizontal line delineates the boundaries between PMBSF and ALBSF. The vertical dashed line divides the wps from the uls over time. The arrows label the stimulation times for the whisker pad (magenta) and upper lip (cyan). **c** Quantification of the PMBSF and ALBSF active fraction to wps or uls ($n = 7$ ctrl, $n = 6$ WPC). **d** Left, cortical evoked responses (GCaMP6f) to whisker pad (magenta) and upper lip (cyan) stimulations in control (ipsilateral) and WPC (contralateral) sides in embWPC at P4. Right, reslice of the yellow line in the left, representing responses elicited in PMBSF or ALBSF by wps or uls. The white horizontal line delineates the boundaries between PMBSF and ALBSF. The vertical dashed line divides the wps from the uls over time. The arrows label the stimulation times for the whisker pad (magenta) and upper lip (cyan). **e** Quantification of the PMBSF and ALBSF active fraction to wps and uls ($n = 6$ ctrl side, $n = 6$ WPC side). **f** Quantification of the percentage of overlap responses between the PMBSF and ALBSF territories at E18 and P4 ($n = 9$ ctrl E18, $n = 6$ embWPC E18, $n = 9$ ctrl P4, $n = 6$ embWPC P4). **g** Schema illustrating the results. Dashed lines delineate PMBSF and ALBSF putative evoked territories at E18. Source data are provided as a Source data file. S1, primary somatosensory cortex; GCaMP6f, calmodulin-based genetically encoded fluorescent calcium indicator 6–fast. Scale bars, 1000 µm. Bar graphs show the means ± SEM. ns not significant. $^{*}p < 0.05$, $^{**}p < 0.01$, $^{***}p < 0.001$.

previous studies in the Th^{Kir} mouse[21], manipulating thalamic activity patterns in the embWPC mice (embWPC-Th^{Kir}) resulted in the absence of thalamic waves (Supplementary Fig. 8a, b) and, the complete loss of barrels, evidenced by a total lack of TCA clustering, in both PMBSF and ALBSF territories (Fig. 3e, g). Rescaling of thalamic and cortical territories, along with thalamocortical circuits, was still observed in the embWPC-Th^{Kir} mouse but was virtually absent in the Th^{Kir} mouse alone, as shown by anatomical and dye tracing analyses (Fig. 3e–h and Supplementary Fig. 8c–g). In sum, our results demonstrate that the patterns of spontaneous activity in prenatal VPM neurons are dispensable for intra-modal thalamic and cortical sub-territories rescaling to input deprivation.

Upper lip input-receiving thalamic neurons adopt a similar transcriptional profile to mystacial input-receiving neurons

Cross-modal and intra-modal changes in the transcriptional programs of thalamic neurons have been shown to generate thalamocortical circuit reorganizations and cortical adaptations, as shown in early blind pups or in mice with an early postnatal ablation of the VPM nucleus[10,23,24]. Therefore, we examined whether the anatomical and functional circuit expansion of the ALBSF in embWPC might be influenced by changes in the transcriptional program of VPM neurons. To assess this, we dissected tissue, at similar distances from the dorsal lateral geniculate (dLG) nucleus, from wpVPM and ulVPM in control and embWPC mice at P0 (Fig. 4a, b) and compared their transcriptional profiles by bulk RNA-sequencing (RNA-seq). Principal component analysis (PCA) revealed that the transcriptomes from wpVPM and ulVPM cells in control mice clustered separately already at P0 (Supplementary Fig. 9a). Differential expression analysis (DEA) further revealed 377 differentially expressed genes (DEGs) enriched in the wpVPM as opposed to 365 in the ulVPM cells. Among the DEGs enriched in each population, we found genes previously identified as being involved in somatosensory development such as *Epha3, Sox2, Hs6st2, Cdh8, or Rorα* enriched in wpVPM[25–29] or *Rorβ, Slitrk6, Foxp2, Calb1, or*

https://doi.org/10.1038/s41467-025-57052-w

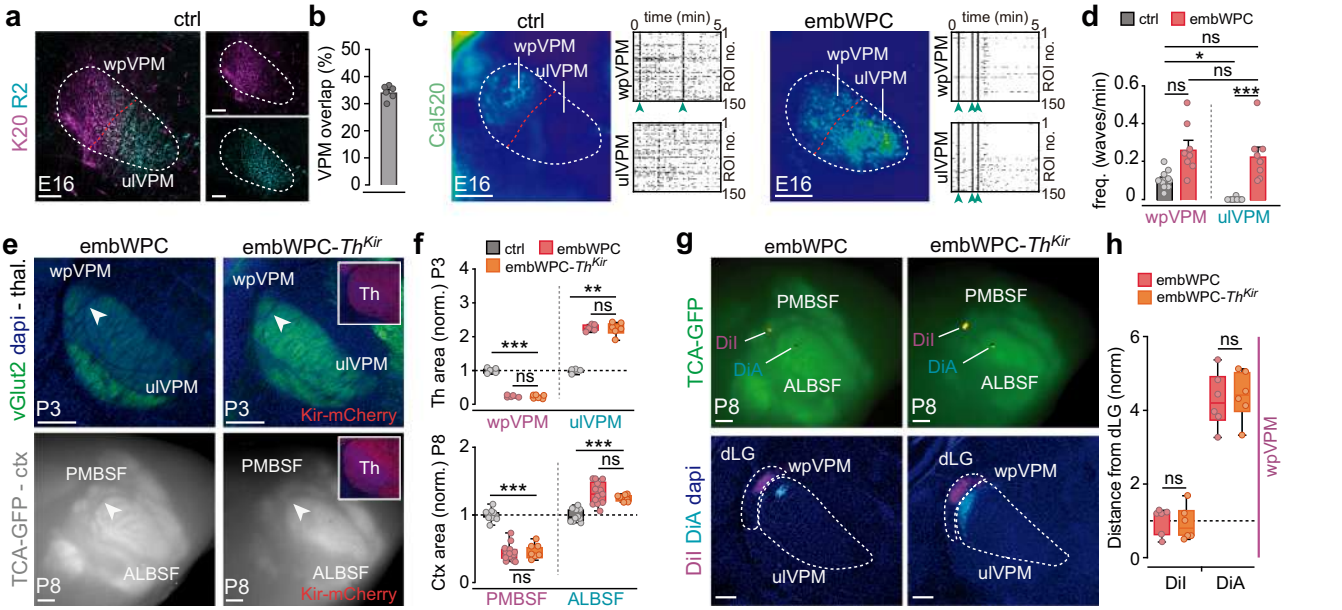

Fig. 3 | ALBSF rescaling is independent of thalamic patterned activity. a Coronal sections from the *Krox20-zsgreen::R2-mCherry* double transgenic mouse showing Krox20-labeled axons (magenta, vPrV) and R2-labeled axons (cyan, dPrV) at the VPM at E16. **b** Quantification of the percentage of overlap of labeled axons ($n = 6$). **c** Maximal projection of ex vivo spontaneous calcium activity in the prospective VPM sub-regions (wpVPM and ulVPM) in acute slices at E16. Raster plots of 5 min. The arrows label the calcium waves of synchronous activity. **d** Quantification of the frequency of wave activity in the VPM ($n = 11$ ctrl, $n = 8$ embWPC). **e** Upper panels, coronal sections of vGlut2 staining (green) in the wpVPM and ulVPM of embWPC and embWPC-Th^{Kir} mouse (Kir-mCherry positive) at P3. Lower panels, surface view of TCA-GFP+ terminals in the PMBSF and ALBSF in embWPC and embWPC-Th^{Kir} mice at P8. The arrows label the limits between wpVPM and ulVPM in the thalamus, and PMBSF and ALBSF in the cortex. **f** Quantification of the data (Thalamus, $n = 5$ ctrl, $n = 5$ embWPC, $n = 6$ embWPC-Th^{Kir}; Cortex, $n = 10$ ctrl, $n = 13$ embWPC, $n = 7$ embWPC-Th^{Kir}). **g** Upper panels, DiI and DiA crystal placements in the PMBSF and ALBSF, respectively. Lower panels, backlabelled cells at the thalamus show shifted positions within the ulVPM thalamic area in both embWPC and embWPC-Th^{Kir} mice at P8. **h** Quantification of the position of backlabelled cells with respect to the distance to the dLG nucleus. The gray horizontal dashed line in the graph represents the separation between wpVPM and ulVPM ($n = 6$ embWPC, $n = 6$ embWPC-Th^{Kir}). Source data are provided as a Source data file. Scale bars, **a** 100 µm; **c**, **g** (bottom) 200 µm; **e** (top) 250 µm, **e** (bottom), **g** (top) 500 µm. Boxplots show the medians with the interquartile range (box) and range (whiskers). Bar graphs show the means ± SEM. ns not significant. $^{*}p < 0.05$, $^{**}p < 0.01$, $^{***}p < 0.001$.

Lhx2[10,30–33] enriched in the ulVPM (Supplementary Fig. 9b, c and Supplementary Data 1).

Then, we compared control versus embWPC transcriptional programs in the VPM. Remarkably, PCA analysis from ulVPM cells in an embWPC mouse indicated that these neurons grouped more closely with control wpVPM than control ulVPM (Fig. 4c and Supplementary Fig. 9d). This transcriptional shift was appreciated when the expression pattern of the upper lip and whisker-pad DEGs was plotted in the ulVPM of the embWPC (Fig. 4d). To investigate this effect, we trained a Support Vector Machine classifier (C-SVM) using differentially expressed genes and compared the results with the ulVPM-embWPC. This machine learning approach predicted that the cauterized model would be classified as the wpVPM control in 70% of cases, compared to 30% for the ulVPM control (Fig. 4e). Additionally, DEA against the wpVPM control revealed a much lower number of differentially expressed genes (93 DEGs) compared to the ulVPM control (268 DEGs) (Fig. 4f).

In total, 150 region-specific DEGs from ulVPM and wpVPM were significantly changed by the embWPC (Fig. 4g). Namely, in the ulVPM of the embWPC mouse, we observed an upregulation of ~17% of the DEGs normally expressed in the control wpVPM and downregulation of about 23% of control ulVPM DEGs, respectively (Fig. 4g, Supplementary Fig. 9e, and Supplementary Data 2). Notably, genes such as *Rorα, Epha4, Hs6st2, Cdh9*, or *Plxna2*, involved in axon guidance, thalamocortical mapping, and wpVPM development[26,34], exhibited a wpVPM-like pattern in the ulVPM of embWPC mice (Fig. 4h, i and Supplementary Fig. 9f), also corroborated by in situ hybridization (Fig. 4j and Supplementary Fig. 9g). Next, we performed a Gene Ontology (GO) functional enrichment analysis of the genes with expression changes in the ulVPM of the embWPC and identified 11 clusters of GO-Terms enriched in biological processes (BP) and molecular functions (MF) (Supplementary Fig. 10 and Supplementary Data 3). The top ranked cluster included 99 genes (46.8%) enriched in BP involved in dendrite development or synapse assembly (e.g., *Robo1 and Flrt3*), and 12 genes (18.8%) enriched in MF involved in voltage-gated channel activity (e.g., *Kcnc2* and *Kcnab1*).

Since the lack of spontaneous thalamic waves in embWPC-Th^{Kir} mice did not prevent the ALBSF reorganization, we investigated whether the changes in ulVPM transcriptome are still observed in embWPC-Th^{Kir} VPM. We conducted in situ hybridization for probes that we identified as wpVPM markers upregulated in the ulVPM of embWPC mice such as *Hs6st2, Rorα*, and *Pou2f2*, or markers downregulated in the ulVPM of embWPC mice such as *Epha4*. Our results show a similar shift in the expression pattern for these genes in both embWPC and embWPC-Th^{Kir} mouse (Supplementary Fig. 11) reinforcing that the transcriptomic changes in VPM territories are mainly independent of thalamic waves, activity. In summary, the spatial rescaling of cortical ALBSF territory in embWPC correlates with transcriptomic changes observed in upper lip thalamic input neurons, which shift towards a molecular signature resembling that of whisker pad input neurons (Fig. 4k).

Increase of barrel size and functional spatial resolution of the cortical ALBSF map

We investigated whether upper lip-recipient thalamic neurons that acquire a whisker pad transcriptional profile during perinatal development might develop additional PMBSF characteristics later in life. At P8, PMBSF and ALBSF cortical areas differ in the average size of their

https://doi.org/10.1038/s41467-025-57052-w

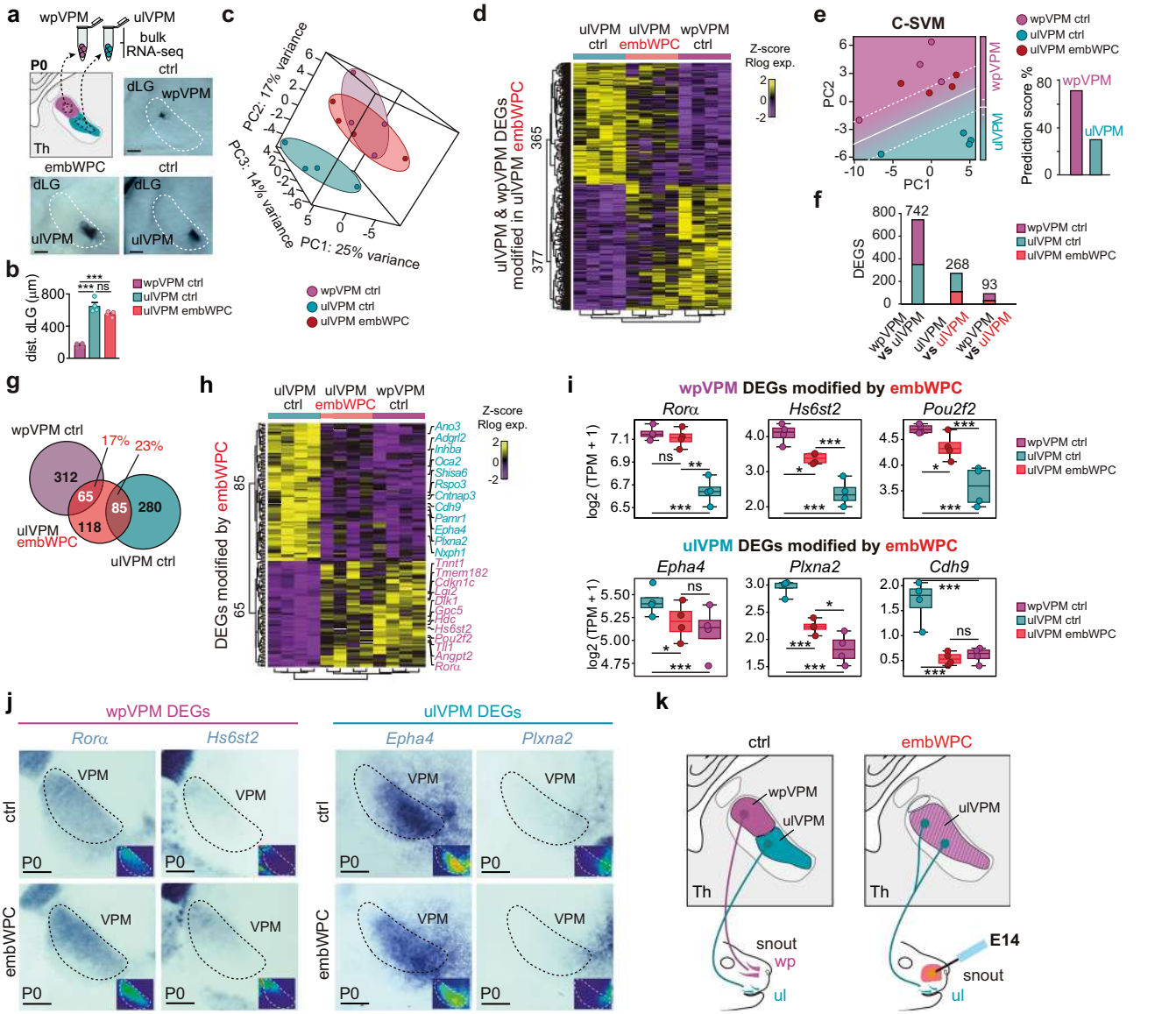

Fig. 4 | Upper lip recipient thalamic neurons switch their transcriptional program to that of whisker-pad neurons. a Top left, schema representing the paradigm. Top right and bottom, coronal images showing the dissected thalamic territories for sequencing. **b** Quantification of the dissected area with respect to the distance to the dLG nucleus ($n = 4$ wpVPM-ctrl slices, $n = 4$ ulVPM-ctrl slices, and $n = 4$ ulWPC embWPC slices, 4 mice per condition). **c** Principal component analysis (PCA) of wpVPM-ctrl ($n = 4$), ulVPM-ctrl ($n = 4$), and ulVPM-embWPC ($n = 4$) at P0. **d** Heatmap of the normalized regularized logarithm (Rlog) Z-score of expression and unbiased clustering of region-specific DEGs showing their expression profile in the ulVPM of the embWPC at P0. The color code (yellow, high expression; purple, low expression) corresponds to the log2FC. **e** Left, C-support vector machine (C-SVM) analysis identifies the optimal demarcation plane between wpVPM (magenta dots) and ulVPM population (cyan dots). The ulVPM-embWPC samples are identified as wpVPM control based on its gene expression pattern (red dots). Right, the prediction score value of ulVPM-embWPC is classified as wpVPM (70%) or ulVPM (30%) controls. **f** Number of differentially expressed genes (DEGs) obtained in their respective differential expression analysis. **g** Venn diagram shows the number of genes modified by embWPC in ulVPM overlapped in every subset of region-specific DEGs. **h** Heatmap of the normalized regularized logarithm (Rlog) Z-score of expression and unbiased clustering of region-specific DEGs whose expression was modified by embWPC in the ulVPM at P0. The color code (yellow, high expression; purple, low expression) corresponds to the log2FC. **i** Boxplots showing TPM expression levels of selected wpVPM-specific and ulVPM-specific DEGs modified by embWPC in the ulVPM. Boxplots show the medians with the interquartile range (box) and range (whiskers). **j** Coronal sections showing in situ hybridization of wpVPM and ulVPM DEGS at P0 ($n = 5$ ctrl, $n = 5$ embWPC, for each probe). **k** Schema illustrating the results. Source data are provided as a Source data file. VPM, ventroposterior medial nucleus. Scale bars, 200 µm. *adj. $p < 0.1$, **adj. $p < 0.01$, and ***adj. $p < 0.001$.

barrels and the extent of clustering of thalamocortical axons. Remarkably, we observed that, in addition to the overall increase in the cortical area occupied by the ALBSF, the average size of the cortical individual barrels in the ALBSF of the embWPC was significantly larger compared to the ALBSF control (Fig. 5a, b). This change appears to follow a gradient, with the largest ALBSF barrels located nearest to the remaining PMBSF (Fig. 5b). Furthermore, the cortical map of the expanded ALBSF gained definition and contrast as thalamocortical terminals appeared more clustered within each barrel, and less innervating the barrel septa, resembling the control PMBSF (Fig. 5c–e). These differences in barrel size and contrast in the ALBSF map of the embWPC were not detected in P0WPC mice (Fig. 5a–c).

Since thalamocortical input is a primary regulator of region-specific cortical features, we next investigated whether other cortical characteristics, besides barrel size and thalamocortical clustering, had also changed in the ALBSF cortex of the embWPC. The postnatal

https://doi.org/10.1038/s41467-025-57052-w

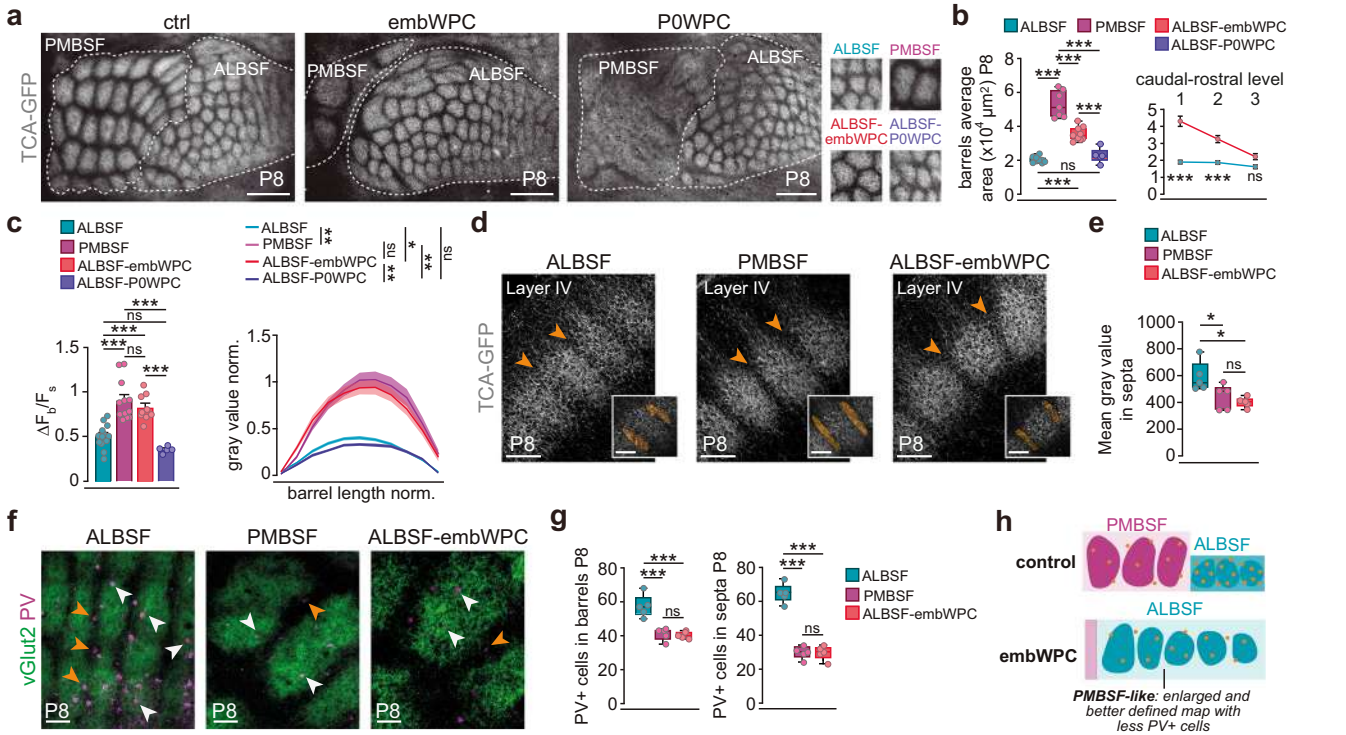

Fig. 5 | ALBSF barrels acquire PMBSF cortical features. a Cortical flattened tangential sections showing thalamocortical terminals (TCA-GFP+) in the PMBSF and ALBSF in control, embWPC and P0WPC mice at P8. Insets show in detail the clustering of TCAs in each condition. **b** Left, quantification of the average area of 34 barrels ($n = 7$ ctrl PMBSF, $n = 9$ ctrl ALBSF, $n = 9$ embWPC ALBSF, $n = 5$ P0WPC ALBSF). Right, quantification of the average area of 4 barrels per three caudal-to-rostral levels ($n = 9$ ctrl ALBSF, $n = 9$ embWPC ALBSF). **c** Left, quantification of the barrel/septum fluorescence ratio (ΔFb/Fs) ($n = 12$ ctrl PMBSF, $n = 13$ ctrl ALBSF, $n = 9$ embWPC ALBSF, $n = 5$ P0WPC ALBSF). Right, quantification of the gray value fluorescence intensity in a barrel ($n = 66$ ctrl PMBSF barrels, $n = 65$ ctrl ALBSF barrels, $n = 42$ embWPC ALBSF barrels, $n = 25$ P0WPC ALBSF barrels). **d** Coronal sections showing thalamocortical terminals in layer IV in the ALBSF and PMBSF of control, and ALBSF of embWPC mice. Insets showing the septa volume analyzed. **e** Quantification of the EGFP expression from TCA in septa of three barrels per animal (orange arrowheads in **d**) ($n = 5$ ctrl ALBSF, $n = 5$ ctrl PMBSF, $n = 5$ embWPC ALBSF). **f** Cortical flattened tangential sections showing thalamocortical terminals (vGlut2+) and parvalbumin (PV) expression in barrel core (white arrowheads) and septa (orange arrowheads) in the ALBSF and PMBSF of control, and ALBSF of embWPC mice at P8. **g** Quantification of PV+ cells in four barrels and septa ($n = 5$ ctrl ALBSF, $n = 5$ ctrl PMBSF, $n = 5$ embWPC ALBSF). **h** Schema illustrating the results. Source data are provided as a Source data file. Scale bars, **a** 500 µm, **d**, **f** 100 µm, **d** (insets) 80 µm. Boxplots show the medians with the interquartile range (box) and range (whiskers). Bar graphs show the means ± SEM. ns not significant. $^{*}p < 0.05$, $^{**}p < 0.01$, $^{***}p < 0.001$.

PMBSF is known to contain fewer parvalbumin (PV) expressing interneurons in layer IV compared to the ALBSF[35]. Like in the PMBSF, we found significantly fewer PV-positive interneurons both in barrels and septa in layer IV of the ALBSF in the embWPC as compared to the ALBSF control (Fig. 5f, g). Hence, our findings demonstrate that, irrespective of receiving input from upper lip peripheral receptors, the VPM territory in embWPC adopts a molecular identity akin to that of a territory receiving input from mystacial whiskers. Consequently, it gains specific features of that circuit, including increased barrel size, better anatomical map definition, and fewer layer IV PV interneurons (Fig. 5h).

Next, we tested whether these anatomical reorganizations might have a functional correlate, for example, an enhanced topographical spatial resolution to upper lip stimulation. Thus, we carried out multipoint stimulations within the whisker pad or upper lip on both control and embWPC mice at P4 (Fig. 6a). On the control mice, cortical evoked responses confirmed a topographic organization of both PMBSF and ALBSF responses; however, while the PMBSF responses exhibited a well-defined and precise organization with virtually non-overlapping responses, those of the ALBSF were broader and less refined in comparison (Fig. 6b, c and Supplementary Movie 9). Thus, beyond their anatomical idiosyncrasies, cortical barrel subfields also have a distinct degree of functional map definition as they emerge during perinatal development. Interestingly, stimulations from distinct locations of the upper lip of embWPC mice resulted in significantly less overlapping responses within the ALBSF (Fig. 6b, c and Supplementary Movie 10), suggesting enhanced spatial discrimination in the ALBSF of embWPC akin to that seen in the control PMBSF map.

Lastly, we investigated whether the rescaled ALBSF with enhanced resolution in the embWPC mice takes on PMBSF functions during somatosensory behavior in adulthood. To do this, we first conducted cFOS staining to label stimulated neurons in the ipsilateral and contralateral barrel subfields of embWPC mice after 10 min of exploring an enriched environment at P60 (Fig. 6d). Our immunostaining for cFOS revealed that, whereas in the ipsilateral (control) side the ALBSF was barely activated as compared to the PMBSF, the ALBSF was the predominantly activated region in the contralateral (cauterized) side after exploration (Fig. 6e, f). Therefore, we hypothesized that the rescaled ALBSF neurons of the embWPC mouse play a prominent role in vibrissae-driven sensory behavior in the adult. We conducted a texture discrimination test to evaluate tactile sensory processing, requiring adult mice to distinguish between novel and familiar textures (Fig. 6g, h). We used control mice, bilateral embWPC mice, and an additional control group where mystacial whiskers were bilaterally trimmed prior to testing. Our findings showed that embWPC mice discriminated textures as effectively as controls, while the trimmed group could not discriminate the new texture using only the remaining upper lip whiskers (Fig. 6i, j and Supplementary Fig. 12). These results

https://doi.org/10.1038/s41467-025-57052-w

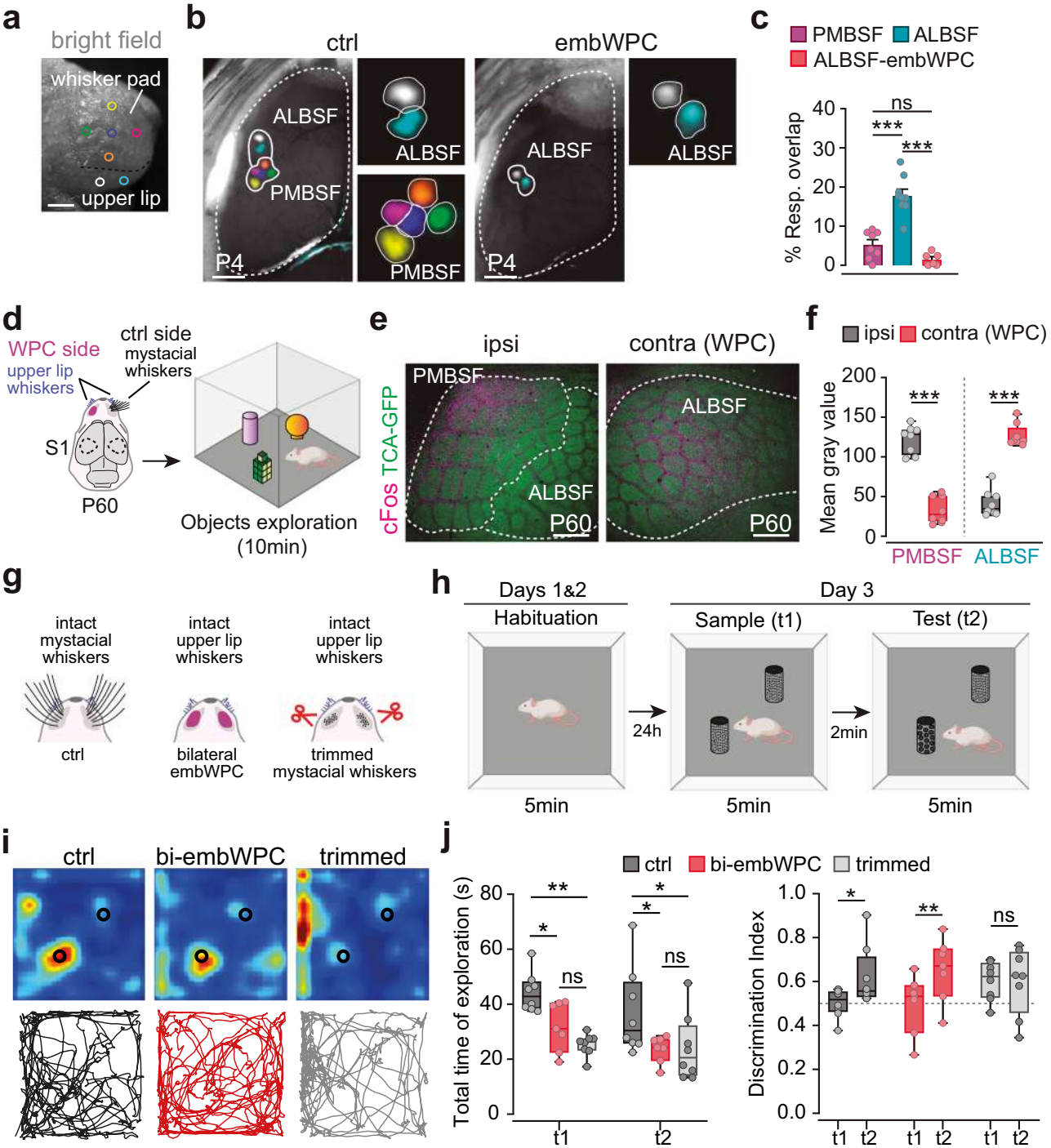

Fig. 6 | Enhance ALBSF functional map in the postnatal embWPC mice. **a** Schema representing the experimental paradigm. **b** Cortical evoked responses (GCaMP6f) within the PMBSF and ALBSF to five distinct wps and two distinct uls in control and embWPC mice at P4. Dashed lines define the cortical hemisphere, and continuous lines indicate the territory covered by elicited responses. **c** Quantification of the percentage of overlap between two distinct PMBSF and two distinct ALBSF responses at P4 ($n = 8$ ctrl for PMBSF responses, $n = 9$ ctrl for ALBSF responses, $n = 6$ embWPC for ALBSF responses). **d** Schema representing the experimental paradigm. **e** Cortical flattened tangential sections showing thalamocortical terminals and cFOS expression in cortical ipsilateral (control) and contralateral (WPC) sides of P60 mice. **f** Quantification of the mean gray value of cFOS expression ($n = 8$ embWPC ipsi PMBSF, $n = 8$ embWPC ipsi ALBSF, $n = 8$ embWPC contra (WPC) PMBSF, $n = 8$ embWPC contra (WPC) ALBSF). **g** Schematic representation of the three experimental groups involved in the behavioral paradigm: mice with intact whiskers (ctrl $n = 8$); mice with bilateral whisker pad cauterization at E14 and intact upper lip whiskers (bi-embWPC $n = 7$) and mice with trimmed mystacial whiskers and intact upper lip whiskers (trimmed $n = 8$). **h** Schema representing the texture discrimination task protocol. **i** Representative heatmaps showing the distribution of snout positions during a 5-min test session for individual mice from each group (top), along with corresponding centroid trajectories (bottom). Warmer colors in the heatmaps denote regions with higher snout position frequency, highlighting areas of increased exploratory interest. **j** Left, boxplots comparing the total time that control, bi-embWPC and trimmed mice spent exploring textured objects across t_1 and t_2 sessions. Right, evaluation of texture discrimination performance comparing the discrimination index for each session. Source data are provided as a Source data file. Scale bars, **a** 1000 µm and **e** 500 µm. Bar graphs show the means ± SEM. ns not significant. $^{*}p < 0.05$, $^{**}p < 0.01$, $^{***}p < 0.001$. Mouse images were created in BioRender. Martini, F. (2025) https://BioRender.com/l19k613.

suggest that the rescaled ALBSF cortex in embWPC mice can support complex tactile discrimination, a function typically mediated by PMBSF neurons in adult mice under normal conditions.

Discussion

Our study underscores the existence of a prenatal temporal window during mouse brain development that allows for the tuning of the size and definition of somatosensory cortical representations. Before cortical barrel fields are anatomically apparent, the thalamic VPM sub-territories exhibit specific transcriptional signatures at birth. Our results suggest that these signatures contribute to the distinct intra-modal anatomical and functional circuitry features specific to PMBSF and ALBSF cortical sub-territories.

Furthermore, our findings suggest that modulations in these transcription programs might enable intra-modal plasticity changes independently of the type of peripheral receptors. In mice lacking the mystacial whiskers, VPM neurons receiving upper lip whisker input can shift their transcriptional features toward a whisker pad-like program, reconfiguring thalamocortical circuits and cortical features to resemble a PMBSF. These changes increase barrel size and functional spatial resolution, thereby enhancing spatial discrimination in regions such as the ALBSF, where cortical representations were otherwise less defined.

The developmental relationship between sensory receptors and somatosensory representations has been thoroughly examined in prior work involving mice and rats. Embryonic ablation of the forelimb in rats resulted in the expansion of S1 representation of the hindlimb without altering the sensory receptors of the spared peripheral region[36]. Moreover, deprivation of a single whisker or a row of whiskers during the first postnatal week, leads to the loss of the corresponding cortical barrels and enlargement of the surrounding barrels[37–42]. And remarkably, rewiring of ipsilateral trigeminal input from mystacial whiskers to the ipsilateral barrel field generates an ectopic barrel field within the normal barrel map[43]. Collectively, these studies highlight the sensitivity of somatosensory regions and barrel maps to manipulations in peripheral or sensory input but also question a direct correlation between the size of cortical barrels and their corresponding peripheral sensory receptors. Our results in the embWPC model define a developmental window for an intra-modal barrel field reorganization, showing that only embryonic, and not postnatal, ablation of the whisker pad induces the ALBSF anatomical and functional enlargement. This reorganization capability is, therefore, temporally constrained during prenatal development and anticipates the closure of the critical time window for somatosensory circuits[39,44].

Thalamic spontaneous activity is key for the emergence of cortical somatosensory maps, as evidenced by the fact that suppressing this activity leads to mice that do not develop barrels despite having normal whiskers[21]. Moreover, in early blind pups, cross-modal changes in activity-dependent gene regulation in VPM neurons correlate to changes in barrel size[10]. Here, we observed a striking intra-modal prenatal reorganization of the frequency and pattern of thalamic waves between VPM subfields in embWPC mice. The ulVPM significantly increased the frequency of thalamic waves compared to control mice. This change in activity pattern might serve as a mechanism to enhance ulVPM barrel size and definition and, in turn, to map these activity-dependent features onto the cortical ALBSF during development. This hypothesis could not be directly tested, as thalamocortical axons in the embWPC-Th^{Kir} mice, in which spontaneous thalamic waves are blocked, fail to cluster in layer IV in both PMBSF and ALBSF, as previously described in Th^{Kir} mice[21].

Notably, using embWPC, we could show that the enlargement of the cortical ALBSF area is guided by the thalamus in an activity-independent manner. Indeed, in embWPC-Th^{Kir} mice, lacking synchronous thalamic activity, the rescaling of the ALBSF still occurs. Moreover, we show that the PrV input reorganizes in the embWPC VPM. Therefore, we propose that remapping within the PrV, initiated at E14 following whisker pad ablation, may significantly influence the development and organization of thalamocortical axons, subsequently affecting thalamic and cortical map reorganization.

Remarkably, our study revealed that thalamic neurons can shift their transcriptional profile intra-modally. We found that the transcriptional profile of ulVPM neurons in embWPC mice mirrors that of the wpVPM neurons in control mice. Crucial genes for thalamocortical barrel field development, such as *Rorα* or *Epha4*[26,34], accordingly altered their expression pattern in the ulVPM neurons innervating the ALBSF. For instance, we observed an upregulation of *Rorα* in this region, suggesting a potential role in increasing the density and clustering of axonal terminals in layer IV in the ALBSF of the embWPC mice. An activity-dependent upregulation of *Rorβ*, a related orphan receptor, in VPM neurons, has been shown to mediate an increased clustering of thalamic axons in S1[10]. ulVPM neurons adopting a region-specific wpVPM transcriptional profile might serve as an intrinsic mechanism to switch a PMBSF developmental program, ensuring an enhanced anatomical and functional definition of thalamocortical axons in the ALBSF cortical barrel map. Additionally, we identified alterations in genes directly associated with neuronal activity[45,46], including ion channels, which may contribute to or reflect the modified pattern of thalamic activity observed in the embWPC model. Yet, it remains to be determined whether the acquisition of wpVPM-like molecular identity by ulVPM neurons is dependent on thalamic spontaneous activity.

Large barrels in the PMBSF correspond to long mystacial whiskers[12,13], whereas ALBSF barrels relate to the short whiskers on the upper lip of the snout and are comparatively smaller, less defined, and densely packed[9,47,48]. Moreover, although the average volume of a single barrel in the ALBSF is smaller than in the PMBSF, the numerical density of parvalbumin (PV)-positive interneurons is higher in ALBSF than in the PMBSF[35]. Somata of PV neurons in the barrels and septa of the ALBSF are reported to receive more vesicular glutamate transporter Type 2–labeled (vGlut2) boutons than those in the PMBSF, suggesting the presence of more potent feedforward inhibitory circuits in the ALBSF[35]. Behaviorally, mystacial vibrissae hold significant behavioral relevance for the animal, being the first ones used for search of objects and gaps, and to discern diverse tactile features such as object position, shape, or texture[49]. Although the function of upper lip shorter whiskers remains largely unexplored, they appear to primarily aid in object discrimination when the snout is near the object[8,50–52]. Given these anatomical and functional disparities, the PMBSF and ALBSF represent two distinct somatosensory subsystems. Consequently, we initially expected minimal reorganization of the ALBSF upon deprivation of the whiskers corresponding to the PMBSF. However, our data from the embWPC mice revealed a notable anatomical reorganization within the ALBSF, leading to the formation of large and well-defined barrels and a decreased density of PV interneurons at the postnatal life. Additionally, our in vivo functional data revealed that this reorganization might contribute to enhance functional resolution of the ALBSF map to point-to-point peripheral stimulations. Our texture discrimination experiments demonstrated that embWPC adult mice, in which the small upper lip whiskers remain intact, can adopt specialized mystacial whisker functions and discriminate between distinct textures as effectively as control mice.

Altogether, these findings highlight a decoupling of mechanisms governing the type, size, and density of sensory peripheral receptors from those influencing the size and definition of cortical representations that might involve adopting subcortical- and subregion-specific transcriptional programs. Specifically, we observed that the prenatal thalamus possesses plasticity mechanisms to drive the development of a barrel field with anatomical and functional features akin to the PMBSF, regardless of the type of peripheral receptor. Therefore, our findings indicate that the brain may still construct a barrel map capable

of processing intricate tactile functions for the animal, even in scenarios involving the availability of only small receptors with subsidiary functions.

Methods

Mouse strains

All animal experiments were conducted in accordance with the Committee on Animal Research at the University Miguel Hernández that approved all the animal procedures, which were carried out in compliance with Spanish and European Union regulations. Similar numbers of male and female mice were used interchangeably. No sex-related differences were observed in the measurements throughout the study. Mice were maintained in pathogen-free facilities under standard housing conditions with continuous access to food and water on a 12 h light-dark cycle. The number of animals used in each experiment is noted in the figure legends.

All mouse transgenic lines in this study were maintained on an ICR/CD-1 genetic background and genotyped by PCR. The *TCA-GFP Tg*, in which the TCAs are labeled with GFP, the $R26^{Kir2.1\text{-}mCherry}$, mouse lines were previously described[10,14,21]. The Cre-dependent mouse line, $R26^{GCaMP6f}$ was obtained from Jackson Laboratories (Stock number 024105) and crossed with an $Emx1^{Cre/+}$ transgenic mouse[53] to conditionally express the fast calcium indicator GCaMP6f in glutamatergic cortical neurons ($Emx1^{GCaMP6f}$)[21,22]. The $R26^{Kir2.1\text{-}mCherry}$ mice were crossed with an inducible Cre^{ERT2} mouse line driven by *Gbx2*, an early specific thalamic promoter ($Gbx2^{CreERT2/+}$)[54]. Double mutants are referred to as Th^{Kir} and triple mutants as *TCA-GFP-*Th^{Kir} [21]. Tamoxifen induction of Cre recombinase in the double/triple mutant embryos was performed by gavage administration of tamoxifen (5 mg dissolved in corn oil, Sigma) at E10 to specifically target all primary sensory thalamic nuclei. Tamoxifen administration in pregnant mice produces non-desirable side effects such as delivery problems and decrease survival of newborn pups[55]. To increase the survival rate of young pups, we administered 125 mg/Kg of progesterone (DEPO-PROGEVERA®) intraperitoneally at E14 and implemented a C-section procedure at E19. Pups were then placed with a foster mother. In all cases, the Cre^{ERT2}-negative littermates were used as controls of the experimental condition. The $r2^{mCherry}$ [19], $Krox20^{Cre}$ [56], and *R26RZsGreen* (Jackson Laboratories, Stock number 007906)[57] lines, were as described. We crossed $Krox20^{Cre}$ with *R26RZsGreen* to generate double transgenic $Krox20^{ZsGreen}$ mice, and we also generated $Krox20^{ZsGreen}$*::*$r2^{mCherry}$ triple transgenic mice.

Histology

For in situ hybridization and immunohistochemistry at postnatal stages, mice were perfused with 4% paraformaldehyde (PFA) in PBS (0.01 M), and their brains were subsequently removed and post-fixed in the same fixative overnight. For the immunohistochemistry of embryonic tissue, the brains were dissected and immediately fixed in 4% PFA overnight. For Nissl staining, a microtome (MICROM) was used to cut paraffin slices of 5 µm. Next, the sections were stained in 0.5% cresyl violet (Sigma) solution for 15–25 min and then rinsed quickly in distilled water. After decolorization in 70% ethyl alcohol for few seconds, the sections were dehydrated in 95%, 100% ethyl alcohol for 2 to 3 min, cleared in xylene (Sigma) for 2 min and mounted with Eukitt (Merk). Cytochrome oxidase staining was performed to label the PrV territories. For cytochrome Oxidase (CytOx) staining, 80 µm vibratome coronal sections were incubated overnight at 37 °C in a CytOx solution: 0.03% cytochrome c (Sigma C2506), 0.05% 3-3′ diaminobenzidine tetrahydrochloride hydrate (DAB, Sigma D5637) and 4% sucrose in PBS. For tangential sections, cortical hemispheres were flattened and cryoprotected through steps of 10, 20, and 30% of sucrose in PBS. Then, a cryotome (MICROM) was used to cut at 80 µm tangential sections. Immunohistochemistry was performed on 80 µm vibratome or cryotome brain sections (coronal and tangential), which were first incubated for 1 h at room temperature in a blocking solution containing 1% BSA (Sigma) and 0.25% Triton X-100 (Sigma) in PBS. Afterwards, the slices were incubated overnight at 4 °C with the following primary antibodies: guinea pig anti-vGlut2 (1:10000, Synaptic Systems, 135404), chicken anti-GFP (1:3000; Aves Labs, GFP-1020), rat anti-RFP (1:1000, Chromotek, 5F8), rabbit anti-cFos (1:500, Synaptic Systems, 226003), rabbit anti-PV (1:5000, Swant PV27), and rabbit anti-RFP (1:1000, Rockland, 600-401-379). Sections were then rinsed in PBS and incubated for 2 h at room temperature with secondary antibodies: Alexa488 donkey anti-guinea pig (1:500, Thermo Fisher, A11073), Alexa488 goat anti-chicken (1:500, Thermo Fisher, A11039), Alexa594 donkey anti-rat (1:500, Thermo Fisher, A21209) and Alexa goat 568 anti-rabbit (1:500, Invitrogen, A11011). Counterstaining was performed using the fluorescent nuclear dye 4′,6-diamidino-2-phenylindole (DAPI) (Sigma). In situ hybridization was performed on 60 µm vibratome sections using digoxigenin-labeled antisense probe for *Rorα*, *Epha4*, *Pou2f2*, *Hs6st2*, *Plxna2*, and *Cdh9*. Hybridization was carried out overnight at 65 °C, and after hybridization, the sections were washed and incubated overnight at 4 °C with an alkaline phosphatase-conjugated anti-digoxigenin antibody (1:2500-1:4000, Roche). To visualize the RNA-probe binding, a colorimetric reaction was performed for 1–2 days at room temperature in a solution containing NBT (nitro-blue tetrazolium chloride, Roche) and BCIP (5-bromo-4-chloro-30-indoly phosphate p-toluidine salt, Roche). After development, the sections were washed and mounted in Glycerol Jelly (Merck Millipore). Images were acquired with a Leica DFC550 camera in a Leica DM5000B microscope, a Leica K5 camera in a Leica DMi8 microscope, or with an Axioscan Z1 widefield microscope (Zeiss).

Immunolabeling-enabled three-dimensional imaging of solvent-cleared organ (iDISCO+)

The whole mount for the iDISCO+ protocol was conducted following the previously described methods[58,59]. After perfusing mice with 4% PFA, heads (without any dissection) were dehydrated using a series of methanol concentrations (50, 80, 100, and 100%) and subsequently incubated overnight in 6% H_2O_2 in methanol to bleach the samples. Following this, heads were incubated in Permeabilization solution (Triton X-100, Glycine, DMSO) and blocked with Blocking solution (Triton X-100, Donkey Serum, DMSO) for 2 days, respectively. For the clearing process, heads underwent dehydration in methanol (20, 40, 60, and 80%) at room temperature on a rotating shaker. Specimens were then immersed twice in 100% methanol for 1 h and treated overnight in 1/3 volumes of 100% dichloromethane (DCM; Sigma-Aldrich; 270997). On the subsequent day, heads were incubated in 100% DCM for 30 min. Finally, samples were cleared in 100% dibenzyl ether (DBE; Sigma-Aldrich; 108014) until they became translucent.

Ultramicroscopy and image processing

3D imaging was primarily performed with an ultramicroscope I (LaVision BioTec) using ImspectorPro software (LaVision BioTec). The light sheet was generated by a laser (wavelength 488 nm, LaVision BioTec). A binocular stereo microscope (MXV10, Olympus) with a 23x objective (MVPLAPO, Olympus) was used at different magnifications (1.25x). Samples were placed in an imaging reservoir made of 100% quartz (LaVision BioTec) filled with ethyl cinnamate and illuminated from the side by the laser light.

Images were generated using Imaris x64 software (version 9.3.1, Bitplane). Stack images were first converted to Imaris files (.ims) using ImarisFileConverter. The whisker pad and upper lip area reconstruction were generated by creating a mask around each one using the "surface tool" and they were pseudo-colored (whisker pad area in magenta and upper lip area in cyan). Each individual follicle was isolated also manually using the same tool, selecting nine follicles arbitrarily at three different points from medial to lateral. The septa volume reconstruction from coronal sections of 80 µm was generated

by creating masks around each barrel using the "surface tool" and they were pseudo-colored (orange).

In utero and postnatal whisker pad cauterization

Embryonic unilateral and bilateral whisker pad cauterization (embWPC and bi-embWPC, respectively) were performed at E14 as described previously for enucleation[10]. Dams were deeply anesthetized with isoflurane, and the uterine horns were exposed through a midline laparotomy. Using a fiber optic light source, embryos were visualized within the uterus. The whisker pads of selected embryos were then cauterized with a 0.1 mm platinum wire (Thermo Fisher) connected to a cautery unit. All follicles within the whisker pad were carefully cauterized. After cauterizing half of the litter, the embryos were returned to the abdominal cavity, the surgical incision was closed, and the embryos were allowed to develop until either E18 or postnatal stages. Postnatal unilateral whisker pad cauterization (P0WPC) was performed on P0 pups. Animals were deeply anesthetized on ice. The right whisker pad was cauterized under the loupe to specifically burn the principal whisker follicles. Pups were then warmed up to 37 °C on a heating pad, before being returned to the mother.

Measurement of brain areas and data analysis

ImageJ software was used to measure the size of individual barrels, barrel field territories in the cortex, thalamus and brainstem, as well as the snout areas in slices. For barrel field territories and snout areas data were normalized. Each barrel field or snout area from a given experimental condition was normalized to the corresponding barrel field or snout mean area in the control, which was considered as 1. For the snout measurements, the skin of the snout was flattened and post-fixed in 4% PFA. Paraffin slices of 5 µm were obtained to quantify the number of follicles and the upper lip snout area using Nissl staining. We measured two slices per animal, one medial and one more lateral, and calculated the average. To quantify the number of cells in the vPrV, dPrV, PrV, wpVPM, ulVPM, and VPM regions, we counted DAPI-stained nuclei within a 55.35 μm^2 region of interest (ROI) in 80 µm coronal sections. This cell count was extrapolated to estimate the total number of cells in each target area. Four slices per animal were analyzed, and the cell count across these slices were summed. TCA-GFP mouse was used for the quantifications of the barrel field definition in flattened tangential sections, barrel field areas in toto and thalamic territories in slices. To assess the rostro-caudal gradient of increased barrel size in embWPC mice, we analyzed three distinct levels along the caudal-to-rostral axis, measuring four barrels per level and calculating the average. The most caudal level was positioned near the remaining PMBSF territory, the most rostral near the S1 rostral boundary, and the medial level at the midpoint between these two. For thalamic rescaling analysis, we examined brain slices at P3, when barreloids become more prominent, facilitating anatomical analysis. For cortical barrels analysis, we chose P8, as barrels are well-established at this stage, allowing for clearer visualization and analysis. To quantify the size of cortical areas in toto, TCA-GFP (control, embWPC, P0WPC, and embWPC-Th^{Kir}) mice were perfused and directly processed to obtain images under the stereo fluorescent microscope (Leica MZ10 F). Coronal serial slices of 80 µm were obtained from TCA-GFP brains, and thalamic barrel field territories were immunolabeled with GFP and vGlut2 in order to better detect the areas. For $\Delta F_b/F_s$ quantifications, we used ImageJ to measure the gray value of EGFP labeling in barrels of flattened tangential sections. $\Delta F_b/F_s$ was calculated using the maximum value of the baseline signal average as F_s in single barrels. To measure the gray value, we used a 20-width segmented line, covering five barrels per condition, and calculated the average. To compare the barrel profile for the different conditions, we normalized each barrel´s gray values to the lowest number (septa), which was considered 0. Next, we took 11 gray value data points per barrel to normalize the length for all the conditions. To quantify the mean gray value in septa, coronal serial slices of 80 µm were obtained from TCA-GFP brains, and barrels from PMBSF and ALBSF (control and embWPC) were immunolabeled with GFP to measure the fluorescence of three barrels of septa per condition using Imaris x64 software, and calculated the average. For PV+ cells quantifications in PMBSF and ALBSF barrels and septa, we counted the number of PV+ cells within four barrels, and their septa for each condition in flattened tangential sections of 80 µm immunolabel with PV and vGlut2. We quantified cFos expression within PMBSF and ALBSF layer IV in flattened tangential sections of 80 µm immunolabel with cFos. The region of interest (ROI) was a square of 600 × 1000 µm on each territory measuring the mean gray value.

Dye-tracing studies

For axonal tracing, animals were perfused with 4% PFA in PBS. Heads were post-fixed overnight to trace innervation from the snout to the trigeminal nucleus, while brains were dissected and post-fixed overnight to trace thalamocortical axons. Small DiI (1,1′-dioctadecyl-3,3,3′,3′-tetramethylindocarbocyanine perchlorate; Invitrogen), DiA (4-[4-(dihexadecylamino) styryl]-*N*-methylpyridinium iodide; Invitrogen) and DiD (1,1′-dioctadecyl-3,3,3′,3′-tetramethylindodicarbocyanine, 4-chlorobenzenesulfonate salt; Invitrogen) crystals were inserted under a stereo fluorescence microscope (MZ10 F, Leica) into the PMBSF, ALBSF, vPrV, dPrV, the whisker pad and upper lip. The dye was allowed to diffuse at 37 °C in PFA solution for 4 to 8 weeks to trace the innervation from the snout to the PrV, and 6 weeks to trace from the vPrV and dPrV to the VPM. To trace the thalamocortical pathway, small DiI and DiA crystals were inserted into distinct PMBSF barrels (C2, C3, D3, and C4) and DiI, DiA, and DiD crystals were placed into ALBSF territory. To reveal the PBMSF and ALBSF, a TCA-GFP transgenic specific mouse line was used. The dye was allowed to diffuse at 37 °C in a PFA solution for 3 weeks. Vibratome sections (80 µm thick) were obtained and counterstained with the fluorescent nuclear dye DAPI (Sigma-Aldrich). Three sections per animal were imaged using a Leica K5 camera in a Leica DMi8 microscope. Image analysis was performed on ImageJ. To quantify the translocation of the backlabeling in the VPM, the distance from the dorsolateral geniculate (dLG) nucleus border was measured to the center of the backlabeled cells in the VPM. The distance from the dLG nucleus border to the separation between wpVPM and ulVPM was determined following the barreloid rows in the VPM of ctrl mice.

Measurement of PrV axons overlap in VPM and data analysis

To label rhombomere 3-derived vPrV neurons, we used the $Krox20^{Cre}$ line[56] to drive the Rosa-Zsgreen reporter (*R26RZsGreen*)[60], whereas to label rhombomere 2-derived dPrV neurons, we used the $r2^{mCherry}$ reporter line[19]. Brains from $Krox20^{Cre}$; *R26RZsGreen*; $r2^{mCherry}$ animals, in which vPrV and dPrV projections are labeled simultaneously, were collected at embryonic stages (E16.5, E18.5) and postnatal stages (P0, P4, and P8) for analysis. Embryonic brains were directly post-fixed in 4% PFA in PBS, while postnatal brains were perfused before post-fixation in the same fixative. Brains were cut on a Vibratome (Leica) at 60 µm thickness throughout the VPM and PrV. To enhance the r2::mCherry signal, the sections were stained with a rabbit anti-RFP primary antibody (1:1000, Rockland, 600-401-379) coupled with an anti-rabbit Alexa 568 secondary antibody (1:500, Invitrogen, A11011), while the endogenous Zsgreen fluorescence was not amplified. At least five sections per animal were imaged using Axioscan Z1 widefield microscope (Zeiss), using a 10x (NA = 0.45) plan-APOCHROMAT objective. Subsequent image analysis was conducted using ImageJ. To quantify the percentage of overlap of vPrV-dPrV axons in the VPM, a wand tool connecting pixels of the same intensity level in a 15-pixel range, was used to automatically delineate the innervation area of Krox20+ and R2+ axons, generating the Regions of Interest (ROIs). Subsequently, the overlapping area and the total innervation area of both Krox20+ and R2+ axons were measured with the measure tool in ImageJ to calculate the percentage of overlap of PrV axons in the VPM.

In vivo mesoscale calcium imaging

As previously described[22], embryos at E18 were extracted from the uterus and maintained at 35 °C. E18 pups were immobilized using soft clay. P4 mice underwent anesthesia with ice, followed by surgical removal of the scalp. A 3D-printed plastic holder was attached to the skull using cyanoacrylate adhesive and dental cement, then affixed to a ball-joint holder to stabilize the head. To maintain body temperature, pups were placed on a controlled temperature heating pad, ensuring a range of 32–34 °C. For recording calcium activity, we used a 16-bit CMOS camera (ORCA-Flash 4.0, Hamamatsu) coupled to a stereo microscope (Stereo Discovery V8, Zeiss), which offered 470 nm LED illumination. For $Emx1^{GCaMP6f}$, images were acquired with a frame size of 1024 × 1024 pixels using a macro magnification of 1.6x at E18 and of 1.25x at P4, resulting in a spatial resolution of 8.12 µm/pixel and 10.64 µm/pixel, respectively. Image frames were captured continuously at a rate of 3.33 frames per second (300 ms frame period) for $Emx1^{GCaMP6f}$, with an average of three movies acquired per animal.

In vivo mechanical stimulation of the whisker pad

We conducted somatosensory stimulations by touching the whisker pad and upper lip using a 0.16 g von Frey filament (TouchTest®, BIOSEB). Each animal was stimulated at least three times, with intervals of 5 min between each stimulus. Subsequently, we calculated the size of responses in the PMBSF and ALBSF elicited by whisker pad and upper lip stimulations.

Analysis of the evoked activity in vivo

For the assignment of cortical territories, the perimeters of the PMBSF and ALBSF were determined using the cortical responses elicited by mechanical stimulation of five sites on the whisker pad, as previously described[21,22], and two or three sites of the upper lip. At embryonic day (E)18, the perimeters were predicted by scaling down and superimposing the limits of the sensory territories observed in the TCA-GFP transgenic line[14] at P2, as previously detailed[22], and using the responses to whisker pad and upper lip stimulations as reference for PMBSF and ALBSF, respectively. Image analysis was performed with ImageJ. The mean fluorescence of five frames just prior to the stimulation established F0 (baseline fluorescence), and a ΔF/F0 time series was then generated from the raw data and subsequently transformed into 8-bit images before processing with a 2-pixel diameter Gaussian filter. A maximum intensity projection of all frames containing evoked responses was obtained. The boundaries of the response were defined using the wand tool, connecting pixels of the same intensity level within a 15-pixel range, and the area of each response was calculated using the measure tool in ImageJ. To measure the active fraction of PMBSF and ALBSF in embWPC mice at E18 and P4, the control side was used to delineate the PMBSF and ALBSF territories following stimulation of the whisker pad or upper lip, respectively. On the WPC side, these areas were superimposed using the mirror image from the control side. The PMBSF and ALBSF active fractions were determined by measuring all elicited responses within each territory and calculating the percentage of the PMBSF and ALBSF theoretical areas occupied by these responses following whisker pad or upper lip stimulations. To quantify the percentage of overlap between responses following the whisker pad and upper lip stimulations (%PMBSF-ALBSF overlap) at E18 and P4, the overlap between all elicited responses following the whisker pad and those following upper lip stimulations was calculated. To quantify the percentage of overlap within PMBSF or ALBSF (% Responses overlap) in ctrl and embWPC, the overlap for two different stimuli on the whisker pad or two different stimuli on the upper lip was calculated.

To visualize the evoked stimuli in different color profiles for the generation of supplementary movies, we utilized custom scripts developed in Matlab™. These scripts were adapted from the image analysis suite WholeBrainDX (referenced in the Data and code availability section). For each movie, frames containing movement artifacts, spontaneous activity, and calcium activity deemed as stimulation byproducts were excluded. Baseline correction was performed using the built-in Matlab function "msbackadj" with a window size of 20 and a step size of 20. Subsequently, ΔF/F0 was computed using the median value of the corrected signal as F0. Movie segmentation and calcium event detection followed the method described[61]. Image segmentation and generation of a binary movie involved Gaussian smoothing with an 80 µm distance and a signal intensity threshold. The binary movie was color-labeled using ImageJ software and customized with a Gaussian filter. Subsequently, the original movie and the color-coded binary movie were merged using the "Image Calculator" function in ImageJ.

Microdissection and RNA isolation for RNA-seq

To capture gene expression changes during the critical period of somatosensory map plasticity, we collected tissue from the wpVPM and ulVPM territories of P0 ctrl and embWPC pups. Pups were euthanized by decapitation, and their brains were dissected under RNase-free conditions to prevent RNA degradation. The brains (five brains were pooled for each sample) were collected in ice-cold KREBS solution and sliced into 300 µm sections using a vibratome (VT1000S Leica). The wpVPM and ulVPM territories were rapidly microdissected under a stereo microscope. The bulk tissue was immediately transferred to the lysis buffer of the Rneasy® Micro Kit (Qiagen, 74004) for total RNA extraction, following the manufacturer's instructions. RNA quality was measured for all samples using an Agilent Bioanalyzer 2100 system, and only samples with RNA integrity number (RIN) >8 were used for library construction.

Library preparation and RNA sequencing

Library construction and sequencing were performed at Novogene Co. Ltd. Genomics core facility (Cambridge, UK). cDNA multiplex libraries were prepared using a custom Novogene NGS RNA Library Prep Set (PT042) kit. Briefly, mRNA was purified from total RNA using poly-T oligo-attached magnetic beads. After fragmentation, the first strand cDNA was synthesized using random hexamer primers followed by the second strand cDNA synthesis. The library was ready after end repair, A-tailing, adapter ligation, size selection, amplification, and purification.

The library was checked with Qubit and real-time PCR for quantification and bioanalyzer for size distribution detection. Libraries were pooled and sequenced in 2x150bp paired-end mode on an S4 flowcell in the Illumina Novaseq6000 platform. A minimum of 40 million reads were generated from each library.

Bioinformatic analysis of the RNA-seq

RNA-seq analysis were performed as previously described[62] with minor modifications: quality control of the raw data was performed with FastQC (v.0.11.9). RNA-seq reads were mapped to the Mouse genome (GRCm39) using STAR (v2.7.9a)[63] and SAM/BAM files were further processed using SAMtools (v1.15). Aligned reads were counted and assigned to genes using Ensembl release 104 gene annotation and FeatureCounts, Subread (v2.0.1). Normalization of read counts and differential expression analyses were performed using DESeq2 (v1.32)[64], Bioconductor (v3.15)[65] in the R statistical computing and graphics platform (v4.2.2 "Innocent and Trusting").

In the analysis of wpVPM and ulVPM datasets (control and embWPC samples) generated for this study, significantly differentially expressed genes (DEGs) were identified using a simultaneous statistical significance threshold (Benjamini–Hochberg (BH) adjusted P value <0.1) and absolute log2 fold change (log2FC) >0.14 by shrunken log2FC using the adaptive T prior Bayesian shrinkage estimator "apeglm" (Supplementary Data 1, 2)[66]. Hierarchical clustering

analysis was performed using "Euclidean" distance and "Complete" clustering methods metrics to visualize significantly upregulated and downregulated genes. A linear support vector machine (SVM) model for classifying RNA-seq samples was developed using the e1071 package (v1.7-14). This model was based on the gene expression profiles of the top 500 most variable genes in ulVPM and wpVPM control samples. Subsequently, the C-SVM model was utilized to predict the classification of ulVPM-embWPC samples based on their transcriptomic profiles.

Functional enrichment analyses were performed using clusterProfiler (v4.4.4)[67] under org.Mm.eg.db package (v3.15) for better annotation data. All enriched terms were considered significant at adjusted *P* values by "BH" <0.1, in the Gene Ontology (GO) overrepresentation Analysis. Enrichment results were further clustered and simplified using the simplifyEnrichment package (version 1.11.1)[68] (Supplementary Data 3).

Ex vivo calcium imaging

At E16, embryos were retrieved from the dam's uterus by cesarean section, their brains were rapidly dissected out, and they were submerged in an ice-cold slicing solution containing (in mM): 2.5 KCl, 7 $MgSO_4$, 0.5 $CaCl_2$, 1 NaH_2PO_4, 26 Na_2HCO_3, 11 glucose, and 228 sucrose. Coronal slices (350-µm thick) were obtained using a vibratome (VT1200S Leica), and they were left to recover for at least 30 min at room temperature in standard artificial cerebrospinal fluid (ACSF) containing (in mM): 119 NaCl, 5 KCl, 1.3 $MgSO_4$, 2.4 $CaCl_2$, 1 NaH_2PO_4, 26 Na_2HCO_3, and 11 glucose. All extracellular solutions were continuously bubbled with a 95% O_2 and 5% CO_2 gas mixture. Slices were loaded with the calcium indicator Cal520TM (AAT Bioquest) as previously described[10,21], transferred to a submersion-type recording chamber, and perfused with warm ACSF (32–34 °C) at a rate of 1.8 ml/min. Images were acquired with a digital charge-coupled device (CCD) camera (ORCA-R2 C10600-10B, Hamamatsu) coupled to an upright microscope (DM-LFSA, Leica) and using a 5x objective. For recordings of spontaneous calcium activity, frames were acquired with an exposure time of 150 ms, an interframe interval of 300 ms, a frame size of 672 × 512 pixel, and a spatial resolution of 2.5 µm/pixel. With each slice, 1 to 5 epochs of 15 min (3000 frames) were recorded.

Analysis of fluorescence spontaneous activity

Analysis of spontaneous thalamic calcium activity was conducted using custom software developed in Matlab™, which was adapted from the CalciumDX toolbox (indexed in the Data and code availability section). For each movie, VPM was delineated, and the two prospective areas (wpVPM and ulVPM) were subdivided into a grid of 6 × 6 pixels where each small square is a region of interest (ROI). Calcium activity events were detected based on the average calcium signal of each ROI over time, employing threshold-based algorithms modified from CalciumDX. To identify significant synchronous activity and discard ROI co-activation that results from random temporal coincidence of calcium events, we generated surrogated calcium events sequences for each experiment using Matlab™. The alternative dataset was built by randomly shuffling the original temporal intervals between calcium transients in every ROI while preserving the spiking frequency and temporal structure of the calcium activity. Subsequently, the maximum value of co-activation from shuffled data was calculated. Through 1000 iterations, we established a synchronicity threshold as the 95th percentile of the maximum values of co-activation obtained from the shuffled dataset. In each experiment, only activity superpassing the synchronicity threshold was used for calculations and visualization. The onset of a synchronic event was defined as the frame in which co-activation overpassed the threshold, while the end was determined as the frame in which co-activation reached 25% of peak synchronicity.

Behavioral testing

Twenty-three mice (9 males, 14 females) from four litters were bred for behavioral testing in adulthood (4 months old). Mice were housed in groups of 2–4 per cage. All behavioral testing was conducted during the light phase.

To evaluate tactile sensory processing, we used mice with bilateral (rather than unilateral) whisker pad cauterization at E14 (bi-embWPC group), enabling a more precise assessment of whisker-dependent processing by eliminating potential compensatory input in response to vibrissae-driven sensory stimuli from the intact contralateral side of the snout in unilateral cauterized mice. Wild-type littermates with intact whiskers served as control mice, while an additional control group of wild-type littermates underwent acute whisker trimming to assess texture discrimination in the absence of mystacial vibrissae input. Whisker trimming occurred on day 2, three hours after the second habituation session (see protocol below). All groups of mice were anesthetized with 5% isoflurane for induction and maintained on 2% isoflurane for 10 min. In the trimmed group, precise trimming to the fur level was achieved using micro spring scissors and a surgical microscope, carefully sparing upper lip whiskers.

Mice were habituated to handling and the testing room over 5–7 days, with dim lighting (20–30 lux) before testing. The behavioral testing arena was a black methacrylate box (40 × 40 × 40 cm) with no visual cues, and illumination was kept low (3–5 lux) to minimize visual information. Target objects consisted of 3D-printed cylinders (4 cm diameter, 9 cm height) covered with sandpaper of either 80 or 180 grit (P80 or P180) using double-sided tape. Six sets of textured covers were prepared a week prior to testing to minimize residual odors; each set contained four covers (three P180 and one P80), avoiding repetitive use and minimizing olfactory interference.

We used a modified whisker-dependent texture discrimination task based on established protocols[69–71]. This 3-day paradigm takes advantage of mice´s innate preference for novelty. During days 1 and 2 (habituation sessions), mice freely explored the empty arena for 5 min each day. On day 3 (testing sessions), two identical P180 sandpaper-covered cylinders were placed diagonally within the arena (12 cm from walls, 15 cm apart) during the sample session (t1). Mice explored these objects for 5 min before being returned to their home cages for a 2-min inter-trial interval (ITI). During this interval, the arena and objects were cleaned with 70% ethanol, one P180 cover was replaced with a P80 sandpaper to create a novel texture, and the other P180 cover was replaced by a new P180 cover. The short ITI minimized the influence of hippocampal processes on texture discrimination. During the test session (t_2), mice were returned to the arena to explore both the familiar (P180) and novel (P80) textures for 5 min. Mice were acclimated to the testing room for 30–60 min prior to each session.

Data analyses were performed offline using custom Matlab scripts to track and analyze locomotor and exploratory behaviors. Texture discrimination was assessed using the discrimination index (DI), calculated as the proportion of time spent exploring the novel texture relative to the total exploration time, according to the formula:

$$DI = \frac{Tnew}{Tnew + Tfamiliar}$$

where T_{new} refers to the time spent exploring the novel texture (P80) and $T_{familiar}$ is the time spent on the familiar texture (P180). In sample session (t_1), T_{new} refers to the texture that will be replaced in the following test session (t_2). DI values range from 0 to 1, with a value of 0.5 indicating no preference, and values above 0.5 indicating a preference for the novel texture.

Statistical analysis

Data were analysed using Prism 9 (GraphPad). A Kolmogorov-Smirnov normality test was conducted on all datasets. For independent data

that conforms to a normal distribution, an unpaired two-tailed Student's *t*-test was employed to compare the two groups. In cases where independent data that did not follow a normal distribution, a Mann–Whitney *U*-test two-tailed test was used for comparison. For analyses involving more than two groups and one factor, one-way ANOVA was applied, followed by a Tukey post hoc analysis when data exhibited a normal distribution. For more than two groups and two factors, two-way ANOVA was conducted, followed by a Tukey post hoc analysis for normally distributed data. When data did not conform to a normal distribution, a Kruskal–Wallis test was performed, followed by Dunn's multiple comparisons without any correction. Results are presented as mean ± standard error of mean (SEM) with the n value for each dataset. Statistically significant effects and n numbers are detailed in the corresponding figure legend or Methods. The significance threshold was set at 0.05, two-tailed (not significant, ns, $p > 0.05$; *$p < 0.05$; **$p < 0.01$; ***$p < 0.001$). In the bioinformatical analysis, DEGs were identified using a statistical significance threshold (BH-adjusted p value <0.1) and set as follows: *adj. $p < 0.1$, **adj. $p < 0.01$, and ***adj. $p < 0.001$. No data exclusion was performed. Data for RNA-seq were processed according to the description in the Methods sections, and statistical details are explained in the results and corresponding figure legends.

Quantifications

Main figures. In Fig. 1b: Whisker pad volume, unpaired two-tailed Student *t*-test. **$p < 0.01$. Upper lip volume, unpaired two-tailed Student *t*-test. ns, $p = 0.11$. Upper lip area, unpaired two-tailed Student *t*-test. ns, $p = 0.32$. 9 follicles volume, two-tailed Mann–Whitney *U*-test. *$p < 0.05$. ns, $p = 0.73$. Upper lip number of follicles, unpaired two-tailed Student *t*-test. ns, $p = 0.78$. In Fig. 1d: unpaired two-tailed Student *t*-test. PMBSF, ***$p < 0.0001$, ALBSF, ***$p = 0.0002$. In Fig. 1f: unpaired two-tailed Student *t*-test. DiI, ***$p = 0.0002$, DiA, ***$p < 0.0001$. In Fig. 1h: unpaired two-tailed Student *t*-test. ns, PMBSF, $p = 0.55$, ALBSF, $p = 0.30$. In Fig. 1j: unpaired two-tailed Student *t*-test. ns, $p = 0.09$. **$p < 0.01$.

In Fig. 2c: unpaired two-tailed Student *t*-test. PMBSF active fraction after wps, *$p = 0.0198$, PMBSF active fraction after uls, ***$p = 0.0001$, ALBSF active fraction after wps, **$p = 0.0037$, ALBSF active fraction after uls, **$p = 0.0014$. In Fig. 2e: PMBSF active fraction, unpaired two-tailed Student *t*-test. **$p < 0.01$. ALBSF active fraction, two-tailed Mann–Whitney *U*-test. ns, $p = 0.06$. *$p < 0.05$. In Fig. 2f: Kruskal–Wallis test, ***$p < 0.001$. Dunn's multiple comparison test post hoc analysis, ctrl E18 vs embWPC E18 ns, $p = 0.37$; ctrl E18 vs ctrl P4, ***$p = 0.0009$; ctrl E18 vs embWPC P4, ***$p < 0.0001$; embWPC E18 vs ctrl P4 ns, $p = 0.77$; embWPC E18 vs embWPC P4 ns, $p = 0.14$; ctrl P4 vs embWPC P4 ns, $p > 0.999$.

In Fig. 3d: Kruskal–Wallis test, ***$p < 0.001$. Dunn's multiple comparison test post hoc analysis, wpVPM-ctrl vs wpVPM embWPC ns, $p = 0.14$; wpVPM-ctrl vs ulVPM-embWPC ns, $p = 0.32$; wpVPM embWPC vs ulVPM-embWPC ns, $p > 0.99$. wpVPM-ctrl vs ulVPM-ctrl, *$p = 0.04$. ulVPM-ctrl vs ulVPM-embWPC, ***$p < 0.0001$. In Fig. 3f: Thalamus, wpVPM, two-way ANOVA test: ***$p < 0.001$. Tukey's multiple comparison test post hoc analysis, ns, $p = 0.98$. ***$p < 0.0001$; ulVPM, Kruskal–Wallis test, ***$p = 0.0005$. Dunn's multiple comparison test post hoc analysis, ns, $p > 0.99$. **$p = 0.0019$. Cortex, PMBSF, two-way ANOVA test: ***$p < 0.0001$. Tukey's multiple comparison test post hoc analysis, ns, $p = 0.99$. ***$p < 0.0001$; ALBSF, two-way ANOVA test: ***$p < 0.0001$. Tukey's multiple comparison test post hoc analysis, ns, $p = 0.52$. ***$p = 0.0002$. In Fig. 3h: DiI, two-tailed Mann–Whitney *U*-test. ns, $p = 0.7$; DiA, unpaired two-tailed Student *t*-test. ns, 0.76.

In Fig. 4b: One-way ANOVA test: ***$p < 0.0001$. Tukey's multiple comparison test post hoc analysis, ns, $p = 0.056$, ***$p < 0.0001$. In Fig. 4i: Negative binomial generalized linear model (GLM) analysis, p values were calculated using a two-tailed Wald's test. Adjusted p values were obtained using the Benjamini–Hochberg (BH) method for multiple comparisons, with a significance threshold of adjusted p value <0.1. *Rorα* wpVPM-ctrl vs ulVPM-ctrl, ***adj. $p < 0.0001$; *Rorα* wpVPM-ctrl vs ulVPM-embWPC ns, adj. $p = 0.98$; *Rorα* ulVPM-ctrl vs ulVPM-embWPC, **adj. $p = 0.002$; *Hs6st2* wpVPM-ctrl vs ulVPM-ctrl, ***adj. $p < 0.0001$; *Hs6st2* wpVPM-ctrl vs ulVPM-embWPC, *adj. $p = 0.04$; *Hs6st2* ulVPM-ctrl vs ulVPM-embWPC, ***adj. $p < 0.0001$; *Pou2f2* wpVPM-ctrl vs ulVPM-ctrl, ***adj. $p < 0.0001$; *Pou2f2* wpVPM-ctrl vs ulVPM-embWPC, *adj. $p = 0.07$; *Pou2f2* ulVPM-ctrl vs ulVPM-embWPC, ***adj. $p = 0.0003$; *Epha4* wpVPM-ctrl vs ulVPM-ctrl, ***adj. $p = 0.0008$; *Epha4* wpVPM-ctrl vs ulVPM-embWPC ns, adj. $p = 0.79$; *Epha4* ulVPM-ctrl vs ulVPM-embWPC, *adj. $p = 0.08$; *Plxna2* wpVPM-ctrl vs ulVPM-ctrl, ***adj. $p < 0.0001$; *Plxna2* wpVPM-ctrl vs ulVPM-embWPC, *adj. $p = 0.06$; *Plxna2* ulVPM-ctrl vs ulVPM-embWPC, ***adj. $p < 0.0001$; *Cdh9* wpVPM-ctrl vs ulVPM-ctrl, ***adj. $p < 0.0001$; *Cdh9* wpVPM-ctrl vs ulVPM-embWPC ns, adj. $p = 0.98$; *Cdh9* ulVPM-ctrl vs ulVPM-embWPC, ***adj. $p < 0.0001$.

In Fig. 5b: Barrels average area (34 barrels), Two-way ANOVA test: ***$p < 0.0001$. Tukey's multiple comparison test post hoc analysis, ns, $p = 0.88$. ***$p < 0.0001$. Average area of four barrels per three caudal-to-rostral levels, Two-way ANOVA test: ***$p < 0.0001$. Tukey's multiple comparison test post hoc analysis, level 1 ALBSF-ctrl vs ALBSF-embWPC, ***$p < 0.0001$; level 2 ALBSF-ctrl vs ALBSF-embWPC, ***$p < 0.0001$; level 3 ALBSF-ctrl vs ALBSF-embWPC, ns, $p = 0.21$; level 1 ALBSF-ctrl vs level 2 ALBSF-ctrl, ns, $p > 0.99$; level 1 ALBSF-ctrl vs level 3 ALBSF-ctrl, ns, $p = 0.88$; level 2 ALBSF-ctrl vs level 3 ALBSF-ctrl, ns, $p = 0.92$; level 1 ALBSF-embWPC vs level 2 ALBSF-embWPC, **$p = 0.0023$; level 1 ALBSF-embWPC vs level 3 ALBSF-embWPC, ***$p < 0.0001$; level 2 ALBSF-embWPC vs level 3 ALBSF-embWPC, **$p = 0.0027$. In Fig. 5c: barrel/septum fluorescence ratio (ΔFb/Fs), Two-way ANOVA test: ***$p < 0.0001$. Tukey's multiple comparison test post hoc analysis, PMBSF-ctrl vs ALBSF-embWPC ns, $p = 0.80$; ALBSF-ctrl vs ALBSF-P0WPC ns, $p = 0.35$; PMBSF-ctrl vs ALBSF-ctrl, ***$p < 0.0001$; ALBSF-ctrl vs ALBSF-embWPC, ***$p < 0.0001$; PMBSF-ctrl vs ALBSF-P0WPC, ***$p < 0.0001$; ALBSF-embWPC vs ALBSF-P0WPC, ***$p < 0.0001$. Gray value fluorescence intensity in a barrel, one-way ANOVA test: ***$p = 0.0002$. Tukey's multiple comparison test post hoc analysis, ns, $p = 0.99$. PMBSF-ctrl vs ALBSF-embWPC ns, $p = 0.99$; ALBSF-ctrl vs ALBSF-P0WPC ns, $p = 0.99$; ALBSF-ctrl vs ALBSF-embWPC, *$p = 0.01$; PMBSF-ctrl vs ALBSF-ctrl, **$p = 0.005$; ALBSF-embWPC vs ALBSF-P0WPC, **$p = 0.005$; PMBSF-ctrl vs ALBSF-P0WPC, **$p = 0.0023$. In Fig. 5e: One-way ANOVA test: *$p = 0.01$. Tukey's multiple comparison test post hoc analysis, PMBSF-ctrl vs ALBSF-embWPC ns, $p = 0.75$; ALBSF-ctrl vs PMBSF-ctrl, *$p = 0.048$; ALBSF-ctrl vs ALBSF-embWPC, *$p = 0.013$. In Fig. 5g: PV+ cells in barrels P8, one-way ANOVA test: ***$p < 0.0001$. Tukey's multiple comparison test post hoc analysis, PMBSF-ctrl vs ALBSF-embWPC ns, $p = 0.98$; PMBSF-ctrl vs ALBSF-ctrl, ***$p = 0.0003$; ALBSF-embWPC vs ALBSF-ctrl, ***$p = 0.0002$. PV+ cells in septa P8, one-way ANOVA test: ***$p < 0.0001$. Tukey's multiple comparison test post hoc analysis, PMBSF-ctrl vs ALBSF-embWPC ns, $p > 0.99$; PMBSF-ctrl vs ALBSF-ctrl, ***$p < 0.0001$; ALBSF-embWPC vs ALBSF-ctrl, ***$p < 0.0001$.

In Fig. 6c: One-way ANOVA test: ***$p < 0.0001$. Tukey's multiple comparison test post hoc analysis, ns, $p = 0.18$. ***$p < 0.0001$. In Fig. 6f: PMBSF, unpaired two-tailed Student *t*-test. ***$p < 0.0001$; ALBSF, two-tailed Mann–Whitney *U*-test. ***$p = 0.0002$. In Fig. 6j: Total time of exploration, Two-way ANOVA test: **$p = 0.0023$. Tukey's multiple comparison test post hoc analysis, t1 ctrl vs bi-embWPC, *$p = 0.05$; t1 ctrl vs trimmed, **$p = 0.001$, t1 bi-embWPC vs trimmed ns, $p = 0.42$; t2 ctrl vs bi-embWPC, *$p = 0.029$; t2 ctrl vs trimmed, *$p = 0.029$, t2 bi-embWPC vs trimmed ns, $p = 0.997$. Discrimination Index, Two-way ANOVA test: **$p = 0.002$. Bonferroni's multiple comparison post hoc test; t1 ctrl vs t2 ctrl, *$p = 0.035$; t1 bi-embWPC vs t2 bi-embWPC, **$p = 0.009$; t1 trimmed vs t2 trimmed ns, $p > 0.999$.

Declaration of generative AI and AI-assisted technologies in the writing process

During the preparation of this work the authors used Chat-GPT in order to streamline some parts of the text. After using this tool, the authors reviewed and edited the content as needed and took full responsibility for the content of the publication.

Reporting summary

Further information on research design is available in the Nature Portfolio Reporting Summary linked to this article.

Data availability

RNAseq datasets have been deposited at the National Center for Biotechnology Information (NCBI) Gene Expression Omnibus (GEO) as GEO: GSE260865 and are publicly available as of the date of publication. The remaining data were available within the Article, Supplementary Information, or Source data file. Any additional information required to reanalyze the data reported in this working paper is available from the lead contact upon request. Source data are provided with this paper.

Code availability

This study did not generate the original code. For ex vivo experiments analysis, calcium imaging code previously reported[21] and deposited at https://github.com/ackman678/CalciumDX. For in vivo calcium imaging experiments, the code from WholeBrainDX repository[61] (available at https://github.com/ackman678/wholeBrainDX) was employed to prepare the supplementary videos. For behavioral experiments, video recordings were processed using custom codes developed with Matlab's Image Processing Toolbox.

References

1. Rakic, P. Specification of cerebral cortical areas. *Science* **241**, 170–176 (1988).
2. O'Leary, D. D. & Sahara, S. Genetic regulation of arealization of the neocortex. *Curr. Opin. Neurobiol.* **18**, 90–100 (2008).
3. O'Leary, D. D., Chou, S. J. & Sahara, S. Area patterning of the mammalian cortex. *Neuron* **56**, 252–269 (2007).
4. Grove, E. A. & Fukuchi-Shimogori, T. Generating the cerebral cortical area map. *Annu. Rev. Neurosci.* **26**, 355–380 (2003).
5. Harris, K. D. & Shepherd, G. M. The neocortical circuit: themes and variations. *Nat. Neurosci.* **18**, 170–181 (2015).
6. Welker, C. Receptive fields of barrels in the somatosensory neocortex of the rat. *J. Comp. Neurol.* **166**, 173–189 (1976).
7. Diamond, M. E., von Heimendahl, M., Knutsen, P. M., Kleinfeld, D. & Ahissar, E. Where' and 'what' in the whisker sensorimotor system. *Nat. Rev. Neurosci.* **9**, 601–612 (2008).
8. Brecht, M., Preilowski, B. & Merzenich, M. M. Functional architecture of the mystacial vibrissae. *Behav. Brain Res.* **84**, 81–97 (1997).
9. Woolsey, T. A. & Van der Loos, H. The structural organization of layer IV in the somatosensory region (SI) of mouse cerebral cortex. The description of a cortical field composed of discrete cytoarchitectonic units. *Brain Res.* **17**, 205–242 (1970).
10. Moreno-Juan, V. et al. Prenatal thalamic waves regulate cortical area size prior to sensory processing. *Nat. Commun.* **8**, 14172 (2017).
11. Lopez-Bendito, G., Anibal-Martinez, M. & Martini, F. J. Cross-modal plasticity in brains deprived of visual input before vision. *Annu. Rev. Neurosci.* **45**, 471–489 (2022).
12. Gaspar, P. & Erzurumlu, R. The birth of the barrels. *Dev. Cell* **27**, 3–4 (2013).
13. Erzurumlu, R. S. & Gaspar, P. How the barrel cortex became a working model for developmental plasticity: a historical perspective. *J. Neurosci.* **40**, 6460–6473 (2020).
14. Mizuno, H. et al. NMDAR-regulated dynamics of layer 4 neuronal dendrites during thalamocortical reorganization in neonates. *Neuron* **82**, 365–379 (2014).
15. Laumonnerie, C. et al. Facial whisker pattern is not sufficient to instruct a whisker-related topographic map in the mouse somatosensory brainstem. *Development* **142**, 3704–3712 (2015).
16. Ozdinler, P. H. & Erzurumlu, R. S. Slit2, a branching-arborization factor for sensory axons in the mammalian CNS. *J. Neurosci.* **22**, 4540–4549 (2002).
17. Oury, F. et al. Hoxa2- and rhombomere-dependent development of the mouse facial somatosensory map. *Science* **313**, 1408–1413 (2006).
18. Kitazawa, T. & Rijli, F. M. Barrelette map formation in the prenatal mouse brainstem. *Curr. Opin. Neurobiol.* **53**, 210–219 (2018).
19. Bechara, A. et al. Hoxa2 selects barrelette neuron identity and connectivity in the mouse somatosensory brainstem. *Cell Rep.* **13**, 783–797 (2015).
20. Zembrzycki, A., Chou, S. J., Ashery-Padan, R., Stoykova, A. & O'Leary, D. D. Sensory cortex limits cortical maps and drives top-down plasticity in thalamocortical circuits. *Nat. Neurosci.* **16**, 1060–1067 (2013).
21. Anton-Bolanos, N. et al. Prenatal activity from thalamic neurons governs the emergence of functional cortical maps in mice. *Science* **364**, 987–990 (2019).
22. Guillamon-Vivancos, T. et al. Input-dependent segregation of visual and somatosensory circuits in the mouse superior colliculus. *Science* **377**, 845–850 (2022).
23. Frangeul, L. et al. A cross-modal genetic framework for the development and plasticity of sensory pathways. *Nature* **538**, 96–98 (2016).
24. Pouchelon, G. et al. Modality-specific thalamocortical inputs instruct the identity of postsynaptic L4 neurons. *Nature* **511**, 471–474 (2014).
25. Ono, K. et al. Development of the prethalamus is crucial for thalamocortical projection formation and is regulated by Olig2. *Development* **141**, 2075–2084 (2014).
26. Vitalis, T. et al. RORalpha coordinates thalamic and cortical maturation to instruct barrel cortex development. *Cereb. Cortex* **28**, 3994–4007 (2018).
27. Gezelius, H. & Lopez-Bendito, G. Thalamic neuronal specification and early circuit formation. *Dev. Neurobiol.* **77**, 830–843 (2017).
28. Rubenstein, J. et al. Genetic control of cortical regionalization and connectivity. *Cereb. Cortex* **9**, 524–532 (1999).
29. Mercurio, S. et al. Sox2 acts in thalamic neurons to control the development of retina-thalamus-cortex connectivity. *iScience* **15**, 257–273 (2019).
30. Nakagawa, Y. & O'Leary, D. D. Dynamic patterned expression of orphan nuclear receptor genes RORalpha and RORbeta in developing mouse forebrain. *Dev. Neurosci.* **25**, 234–244 (2003).
31. Yuge, K. et al. Region-specific gene expression in early postnatal mouse thalamus. *J. Comp. Neurol.* **519**, 544–561 (2011).
32. Ebisu, H., Iwai-Takekoshi, L., Fujita-Jimbo, E., Momoi, T. & Kawasaki, H. Foxp2 regulates identities and projection patterns of thalamic nuclei during development. *Cereb. Cortex* **27**, 3648–3659 (2017).
33. Puelles, L., Sanchez, M. P., Spreafico, R. & Fairen, A. Prenatal development of calbindin immunoreactivity in the dorsal thalamus of the rat. *Neuroscience* **46**, 135–147 (1992).
34. Dufour, A. et al. Area specificity and topography of thalamocortical projections are controlled by ephrin/Eph genes. *Neuron* **39**, 453–465 (2003).
35. Shigematsu, N., Miyamoto, Y., Esumi, S. & Fukuda, T. The anterolateral barrel subfield differs from the posteromedial barrel subfield in the morphology and cell density of parvalbumin-positive

GABAergic interneurons. *eNeuro* https://doi.org/10.1523/ENEURO.0518-22.2024 (2024).
36. Killackey, H. P. & Dawson, D. R. Expansion of the central hindpaw representation following fetal forelimb removal in the rat. *Eur. J. Neurosci.* **1**, 210–221 (1989).
37. Van der Loos, H. & Woolsey, T. A. Somatosensory cortex: structural alterations following early injury to sense organs. *Science* **179**, 395–398 (1973).
38. Killackey, H. P. & Belford, G. R. The formation of afferent patterns in the somatosensory cortex of the neonatal rat. *J. Comp. Neurol.* **183**, 285–303 (1979).
39. Woolsey, T. A., Anderson, J. R., Wann, J. R. & Stanfield, B. B. Effects of early vibrissae damage on neurons in the ventrobasal (VB) thalamus of the mouse. *J. Comp. Neurol.* **184**, 363–380 (1979).
40. Belford, G. R. & Killackey, H. P. The development of vibrissae representation in subcortical trigeminal centers of the neonatal rat. *J. Comp. Neurol.* **188**, 63–74 (1979).
41. Woolsey, T. A. & Wann, J. R. Areal changes in mouse cortical barrels following vibrissal damage at different postnatal ages. *J. Comp. Neurol.* **170**, 53–66 (1976).
42. Killackey, H. P., Belford, G., Ryugo, R. & Ryugo, D. K. Anomalous organization of thalamocortical projections consequent to vibrissae removal in the newborn rat and mouse. *Brain Res.* **104**, 309–315 (1976).
43. Renier, N. et al. A mutant with bilateral whisker to barrel inputs unveils somatosensory mapping rules in the cerebral cortex. *Elife* https://doi.org/10.7554/eLife.23494 (2017).
44. Belford, G. R. & Killackey, H. P. The sensitive period in the development of the trigeminal system of the neonatal rat. *J. Comp. Neurol.* **193**, 335–350 (1980).
45. Martini, F. J., Guillamon-Vivancos, T., Moreno-Juan, V., Valdeolmillos, M. & Lopez-Bendito, G. Spontaneous activity in developing thalamic and cortical sensory networks. *Neuron* **109**, 2519–2534 (2021).
46. Mire, E. et al. Spontaneous activity regulates Robo1 transcription to mediate a switch in thalamocortical axon growth. *Nat. Neurosci.* **15**, 1134–1143 (2012).
47. Land, P. W. & Simons, D. J. Cytochrome oxidase staining in the rat SmI barrel cortex. *J. Comp. Neurol.* **238**, 225–235 (1985).
48. Jan, T. A., Lu, L., Li, C. X., Williams, R. W. & Waters, R. S. Genetic analysis of posterior medial barrel subfield (PMBSF) size in somatosensory cortex (SI) in recombinant inbred strains of mice. *BMC Neurosci.* **9**, 3 (2008).
49. Kleinfeld, D., Ahissar, E. & Diamond, M. E. Active sensation: insights from the rodent vibrissa sensorimotor system. *Curr. Opin. Neurobiol.* **16**, 435–444 (2006).
50. Grant, R. A., Sperber, A. L. & Prescott, T. J. The role of orienting in vibrissal touch sensing. *Front. Behav. Neurosci.* **6**, 39 (2012).
51. Kuruppath, P., Gugig, E. & Azouz, R. Microvibrissae-based texture discrimination. *J. Neurosci.* **34**, 5115–5120 (2014).
52. Morita, T., Kang, H., Wolfe, J., Jadhav, S. P. & Feldman, D. E. Psychometric curve and behavioral strategies for whisker-based texture discrimination in rats. *PLoS ONE* **6**, e20437 (2011).
53. Gorski, J. A. et al. Cortical excitatory neurons and glia, but not GABAergic neurons, are produced in the Emx1-expressing lineage. *J. Neurosci.* **22**, 6309–6314 (2002).
54. Chen, L., Guo, Q. & Li, J. Transcription factor Gbx2 acts cell-nonautonomously to regulate the formation of lineage-restriction boundaries of the thalamus. *Development* **136**, 1317–1326 (2009).
55. Franco, S. J. et al. Fate-restricted neural progenitors in the mammalian cerebral cortex. *Science* **337**, 746–749 (2012).
56. Voiculescu, O., Charnay, P. & Schneider-Maunoury, S. Expression pattern of a Krox-20/Cre knock-in allele in the developing hindbrain, bones, and peripheral nervous system. *Genesis* **26**, 123–126 (2000).
57. Madisen, L. et al. Transgenic mice for intersectional targeting of neural sensors and effectors with high specificity and performance. *Neuron* **85**, 942–958 (2015).
58. Renier, N. et al. iDISCO: a simple, rapid method to immunolabel large tissue samples for volume imaging. *Cell* **159**, 896–910 (2014).
59. Renier, N. et al. Mapping of brain activity by automated volume analysis of immediate early genes. *Cell* **165**, 1789–1802 (2016).
60. Madisen, L. et al. A robust and high-throughput Cre reporting and characterization system for the whole mouse brain. *Nat. Neurosci.* **13**, 133–140 (2010).
61. Ackman, J. B., Zeng, H. & Crair, M. C. Structured dynamics of neural activity across developing neocortex. Preprint at *bioRxiv* https://doi.org/10.1101/012237 (2014).
62. Herrero-Navarro, A. et al. Astrocytes and neurons share region-specific transcriptional signatures that confer regional identity to neuronal reprogramming. *Sci. Adv.* https://doi.org/10.1126/sciadv.abe8978 (2021).
63. Dobin, A. et al. STAR: ultrafast universal RNA-seq aligner. *Bioinformatics* **29**, 15–21 (2013).
64. Love, M. I., Huber, W. & Anders, S. Moderated estimation of fold change and dispersion for RNA-seq data with DESeq2. *Genome Biol.* **15**, 550 (2014).
65. Huber, W. et al. Orchestrating high-throughput genomic analysis with Bioconductor. *Nat. Methods* **12**, 115–121 (2015).
66. Zhu, A., Srivastava, A., Ibrahim, J. G., Patro, R. & Love, M. I. Nonparametric expression analysis using inferential replicate counts. *Nucleic Acids Res.* **47**, e105 (2019).
67. Gu, Z. & Hubschmann, D. simplifyEnrichment: a bioconductor package for clustering and visualizing functional enrichment results. *Genomics Proteomics Bioinformatics* **21**, 190–202 (2023).
68. Yu, G., Wang, L. G., Han, Y. & He, Q. Y. clusterProfiler: an R package for comparing biological themes among gene clusters. *OMICS* **16**, 284–287 (2012).
69. Wu, H. P., Ioffe, J. C., Iverson, M. M., Boon, J. M. & Dyck, R. H. Novel, whisker-dependent texture discrimination task for mice. *Behav. Brain Res.* **237**, 238–242 (2013).
70. Benamer, N., Vidal, M., Balia, M. & Angulo, M. C. Myelination of parvalbumin interneurons shapes the function of cortical sensory inhibitory circuits. *Nat. Commun.* **11**, 5151 (2020).
71. Balasco, L. et al. Somatosensory cortex hyperconnectivity and impaired whisker-dependent responses in Cntnap2(-/-) mice. *Neurobiol. Dis.* **169**, 105742 (2022).

Acknowledgements

We thank Belén Andrés and María Aurelia Torregrosa for their technical support. We thank Teresa Guillamón-Vivancos and Miguel Valdeolmillos for their comments and input on the manuscript and other members of López-Bendito's laboratory for stimulating discussions. This work was supported by grants from the Swiss National Science Foundation (31003A_175776 and 310030_219370) and the Novartis Research Foundation to F.M.R., and by grants from the European Research Council (ERC) under the European Union's Horizon 2020 research and innovation program (ERC-2021-ADG-101054313 SPONTSENSE), PID2021-127112NB-I00 from the MCIN/AEI /10.13039/501100011033/ and ERDF A way to make Europe, and Generalitat Valenciana, Conselleria d'Educació, Universitats, i Ocupació (PROMETEO 2021/052) to G.L.-B. This work was also funded by the Spanish State Research Agency (AEI/10.13039/501100011033), through the 'Severo Ochoa' Center of Excellence grant to the IN (CEX2021-001165-S).

Author contributions

Conceptualization, M.A.-M. and G.L.-B.; methodology, M.A.-M., E.P.-M., G.P., M.P.M. and L.M.R.-M.; data curation, M.A.-M., E.P.-M., G.P., M.P.M., and L.P.; transcriptomic analysis, L.P.; writing—original draft, M.A.-M., and G.L.-B.; writing—review & editing, M.A.-M., L.P., E.P.-M., G.P., FJ.M.,

F.M.R., and G.L.-B.; funding acquisition, FM.R., and G.L-B.; resources, FM.R., and G.L-B.; supervision, FJ.M., FM.R., and G.L-B.

Competing interests
The authors declare no competing interests.

Additional information
Supplementary information The online version contains supplementary material available at https://doi.org/10.1038/s41467-025-57052-w.

Correspondence and requests for materials should be addressed to Guillermina López-Bendito.

Peer review information *Nature Communications* thanks Leena Ibrahim who co-reviewed with Mansour Alyahyay, and the other, anonymous, reviewers for their contribution to the peer review of this work. A peer review file is available.

Input-dependent segregation of visual and somatosensory circuits in the mouse superior colliculus

Teresa Guillamón-Vivancos, Mar Aníbal-Martínez, Lorenzo Puche-Aroca, Juan Antonio Moreno-Bravo, Miguel Valdeolmillos, Francisco J. Martini, Guillermina López-Bendito*

Instituto de Neurociencias de Alicante, Universidad Miguel Hernández-Consejo Superior de Investigaciones Científicas (UMH-CSIC), San Juan de Alicante, Alicante, Spain.

* Corresponding author: g.lbendito@umh.es

Science 2022 Aug; 377(6608):845-850. DOI: 10.1126/science.abq2960.

NEURODEVELOPMENT

Input-dependent segregation of visual and somatosensory circuits in the mouse superior colliculus

Teresa Guillamón-Vivancos, Mar Aníbal-Martínez, Lorenzo Puche-Aroca, Juan Antonio Moreno-Bravo, Miguel Valdeolmillos, Francisco J. Martini, Guillermina López-Bendito*

Whereas sensory perception relies on specialized sensory pathways, it is unclear whether these pathways originate as modality-specific circuits. We demonstrated that somatosensory and visual circuits are not by default segregated but require the earliest retinal activity to do so. In the embryo, somatosensory and visual circuits are intermingled in the superior colliculus, leading to cortical multimodal responses to whisker pad stimulation. At birth, these circuits segregate, and responses switch to unimodal. Blocking stage I retinal waves prolongs the multimodal configuration into postnatal life, with the superior colliculus retaining a mixed somato-visual molecular identity and defects arising in the spatial organization of the visual system. Hence, the superior colliculus mediates the timely segregation of sensory modalities in an input-dependent manner, channeling specific sensory cues to their appropriate sensory pathway.

In the mature cerebral cortex, sensory modalities are segregated into specialized areas known as primary sensory cortices. So that cortical areas ultimately respond to a specific sensory stimulus, this segregation is thought to occur during development, and it is first instructed by intrinsic factors and later by sensory experience (*1*–*5*). However, this early inception of sensory identity has not been directly demonstrated because there is no functional evidence of the sensory specificity of emerging circuits. It remains to be determined whether sensory identities arise directly as unimodal entities or whether they are initially multimodal and become specified over time. We found that the nascent somatosensory and visual pathways of mice are functionally interconnected, with both cortices responding to tactile stimulation at prenatal stages yet segregating into independent pathways at birth. This segregation happens in the superior colliculus (SC) and depends on retinal input. Blocking stage I retinal waves or removing retinal projections in embryos leads to a failure in the timely developmental segregation of visual circuits in the SC. Consequently, the activation of the visual cortex by somatosensory stimuli extends into postnatal life and is associated with long-term circuit abnormalities.

S1 and V1 emerge functionally intermingled

A functional map of the periphery is present in the mouse somatosensory cortex at perinatal stages, as shown through whisker pad stimulation in a transgenic mouse line in which glutamatergic neurons in the neocortex express GCaMP6f (hereafter $Cx^{GCaMP6f}$) (*6*). Hence, there appears to be a high level of intramodal functional organization of sensory circuits at these early stages. We used the same approach to test whether developing sensory circuits also show early specificity to stimulus modalities. We found that at embryonic stages, a somatosensory stimulus not only triggered the expected contralateral response in the barrel field of the primary somatosensory cortex (S1) but also a bilateral response in the presumptive primary visual cortex (V1). This multimodal response was observed in 33% of the mice analyzed at embryonic day 18 (E18) but disappeared by postnatal day 0 (P0) (Fig. 1, A to C, and movies S1 and S2), suggesting that we were revealing the end of a developmental process. We next tested whether the disappearance of this cortical multimodal response might be related to the arrival of retinal inputs to central structures, which occurs close to birth (*7*–*9*). To test this possibility, we used $Cx^{GCaMP6f}$ mice in which their eyes were eliminated bilaterally at E14 (embBE mice) (*10*). Whereas whisker pad stimulation at P0 triggered only the cortical somatosensory response in control mice, in the embBE mice, this response was consistently multimodal, activating both S1 and V1 in 100% of the cases, even at E18 (Fig. 1, D to F, and movies S3 and S4). This multimodal response extended into the first postnatal days and lasted until P6 (Fig. 1G and fig. S1). Thus, it appears that somatosensory and visual circuits are not segregated by default but require the arrival of retinal input to do so.

We then designed experiments to identify the circuits responsible for this lack of segregation and the ensuing multimodal response in embBE mice. Electrical stimulation of either S1 or V1 in the embBE mice failed to reproduce the bilateral V1 responses to whisker pad stimulation (fig. S2, A to D). Moreover, these responses were still triggered by whisker pad stimulation when the barrel field was inhibited by tetrodotoxin (TTX) (fig. S2, E and F). Hence, these experiments demonstrate that the sensory-modality interconnection in embBE mice is not driven by a cortico-cortical mechanism.

SC circuit reorganization provides sensory-modality specificity

Before reaching the cortex, sensory-modality pathways converge in nearby territories of the thalamus and also in the SC (*11*). Therefore, the multimodal responses observed might involve direct communication between modalities at either of these structures. The SC is a midbrain multisensory structure that receives visual input in its superficial layers (sSC) and somatosensory input in its deep layers (dSC) (*11*, *12*). Using mice that express GCaMP6f in SC neurons (hereafter $SC^{GCaMP6f}$), we found that whisker pad stimulations at P0 evoked a bilateral response in the sSC of all embBE mice, whereas no responses were evoked in the sSC of control mice (Fig. 2, A to C, and movies S5 and S6). To confirm that the cortical multimodal response requires the SC, we inactivated the SC with TTX in embBE triple transgenic mice that expressed GCaMP6f in the cortex and SC ($Cx\text{-}SC^{GCaMP6f}$) and found that the cortical response became unimodal (Fig. 2, D to F). Similar results were found when the SC was acutely lesioned (fig. S3, A and B). Last, we looked for sensory modality changes in the circuits downstream of the SC and, using dye tracing, demonstrated that the connectivity from the SC to the thalamus was normal in embBE mice (fig. S3, C and D). Similarly, we found no differences in the specificity of the sensory modality of thalamic afferents or efferents in these embBE mice (fig. S4). Therefore, these results demonstrate that the SC mediates the multimodal cortical responses in embBE mice and suggest that the SC is involved in the developmental segregation of sensory modalities observed in control mice.

We next assessed how the SC channels somatosensory information into the presumptive V1 by testing the connectivity between the dSC (somatosensory) and sSC (visual) layers in embBE mice. At P0, whereas unilateral electrical stimulation of the dSC layers in $SC^{GCaMP6f}$ control slices only elicited responses in the contralateral dSC layer, the responses in the embBE mice also propagated to both the ipsilateral and contralateral sSC layers (Fig. 2, G and H, and movies S7 and S8), an effect that was not observed by stimulating the superficial layers (fig. S5). In addition, these functional results were supported by anatomical tracing. Unilateral injection of lentivirus-expressing enhanced green fluorescent protein (EGFP) into the SC produced widespread

Instituto de Neurociencias de Alicante, Universidad Miguel Hernández–Consejo Superior de Investigaciones Científicas (UMH-CSIC), San Juan de Alicante, Alicante, Spain.
***Corresponding author. Email: g.lbendito@umh.es**

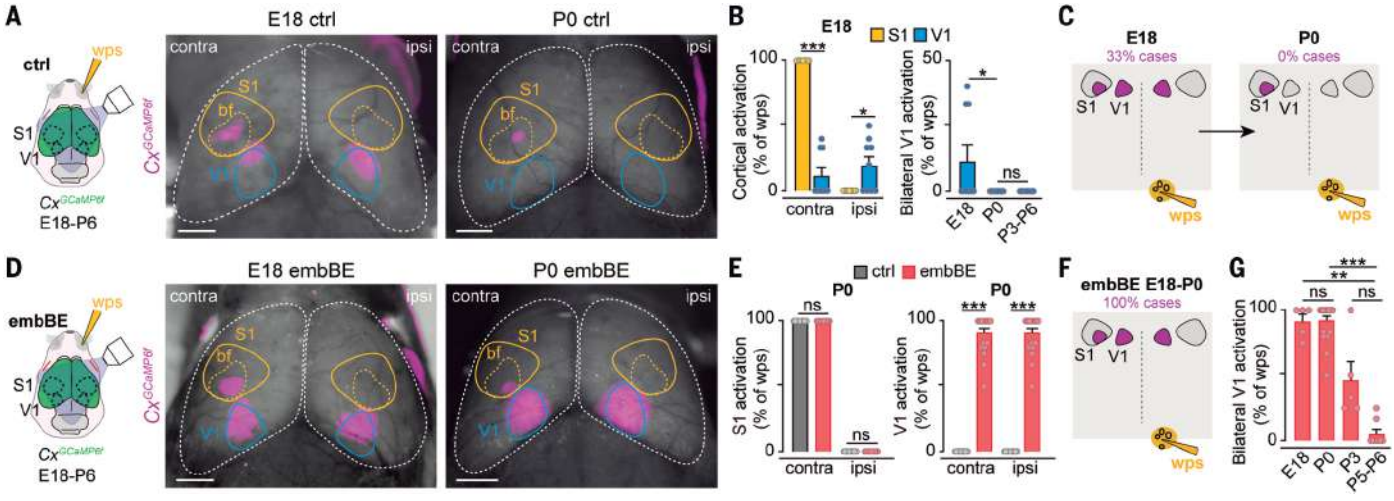

Fig. 1. Embryonic somatosensory and visual cortices originate as multimodal. (**A**) (Left) Experimental design. (Right) Calcium responses in the cortex (pink) elicited by mechanical stimulation of the whisker pad in control mice at E18 and P0. (**B**) Proportion of the whisker pad stimulations that evoked a contralateral or ipsilateral response in S1 and V1 of control mice at E18, and in V1 from E18 to P6 (E18, *n* = 9 mice; P0, *n* = 13 mice; P3 to P6, *n* = 8 mice). (**C**) Scheme summarizing the results. (**D**) (Left) Experimental design. (Right) Calcium responses in the cortex (pink) elicited by mechanical stimulation of the whisker pad in embBE mice at E18 and P0. (**E**) Proportion of the whisker pad stimulations that evoked a contralateral or ipsilateral response in S1 and V1 of control and embBE mice at P0 (*n* = 19 control mice, *n* = 21 embBE mice). (**F**) Scheme summarizing the results. (**G**) Proportion of the whisker pad stimulations that evoked a bilateral V1 response in embBE from E18 to P6 (E18, *n* = 5 mice; P0, *n* = 21 mice; P3, *n* = 5 mice; P5 to P6, *n* = 8 mice). Scale bars, 1000 μm. Bar graphs show the means ± SEM. ns, not significant; **P* < 0.05, ***P* < 0.01, ****P* < 0.001.

labeling of the contralateral dSC and sSC layers in embBE mice, whereas only the contralateral dSC layer was labeled in their control littermates (Fig. 2, I and J). Conversely, when the multimodal response finally switched to unimodal in the embBE mice at P6, we observed a significant reduction, as compared with P0, both in the number of axons in the sSC and in the bilateral V1 or SC activation elicited by whisker pad stimulation (fig. S6).

The data from the embBE suggest that the multimodal embryonic response in control mice could also be mediated by the SC. Using the *Cx-SC*^{GCaMP6f}, we found that whisker pad stimulation at E18 in control mice elicited a bilateral V1 response in 37% of the cases, which was always accompanied by concomitant bilateral sSC activation. However, activation of the sSC was not detected when the cortical multimodal response switched to unimodal at P0 (Fig. 3, A to C). We then tested whether the switch from multimodal to unimodal cortical responses involved a developmental reconfiguration of the intracollicular circuits. As such, we injected a lentivirus-expressing EGFP unilaterally into the SC at E14 and analyzed the disposition of the axons in the contralateral sSC at E18 and P0. We detected significantly more labeled axons in the sSC layer at E18 than at P0 (Fig. 3D). This unplugging of the sSC layer from the dSC layer, which was delayed in embBE mice, coincides with the peak innervation of retinocollicular axons (Fig. 3E) (*7*). These results suggest that the arrival of retinal axons to the SC prompts the segregation of somatosensory and visual circuits.

Perinatal retinal waves drive the SC circuit reorganization

Developing retinal axons convey a stereotyped pattern of spontaneous activity known as retinal waves. Stage I retinal waves, which are mediated by gap junctions, last approximately from E17 until P1 in mice (Fig. 3F) (*13*), and therefore, we tested whether these waves might play a role in directing intracollicular sensory-modality segregation. We blocked stage I retinal waves by injecting the gap junction blocker carbenoxolone (cbx) (*13*, *14*) into both eyes of *Cx*^{GCaMP6f} mice at P0. To confirm that cbx blocks gap junction–mediated retinal waves in vivo, we recorded spontaneous activity in V1, the frequency of which was reduced significantly 1 hour after the administration of cbx at P0 (fig. S7, A and B). This reduction was not due to the degeneration of retinofugal axons because these axons reached both the thalamus and the SC (fig. S7C), and visual spontaneous activity was recovered at P6 (fig. S7, A and B). Accordingly, acute administration of epibatidine, a high-affinity cholinergic agonist that inhibits postnatal stage II retinal waves (*15*–*17*), significantly reduced the frequency of spontaneous activity in V1 at P6, whereas cbx had no such effect at this stage (fig. S7, D and E). Altogether, these experiments show that most of V1 activity at the perinatal stage in vivo is driven by gap junction–mediated retinal waves.

We next recorded the cortical activity after whisker pad stimulation in *Cx*^{GCaMP6f} mice treated with cbx at P0 (Fig. 3G). Seven to 8 hours after cbx administration, stimulation of the whisker pad triggered in all mice a multimodal response that was elicited in 44% of the trials and that rose to 64% after a second injection of cbx on the following day (Fig. 3, G to I, and movies S9 and S10). By contrast, this multimodal response was not triggered by the injection of saline or epibatidine (Fig. 3, G to I). Cbx administration to *Cx-SC*^{GCaMP6f} mice at P0 showed concomitant bilateral responses in the V1 and SC at P1 (fig. S8, A to C, and movie S11), which were abolished by TTX acute injection into the SC (fig. S8, D and E). As in the embBE, lentiviral tracing in the SC of cbx-treated mice showed the abnormal invasion of axons from the dSC layer into the sSC layer at P1 (Fig. 3J). Last, we checked whether the responses to whisker pad stimulation eventually switch to unimodal in the cbx-treated mice. When we performed the whisker pad stimulation in the *Cx*^{GCaMP6f} and triple *Cx-SC*^{GCaMP6f} mice, we found that the multimodal responses both in the V1 and SC were almost absent by P6 (fig. S8, F to I). These data show that the timely segregation of somatosensory and visual pathways require a perinatal reorganization of intracollicular circuits that depends on gap junction–mediated retinal waves.

Failure to timely segregate drives long-lasting circuit alterations

Although reversed by the end of the first postnatal week, the transient expansion of the multimodal phase may have long-term effects

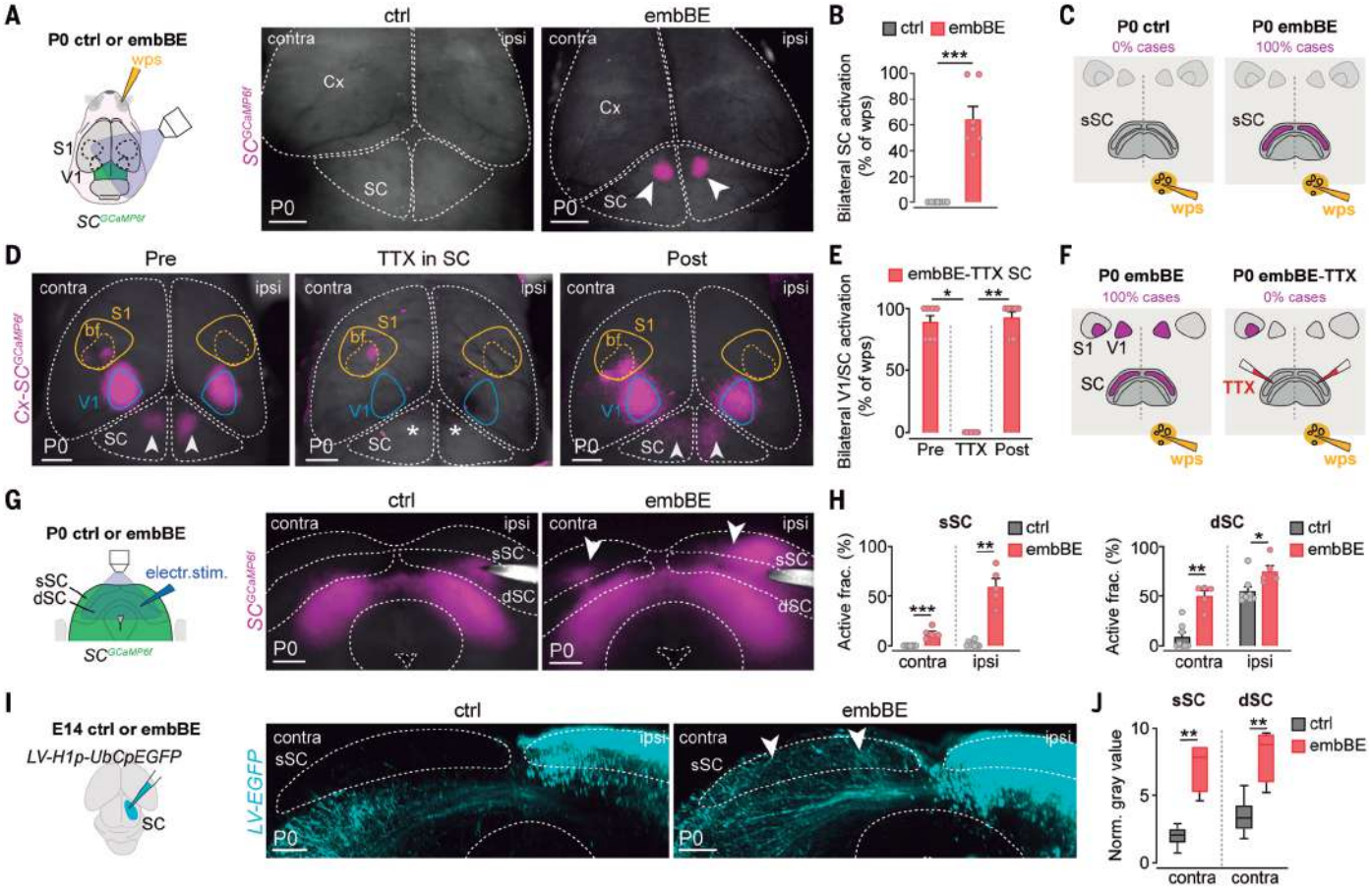

Fig. 2. Somatosensory and visual SC circuits remain intermingled in embBE mice. (**A**) (Left) Experimental design. (Right) Calcium responses (pink) in the SC elicited by mechanical stimulation of the whisker pad in control and embBE mice at P0. (**B**) (Left) Quantification of the data shown in (A) (n = 7 control mice, n = 7 embBE mice). (**C**) Scheme summarizing the data. (**D**) Cortical and SC calcium responses elicited by mechanical stimulation of the whisker pad in embBE mice at P0 before, during, and 1 hour after bilateral TTX injection in the SC (asterisks). (**E**) Quantification of the data shown in (D) (n = 6 mice). (**F**) Scheme summarizing the data. (**G**) (Left) Experimental design. (Right) Calcium responses elicited by electrical stimulation of the dSC in control and embBE slices at P0. There is spreading to the ipsilateral and contralateral superficial layers of the SC in embBE mice (arrowheads). (**H**) Proportion of the total area (active fraction) of the sSC and dSC layers activated by a perithreshold stimulus in the dSC at P0 (n = 8 control mice, n = 5 embBE mice). (**I**) (Left) Experimental design. The lentivirus was injected into the SC at E14. (Right) Optical coronal sections from three-dimensional (3D) light-sheet images showing the EGFP lentiviral–labeled axons in the sSC of embBE mice at P0 (arrowhead). (**J**) Quantification of the normalized EGFP expression in contralateral sSC and dSC (n = 8 control mice, n = 4 embBE mice). Scale bars, (A) and (D) 1000 μm; (G) and (I) 150 μm. Boxplots show the medians with the interquartile range (box) and range (whiskers). The bar graphs show the means ± SEM. ns, not significant; *P < 0.05, **P < 0.01, ***P < 0.001.

on the specification of sensory circuits. For example, perinatal blockage of retinal activity might cause enduring changes in the transcriptional program of SC layers. To assess this, we performed bulk RNA-sequencing (RNA-seq) of the sSC and dSC layers at P6 in mice treated with saline or cbx at P0 to P1 (Fig. 4A). A principal components analysis (PCA) revealed that sSC and dSC cells clustered according to their anatomic origins (fig. S9A). Moreover, a differential expression analysis (DEA) in saline conditions revealed 1544 differentially expressed genes (DEGs) enriched in the sSC as opposed to 1549 in the dSC layers (Fig. 4A and table S1). Among the DEGs enriched in each population, we found genes previously identified as layer-specific markers, including those encoding transcription factors such as *Rorb* and *Barhl1* in the sSC layer or *Pou4f1* and *Pou4f2* in the dSC layer (*18*, *19*). To determine whether cbx may influence SC layer–specific genes, we compared the RNA-seq data between mice that received saline or cbx and found that cbx significantly modified 24% (370 genes) of the sSC-specific genes and 21.1% (326 genes) of the dSC-specific genes (Fig. 4B, fig. S9B, and table S2). Among these, cbx induced the expression of a large proportion of the dSC-specific genes (285 out of 326 genes) in the sSC layer, and that of sSC-specific genes (168 out of 370 genes) in the dSC layer. Likewise, it provoked the down-regulation of layer-specific gene expression to levels resembling those in the other layer (Fig. 4C and fig. S9, C and D). Together, these results demonstrate that the somatosensory and visual molecular identity of SC layers was altered by the blockade of stage I retinal waves (Fig. 4D).

The alterations to the modality-specific identity of sSC and dSC may somehow affect the stereotypic organization of incoming inputs to these layers. Within the visual system, retinocollicular axons are organized in eye-specific segregated clusters in the sSC (*7*, *20*), and therefore, we tested whether eye-specific segregation is disrupted in cbx-treated mice. Cholera toxin subunit B (CTB) injection into the eyes of perinatally cbx-treated mice (fig. S10A) showed a compromised eye-specific segregation in the sSC at P15. Whereas in the saline condition, contralateral and ipsilateral axons segregated into dorsal and ventral sSC compartments, respectively, the ipsilateral axons in cbx-treated mice invaded the dorsal compartment and

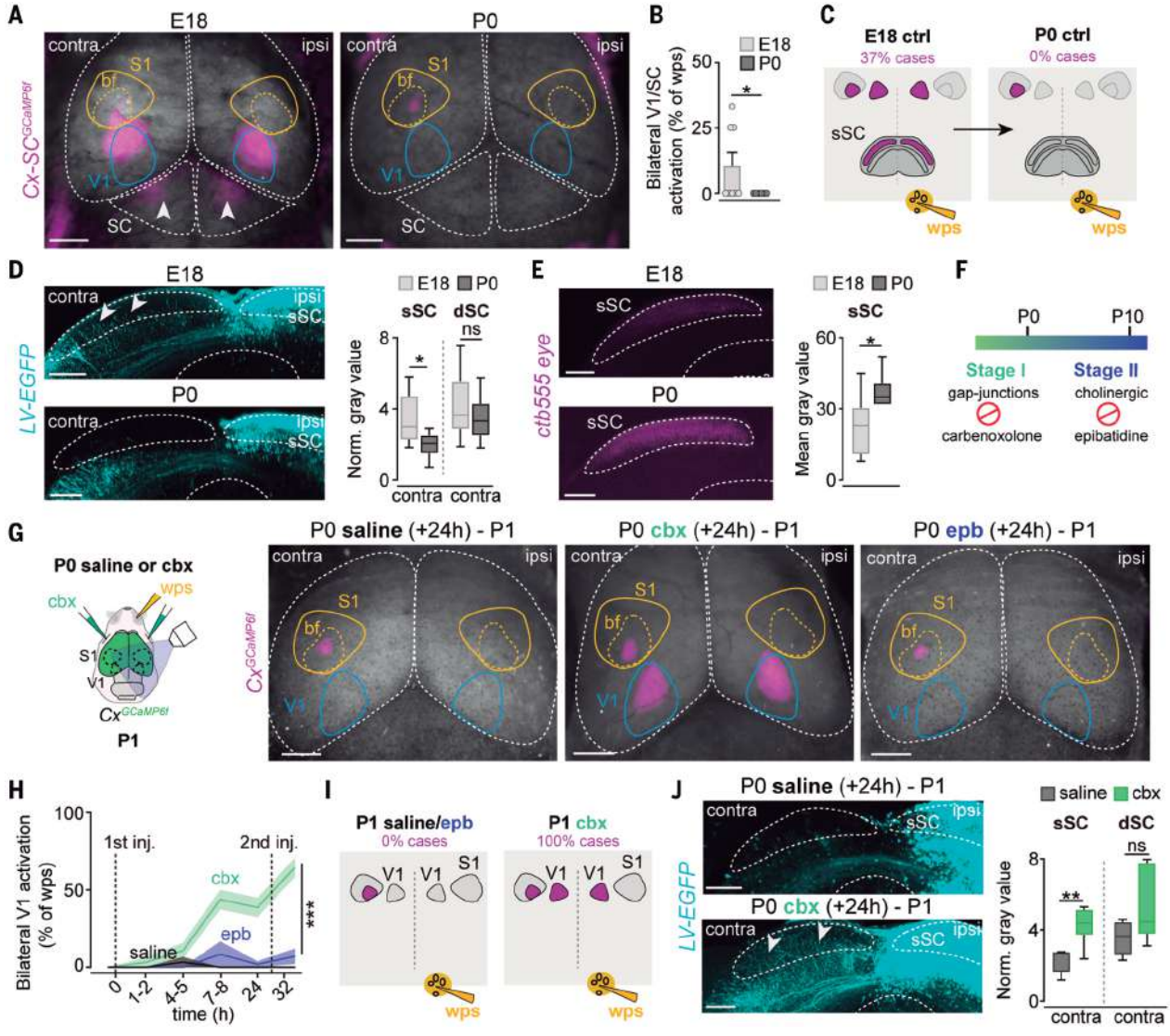

Fig. 3. Blocking stage I retinal waves prolongs the multimodal configuration. (**A**) Whisker pad stimulation leads to the concomitant bilateral activation of both V1 and SC in control E18 mice, which switches to unimodal at P0. (**B**) Quantification of the data shown in (A) (n = 8 E18, n = 13 P0). (**C**) Scheme summarizing the data. (**D**) (Left) Optical coronal sections from 3D light-sheet images showing EGFP lentiviral–labeled axons in the sSC of control E18 (arrowheads) but not P0 mice. The lentivirus was injected into the SC at E14. (Right) Quantification of the normalized EGFP expression in contralateral sSC and dSC (n = 9 E18 mice, n = 8 P0 mice). (**E**) (Left) Coronal views of retinal axons labeled by CTB injection of the eye at E14 that reach the SC at E18 and P0. (Right) Quantification of the data shown at left (n = 9 E18 mice, n = 6 P0 mice). (**F**) Scheme showing early phases of retinal waves. (**G**) (Left) Experimental design. (Right) Cortical calcium responses at P1 elicited by mechanical stimulation of the whisker pad after bilateral injection of (left) saline, (middle) cbx, and (right) epibatidine (epb) into the eye at P0. (**H**) Proportion of the whisker pad stimulations that evoked a bilateral V1 response before and after the injection of saline, cbx, or epb: time (t) = 0, n = 20 mice injected with saline, n = 24 cbx, n = 17 epb; t = 1 to 2 hours, n = 4 saline, n = 8 cbx, n = 6 epb; t = 4 to 5 hours, n = 6 saline, n = 7 cbx, n = 9 epb; t = 7 to 8 hours, n = 7 saline, n = 4 cbx, n = 3 epb; t = 24 hours, n = 19 saline, n = 14 cbx, n = 13 epb; and t = 32 hours, n = 11 saline, n = 12 cbx, n = 7 epb. (**I**) Scheme summarizing the data. (**J**) (Left) Optical coronal sections from 3D light-sheet images showing lentiviral EGFP–labeled axons in the sSC of P1 mice treated at P0 with cbx (arrowheads) but not with saline. The lentivirus was injected into the SC at E14. (Right) Quantification of the normalized EGFP expression in contralateral sSC and dSC (n = 5 saline, n = 6 cbx). Scale bars, (A) and (G) 1000 μm; (D) 200 μm; (E) 250 μm; (J) 200 μm. Boxplots show the medians with the interquartile range (box) and range (whiskers). The bold lines in (H) indicate the mean, and the shading indicates the SEM. The bar graphs in (B) show the mean ± SEM. ns, not significant; $^*P < 0.05$, $^{**}P < 0.01$, $^{***}P < 0.001$.

mingled with the contralateral axons (Fig. 5, A and B, and movies S12 and S13). In addition, small dye crystals placed in V1 at the azimuth and elevation axis at this stage also showed alterations in the fine-scale organization of the geniculo-cortical pathway (Fig. 5, C and D, and fig. S10, B to D). Together, these results demonstrate that early perturbations in retinal activity leads to long-lasting circuit reconfiguration at central stations within the visual pathway.

Discussion

Our findings demonstrate that visual and somatosensory pathways emerge as multimodal circuits, and that during perinatal life, they segregate in a manner that is orchestrated in the SC. The multimodal-to-unimodal transition requires a reconfiguration of intracollicular circuits at birth, in which dSC layers disconnect from the sSC layers. This reconfiguration drives the specificity of sensory circuits, so that whisker pad stimulation exclusively triggers S1 responses in the cortex after birth. The switch

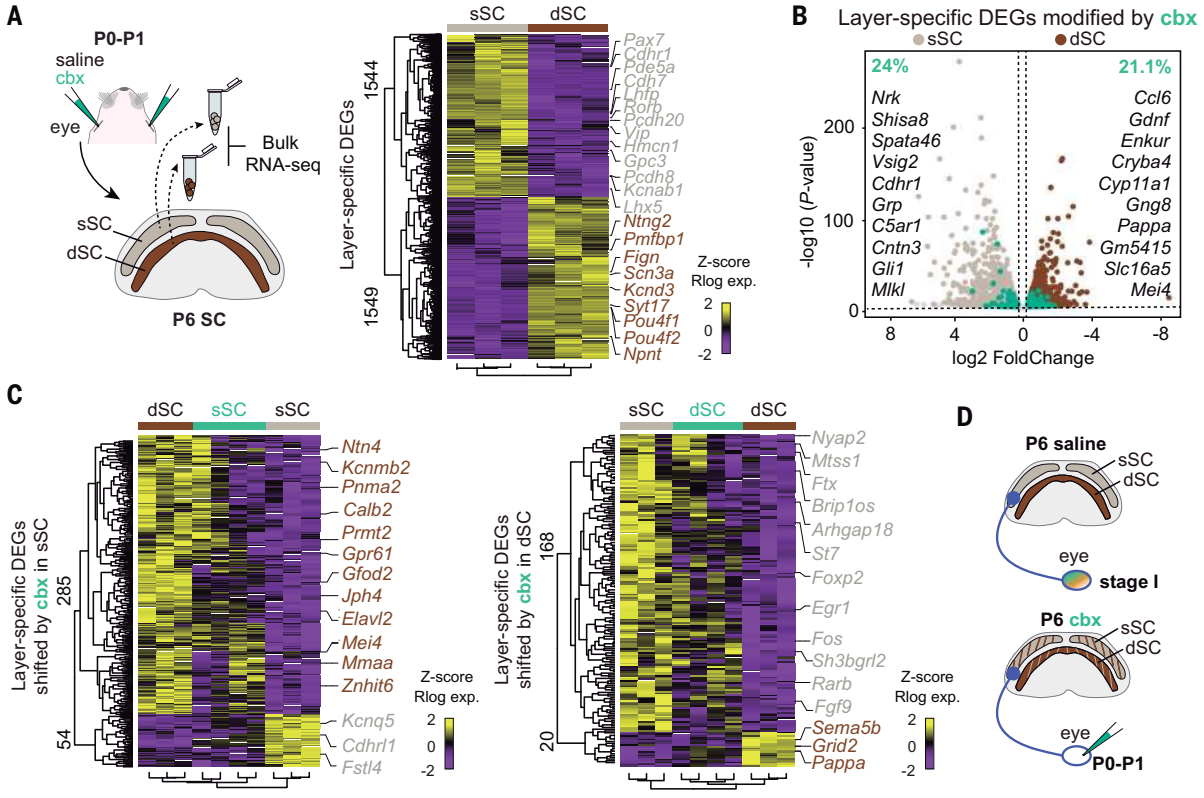

Fig. 4. Transcriptomic SC alterations following blockade of perinatal retinal waves. (**A**) (Left) Scheme of the RNA-seq experiments of sSC and dSC tissue from P6 mice treated with saline and cbx at P0-P1. (Right) Heatmap of normalized, regularized logarithm (Rlog) *z*-score of expression, and unbiased clustering of significant DEGs between the sSC and dSC in saline-treated mice. Each row represents a gene, and the columns are biological replicates. The color code indicates the normalized expression for up-regulated genes in yellow versus down-regulated genes in purple. Highlighted genes are those previously identified as layer-specific markers. (**B**) Volcano plot showing the significance and *P* value distribution of DEGs. The light brown and dark brown dots indicate sSC and dSC DEGs, respectively, and the green dots and the percentages indicate layer-specific DEGs shifted by cbx, with the top 10 protein coding genes listed in every region. (**C**) Heatmaps of the normalized regularized logarithm (Rlog) *z*-score of expression and unbiased clustering of layer-specific DEGs whose expression was modified by cbx in the sSC and dSC regions. (**D**) Scheme summarizing the data.

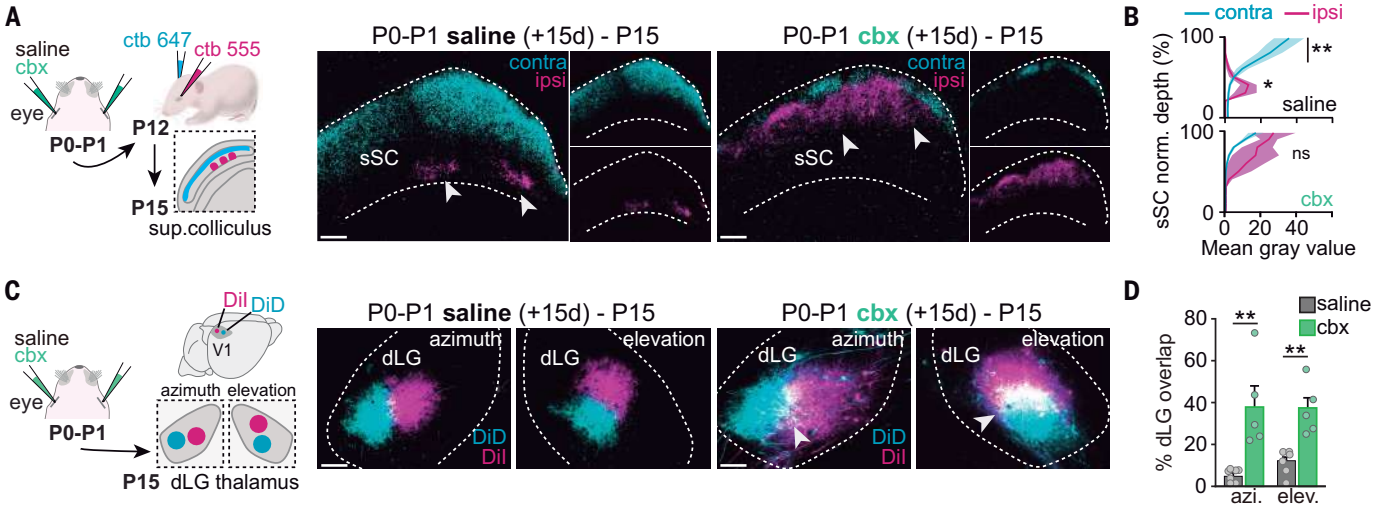

Fig. 5. Long-term alterations in eye-specific segregation and retinotopy after blockade of perinatal retinal waves. (**A**) (Left) Experimental design. (Right) Coronal view of the SC showing axons from the ipsilateral (CTB-555) and contralateral (CTB-647) eye at P15 in saline- and cbx-treated mice. (**B**) Quantification of the data in (A) (contralateral, *n* = 10 saline, *n* = 6 cbx; ipsilateral, *n* = 7 saline, *n* = 5 cbx). (**C**) (Left) Experimental design. (Right) Coronal view of the dLG showing back label from DiI and DiD crystals in V1 at P15 in saline- and cbx-treated mice. (**D**) Quantification of the data shown in (C) (azimuth, *n* = 7 saline, *n* = 5 cbx; elevation, *n* = 6 saline, *n* = 5 cbx). Scale bars, 100 μm. The bold lines in (B) indicate the mean, and the shading indicates the SEM. Bar graphs show the mean ± SEM. ns, not significant; *$P < 0.05$, **$P < 0.01$.

from multimodal to unimodal requires early retinal activity because perturbation of stage I retinal waves prevents the reconfiguration of the circuits in the SC and leads to the extension of the multimodal phase into postnatal life. Therefore, these data broaden our understanding of retinal wave function by revealing their instructive role in the acquisition of sensory modality specificity, which is beyond their classic role in the postnatal refinement of visual circuits (*21*–*25*).

The segregation of visual from somatosensory systems must occur in a limited developmental window because any delay in this segregation will cause long-lasting changes in the intramodal organization of visual circuits. The mechanisms that mediate the final closing of the multimodal phase in embBE and cbx-treated mice remain unexplored, although they may include the influence of passive whisking during the first days of life (*26*) or the progressive assembly of inhibitory cells into the networks of the SC, as described for cortical networks (*27*). A longitudinal analysis of both the molecular identity of collicular neurons and the maturation of their connectivity in physiological and in manipulated scenarios will help identify the cell types and potential factors involved in this circuit segregation and plasticity.

Last, our findings reveal that the SC, a highly conserved structure in vertebrates (*28*, *29*), participates in the construction of brain regions that appeared more recently in phylogenetic terms such as the neocortex, a role that goes far beyond the SC's well-established sensorimotor and multimodal integrative functions (*30*). From the phylogenetic perspective, it has been stated that the visual cortex has inherited an increasing number of functions from the SC related to the processing of visual features (*31*–*33*). Our results spotlight the ontogenetic perspective, in which the developing SC exerts a master control on cortical specification and configuration of visual circuits. Thus, we believe that a deeper understanding of the functional development of phylogenetically ancient structures is crucial to understand how the neocortex is formed and its functional areas are specified.

REFERENCES AND NOTES

1. B. Tasic *et al*., *Nature* **563**, 72–78 (2018).
2. C. R. Cadwell, A. Bhaduri, M. A. Mostajo-Radji, M. G. Keefe, T. J. Nowakowski, *Neuron* **103**, 980–1004 (2019).
3. A. Simi, M. Studer, *Curr. Opin. Neurobiol.* **53**, 96–102 (2018).
4. F. J. Martini, T. Guillamón-Vivancos, V. Moreno-Juan, M. Valdeolmillos, G. López-Bendito, *Neuron* **109**, 2519–2534 (2021).
5. Z. Molnár, H. J. Luhmann, P. O. Kanold, *Science* **370**, eabb2153 (2020).
6. N. Antón-Bolaños *et al*., *Science* **364**, 987–990 (2019).
7. P. Godement, J. Salaün, M. Imbert, *J. Comp. Neurol.* **230**, 552–575 (1984).
8. M. A. Edwards, V. S. Caviness Jr., G. E. Schneider, *J. Comp. Neurol.* **248**, 395–409 (1986).
9. M. A. Edwards, G. E. Schneider, V. S. Caviness Jr., *J. Comp. Neurol.* **248**, 410–421 (1986).
10. V. Moreno-Juan *et al*., *Nat. Commun.* **8**, 14172 (2017).
11. J. Cang, D. A. Feldheim, *Annu. Rev. Neurosci.* **36**, 51–77 (2013).
12. M. Ahmadlou, L. S. Zweifel, J. A. Heimel, *Nat. Commun.* **9**, 3895 (2018).
13. A. G. Blankenship, M. B. Feller, *Nat. Rev. Neurosci.* **11**, 18–29 (2010).
14. W. T. Wong, J. R. Sanes, R. O. Wong, *J. Neurosci.* **18**, 8839–8852 (1998).
15. J. B. Ackman, T. J. Burbridge, M. C. Crair, *Nature* **490**, 219–225 (2012).
16. A. A. Penn, P. A. Riquelme, M. B. Feller, C. J. Shatz, *Science* **279**, 2108–2112 (1998).
17. C. Sun, C. M. Speer, G. Y. Wang, B. Chapman, L. M. Chalupa, *J. Neurophysiol.* **100**, 3253–3263 (2008).
18. Z. Xie *et al*., *eLife* **10**, e69825 (2021).
19. A. Zeisel *et al*., *Cell* **174**, 999–1014.e22 (2018).
20. T. A. Seabrook, T. J. Burbridge, M. C. Crair, A. D. Huberman, *Annu. Rev. Neurosci.* **40**, 499–538 (2017).
21. T. J. Burbridge *et al*., *Neuron* **84**, 1049–1064 (2014).
22. J. B. Ackman, M. C. Crair, *Curr. Opin. Neurobiol.* **24**, 166–175 (2014).
23. C. L. Torborg, M. B. Feller, *Prog. Neurobiol.* **76**, 213–235 (2005).
24. J. Cang *et al*., *Neuron* **48**, 797–809 (2005).
25. H. P. Xu *et al*., *Neuron* **70**, 1115–1127 (2011).
26. A. Tiriac, B. D. Uitermarkt, A. S. Fanning, G. Sokoloff, M. S. Blumberg, *Curr. Biol.* **22**, 2075–2080 (2012).
27. L. Modol *et al*., *Neuron* **105**, 93–105.e4 (2020).
28. J. Cang, E. Savier, J. Barchini, X. Liu, *Annu. Rev. Vis. Sci.* **4**, 239–262 (2018).
29. M. A. Basso, P. J. May, *Annu. Rev. Vis. Sci.* **3**, 197–226 (2017).
30. T. Isa, E. Marquez-Legorreta, S. Grillner, E. K. Scott, *Curr. Biol.* **31**, R741–R762 (2021).
31. L. Zhaoping, *Curr. Opin. Neurobiol.* **40**, 94–102 (2016).
32. R. Beltramo, M. Scanziani, *Science* **363**, 64–69 (2019).
33. L. L. Glickfeld, M. H. Histed, J. H. Maunsell, *J. Neurosci.* **33**, 19416–19422 (2013).

ACKNOWLEDGMENTS

We thank L. M. Rodríguez, R. Susín, and B. Andrés for their technical support; S. Martinez for providing the *Engrailed 1-Cre* mouse; and S. Jurado for the plasmid used to generate the lentivirus-EGFP. We thank D. Jabaudon, J. López-Atalaya, and B. Berninger for critical reading of the manuscript and the members of López-Bendito's laboratory for stimulating discussions. **Funding:** This work was supported by the European Research Council (ERC-2014-CoG-647012), the Spanish Ministry of Science, Innovation and Universities (PGC2018-096631-B-I00), a Severo Ochoa Grant (SEV-2017-0723), and the European Research Council (ERC-2020-StG-950013). **Author contributions:** T.G.-V. and G.L.-B. designed the experiments. T.G.-V. and F.J.M. performed the analysis of the activity data. T.G.-V. conducted all the meso-scale calcium imaging in vivo. J.A.M.-B. and M.A.-M. performed the tracing experiments. M.A.-M. performed the bulk-sequencing experiments, and L.P.-A. performed the bioinformatics analysis. F.J.M. adapted and developed the Matlab codes for the analysis. G.L.-B. acquired the funding, and T.G.-V., F.J.M., M.V., and G.L.-B. wrote the paper. **Competing interests:** The authors have no competing interests to declare. **Data and materials availability:** All the data are available in the main text or the supplementary materials. The RNA-seq data generated in this study has been deposited in the NCBI Gene Expression Omnibus repository under accession GSE198112 (https://www.ncbi.nlm.nih.gov/geo/query/acc.cgi?acc=GSE198112).

SUPPLEMENTARY MATERIALS

science.org/doi/10.1126/science.abq2960
Materials and Methods
Figs. S1 to S11
References (*34*–*38*)
MDAR Reproducibility Checklist
Movies S1 to S13
Tables S1 and S2

View/request a protocol for this paper from *Bio-protocol*.

Submitted 10 April 2022; accepted 21 July 2022
10.1126/science.abq2960

Science

Input-dependent segregation of visual and somatosensory circuits in the mouse superior colliculus

Teresa Guillamón-VivancosMar Aníbal-MartínezLorenzo Puche-ArocaJuan Antonio Moreno-BravoMiguel ValdeolmillosFrancisco J. MartiniGuillermina López-Bendito

Science, 377 (6608), • DOI: 10.1126/science.abq2960

Allocating sensory responsibilities

During late embryogenesis, the developing mouse brain has inputs from both visual and sensory systems that activate overlapping regions of the cortex. Guillamón-Vivancos *et al*. now show how spontaneous activity in the perinatal retina tunes the visual cortex to specialize in interpreting retinal activity as vision. Without such spontaneous retinal activity, this part of the brain will take on somatosensory responsibilities instead. This handshake between the sensory system and the cortical recipient is established during a limited time in the perinatal phase of development. —PJH

Science (ISSN) is published by the American Association for the Advancement of Science. 1200 New York Avenue NW, Washington, DC 20005. The title *Science* is a registered trademark of AAAS.

AGRADECIMIENTOS

Todavía recuerdo el día en que decidí volver a Alicante, a casa. Estaba empeñada en hacer la tesis en Madrid, y en el proceso, había perdido un poco el norte sobre lo que realmente quería: el tipo de laboratorio en el que me gustaría investigar y el enfoque que deseaba darle a mi trabajo. Tras varias solicitudes para posiciones que no terminaban de motivarme, lo vi claro. En Alicante había un grupo que estudiaba la plasticidad en los sistemas sensoriales durante el desarrollo, y la idea me enamoró. Además, este grupo tenía una proyección muy buena, y no me equivoqué; de hecho, terminó superando todas mis expectativas.

Decidí escribir a Guille, fui a la entrevista, conocí al equipo y sus proyectos, y me cautivaron dos en particular: uno sobre cómo el cerebro potencia el sistema del tacto en individuos ciegos de nacimiento y otro sobre el papel de la actividad espontánea del tálamo en la formación de los mapas táctiles durante el desarrollo. Y boom! Lo tuve claro. Aquello sí me motivaba: las preguntas eran fascinantes y las técnicas, impresionantes. No tuve que pensarlo mucho, acepté, me mudé, volví a casa de mis padres (por poco tiempo) y, sin saberlo, inicié el viaje que más me ha cambiado la vida.

En primer lugar, gracias, Guille, por darme la oportunidad de hacer la tesis contigo. He aprendido mucho de ti, tanto a nivel personal como a nivel científico. Me has impulsado a superarme cada día, pero también has estado ahí para escucharme y apoyarme en los momentos en que necesitaba respirar hondo. Siempre he sentido tu confianza y tu orgullo hacia mí, y eso ha significado muchísimo. Ha sido un honor y un privilegio formar parte de tu equipo. Gracias por todo, Guille.

A todas las personas que han pasado por el laboratorio y, por tanto, por mi vida, gracias. Fran y Miguel, siempre habéis sido ese lugar de calma al que acudir en busca de ayuda. Fran, recuerdo cuando dijiste que lo que más valorabas de Miguel era su disposición a dejar lo que estuviera haciendo en ese momento para intentar echar una mano a quien tocara a su puerta, y así es como también lo recuerdo yo. Quiero que sepas, Fran, que tú aprendiste bien esa lección.

Belén y Luis, habéis sido los mejores compañeros de viaje. Me habéis cuidado como solo lo hace la familia. Luis, gracias por esa sonrisa, mueca o toquecito en las costillas cada día, gracias por tu mirada cómplice y por estar tan pendiente de mí. Belén, gracias por ser mi salvavidas cada vez que me he caído por la borda, no he necesitado gritar ayuda porque tú

siempre estabas preparada para lanzarte al mar. Soy muy afortunada de haberos tenido a mi lado y de llevarme dos amigos tan valiosos.

A mis compañeros Lorenzo, Chrysa y Elena. Lorenzo, hemos estado mano a mano librando mil batallas, siempre con paciencia y buen humor. Echaré de menos un compañero como tú en cualquier trabajo futuro. Chrysa, pequeña Chrysoulina, gracias por tu calidez y por estar siempre ahí con un abrazo para mí, eres una persona muy bonita. Elena, llegaste tarde a esta fiesta, pero desde el principio supe que hacíamos match. Me has acompañado en esta dura recta final, y sé que nos seguiremos acompañando en mucho más.

Noe, Kika y Álvaro, fuisteis un referente para mí al llegar al laboratorio, erais el espejo en el que quería reflejarme. Me transmitisteis motivación, perseverancia, resiliencia y espíritu crítico. Vuestra ausencia pesó muchísimo en el laboratorio, y espero haber estado a la altura de vuestro legado.

A Irene, Ana, Helena, Alejandro, Juan Antonio, Tere, Pablo, Dorien, Edu, Vero, Aurelia, Luwei, Eleni, Jessica y Emily, gracias por estar ahí. Gracias por ser siempre un confort place para mí. Ana, eres una tía estupenda y me alegra mucho saber que seguiremos compartiendo risas, cañas y piscinas con los niños. Helen, qué quebraderos de cabeza me has dado y qué cariño te he cogido. Alejandro, otro que no pasaba desapercibido ni un solo día; compartir el 133 contigo fue divertido (aunque a veces exasperante). Juan Antonio, gracias por tu sabiduría y tu toque de marujeo. Tere, siempre con una palabra de aliento, ha sido un placer trabajar contigo. Edu y Vero, trajisteis frescura y buen rollo al laboratorio. Eleni, you are worth so much, and you're going to do great, I have so much faith in you. Jessica, eres una personaja de cuidado y me encanta haberte conocido. Emily, your laughter and sense of humor are one of a kind, never change.

Gracias a todas las demás personas del instituto con quienes he compartido momentos, espero no olvidarme de nadie. A las chicas del animalario y a Gonzalo. Jenni, Erika, Lorena, Patri, Vero, Rebeca y Fani, siempre habéis hecho excepciones conmigo cuando me he colado con algún servicio y os he llamado suplicando clemencia. A Maite, por haberme ayudado cuando lo he necesitado. A Almu por estar ahí con el confocal en la recta final de mi paper, lo valoro mucho. A Raquel y Ana Moreno, por ser un refugio seguro y divertido al que acudir, me lo he pasado muy bien con vosotras, chicas. Y a Cristian, por ser tan buena gente, porque si hubiera más Cristians, el mundo sería un lugar mejor.

Ah, y cómo no mencionar a mis Sevillanos... Cada año, sin falta, nos hemos juntado en un lugar diferente del mundo para hacer que la SENC o FENS de turno fuera inolvidable. Marta, Silvia, Génova, Rosendo, Ana, Nene y Edu, gracias por todos esos momentos.

Óscar, gracias por ser el mejor compañero de buceo, por las maniobras de rescate subacuático cuando me da una rampa y por mostrar cero interés cuando te enseño nudibranquios. Gracias por compartir conmigo el placer de la comida.

Cris, también conocida como Cris GPS por tus grandes dotes de geolocalización, eres una amiga increíble y la persona más detallista que conozco. Gracias por alegrarte de cada logro y celebrarlo conmigo, me acuerdo mucho de aquella botella de cava que nos pimplamos en la Almadraba para celebrar mi primer paper, y sé que siempre vamos a estar la una para la otra.

Pili, juntas somos MariPili, y yo siento que contigo todo es siempre muy fácil. Cada entrenamiento contigo ha sido un espacio de desconexión y desahogo, nos hemos superado juntas haciendo el monkey bar o trepando la cuerda. Aún recuerdo cuando, espalda con espalda hicimos varias dominadas seguidas y corriendo nos giramos para decírselo a la otra flipando. Me has hecho superarme en muchos sentidos (tú siempre fuiste perfecta). Me haces bien.

Fuera del instituto, he estado siempre apoyada por mi familia y amigos. Patricia, gracias por todo tu cariño. Iris, has estado en mi vida desde los 4 años, estabas incluso cuando rellenamos el formulario para entrar en la universidad, tú a empresariales y yo a biología. Y cómo no, has seguido acompañándome en cada paso que he dado desde entonces hasta aquí, y sé que así seguirá siendo. Ana Palazón, tú también has vivido muy de cerca todo esto y siempre he sentido tu apoyo y confianza. No voy a olvidar el sinfín de risas, las mil cervezas a tu lado, ni nuestro romance en cuarentena viéndonos en los límites de Campello y Alicante. Pablo Arnaiz, eres una de esas personas que dejan una huella cálida y confortable, gracias por ser y estar. Andrés, eres un tío único, creativo, inteligente y muy buena gente, gracias por dejarme conocerte y por abrirte conmigo (cada día un poquito más).

A mis tíos Cris y Tomás, por confiar siempre en mí y hacerme sentir vuestro orgullo. Gracias Cris por tu ternura y por ser tan divertida. A mis tías, Ana e Isabel, que me animaron a estudiar biología cuando todos pensaban que era una carrera sin salidas. Gracias por la profunda conexión que hemos construido, donde hay amor, confianza, respeto y admiración mutua. Nada habría sido lo mismo sin vosotras.

A mis abuelos, Paco y Rodolfo, al primero por enseñarme a ser curiosa haciéndome vivir aventuras, y al segundo por todas esas clases de maestro de verano cuando era niña. Y a mi abuela Dorita, mi Tita, por ser un ejemplo de bondad sin dobleces, fuiste una de las mayores suertes de mi vida.

Y, cómo no, mis dos pilares: Julia y Pablo. Me siento tan afortunada de teneros, que no podría encontrar las palabras apropiadas para expresarlo. Con vosotros me siento en casa, en una casa segura donde ser yo, sin juicios ni castigos, sois mis constantes desde hace 16 años. A Pablo, gracias por compartir conmigo el primer año y medio de tesis, por ser comprensivo, cuidarme, escucharme, animarme y ser el mejor amigo del mundo. Hemos crecido tanto y cambiado tanto a lo largo de este tiempo, que me emociona profundamente saber que seguimos en la misma línea. Somos las mismas placentas lloronas de siempre cuando nos ponemos intensas, y las mismas disfrutonas cuando estamos juntas con cerveza en mano. A Julia, gracias por aparecer siempre cuando te necesito, por ser mi vía de escape, por recordarme lo realmente importante en la vida. Te admiro muchísimo, no sería quién soy si tú no hubieras pasado por mi vida, he aprendido mucho de ti. Tenemos mil anécdotas, pero ahora recuerdo mucho las quedadas en el espigón en cuarentena y los toques de queda, saliendo de tu casa como el rey de los guardias. Tal vez lo recuerdo porque me siento igual de encerrada durante este mes y medio de escritura, pero esos momentos eran un bálsamo para mí con todo lo que estaba pasando en el mundo. Este viaje ha terminado, pero mi pasaporte va grapado de por vida al vuestro.

Vero, chulita, gracias por aparecer en el peor de los timings y, aun así, quedarte. Gracias por cuidarme como lo haces, por cambiarme la vida y por creer tanto en mí. Terminar esta etapa contigo ha sido todo un regalo. Te diría un millón de cosas que ya sabes, pero lo voy a resumir con algo de la primera peli que vimos juntas: has llenado mi vida de recuerdos esenciales. Gracias por todo. Lo mejor está por venir.

Gracias a mi hermano por su apoyo paciente, prudente, atento, guasón y cariñoso, aunque no te guste reconocerlo. Y, finalmente, gracias a mis padres, por estar siempre ahí, creer en mí y hacerme sentir su orgullo incondicional. Mamá, gracias por apoyarme en todo y anteponerme siempre. Papá, siempre dijiste que aparecerías en los agradecimientos de algo grande mío porque creías que llegaría lejos… Y aquí estás, no solo por imprimir apuntes, sino por mucho más. Habéis sido mi motor en cada paso. No puedo estar más orgullosa de vosotros.